

TALLINN UNIVERSITY OF TECHNOLOGY
DOCTORAL THESIS
53/2018

**Continuous Monitoring of Power System
Inertia and Transmission Loss
Components using Synchronized Phasor
Measurements**

KAUR TUTTELBERG

TALLINN UNIVERSITY OF TECHNOLOGY

School of Engineering

Department of Electrical Power Engineering and Mechatronics

This dissertation was accepted for the defence of the degree 15/08/2018

Supervisor: Dr. Jako Kilter
School of Engineering
Tallinn University of Technology
Tallinn, Estonia

Opponents: Prof. Vladimir Terzija
School of Electrical and Electronic Engineering
The University of Manchester
Manchester, United Kingdom

Prof. Dr.-Ing. Kai Strunz
Institute of Energy and Automation Technology
Technische Universität Berlin
Berlin, Germany

Defence of the thesis: 10/09/2018, Tallinn

Declaration:

Hereby I declare that this doctoral thesis, my original investigation and achievement, submitted for the doctoral degree at Tallinn University of Technology, has not been previously submitted for doctoral or equivalent academic degree.

Kaur Tuttelberg

signature

This work has received funding from the European Union's Horizon 2020 research and innovation programme under grant agreement No 691800 (MIGRATE project).

This research was supported by the national scholarship program Kristjan Jaak, which is funded and managed by the Archimedes Foundation in collaboration with the Ministry of Education and Research.

This work was supported by the Dora Pluss scholarship program.

This research was supported by Elering AS under the project "Development and analysis of wide area measurement system (WAMPAC)".



European Union
European Regional
Development Fund



Investing
in your future



HARIDUS- JA
TEADUSMINISTERIUM

ARCHIMEDES

elering
ÜHENDAME ENERGIAD

Copyright: Kaur Tuttelberg, 2018

ISSN 2585-6898 (publication)

ISBN 978-9949-83-316-0 (publication)

ISSN 2585-6901 (PDF)

ISBN 978-9949-83-317-7 (PDF)

TALLINNA TEHNIKAÜLIKOOL
DOKTORITÖÖ
53/2018

**Elektrisüsteemi inertsi ja
ülekandekadude komponentide pidev
jälgimine faasimõõtmiste abil**

KAUR TUTTELBERG

Contents

List of Publications	7
Author's Contribution to the Publications	9
Introduction	11
1 Wide Area Monitoring of Power Systems	15
1.1 Synchronized Phasor Measurements	15
1.2 Examples of Wide Area Monitoring Applications	18
1.3 Monitoring of Transmission Line Parameters	19
1.4 Summary	25
2 Uncertainties in Transmission Line Monitoring	27
2.1 Measurement Errors in the Measurement Chain	27
2.2 Uncertainty Analysis in Phasor Measurements	29
2.3 Uncertainty Propagation in Line Parameter Estimation	31
2.4 Analysis of Monitoring Data from a Real System	35
2.5 Conclusions	40
3 Monitoring of Corona Losses	41
3.1 Available Methods of Estimating Corona Losses	41
3.2 Transmission Losses from Synchronized Phasors	42
3.3 Uncertainty Propagation in Transmission Loss Monitoring	49
3.4 Validation of Estimated Corona Losses	51
3.5 Conclusions	54
4 Monitoring of Power System Inertia	55
4.1 Basics of Inertia and Frequency Dynamics	55
4.2 Available Methods of Estimating Inertia	58
4.3 Estimation of Area Inertia from Ambient Measurements	59
4.4 Validation of Inertia Estimation	66
4.5 Conclusions	73
Summary	75
References	79
Acknowledgments	87
Abstract	89
Lühikokkuvõte	91
Appendix A — Instrument Transformer Errors	93
Appendix B — Included Publications	97
Publication I	97
Publication II	109
Publication III	123
Publication IV	135
Publication V	143
Publication VI	151
Curriculum Vitae	159
Elulookirjeldus	161

List of Publications

The list of author's publications, on the basis of which the thesis has been prepared:

Publications in journals

- I K. Tuttelberg and J. Kilter, "Uncertainty propagation in PMU-based transmission line monitoring," in *IET Generation, Transmission & Distribution*, vol. 12, no. 3, pp. 745–755.
- II K. Tuttelberg and J. Kilter, "Estimation of transmission loss components from phasor measurements," in *International Journal of Electrical Power & Energy Systems*, vol. 98, pp. 62–71.
- III K. Tuttelberg J. Kilter, D. Wilson, and K. Uhlen, "Estimation of power system inertia from ambient wide area measurements," in *IEEE Transactions on Power Systems*, accepted for publication.

Publications in conference proceedings

- IV K. Tuttelberg and J. Kilter, "Real-time estimation of transmission losses from PMU measurements," *2015 IEEE Eindhoven PowerTech*, Eindhoven, The Netherlands, June 2015.
- V K. Tuttelberg, J. Kilter, and K. Uhlen, "Comparison of system identification methods applied to analysis of inter-area modes," *International Conference on Power System Transients (IPST 2017)*, Seoul, South Korea, June 2017.
- VI K. Tuttelberg and J. Kilter, "Predicting frequency disturbances from wide area monitoring of ambient power system dynamics," *8th IEEE PES Innovative Smart Grid Technologies Conference Europe (ISGT Europe 2018)*, Sarajevo, Bosnia and Herzegovina, October 2018.

The list of author's publications written during doctoral studies, not included in the thesis:

- K. Tuttelberg and J. Kilter, (2015). "Optimal placement of branch PMUs for specified redundancy and line observability," *2015 IEEE Power & Energy Society General Meeting (PESGM 2015)*, Denver, CO, July 2015.
- K. Tuttelberg and J. Kilter, "Modal transformation matrices for phasor measurement based line parameter estimations," *International Conference on Power System Transients (IPST 2015)*, Cavtat, Croatia, June 2015.
- I. Mickus, J. Dufek, and K. Tuttelberg, "Performance of the Explicit Euler and Predictor-Corrector-Based Coupling Schemes in Monte Carlo Burnup Calculations of Fast Reactors," in *Nuclear Technology*, vol. 191, no. 2, pp. 193–198.
- J. Dufek and K. Tuttelberg, "Monte Carlo criticality calculations accelerated by a growing neutron population," in *Annals of Nuclear Energy*, vol. 94, pp. 16–21.
- I. Kiitam, P. Taklaja, and K. Tuttelberg, "Voltage withstand properties of the insulation of different types of medium voltage covered overhead line conductors," *19th International Scientific Conference Electric Power Engineering 2018 (EPE 2018)*, Brno, Czech Republic, May 2018
- T. Kangro, J. Kilter, J. De Silva, K. Tuttelberg, and T. Sarnet, "Assessment of HV XLPE cable sheath layer modelling approaches for EMT studies," submitted for publication.
- I. Kiitam, P. Taklaja, and K. Tuttelberg, "Effect of Electrode Shape on Medium Voltage Covered Conductor Insulation Durability Under Electric Stress," submitted for publication.

Author's Contribution to the Publications

The author of the thesis is the main author of all of the included publications. The author developed the presented solutions, implemented them, and performed the testing.

Publication I presents a thorough analysis of uncertainty propagation in quantities estimated from measured synchronized phasors. The publication analyzes quantities monitored on transmission lines. The author applied the methods of uncertainty analysis in multidimensional quantities in order to determine the causes of poor accuracy seen in a practical implementation of commonly published PMU-based line monitoring methods. Such an analysis had not been published before and it provides a better understanding of the accuracy and the lack of it in certain monitoring applications.

Publication II develops and analyzes another PMU-based transmission line monitoring application that had not been discussed in the literature before. The author presented a thorough theoretical analysis of calculating different components of transmission losses corresponding to elements of the multi-conductor distributed parameter transmission line model. The author further demonstrated the results of monitoring different components of transmission losses on real transmission lines and showed the feasibility of such monitoring applications.

Publication III demonstrates the possibility of monitoring power system inertia in near real-time based on ambient PMU measurements. The author developed a measurement based method that determines the inertia of the power system and specific areas in the system from normal operating conditions (not based on disturbances). As far as the author is aware, this is the first measurement-based continuous inertia monitoring method that has been published.

Publication IV presented preliminary results of the work on monitoring transmission losses based on PMU measurements. The author applied the estimation of loss components on real measurement data and demonstrated the results.

Publication V presents a comparison of system identification methods applied to modal analysis of a power system model. The author compared the applicability of various common system identification methods to identifying and analyzing inter-area modes. The study showed which methods are better suited for this type of monitoring applications.

Publication VI demonstrates predicting the courses of frequency disturbances based on models identified from ambient PMU measurements. The author developed a measurement based method that identifies an equivalent model of the dynamics between frequency and active power from normal operating conditions. The author demonstrates on real measurement data how these models are capable of predicting the critical periods of given disturbances.

Introduction

Preface

This thesis presents the results of research and development work carried out by the author during PhD studies at Tallinn University of Technology (TTU). While most of the work was done at TTU, important parts of it were carried out during research visits at the Norwegian University of Science and Technology (NTNU) and the Icelandic TSO, Landsnet. The work was mainly related to two research projects—“Development and analysis of wide area measurement system (WAMPAC)” initiated by the Estonian TSO, Elering and the Horizon 2020 project “MIGRATE (Massive InteGRation of power Electronic devices)”.

Electric Power Systems

It would be an understatement to say that modern societies are highly dependent on the use of electricity—they are defined by it. Everyday lives of people would be unimaginable without the most trivial technology, like electric lighting in homes, and services we have come to depend on, like the Internet or card payments. Not only does electricity support everyday lives of individuals, it enables entire economies. With most services and industries depending on electric power, ensuring its reliable supply is essential.

An electric power system is a network of devices designed to supply, transfer, and use electric power. It is what connects the consumers and producers of electrical energy to each other and manages the transfer of energy between them. However, it is far more than a network of power lines—it is an extremely large control system. Due to physical constraints it has to be constantly controlled in order to maintain stability in the short term, while in order to meet the expectations of consumers it has to achieve the highest level of reliability in the long term.

Power systems have been around for more than a century and the principles of their operation and planning have been well established. Because of the high requirements on reliability, the power systems industry is a very conservative one. Despite all of this, power systems have to evolve and adapt to changes. Attempts to decelerate and stop climate change have led to an increased use of renewable energy sources in electric power generation, changing the composition of power systems. High population density, ‘not in my backyard’ attitude, and conservationism are challenging the construction of new lines needed to accommodate growing transfer capacities. Deregulation of the energy sector has changed the responsibilities of parties, like those of transmission system operators.

The increasing share of renewable sources in electric power generation has changed, and is continuing to change, some key aspects of power systems. Traditionally, power generation used to be very centralized, based on large generating stations aiming at maximizing efficiency by economies of scale. These generating stations have large synchronous generators with a stable and controllable power output, synchronized to the frequency of the AC power system. Renewable sources, on the other hand, only enable intermittent power generation that cannot be increased on demand. In most cases, it is not feasible for either wind generating units or photovoltaic (PV) panels to supply voltages at system frequency and they are connected through power electronics interfaces instead. The displacement of large synchronous units has the side effect of decreasing inertia of the power system and making it harder to maintain frequency stability.

Historically it has been common to have large energy utilities that own power plants, transmission systems, and distribution systems, controlling the entire chain of supply from production to wholesale and operating with regulated prices. Current policies have led

to the formation of transmission system operators (TSOs) that only handle transmission of electric energy from producers to distribution systems. Electric energy is traded on markets and TSOs are to facilitate the transfer of energy sold on those markets. In addition to that, TSOs are also tasked with procuring the energy needed to cover transmission losses. In order to minimize costs, TSOs have to find ways to forecast these losses more accurately.

These are just a couple of brief examples of the many challenges facing the power systems industry. These problems are multifaceted and present themselves differently in different power systems. This thesis tackles some of the related questions arisen from practical experiences of TSOs.

Monitoring and Learning

One of the rising technologies in power systems are undoubtedly phasor measurement units (PMUs) and wide area monitoring systems (WAMS) based on the former. Despite the technologies being three decades old, their deployment and use has been gearing up in the past decade. There are several reasons for their increased prevalence in transmission systems—practical need, development of supporting technologies, managerial fallout following blackouts, etc. There are varying applications of the technology, from the simplest monitoring of angle differences to adaptive control schemes protecting the system. In certain power systems, the technology can already be considered prevalent and essential by now.

In parallel, in the fields of computer science and information technology, the last years have turned big data and associated technologies into buzzwords. The amounts of data being gathered has increased tremendously and the value of analyzing this data has increasingly been seen. At present, most PMUs record 50 measurements per second and a single PMU can measure anything from a few signals to tens of signals instantaneously. Recorded by tens or hundreds of devices over days and months and years, this amounts to significant datasets. Extracting useful information from these vast amounts of data requires appropriate algorithms and will inevitably bring data science methods to the monitoring of power systems.

Coincidentally, the two main topics discussed in the thesis also develop a link between wide area monitoring of power systems and certain data analysis or machine learning methods. The first topic covers extracting additional useful information about transmission losses from PMU measurements. The goal of this work was to obtain this additional information so that it could be used in conjunction with other information as training data to improve the machine learning tools that forecast transmission losses. The second topic covers extracting features of a power system by observing the small dynamic changes caused by ambient signals present in normal operation. Even though the system identification methods applied here are not generally considered to be machine learning tools, they are effectively learning the dynamics of the system from patterns in measured data.

Objectives and Structure of Thesis

The thesis covers two separate topic areas, both about applications of wide area monitoring systems. The first stems from one of the most basic proposed applications of synchronized phasor measurements—on-line transmission line parameter estimation. The principle, although trivial, has been published numerous times and has even been patented. PMUs provide simultaneous (time synchronized) measurements of voltage and current phasors at both ends of a transmission line. If one assumes the two conductor model of

the line, its parameters can be expressed explicitly from the voltage and current phasors. The thesis presents some new aspects of this problem.

First of all, the trivial solution for on-line monitoring of transmission line parameters was tested in practice on real measurement data from the Estonian transmission system. The results showed a lot less quality than expected, which led to a search for the source of errors in these measurements. It was identified that most of the proposed implementations of this application assumed either explicitly or—more often—implicitly that instrument transformers have been calibrated, i.e. contribute no significant errors, which is rarely the case in real transmission systems. The work presents an uncertainty propagation analysis of a practical implementation on real data, which illustrates and explains how different sources of errors affect such applications.

Following that, the same basic concept was expanded to analyze the balance of power on a transmission line. When we look at the transmission line model and extract its parameters from simultaneously measured voltage and current phasors, we can also analyze both active and reactive power consumed or generated in each element of the model. For example, the same resistance, which is calculated as a parameter, models resistive losses in the conductors of the line, while the reactance models consumption of reactive power. The thesis presents a thorough derivation of components of transmission losses based on a detailed multiconductor model of a transmission line. The resulting expressions are intuitive and could be considered trivial, but they were not found to have been presented in any previous publications.

The main goal of this part of the thesis is to provide a new method of detecting and monitoring corona losses in a transmission system. In the aforementioned approach, one of the components of transmission losses can be assumed to largely correspond to corona losses on the line. This provides an on-line measurement-based method to monitor corona losses and gather corresponding data from across the system. Since the phenomenon of corona losses on transmission lines is mostly dependent on weather conditions, this data can be used in conjunction with weather observations in statistical analysis and forecasting tools. Model building and forecasting are not in the scope of this work, but some examples of both types of data from real world conditions are given for validation purposes.

The second topic area ventures into a sort of dynamic state estimation, where certain features of power system dynamics are extracted from wide area measurements. The work proposes a method of estimating approximate models of dynamics between active power and frequency. The method observes the system in normal operation over periods of several minutes and identifies patterns of these dynamics in ambient measurement data. It was found that normal load variations excite the system sufficiently in order to identify these approximate models from PMU measurements of active power and frequency.

The main goal of this estimation is to determine the inertial response of the system from ambient data, not specific disturbances. With the displacement of conventional generation, inertia is both decreasing and varying in time and it is becoming desirable to monitor its value continuously. The key challenge in this is distinguishing the inertial response from frequency control and other effects during normal operation of the system. The work demonstrates that it is possible to do that. The method further incorporates the notion of area inertia, where the system is separated into areas and inertia of each of those is estimated.

The thesis is structured as follows. Chapter 1 provides a brief overview of phasor measurement units, wide area monitoring systems, and WAMS applications, including

the example of transmission line parameter estimation that is demonstrated on measurement data. Chapter 2 discusses transmission line monitoring further, offering a thorough analysis of the propagation and sources of errors. Chapter 3 proposes the monitoring of transmission losses on transmission lines, with the emphasis on estimation of corona losses. Chapter 4 demonstrates continuous monitoring of power system inertia based on ambient measurement data.

1 Wide Area Monitoring of Power Systems

“In the future, we shall have to look upon the collection of data in a different way, and I am proposing an ideal solution. I should like to have all the data in digital form and recorded directly on magnetic tape. In the case of the rotor angle, for example, pulses initiated by the shaft of the machine, and the reference voltage, would be recorded directly on to magnetic tape, together with a counting frequency synchronized to the mains supply frequency, thus giving the rotor angle. All data, such as voltages and currents, should be recorded in this way, and a large and fast electronic computer should be used for the task of analysis. Only in this way will the deductions made from the test information match, in some measure, the diligence of those collecting the results.”

— Dr. P. D. Aylett, 1958 [1]

1.1 Synchronized Phasor Measurements

An alternating current (AC) power system is based on generators that supply alternating voltages, synchronized to one common frequency. In engineering practice, these perpetually oscillating quantities are mostly analyzed as phasors—described by a magnitude and a phase angle. While it is relatively easy to measure magnitudes (or RMS values) of AC currents and voltages, it is somewhat more difficult to measure their phase angles. Phase angles rotate in time and only have a meaning when they are compared to one another or a common reference measured at exactly the same time.

Most commonly phase angles are obtained from a state estimator, where they are deduced from other measurements combined with a power flow model of the system. State estimators are widely used and provide valuable information about the steady state operation of the system. However, acquiring measurements and estimating a state of the system usually takes several seconds to tens of seconds. This is too slow to observe fast changes and dynamic phenomena. In order to capture such dynamics, it is necessary to measure the relevant state variables directly.

There has been interest in directly measuring phase angle differences for a long time. Already in 1956, during the commissioning tests of the Cliff Quay generating station, three experimental measurement devices were used to record the tests. The first two were concerned with measuring the rotor angle relative to local bus voltage [2, 3], while the third measured changes in voltage phase angle differences between two distant substations [4]. The latter enabled the recording of disturbances in the system, but it assumed a constant communication delay instead of being properly synchronized in time. Other proposed solutions to this problem followed, attempting to compensate for communication delays [5, 6].

Feasible means of properly synchronizing geographically distant phase angle measurements were found in the beginning of 1980s when measurement of synchronized voltage phase angles was proposed and demonstrated [7, 8]. The last piece of the puzzle was added by proposing the contemporary solution to calculating phasors [9]. A couple of years later time synchronization was incorporated, already introduced before, and synchrophasors or synchronized phasor measurements as they are known today were established [10].

At the time of writing the thesis, synchronized phasor measurements were specified by the IEEE standard C37.118.1-2011 [11] and other associated standards. This standard makes a distinction between a phasor and a synchrophasor [11]. Phasors in their conven-

tional meaning have commonly been used to simplify the analysis of AC circuits. A sinusoidal waveform with an amplitude X_m and phase shift ϕ

$$x(t) = X_m \cos(\omega t + \phi) \quad (1.1)$$

is represented by a phasor expressed as

$$\underline{x} = \frac{X_m}{\sqrt{2}} e^{j\phi}. \quad (1.2)$$

All phasors in a common analysis are defined for a fixed frequency f in $\omega = 2\pi f$.

In an AC power system, small variations from system frequency are inevitable. In this case, frequency itself can be seen as a function of time. By writing for the time-dependent frequency $f(t)$ and system rated frequency f_n

$$g = g(t) = f(t) - f_n, \quad (1.3)$$

the sinusoid for an AC quantity can be expressed as [11]

$$x(t) = X_m \cos(2\pi \int f dt + \phi) \quad (1.4)$$

$$= X_m \cos(2\pi f_n t + 2\pi \int g dt + \phi). \quad (1.5)$$

The synchrophasor representation is thus defined as

$$\underline{x}(t) = \frac{X_m(t)}{\sqrt{2}} \exp [j(2\pi \int g dt + \phi)]. \quad (1.6)$$

For a constant amplitude $X_m(t) = X_m$ and constant frequency deviation $\Delta f = f - f_n = g$, the synchrophasor becomes

$$\underline{x}(t) = \frac{X_m}{\sqrt{2}} \exp [j(2\pi \Delta f t + \phi)]. \quad (1.7)$$

This quantity rotates at the frequency Δf [11]. This distinction explains a common phenomenon in synchronized phasor measurements—even if phase angle differences between nodes do not change, synchrophasors rotate in time. In this work, measured synchrophasors are referred to as phasors for the sake of brevity.

In addition to phasor measurements, the standard specifies measurement of frequency and rate of change of frequency (RoCoF) [11]. For a sinusoid as in (1.1), frequency is defined as

$$f(t) = \frac{1}{2\pi} \frac{d\phi(t)}{dt} \quad (1.8)$$

and its rate of change as

$$RoCoF(t) = \frac{df(t)}{dt}. \quad (1.9)$$

When it comes to requirements on accuracy, the standard defines the total vector error (TVE) as [11]

$$TVE(t) = \sqrt{\frac{(\hat{x}_{re}(t) - x_{re}(t))^2 + (\hat{x}_{im}(t) - x_{im}(t))^2}{x_{re}^2(t) + x_{im}^2(t)}} = \frac{|\hat{\underline{x}}(t) - \underline{x}(t)|}{|\underline{x}(t)|}, \quad (1.10)$$

where $\hat{x}(t)$ is the estimate (measured value) of a phasor $x(t)$ at time t . For frequency and RoCoF, absolute errors are used [11].

Phasor measurements units (PMU) are devices that measure phasors, frequency, and RoCoF and tag them with time-stamps using a synchronized time source. The devices are similar to computer relays, the main difference being the added time synchronization component. The standard sets certain requirements, but PMUs from various manufacturers can be quite different in their implementations. However, in general, a PMU as a device is connected to instrument transformers that output converted analog AC current and voltage signals. On these inputs the PMU performs certain operations and outputs time-stamped phasors conforming to the standard.

Inside the PMU, the measured analog signals are filtered and converted from analog to digital signals. Following that, the device performs a Fourier transform in order to extract the fundamental component of each measured signal. For frequency and RoCoF measurements a numerical calculation of derivatives is performed. The PMU is also connected to a time synchronization signal that is used to generate the time-stamps. Finally, the device outputs the measured quantities alongside their time-stamps [12]. The internal operations may be implemented as decided by manufacturers as long as they conform to the standard.

In large part, a commercial PMU is a black box device between the inputs and outputs with its proprietary algorithms. However, several manufacturers offer configuration options, some more than others. Most often there are options to configure filtering of measured inputs, where it is possible to select window length for example. These settings can affect the output results to a certain extent, especially in dynamic conditions [13]. If possible, these aspects should be considered when measurement results are applied or even when PMUs are installed.

In order to function on a real transmission line, the PMU is connected to current and voltage transformers, as illustrated in Fig. 1.1. The outputs of instrument transformers are the actual inputs to the PMU. Even though this may sound trivial, it is important to consider this fact when analyzing the accuracy of phasor measurements. Instrument transformers have errors with rather complicated characteristics that influence PMU measurements. In practice, measurement errors in instrument transformers can be an order of magnitude larger than measurement errors of the PMU itself, as discussed in the following chapter.

Apart from the analog voltage and current signals, the PMU needs a time synchronization signal as another input. In most cases, the Global Positioning System (GPS) is used as the time source, but other sources can be used. GPS satellites provide a time signal with a synchronization accuracy of at least one microsecond, accessible to all PMUs at the same time [12]. However, if a PMU loses the reference time signal, significant errors may be introduced into the measurements. As angle measurements are related to time measurements, an error in the time signal results in an error in measured angles.

On the output side, PMUs are connected to a communications network. The measurement data is transferred to Phasor Data Concentrators (PDC) that gather and store the information. This may again be carried out over different types of communication channels and protocols [12]. As far as monitoring applications are concerned, communications delays are not critical since measurements are time-stamped at the time of measurement. However, real-time monitoring would require short delays and fast communications.

PDCs concentrate measurements gathered from various geographically and electrically distant points of the system. Thanks to time synchronization, it is then possible to observe these distant points of the system at one location and measure the quantities

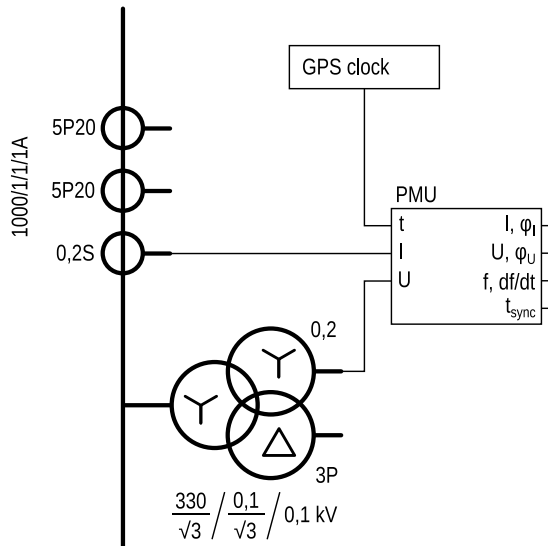


Figure 1.1 Basic principle of connecting a PMU to a transmission line feeder. The example is based on a 330 kV transmission line.

simultaneously. This is how PMUs and PDCs enable to construct wide area monitoring systems (WAMS). A WAMS takes the measurements provided by PMUs and processes them in such a way that provides useful information about the performance of the power system.

1.2 Examples of Wide Area Monitoring Applications

There is a variety of power system monitoring applications that have been proposed and implemented since the introduction of PMU technology and wide area monitoring systems. Some of these are improvements of what is possible with SCADA/EMS systems while some offer new capabilities. The simplest example (and the first that was implemented) is monitoring of the angle differences on a longer transmission line [14]. While it is possible to obtain an estimated angle from a state estimator, it is only available in intervals of several seconds. A WAMS application can provide this information continuously in real-time to the operator or dispatcher, which can make a significant difference.

Another common way of improving existing capabilities is the so-called hybrid state estimator, which combines a conventional state estimator with PMU measurements in order to improve the former. The basic concept of including PMU measurements in the state estimator was one of the first ever proposed applications for the new measurement technology [10]. However, as long as the state estimation step is included, the application can be improved but it does not change fundamentally.

PMU measurements offer new capabilities where either their higher sampling ratio or time-synchronization can be utilized. One of such applications is monitoring of power oscillations. Local and inter-area oscillations occur with frequencies below one hertz up to a few hertz. These dynamics are fast enough not to be detected in state estimation, while still slow enough to be monitored with PMU measurements. Such oscillations are critical in the operation of many power systems and applications of monitoring power oscillations

are one of the most commonly deployed WAMS applications [15–18].

Some of the more commonly deployed applications are offline in nature. WAMS can be used for post-event analysis of disturbances, e.g. short-circuits or frequency disturbances [14, 15, 17]. Another application is the validation of dynamic models [14, 15, 17, 18]. With a WAMS it is possible to record various dynamic events and compare them to simulations of equivalent conditions. This allows the TSO to both validate and improve its dynamic models of the power system.

The applications mentioned so far are the ones most often deployed and used in real power systems. Of course, there is a large number of other WAMS applications that are either less common, in development or only proposed without being implemented in practice. Another application that is based on PMU measurements, is well known, and discussed in many publications is the estimation of transmission line parameters and dynamic line rating based on the measured resistance. This application has also been patented and demonstrated in practice by ABB [19, 20]. However, this application is very sensitive to the accuracy of measurement devices, making it difficult to obtain good results. These limitations are demonstrated in the next section and analyzed in detail in the next chapter.

1.3 Monitoring of Transmission Line Parameters

Transmission lines are one of the main building blocks of power systems, connecting all other elements into one network. To a large extent they determine transfer capacities between regions and affect other aspects of operating the system, e.g. voltage stability. While transmission lines as elements of the system are rather simple, there is still interest in monitoring some aspects of their operation. For example, it is possible to determine both the thermal and stability limits of transfer capacity based on certain measurements. This is valuable information in networks that are becoming more congested with changes in the distribution of generation and limits to the construction of new transmission lines.

The stability limits in power transfer capacity depend on angle differences between the two ends of the line and parameters of the line itself [21, 22]. As discussed in the previous chapter, PMUs offer a good capability of monitoring angle differences. However, in principle it is also possible to monitor parameters of transmission lines based on PMU measurements. This also relates to the thermal limit of power transfer capacity. The thermal limit is determined by the temperature of line conductors, however, the temperature of the conductor also affects its resistance. If it is possible to monitor the resistance of a conductor with very good accuracy, it is possible to infer its temperature.

These principles are the basis of well known examples of wide area monitoring applications. However, the same principles offer another, less discussed application. Based on synchronized phasor measurements, it is also possible to analyze the balance of power on a transmission line in more detail than conventional metering would allow. Here the balance of power refers to components of active losses and both consumed and generated reactive power on the transmission line. Most interestingly, this offers the ability to detect and monitor corona losses independently of thermal losses, which will be discussed as a separate topic in another chapter.

The most common transmission line model is the Π equivalent circuit, depicted in Fig. 1.2. It models the line as a series impedance and two shunt admittances, one at either end of the line. The two ends of the line are often referred to as the sending and receiving

end. The voltage and current phasors at the two ends of the line are related by

$$\underline{U}_S = \left(1 + \frac{\underline{ZY}}{2}\right) \underline{U}_R + \underline{Z} \underline{I}_R, \quad (1.11)$$

$$\underline{I}_S = \left(1 + \frac{\underline{ZY}}{4}\right) \underline{Y} \underline{U}_R + \left(1 + \frac{\underline{ZY}}{2}\right) \underline{I}_R. \quad (1.12)$$

This model is sufficient for steady state analysis of short transmission lines. It is usually applied with the assumption that only positive sequence voltages and currents are analysed. It is also simple to see that if one knows the values of voltage and current phasors at both ends at the same moment in time, the values of line parameters can be calculated.

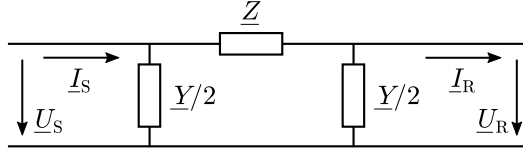


Figure 1.2 Transmission line modeled as a Π equivalent circuit. Line parameters are expressed as a series impedance $\underline{Z} = R + jX$ and shunt admittance $\underline{Y} = G + jB$.

The second most common transmission line model is the distributed parameter equivalent circuit, shown in Fig. 1.3. In this model, the line is divided into infinitesimally short sections, each of which have a series impedance and a shunt admittance. The equations for these sections are integrated over the length of the line and the distributed parameter transmission line equations are expressed as

$$\underline{U}(l) = \cosh(\gamma l) \underline{U}(0) + z_C \sinh(\gamma l) \underline{I}(0), \quad (1.13)$$

$$\underline{I}(l) = \frac{1}{z_C} \sinh(\gamma l) \underline{U}(0) + \cosh(\gamma l) \underline{I}(0), \quad (1.14)$$

where $\underline{U}(l)$ and $\underline{I}(l)$ are the voltage and current phasors at a distance l toward the sending end of the line ($\underline{U}(0)$ and $\underline{I}(0)$ are the phasors at the receiving end), $\gamma = (zy)^{1/2}$, and $z_C = (z/y)^{1/2}$. This model is more accurate and also applies to long transmission lines.

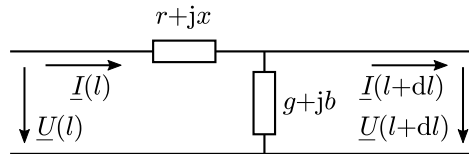


Figure 1.3 Distributed parameter model of a transmission line. Voltages and currents are given as functions of the position along the length of the line. The line is divided into infinitesimally short sections of length dl with per unit distance parameters $z = r + jx$ [Ω/km] and $y = g + jb$ [S/km].

In the analysis of transmission lines, it is often assumed that a common linear transformation of phase quantities (e.g. symmetrical components or Clarke transform) can be used to remove the effects of mutual coupling between the quantities [23, 24]. The problem of mutual coupling between phase quantities and the justification behind these assumptions are explained in Sec. 3.2. However, once this assumption is made, (1.13) and (1.14) apply for each of the symmetrical components (or Clarke transform modes) and

the transmission line is modeled as three independent circuits for these quantities as in Fig. 1.3. Just like it was the case with the Π equivalent circuit, it becomes trivial to calculate the parameters of the transmission line if simultaneous values of voltage and current phasors at both ends of the line are known.

Computing transmission line parameters from synchronized measurements of voltage and current phasors was already proposed two decades ago [25]. In this case it was proposed as a part of a fault location application [26, 27]. Following that, there have been numerous papers proposing and discussing variations of on-line monitoring of line parameters [28–32]. Some have suggested different calculation or missing data mitigation techniques; however, they have all been based on either (1.11) and (1.12) or (1.13) and (1.14). An application for dynamic line rating based in part on these equations has also been patented by ABB [19].

For the equivalent circuit in Fig. 1.3, line parameters can be expressed explicitly from (1.13) and (1.14). Writing the sum and the difference of the two equations results in

$$\underline{U}(l) + z_c \underline{I}(l) = (\underline{U}(0) + z_c \underline{I}(0)) e^{\gamma l}, \quad (1.15)$$

$$\underline{U}(l) - z_c \underline{I}(l) = (\underline{U}(0) - z_c \underline{I}(0)) e^{-\gamma l}. \quad (1.16)$$

From the first equation, the characteristic impedance is expressed as

$$z_c = \frac{\underline{U}(0)e^{\gamma l} - \underline{U}(l)}{\underline{I}(l) - \underline{I}(0)e^{2\gamma l}} \quad (1.17)$$

so that the other equation can be written as

$$\underline{U}(l) - \underline{I}(l) \frac{\underline{U}(0)e^{\gamma l} - \underline{U}(l)}{\underline{I}(l) - \underline{I}(0)e^{2\gamma l}} = e^{-\gamma l} \left(\underline{U}(0) - \underline{I}(0) \frac{\underline{U}(0)e^{\gamma l} - \underline{U}(l)}{\underline{I}(l) - \underline{I}(0)e^{2\gamma l}} \right). \quad (1.18)$$

Multiplying by the denominator of the fractions yields

$$2\underline{U}(l)\underline{I}(l) + 2\underline{U}(0)\underline{I}(0) = (\underline{U}(0)\underline{I}(l) + \underline{U}(l)\underline{I}(0)) (e^{\gamma l} + e^{-\gamma l}), \quad (1.19)$$

which leads to the explicit expressions [25]

$$\gamma L = \operatorname{arcosh} \left(\frac{\underline{U}(L)\underline{I}(L) + \underline{U}(0)\underline{I}(0)}{\underline{U}(0)\underline{I}(L) + \underline{U}(L)\underline{I}(0)} \right), \quad (1.20)$$

$$z_c = \frac{\underline{U}(L) - \underline{U}(0) \cosh(\gamma L)}{\underline{I}(0) \sinh(\gamma L)}, \quad (1.21)$$

where L is the length of the line. The per unit distance impedance and admittance are $\underline{z} = \gamma z_c$ and $\underline{y} = \gamma / z_c$, respectively.

PMUs installed on a transmission line measure voltages and currents of phases. If all phases of a line are measured, it is possible to calculate the symmetric components—positive, negative and zero sequence. Without much discussion, most proposed applications of calculating transmission line parameters from PMU measurements assume that positive sequence quantities are used. The differences between using phase and sequence quantities are discussed in Sec. 3.2.

Assuming that positive sequence quantities are used, it is trivial to apply (1.20) and (1.21) on measured phasors. However, it is not as simple to obtain very accurate results in the general case. In order to illustrate this, some exemplary results are presented in this

section. Synchronized phasor measurements from both ends of a 330 kV transmission line have been gathered and processed. Expressions (1.20) and (1.21) have been applied on symmetrical components of voltages and currents in order to calculate the corresponding line parameters.

The measurement data was taken in the span of 18 hours from 26 January 2018 17:00 to 27 January 11:00. Based on weather data from nearby weather stations, the approximate temperature of the conductors was found to vary between 1–5°C [33, 34]. For comparison, the impedance of the transmission line obtained from offline measurements is $0.0243 + j0.295 \Omega/\text{km}$ (adjusted to 25°C). For this example, the PMU measurements were downsampled to 0.1 samples per second as the period is rather long (there would be three million samples with the original 50 Hz sampling rate). Parameters were calculated with this 10 s step and also smoothed with a moving window of 30 samples.

The four parameters of the distributed line model—resistance, reactance, conductance, and susceptance—are plotted in Figs. 1.4-1.7. In all four figures, the values calculated from single samples and the values smoothed over 30 samples have been plotted. For reference, the magnitudes of current and voltage phasors have been plotted in Figs. 1.8 and 1.9. As expected, it is possible to calculate the parameters; however, the values exhibit some unexpected changes in time and large errors in some cases.

The estimates of positive sequence resistance show the largest errors, clearly visible in the results. Even the lowest values seen in this period are significantly larger than the true value could be, with the highest values reaching three times that. The changes in estimates of resistance coincide with changes in measured current, which shows a dependence of measurement errors on the value of current measured. The changes in the estimates of reactance coincide with both the changes in measured current and measured voltage. These dependencies and the causes behind them are investigated in the next chapter.

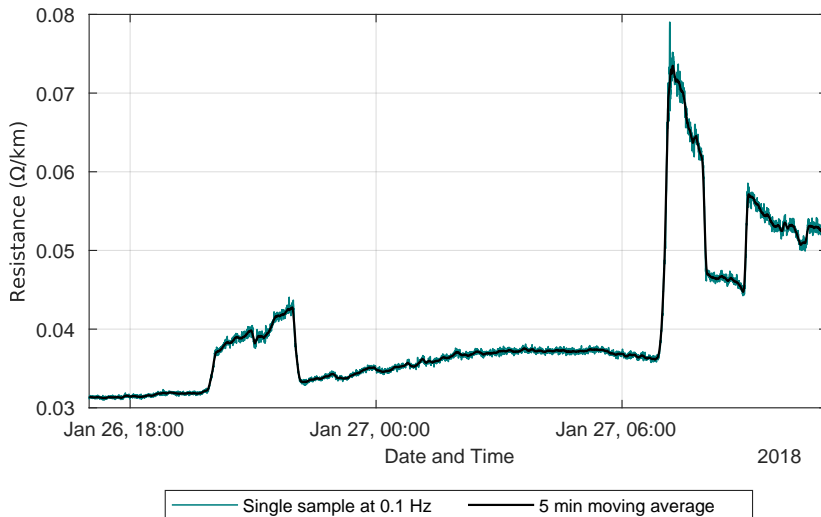


Figure 1.4 Positive sequence resistance estimated from PMU measurement data. Values calculated from single instantaneous samples plotted alongside values smoothed with a window of 30 samples.

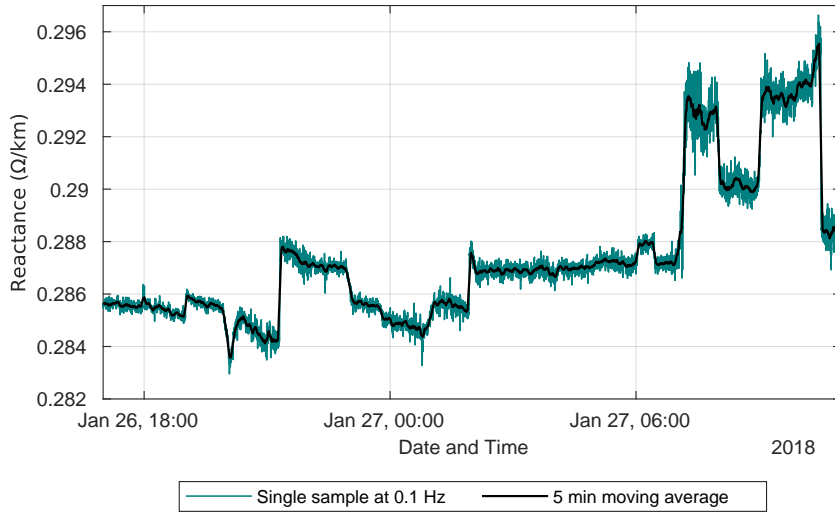


Figure 1.5 Positive sequence reactance estimated from PMU measurement data. Values calculated from single instantaneous samples plotted alongside values smoothed with a window of 30 samples.

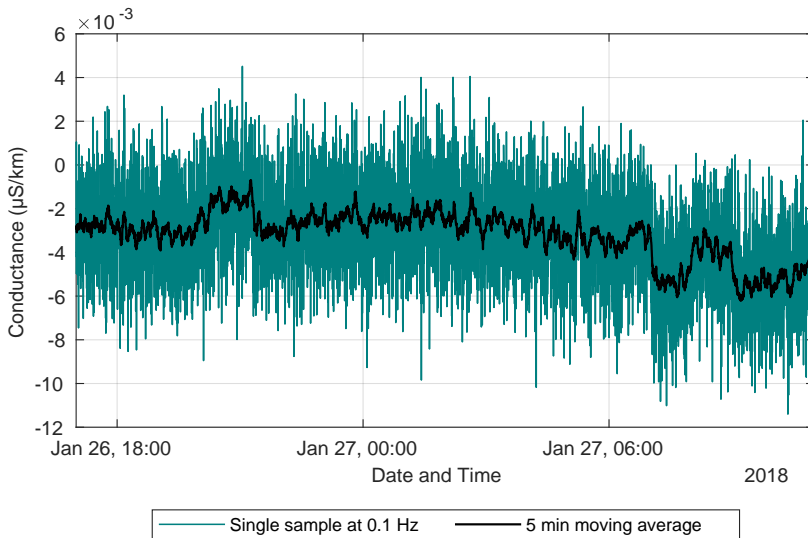


Figure 1.6 Positive sequence shunt conductance estimated from PMU measurement data. Values calculated from single instantaneous samples plotted alongside values smoothed with a window of 30 samples.

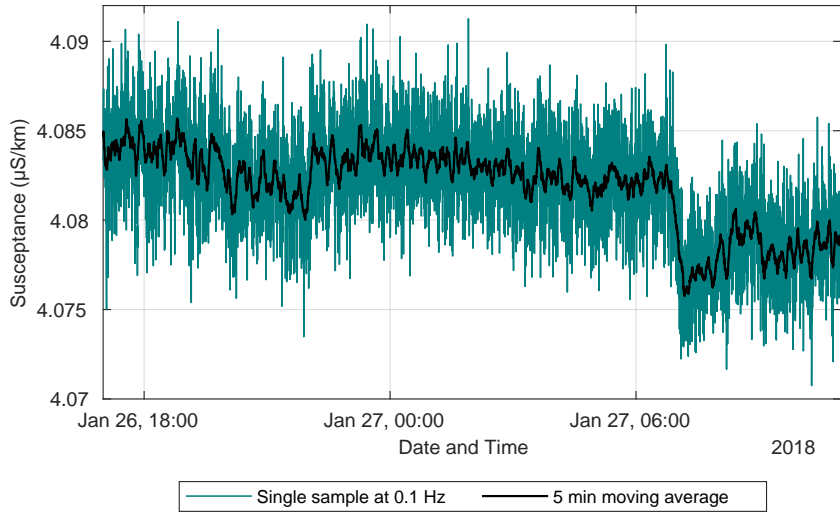


Figure 1.7 Positive sequence shunt susceptance estimated from PMU measurement data. Values calculated from single instantaneous samples plotted alongside values smoothed with a window of 30 samples.

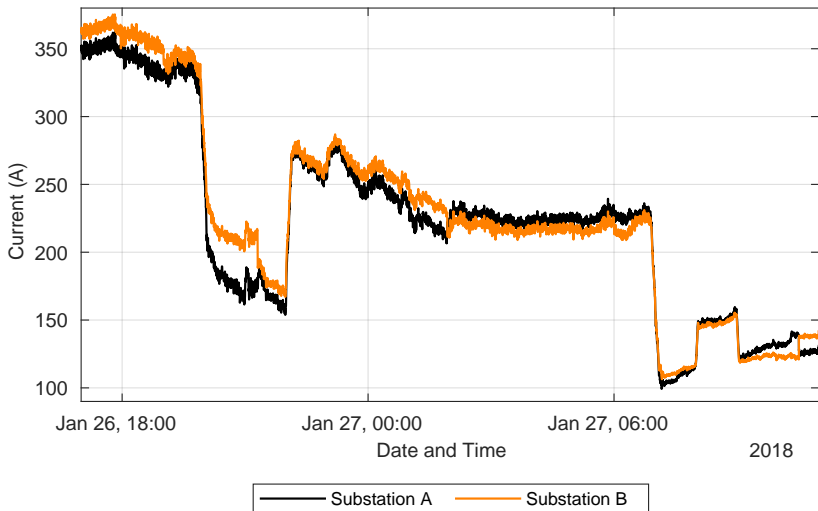


Figure 1.8 PMU measurements of positive sequence current magnitudes from both ends of the transmission line.

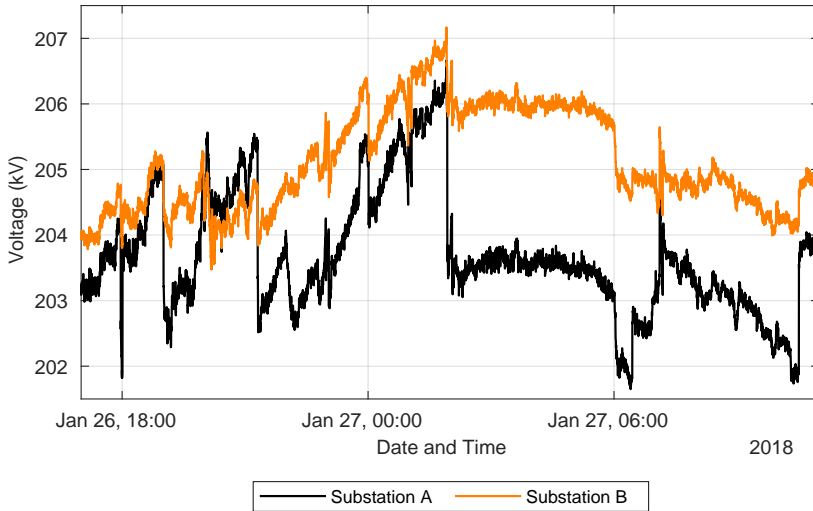


Figure 1.9 PMU measurements of positive sequence voltage magnitudes from both ends of the transmission line.

1.4 Summary

This thesis presents the development of new power system monitoring applications based on phasor measurement units and wide area monitoring systems. This chapter summarized the main background of the technology and related terms used throughout the thesis. Some of the most commonly deployed WAMS applications were introduced as examples. One of the applications, monitoring of transmission line parameters based on PMU measurements, was explained in more detail with some real life results presented for illustration.

2 Uncertainties in Transmission Line Monitoring

Monitoring of transmission line parameters based on PMU measurements from both ends of the lines as described in Sec. 1.3 is simple to implement. The parameters can be calculated in real-time with explicit expressions. However, as the example showed, the results can be quite inaccurate. The main hypothesis of this chapter is that the accuracy of monitoring certain quantities on a transmission line can be very strongly affected by measurement errors, even if the accuracy of the measurement devices is generally assumed sufficient.

This chapter analyzes measurement uncertainties in the entire measurement chain (as illustrated in Fig. 1.1) and uncertainty propagation in the uncorrected measurement model. The monitored quantities are calculated from explicit expressions, allowing us to derive explicit expressions for their uncertainties. Possible sources of errors are identified and their uncertainties quantified. Following that, uncertainty propagation is analyzed and evaluated based on real measurement data. Based on the results, the accuracy of different monitored quantities and the influence of various measurement errors are discussed. The results have been published as Publication I.

2.1 Measurement Errors in the Measurement Chain

As discussed in the previous chapter, PMUs are connected to instrument transformers and require a time synchronization signal. With that in mind, there are three main sources of error in the measurements—the PMU itself, instrument transformers, and the time source. The possible errors from these sources are discussed in this section.

Phasors measured by PMUs are limited to the accuracy of 1% TVE in steady state conditions by the C37.118 standard [11]. This means that the errors in a measured phasor are limited by a circle, depicted in Fig. 2.1, where the maximum error in magnitude can be 1% or maximum error in angle 0.573° if the other of the two is zero. If the accuracy of a PMU is given only in terms of TVE, it is impossible to know specifically how large the errors in either the magnitude or angle are. If this information is not available, the maximum errors of 1% and 0.573° should be assumed. Fortunately, some manufacturers separately report specific measurement error limits for magnitude and angle and they can be significantly smaller than the 1% TVE requirement [35].

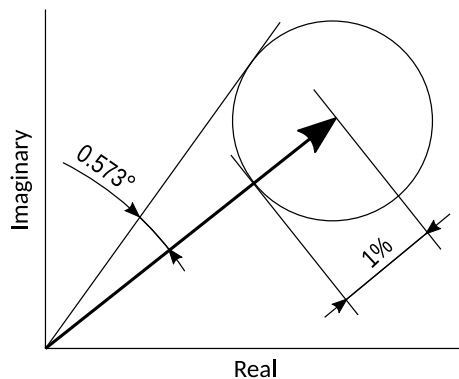


Figure 2.1 Circle of 1% TVE surrounding a phasor [11]. Maximum errors in magnitude and angle given for reference.

The accuracy requirements for current and voltage transformers are set in IEC standards 60044-1 and 60044-2 [36, 37]. For more accurate measurements, metering transformer classes are defined, while protection class transformers require lower accuracy. For current transformers (CT), the metering classes are 0.2S and 0.5S, for voltage transformers (VT) 0.2 and 0.5. The class designations refer to the maximum relative magnitude error in percent at rated measurement value. The standards specify separate limits to magnitude and angle errors at various values of the measured quantity relative to the rated value (I/I_n). The 0.2S and 0.5S accuracy classes for current transformers are illustrated in Fig. 2.2. Even though levels of I/I_n below 20% may sound very low, installed current transformers tend to be over-dimensioned. For example, on a 330 kV transmission line transferring 100 MW, a CT rated at 2 kA is operating below 9% I/I_n .

It should be noted that most authors that have proposed calculating transmission line parameters from PMU measurements have assumed that instrument transformers have been calibrated so that their errors can be compensated for. In practice this would require on-site calibration of each of the instrument transformers used in the estimation. Instrument transformers are usually tested by the manufacturer and some information about measurement errors may be available in factory test reports. However, these tests are usually carried out for one or two values of burden and a few values of I/I_n , which is not sufficient for calibration. The measurement errors depend strongly on the value of burden, which is determined by the specific installation in the substation. Examples of instrument transformer errors from factory test reports may be seen in Appendix A.

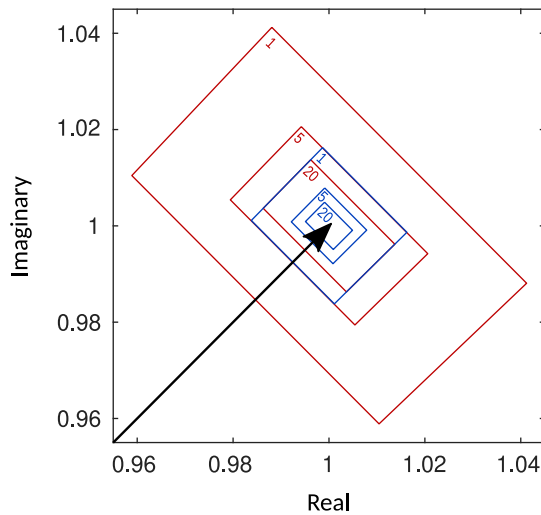


Figure 2.2 Current phasor of length $\sqrt{2}$ with maximum errors permitted by 0.2S (denoted by blue) and 0.5S (red) accuracy classes. Numbers inside the sectors give the percentage ratio of measured to rated value, i.e. I/I_n . Maximum errors are equal for 20–100% ratios [11].

Assuming that a GPS clock is used and it is operating correctly, time-synchronization errors caused by the clock are expected to remain below 100 ns [38, 39]. If a time distribution system is used in the substation, e.g. IRIG-B, an additional error of a few hundred nanoseconds may be introduced. Considering this, it can be assumed that in practice time-synchronization errors remain below 1 μ s in normal conditions [40, 41]. An error of 1 μ s would correspond to an angle measurement error of 0.018°.

2.2 Uncertainty Analysis in Phasor Measurements

A phasor is expressed as a complex number—it consists of a real and an imaginary part or it can also be represented as a magnitude and an angle. In either case, a complex number consists of two independent components and it can be seen as a two-dimensional quantity. When a measured quantity is expressed as a complex number, it has uncertainties in both dimensions. As long as there is no reason to assume otherwise, uncertainties in the two dimensions may be unequal. This phenomenon is illustrated in Fig. 2.3, where two measured voltage phasors have been plotted. The uncertainty ellipse of one of the phasors has also been drawn, formed by the uncertainties in the measured magnitude and angle.

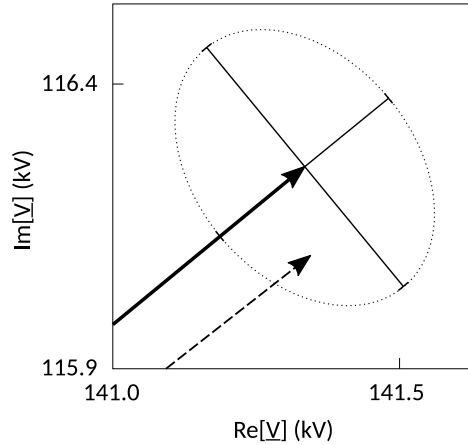


Figure 2.3 Voltage phasors at separate ends of a transmission line measured by PMUs. One phasor is accompanied by its uncertainty ellipse.

The analysis of uncertainties and their propagation in two-dimensional quantities is a generalization of the more known single dimensional case, however, there are several important differences [42, 43]. In order to determine the uncertainties in the two dimensions and the uncertainty ellipse (like in Fig. 2.3), a series of calculations are needed. The main principles and transformation are summarized below. Following that, propagation of uncertainties into line parameters derived in the previous section are analyzed.

A complex quantity \underline{x} is estimated by a measured value \underline{x} , written as

$$\underline{x} = x_{re} + jx_{im}, \quad (2.1)$$

where the real and imaginary parts are denoted by corresponding subscripts. The covariance matrix of this estimate \underline{x} is then given as

$$\mathbf{C}(\underline{x}) = \begin{bmatrix} [u(x_{re})]^2 & u(x_{re})ru(x_{im}) \\ u(x_{im})ru(x_{re}) & [u(x_{im})]^2 \end{bmatrix}, \quad (2.2)$$

where $u(x)$ denotes the uncertainty of x and

$$r = r(x_{re}, x_{im}) = r(x_{im}, x_{re}) = u(x_{re}, x_{im})/[u(x_{re})u(x_{im})] \quad (2.3)$$

is the correlation between the real and imaginary components of \underline{x} [44].

The uncertainties of a quantity \underline{x} , which is measured in terms of magnitude x_m and angle x_ϕ

$$\underline{x} = x_m e^{jx_\phi} \quad (2.4)$$

are transformed from polar coordinates into the (Cartesian) complex plane. Firstly, a radial-tangential covariance matrix is formed

$$\mathbf{C}_{rt}(\underline{x}) = \begin{bmatrix} [u(x_m)]^2 & u(x_m)r_t u(x_t) \\ u(x_t)r_t u(x_m) & [u(x_t)]^2 \end{bmatrix}, \quad (2.5)$$

where $r_t \cong r(x_m, x_\phi)$ is the correlation between the magnitude and angle measurements and $u(x_t)$ is a tangential uncertainty component, found as [45]

$$u(x_t) = x_m \tan [u(x_\phi)]. \quad (2.6)$$

The matrix is then rotated by the measured angle x_ϕ

$$\mathbf{T} = \begin{bmatrix} \cos x_\phi & -\sin x_\phi \\ \sin x_\phi & \cos x_\phi \end{bmatrix}. \quad (2.7)$$

The covariance matrix for the quantity in the complex plane is obtained as [45]

$$\mathbf{C}(\underline{x}) = \mathbf{T}\mathbf{C}_{rt}(\underline{x})\mathbf{T}^\top. \quad (2.8)$$

If a stationary quantity \underline{x} is estimated as the mean of n repeated measurements \underline{x}_i , type A evaluation of uncertainty is carried out as follows

$$u_A(x_{re}, x_{im}) = \frac{1}{n(n-1)} \sum_{i=1}^n (x_{re} - x_{ire})(x_{im} - x_{iim}), \quad (2.9)$$

$[u_A(x_{re})]^2 = u_A(x_{re}, x_{re})$, and $[u_A(x_{im})]^2 = u_A(x_{im}, x_{im})$. If systematic errors are present in the measurement, type B uncertainties $u_B(x_{re})$, $u_B(x_{im})$, etc. are also evaluated [46]. If both types of uncertainties are included, the resulting covariances are added so that

$$\mathbf{C}(\underline{x}) = \mathbf{C}_A(\underline{x}) + \mathbf{C}_B(\underline{x}). \quad (2.10)$$

The procedure of estimating a quantity \underline{Y} from the measurements of n quantities $\underline{X}_1, \underline{X}_2, \dots, \underline{X}_n$ can be expressed as [46]

$$\underline{Y} = f(\underline{X}_1, \underline{X}_2, \dots, \underline{X}_n). \quad (2.11)$$

An estimated value of \underline{Y} is then given as

$$\underline{y} = f(x_1, x_2, \dots, x_n). \quad (2.12)$$

As the quantity of interest is estimated from a number of measured quantities, the propagation of uncertainties has to be analysed. The propagated uncertainties can be found from the covariance matrix of \underline{y} , computed as [44]

$$\mathbf{C}(\underline{y}) = \sum_{k=1}^n \sum_{l=1}^n \mathbf{W}(\underline{x}_k) \mathbf{R}(\underline{x}_k, \underline{x}_l) \mathbf{W}(\underline{x}_l)^\top, \quad (2.13)$$

where

$$\mathbf{W}(\underline{x}_k) = \mathbf{J}_y(\underline{x}_k)\mathbf{U}(\underline{x}_k) = \begin{bmatrix} \frac{\partial y_{re}}{\partial x_{kre}} & \frac{\partial y_{re}}{\partial x_{kim}} \\ \frac{\partial y_{im}}{\partial x_{kre}} & \frac{\partial y_{im}}{\partial x_{kim}} \end{bmatrix} \begin{bmatrix} u(x_{kre}) & 0 \\ 0 & u(x_{kim}) \end{bmatrix} \quad (2.14)$$

and

$$\mathbf{R}(\underline{x}_k, \underline{x}_l) = \begin{bmatrix} r(x_{kre}, x_{lre}) & r(x_{kre}, x_{lim}) \\ r(x_{kim}, x_{lre}) & r(x_{kim}, x_{lim}) \end{bmatrix}, \quad (2.15)$$

which includes the correlations between the components of \underline{x}_k and \underline{x}_l .

The evaluation of Jacobians can be carried out based on the following notion [44]

$$\frac{\partial \underline{y}}{\partial \underline{x}} = \underline{z} \Rightarrow \mathbf{J}_y(\underline{x}) = \begin{bmatrix} z_{re} & -z_{im} \\ z_{im} & z_{re} \end{bmatrix}, \quad (2.16)$$

which simplifies the process in some cases.

For a certain confidence level p , the coverage factors $k_{2,p}$ are evaluated and the uncertainties given as follows

$$U_p(Y_{re}) = k_{2,p}u(y_{re}) = k_{2,p}\sqrt{\mathbf{C}_{11}(\underline{y})}, \quad (2.17)$$

$$U_p(Y_{im}) = k_{2,p}u(y_{im}) = k_{2,p}\sqrt{\mathbf{C}_{22}(\underline{y})}. \quad (2.18)$$

The coverage factors for 2-dimensional quantities are discussed in [46].

The uncertainty of a measurement can originate from one or more different sources of error, which can be either random or systematic. Random errors are different in each repeated measurement and their effects can be reduced by averaging a larger number of independent repeated measurements. The uncertainties of the resulting values can be evaluated by propagating the type A estimates of uncertainties, as in (2.9), etc. However, it should be kept in mind that repeated measurements can only decrease the uncertainty of estimating a stationary quantity, not a quantity that changes in time.

Measurement results can also include systematic errors, which cannot be removed by repeated measurements. In general, it is assumed that such systematic effects in a measurement setup can be identified and corrected [42]. For example, if a measurement device has a fixed bias, it can easily be compensated for. However, these biases are not always known and they can have a non-linear dependence on the measured quantity itself. If systematic effects are not corrected for, type A evaluation would underestimate the resulting uncertainties. In order to account for systematic errors, type B uncertainties are used.

2.3 Uncertainty Propagation in Line Parameter Estimation

As described in Sec. 1.3, the impedance and admittance of a distributed parameter transmission line can be calculated as

$$\underline{z} = \gamma \underline{z}_c, \quad (2.19)$$

$$\underline{y} = \frac{\gamma}{\underline{z}_c}, \quad (2.20)$$

where

$$\underline{\gamma} = \frac{\text{arcosh}(\underline{p})}{L}, \quad (2.21)$$

$$\underline{z}_c = \frac{v_2 \sqrt{(\underline{p} + 1)(\underline{p} - 1)}}{i_1 - i_2 \underline{p}}, \quad (2.22)$$

$$\underline{p} \equiv \frac{q}{t} \equiv \frac{v_1 i_1 + v_2 i_2}{v_2 i_1 + v_1 i_2}.$$

The quantities \underline{p} , \underline{q} , and \underline{t} have been introduced to shorten the notation. Here it is assumed that $\underline{q} = f(v_1, i_1, v_2, i_2)$ and $\underline{t} = f(v_1, i_1, v_2, i_2)$ are functions of complex representations of measured voltages and currents. These and other terms expressed using \underline{q} and \underline{t} are differentiable with respect to $v_1, i_1, v_2,$ and i_2 and satisfy the Cauchy-Riemann equations.

Type A uncertainties are calculated following (2.9) and covariance matrices $\mathbf{C}_A(v_{a1}), \mathbf{C}_A(i_{a1}),$ etc. are evaluated accordingly. In order to account for systematic effects, uncertainties of type B have to be evaluated with some assumed levels of systematic errors. Since the true systematic errors are not known, this can only be an estimate based on information about measurement devices that is available. Systematic errors should be assumed to be large enough to account for real errors yet still small enough to obtain meaningful uncertainty intervals.

As discussed earlier, the maximum measurement errors of PMUs are limited by the total vector error (TVE). This is a scalar quantity and it removes the distinction between different errors in different dimensions. However, some manufacturers report separate magnitude and angle errors, which are better suited for a more thorough uncertainty analysis. If only the TVE limit is reported for a PMU, either a judgement has to be made how large the share of magnitude and phase errors could be in this TVE limit or the maximum errors of 1% magnitude and 0.573° angle error should be assumed.

Measurement errors of instrument transformers are limited by the maximum error permitted in the respective accuracy class. Actual errors depend on the value of the measured quantity itself (non-linear relationship) and also the size of the burden in the metering circuit. In practice actual systematic errors may be smaller than limited by the accuracy class, even up to an order of magnitude, but they can be very hard to determine. Manufacturers may provide factory test reports, where measurement errors are reported for certain measured values at certain burden values, but these are insufficient for a proper calibration. The actual burden in the circuit may also not be known exactly.

Type B uncertainties in the measurements of voltage and current magnitudes are obtained by taking the product of the measured value and the combined relative errors of instrument transformers and PMUs; for angle measurements the absolute errors are combined so that [42]

$$u_B(v_m) = v_m \sqrt{[\varepsilon_{rVT}]^2 + [\varepsilon_{vPMU}]^2} / k_p, \quad (2.23a)$$

$$u_B(v_\phi) = \sqrt{[\varepsilon_{pVT}]^2 + [\varepsilon_{pPMU}]^2 + [\varepsilon_{pSync}]^2} / k_p, \quad (2.23b)$$

$$u_B(i_m) = i_m \sqrt{[\varepsilon_{rCT}(i_m)]^2 + [\varepsilon_{cPMU}]^2} / k_p, \quad (2.23c)$$

$$u_B(i_\phi) = \sqrt{[\varepsilon_{pCT}(i_m)]^2 + [\varepsilon_{pPMU}]^2 + [\varepsilon_{pSync}]^2} / k_p, \quad (2.23d)$$

where ε_{rVT} and ε_{rCT} are the ratio errors and ε_{pVT} and ε_{pCT} the phase errors introduced in the voltage and current transformers according to their accuracy classes in [36] and [37]; ε_{vPMU} , ε_{cPMU} and ε_{pPMU} denote the voltage, current and phase measurement errors in the PMU. Time-synchronization error is specified in ε_{pSync} , which is only present in $u_B(v_\phi)$ and $u_B(i_\phi)$. Here k_p is the 1-dimensional coverage factor corresponding to the confidence level the measurement errors are given for.

How these errors are reported, depends on the manufacturer, but here they are assumed to be the uncertainties of the measured quantities at a confidence level p so that k_p is the corresponding 1-D coverage factor [42, 46]. The evaluated uncertainties are then transformed into the complex plane by Eqs. (2.6)–(2.8), assuming the measurement of magnitude and angle are independent of each other ($r_t = 0$).

There is no physical correlation between the magnitude and angle of a current phasor. However, the ratio and phase errors in the current transformer accuracy class vary with primary current and are, as such, dependent on the magnitude of measured current.

The voltage and current measurements are also assumed to be independent, i.e. all the correlations between voltage and current components are zero

$$r(v_{re}, i_{re}) = 0, \quad \text{etc.}$$

Thus, there are only two non-zero correlation matrices per every pair of phase voltage and current $\underline{v}_{a1}, \underline{i}_{a1}$, etc.

$$\mathbf{R}(\underline{v}) = \begin{bmatrix} 1 & r(v_{re}, v_{im}) \\ r(v_{im}, v_{re}) & 1 \end{bmatrix} \quad (2.24)$$

and an equivalent for any current estimate \underline{i} or \underline{j} . The uncertainty matrices are formed as

$$\mathbf{U}(\underline{v}) = \begin{bmatrix} u(v_{re}) & 0 \\ 0 & u(v_{im}) \end{bmatrix} \quad (2.25)$$

and again, an equivalent for a current \underline{i} .

The elements of these four matrices are readily calculable from the elements of $\mathbf{C}(\underline{v})$, etc.

$$u(v_{re}) = \sqrt{\mathbf{C}_{11}(\underline{v})}, \quad (2.26)$$

$$u(v_{im}) = \sqrt{\mathbf{C}_{22}(\underline{v})}, \quad (2.27)$$

$$r(v_{re}, v_{im}) = \frac{\mathbf{C}_{12}(\underline{v})}{u(v_{re})u(v_{im})}, \quad (2.28)$$

where the indices specify an element of the matrix by the row and column numbers [45]. The covariance matrices include both type A and B uncertainties, i.e. $\mathbf{C}(\underline{v}) = \mathbf{C}_A(\underline{v}) + \mathbf{C}_B(\underline{v})$, if both are evaluated. The same applies to every voltage and current phasor $\underline{v}_{a1}, \underline{i}_{a1}$, etc.

The Jacobians can be found by the procedure introduced in Eq. (2.16)

$$\forall \underline{x} \in \{v_1, v_2, i_1, i_2\} : \quad \mathbf{J}_{\underline{z}}(\underline{x}) = \begin{bmatrix} \left(\frac{\partial \underline{z}}{\partial \underline{x}}\right)_{re} & -\left(\frac{\partial \underline{z}}{\partial \underline{x}}\right)_{im} \\ \left(\frac{\partial \underline{z}}{\partial \underline{x}}\right)_{im} & \left(\frac{\partial \underline{z}}{\partial \underline{x}}\right)_{re} \end{bmatrix}, \quad (2.29)$$

$$\mathbf{J}_y(\underline{x}) = \begin{bmatrix} \left(\frac{\partial y}{\partial \underline{x}}\right)_{\text{re}} & -\left(\frac{\partial y}{\partial \underline{x}}\right)_{\text{im}} \\ \left(\frac{\partial y}{\partial \underline{x}}\right)_{\text{im}} & \left(\frac{\partial y}{\partial \underline{x}}\right)_{\text{re}} \end{bmatrix}. \quad (2.30)$$

The differentiation can be handled as follows

$$\forall \underline{x} \in \{v_1, v_2, i_1, i_2\} : \quad (2.31)$$

$$\frac{\partial z}{\partial \underline{x}} = z_c \frac{\partial \gamma}{\partial \underline{x}} + \gamma \frac{\partial z_c}{\partial \underline{x}},$$

$$\frac{\partial y}{\partial \underline{x}} = \frac{1}{z_c} \frac{\partial \gamma}{\partial \underline{x}} - \frac{\gamma}{z_c^2} \frac{\partial z_c}{\partial \underline{x}}, \quad (2.32)$$

$$\frac{\partial \gamma}{\partial \underline{x}} = \frac{\partial \underline{p} / \partial \underline{x}}{L \sqrt{(\underline{p} + 1)(\underline{p} - 1)}}, \quad (2.33)$$

$$\frac{\partial z_c}{\partial \underline{x}} = \frac{v_2 \underline{p} (\partial \underline{p} / \partial \underline{x}) + (\partial v_2 / \partial \underline{x}) (\underline{p} + 1)(\underline{p} - 1)}{\sqrt{(\underline{p} + 1)(\underline{p} - 1)} (i_1 - i_2 \underline{p})} - \frac{v_2 \sqrt{(\underline{p} + 1)(\underline{p} - 1)}}{(i_1 - i_2 \underline{p})^2} \left(\frac{\partial i_1}{\partial \underline{x}} - \underline{p} \frac{\partial i_2}{\partial \underline{x}} - i_2 \frac{\partial \underline{p}}{\partial \underline{x}} \right), \quad (2.34)$$

$$\frac{\partial \underline{p}}{\partial \underline{x}} = \frac{1}{t^2} \left(t \frac{\partial q}{\partial \underline{x}} - q \frac{\partial t}{\partial \underline{x}} \right), \quad (2.35)$$

where the derivatives by the measured quantities are

$$\frac{\partial q}{\partial v_1} = i_1, \quad \frac{\partial t}{\partial v_1} = i_2, \quad (2.36a,b)$$

$$\frac{\partial q}{\partial v_2} = i_2, \quad \frac{\partial t}{\partial v_2} = i_1, \quad (2.36c,d)$$

$$\frac{\partial q}{\partial i_1} = v_1, \quad \frac{\partial t}{\partial i_1} = v_2, \quad (2.36e,f)$$

$$\frac{\partial q}{\partial i_2} = v_2, \quad \frac{\partial t}{\partial i_2} = v_1. \quad (2.36g,h)$$

This leads to the covariance matrices

$$\mathbf{C}(z) = \sum_{\underline{x} \in \{v_1, v_2, i_1, i_2\}} \mathbf{J}_z(\underline{x}) \mathbf{U}(\underline{x}) \mathbf{R}(\underline{x}) [\mathbf{J}_z(\underline{x}) \mathbf{U}(\underline{x})]^\top, \quad (2.37)$$

$$\mathbf{C}(y) = \sum_{\underline{x} \in \{v_1, v_2, i_1, i_2\}} \mathbf{J}_y(\underline{x}) \mathbf{U}(\underline{x}) \mathbf{R}(\underline{x}) [\mathbf{J}_y(\underline{x}) \mathbf{U}(\underline{x})]^\top, \quad (2.38)$$

which hold information about the uncertainties $u(z_{\text{re}})$, $u(z_{\text{im}})$, $u(y_{\text{re}})$, and $u(y_{\text{im}})$ of the impedance and admittance estimates.

If ideal transposition is assumed, positive sequence impedance becomes the mean of three phase quantities, i.e.

$$\underline{z}_+ = (\underline{z}_a + \underline{z}_b + \underline{z}_c) / 3 \quad (2.39)$$

the covariances become

$$\mathbf{C}(z_+) = \mathbf{C}(z_a) + \mathbf{C}(z_b) + \mathbf{C}(z_c), \quad (2.40)$$

where

$$\mathbf{C}(z_a) = \sum_{\mathbf{x} \in \{v_{a1}, v_{a2}, i_{a1}, i_{a2}\}} (\mathbf{J}_z(\mathbf{x})/3) \mathbf{U}(\mathbf{x}) \mathbf{R}(\mathbf{x}) [(\mathbf{J}_z(\mathbf{x})/3) \mathbf{U}(\mathbf{x})]^\top, \quad (2.41)$$

etc.

2.4 Analysis of Monitoring Data from a Real System

In this section, the results seen in Sec. 1.3 are complemented by the analysis of uncertainty propagation. The same monitoring period from 26–27 January 2018 with a length of 18 hours was used. Parameters were calculated from single samples with a 10 s step and also smoothed with a moving window. Based on available information about the devices in the measurement chain, uncertainties propagated into the estimates were analyzed.

The observed transmission line is 210 km long and the reference value of impedance is $0.0243 + j0.295 \Omega/\text{km}$ (adjusted to 25°C) with a typical error of 0.5% in reactance and 10% in resistance. Based on weather data from nearby weather stations, the approximate temperature of the conductors was found to vary between $1\text{--}5^\circ\text{C}$ during this 18 hour period, which would result in a resistance of approximately $0.022 \Omega/\text{km}$ instead [33, 34].

The line is equipped with PMUs at both substations. The PMUs are connected to voltage transformers (VT) of class 0.2 and current transformers (CT) of class 0.2S in one substation and corresponding VTs and CTs of classes 0.5 and 0.5S at the other end. The CTs are rated at 1 kA and 2 kA, respectively. Reported errors of all instrument transformers and approximate values of burden are presented in Appendix A. The PMUs installed in the system are identical and have an 0.01° angle measurement error, 0.03% current and 0.02% voltage magnitude relative measurement error, reported by the manufacturer. The substation has one common GPS clock and the PMUs are synchronized over IRIG-B. In this work, time synchronization errors are assumed to be included in the angle errors. An 0.95 confidence level is assumed so that $k_p = 1.96$ and $k_{2,p} = 2.45$ [46].

The instrument transformers have not been calibrated; however, there is limited information about their measurement accuracy from factory test reports. The test reports give errors for a few operating points with two different values of burden. Exact burden values in the circuits are not known, but some approximated values are available. The available information is too incomplete to make accurate corrections in the measured values; however, it gives a better understanding how measurement errors change with changes in current and voltage.

For each measured quantity, two uncertainty intervals have been calculated. As a more generic solution, it has been assumed that instrument transformer errors can reach the maximum limits allowed in the standards [36, 37]. As a result, this gives very conservative uncertainty intervals. These are referred to as accuracy class uncertainty bounds. As long as specific information about the measurement errors of instrument transformers is not available, this is an appropriate assumption based on metrological principles [42].

In addition to that, another uncertainty interval has been calculated for each quantity, referred to as reported error uncertainties. These uncertainties are based on the limited information that is available about the instrument transformers and their burdens. The results of the factory test reports and the approximate burden values have been used to approximate the measurement errors. These uncertainty bounds are less conservative

and are better at characterizing the dependence of measurement errors on the measured quantities. However, calculating uncertainties this way is not strictly correct in metrological terms. Because the approximate errors are close to actual errors, either the higher or lower uncertainty bound of each quantity should be close to the correct value.

Another question of metrology is the stationarity of the measured quantities. When measuring transmission line parameters, there are certain quantities that could be considered stationary, e.g. the reactance of a line, while others change in time. The various quantities change in time at different rates and if consecutive measurements are averaged, this rate of change has to be considered. For the sake of clearer visualization, the shunt admittance parameters have been smoothed with a moving window of six samples, corresponding to a one minute average.

The calculated line parameters were accompanied by the results of uncertainty propagation analysis. Fig. 2.4 and Fig. 2.5 present the series resistance and reactance estimates and their uncertainties. The impedance components were computed as the mean of the resistance and reactance of each of the phases as in (2.39), assuming an ideally balanced line, and uncertainties according to (2.23) and (2.37). As described earlier, two ranges of uncertainties are given—one based on accuracy classes and the other based on approximate reported errors. The active and reactive power flows at one end of the transmission line are plotted in Figs. 2.8 and 2.9 while magnitudes of current and voltage phasors were given in Figs. 1.8 and 1.9 in Chap. 1.

The measured values of positive sequence phase resistance present large systematic measurement errors. The estimates deviate greatly from the reference value and display larger changes in time than expected. However, the measurement also has large uncer-

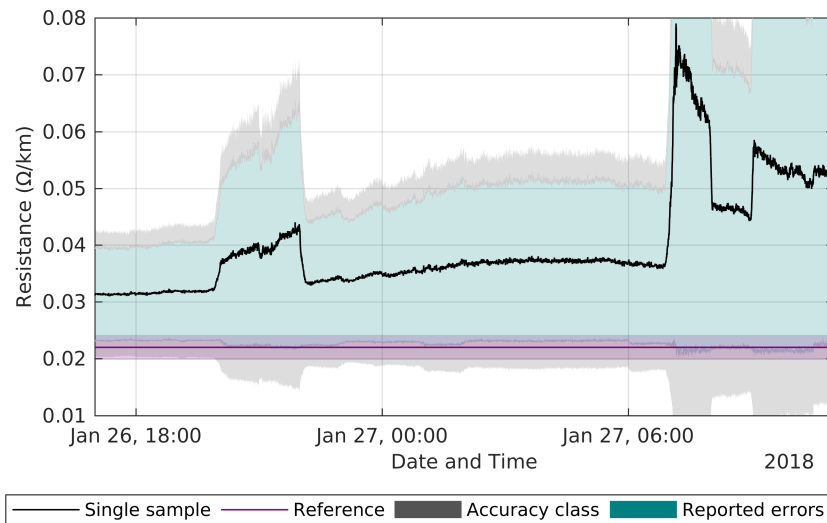


Figure 2.4 Positive sequence resistance estimated from PMU measurements and the two uncertainty regions, depicted as black line and two filled areas, respectively. Grey corresponds to uncertainties based on accuracy class errors and light blue to uncertainties based on approximated reported errors. Measured reference resistance adjusted to temperature given for comparison, purple line and error interval.

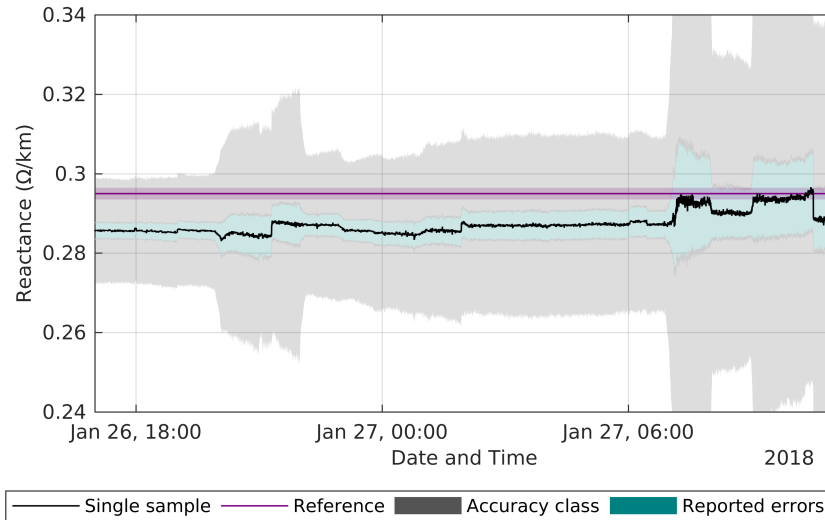


Figure 2.5 Positive sequence reactance estimated from PMU measurements and the two uncertainty regions, depicted as black line and two filled areas, respectively. Grey corresponds to uncertainties based on accuracy class errors and light blue to uncertainties based on approximated reported errors. Measured reference reactance given for comparison as a purple line and error interval.

tainties and the resulting uncertainty intervals contain the reference value. The measured value of reactance is close to the reference and its uncertainty is relatively smaller than the uncertainty of resistance. The values exhibit changes in time that are aligned with changes in reactive power, indicating that the measurement error may vary with (and depend on) such changes. It also appears that the uncertainties of both quantities increase when the load on the line decreases.

Fig. 2.6 and Fig. 2.7 present the measured values of shunt conductance and susceptance and their uncertainties. The negative values of shunt conductance also indicate measurement errors, since this conductance cannot be negative. The higher bound of uncertainties of conductance based on approximated reported errors shows a rather stable value close to zero throughout the measurement period. In shunt admittance measurements the uncertainties based on accuracy class errors increase with higher load on the line while uncertainties based on approximated reported errors show minimal dependence on loading of the line.

The parameters of a transmission line do not generally vary significantly in time. The resistance of a conductor does change with temperature, increasing approximately 3–5% with a 10 °C increase in temperature, while inductance and capacitance are expected to change very little. A larger current would heat a conductor, leading to changes in resistance with a time constant of a few minutes. Shunt conductance differs from other parameters, as it is instead an element in the line model that represents active losses that are not dissipated as heat in the resistance. However, neither resistance, reactance, nor susceptance are expected to change in steps, as instant changes corresponding to varying current or voltage. It can be observed how both the changes in certain estimated quantities and their uncertainties change with variations in active and reactive power,

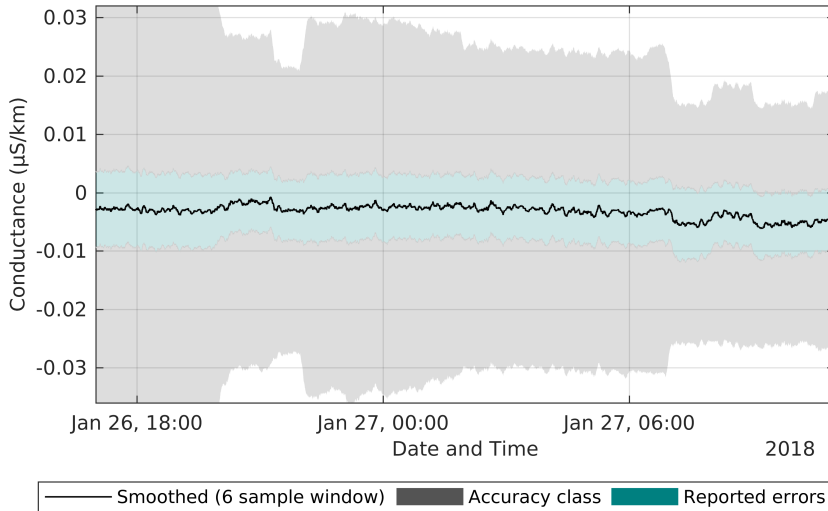


Figure 2.6 Positive sequence shunt conductance estimated from PMU measurements and the two uncertainty regions, depicted as black line and two filled areas, respectively. Grey corresponds to uncertainties based on accuracy class errors and light blue to uncertainties based on approximated reported errors.

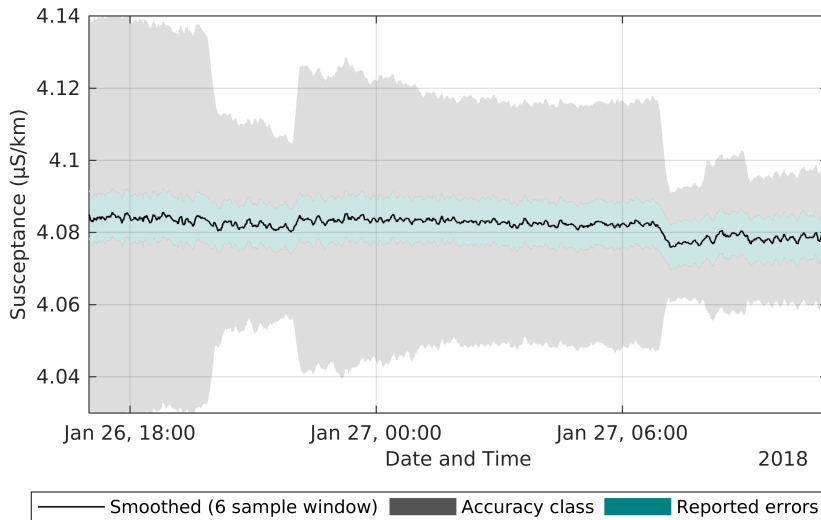


Figure 2.7 Positive sequence shunt susceptance estimated from PMU measurements and the two uncertainty regions, depicted as black line and two filled areas, respectively. Grey corresponds to uncertainties based on accuracy class errors and light blue to uncertainties based on approximated reported errors.

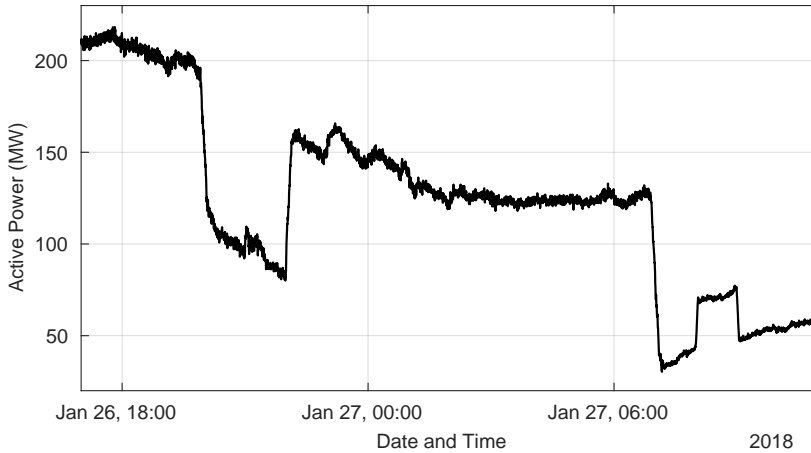


Figure 2.8 PMU measurements of active power flow at one end of the transmission line.

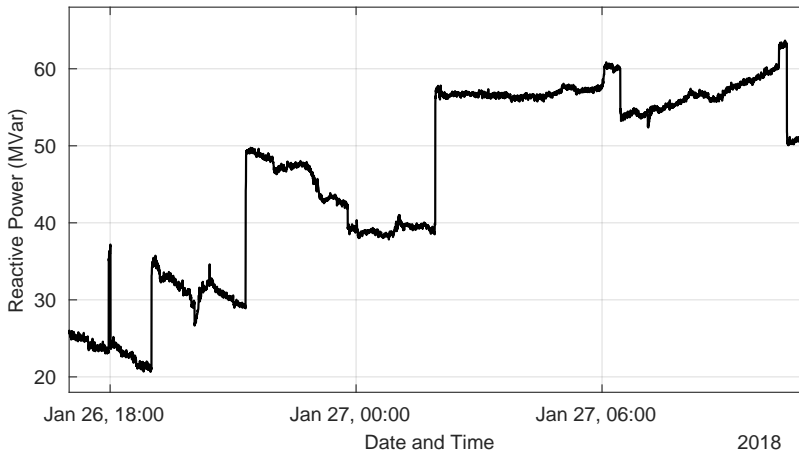


Figure 2.9 PMU measurements of reactive power flow at one end of the transmission line.

corresponding to variations in current and voltage.

Most of the changes in time seen in the results of estimated line parameters could not be physically correct and are assumed to be caused by measurement errors instead. Uncertainties calculated considering the possible extent of measurement errors support this assumption. The uncertainties based on approximated reported errors assume errors close to their real values and showed more realistic values for both resistance and reactance throughout the measurement period. However, even in these bounds sudden variations were still present, corresponding to changes in voltage and current.

In the measured values of resistance, it can be seen that the values were closer to the expected true value when the measured currents or active power were larger. The values of reactance differed from the reference value most of the time, but the values were more stable with higher measured currents. Both uncertainty regions for both resistance and reactance became narrower as measured currents increased, indicating a dependence

of errors on measured current. As seen in Appendix A, current magnitude errors vary little with varying current, while current angle errors increase significantly with lower measured current. Thus, estimates of reactance are especially influenced by current angle errors. Estimates of resistance also improved at higher loading of the line, because current transformers are more accurate when they are measuring a current closer to the rated value. However, there were still significant errors present. This is mostly because the voltage drop across the line is determined by the impedance and the voltage drop is a difference of two close values. Also, reported voltage magnitude errors are the ones closest to accuracy class limits.

Correct shunt parameters are not known and it is difficult to determine whether they were more accurate when measured currents were smaller or larger. Here it is especially important to compare the two different uncertainty intervals. While uncertainties based on accuracy class errors would indicate that confidence in the measurements decreases with higher currents, uncertainties based on approximated reported errors do not show this. In fact, throughout the measurement period uncertainties based on approximated reported errors remained nearly constant. In case of conductances, the higher bound of uncertainties based on approximated reported errors was also close to zero. These uncertainty estimates may underestimate some of the systematic errors, but they demonstrate that accuracy class errors clearly overestimate the uncertainty of shunt parameters with larger measured currents.

2.5 Conclusions

This chapter presented a thorough analysis of errors and uncertainty propagation in PMU based transmission line parameter monitoring. The uncertainty analysis helped to explain how the errors in measured voltages and currents are propagated into estimated line parameters. It was also shown that the principles of analysing uncertainty propagation in two-dimensional quantities are appropriate for complex valued phasors and provide useful information about the confidence in obtained results. The analysis showed how PMU based transmission line monitoring is affected by measurement errors, what accuracy can be expected, and under which conditions certain estimates become more accurate. Resistance and reactance can be monitored better when the loading of the line is larger, but acceptable resistance estimates require significantly higher measurement accuracy in any case. Shunt admittance parameters are difficult to validate, but their uncertainties based on approximated reported errors were not very large and behaved similarly under varying operating conditions.

The work shows that if more accurate estimates of line parameters are needed, either calibration or replacement of the instrument transformers would be required. Even metering class transformers were not sufficient to obtain usable estimates of line resistance in the given configuration. Current transformers should not be overdimensioned and burdens outside the prescribed range should be avoided if more accurate PMU measurements are desired. As discussed in Chap. 1, the accuracy of PMUs is only limited by a 1% TVE in the phasors. If a PMU would have errors as large as 1% in the measured phasors, the accuracy of estimate line parameters would be significantly poorer and the errors could be several times larger than seen in the examples. Moreover, since TVE does not distinguish between magnitude and phase errors, it is also difficult to analyze uncertainties in phasors and complex quantities derived from phasors based on this information.

3 Monitoring of Corona Losses

One of the many tasks of a transmission system operator (TSO) is to cover the energy consumed as losses in the transmission system. For a TSO operating in a deregulated energy market, this consequently introduces the need to forecast transmission losses so that the energy could be bought at the lowest possible cost. In a small system like the Estonian transmission system the annual cost of loss energy is 10–15 million EUR. For comparison, the TSO is paid around 90 million EUR annually for providing the transmission system service [47]. Even a small improvement in transmission loss forecasting could help the TSO save considerable sums, significant even in terms of its overall spending.

The majority of transmission losses are resistive (or Joule) losses. This is the energy dissipated in the resistances of elements of the transmission network as current flows through them. Forecasting of resistive losses is based on forecasting load—once load is forecast, it is simple to estimate corresponding losses from a power flow solution. However, in addition to resistive losses, significant corona losses can also occur on transmission lines in certain weather conditions. Since corona losses are not load dependent, they are usually not captured in the forecasts. Without good forecasts of corona losses, the overall forecast of losses can sometimes contain significant errors.

Accounting for corona losses is further complicated by the difficulties of monitoring them. Corona losses have conventionally been measured with dedicated experimental equipment that is not available for continuous monitoring across the system [48–51]. In addition to that, different empirical formulas have been developed for the estimation of corona losses [52–54]. However, these equations require a lot of tuning and are difficult to use in the field in varying conditions over longer periods.

Synchronized phasor measurements and wide area monitoring systems offer new possibilities for monitoring transmission losses. Similarly to estimating transmission line parameters it is possible to analyze what share of total losses corresponds to resistive (Joule) losses and what share of losses is caused by other effects. The main hypothesis of this chapter is that corona losses on transmission lines can be detected and monitored with PMU measurements from both ends of the line. Once it is possible to monitor corona losses continuously across the system, it is a lot easier to improve forecasts of this component of transmission losses. The theoretical basis of the work and preliminary results were presented in Publication II and Publication IV.

3.1 Available Methods of Estimating Corona Losses

The first empirical formulas for corona losses were developed from experiments in the beginning of the last century [52–54]. These empirical formulas usually take one of the following two forms [55]. Expressed in terms of voltages as

$$\Delta P_{C,U} = f(U, U_C), \quad (3.1)$$

where U is voltage on the conductor, U_C is the critical or corona on-set voltage, and f is an empirical function [54, 56]. Expressed in terms of electric field strengths

$$\Delta P_{C,E} = f(E, E_C), \quad (3.2)$$

where E is the superficial electric field strength, E_C is the critical or corona on-set electric field strength, and f is an empirical function [57].

In the Soviet Union, thorough guidelines on accounting for corona losses and radio interference were compiled based on experimental work and existing practices [58]. The

guidelines were meant for planning and design of transmission lines. This means all the calculations were made for the long term and were based on average seasonal data of various regions. This work is a good example of cases where the empirical equations can be applied. It also provides interesting information on how different weather conditions affect corona losses.

The empirical functions and the on-set (critical) values are determined experimentally and depend on many factors; for example, design of the conductor (or bundle), material surface properties, air properties, precipitation, extent of frost on conductors, etc. [52–59]. Several such empirical formulas are available, however, it is difficult to apply these on operational transmission lines in the power system. Recently, a practical application attempting to do that was proposed [60]. The study showed promising results but still demonstrated the difficulties of determining the unknown parameters of the empirical formulas.

In other approaches, statistical methods for forecasting corona losses based on weather data have been proposed [55, 61]. The variable share of corona losses is mostly caused by changes in weather conditions, while the dependence on conductor properties and line configuration are more constant in time. By collecting large enough amounts of weather data and applying statistical methods, it is possible to develop models that can estimate and forecast corona losses [55, 61]. However, even in this case it is necessary to obtain the historical values of corona losses in order to determine these correlations with weather conditions.

3.2 Transmission Losses from Synchronized Phasors

The distributed parameter transmission line model was discussed in Sec. 1.3 and Fig. 1.3 gave a schematic of the model. When the voltage and current phasors in the ends of the line and the parameters of the line are known, it is also possible to analyze the power consumed in the elements of the line model, i.e. transmission losses. Current flowing in the line will cause resistive losses to be dissipated in the resistances r and reactive power to be consumed in reactances x . At the same time, voltage applied over the shunt elements also causes active losses in conductances g and generation of reactive power in susceptances b .

The shunt conductance is somewhat different from the rest of the line parameters. It can mostly represent two phenomena—leakage currents in insulators and losses dissipated in corona discharges. For most operational transmission lines, we can assume that the leakage effect is small enough that the losses caused by it are several orders of magnitude smaller than resistive (Joule) losses, and thus, can be considered negligible. Transmission lines are designed so that in good weather conditions the occurrence of corona losses is minimal and they too can be considered negligible. Thus, in modeling, the common practice is to assume that shunt conductance is zero.

There is an important exception to this, however. In certain weather conditions, corona losses can reach the same order of magnitude as resistive losses [51]. In very rare occasions it is also possible that leakage losses become considerable. When either of these happens, there are active losses that are dissipated on the line but not in the series resistance. Still, the power balance on the transmission line is affected and the model has to account for this. In this situation, the change in the power balance causes the calculated value of shunt conductance to increase in order to account for these losses. Thus, losses dissipated in the shunt conductance elements in the transmission line model can be assumed to correspond to any active losses that are not resistive. In the majority of cases, we can assume these are corona losses.

3.2.1 Losses on Two Conductor Transmission Lines

Continuing with the example of the basic distributed parameter line model, we can express the transmission losses from measured voltages and currents. Transmission losses across a two conductor line of length L can be computed as $\underline{U}(L)\underline{I}^*(L) - \underline{U}(0)\underline{I}^*(0)$, where $*$ denotes the complex conjugate. In the line model, at a location l , the losses dissipated in the distributed elements can be expressed as $|\underline{I}(l)|^2 z dl$ and $|\underline{U}(l)|^2 y dl$. If the losses in the infinitesimally short sections are integrated over the length of the line, transmission losses and reactive power balance become

$$\Delta P = r \int_0^L |\underline{I}(l)|^2 dl + g \int_0^L |\underline{U}(l)|^2 dl, \quad (3.3)$$

$$\Delta Q = x \int_0^L |\underline{I}(l)|^2 dl - b \int_0^L |\underline{U}(l)|^2 dl, \quad (3.4)$$

where the reactive power of the capacitance is considered to be negative.

If line parameters are calculated from simultaneous phasor measurements, the equations for $\underline{I}(l)$ and $\underline{U}(l)$ can be solved and integrated numerically. Thus, the total losses can be calculated as $\underline{U}(L)\underline{I}^*(L) - \underline{U}(0)\underline{I}^*(0) = \Delta P + j\Delta Q$. Publication IV presented this approach and tested it on measurement data [62]. This work made the assumption that each phase is analyzed independently since PMUs measure phase quantities. However, as the work showed, this assumption applied to computing losses in individual phases resulted in significant errors.

The majority of analyses treat transmission lines as two conductor lines. However, in certain cases this simplification is not valid. An AC transmission line is a multiconductor line where phase voltages and currents are mutually coupled. For example, in electromagnetic transient simulations it is common to use multiconductor transmission line models, which model all of the phases and the mutual couplings between them. As the results in Publication IV showed, the calculation of the components of transmission losses should first be analyzed based on a multiconductor model to account for the effects of mutual coupling.

3.2.2 Losses on Multiconductor Lines in Phase Domain

The following analysis considers a three phase AC transmission line. A multiconductor distributed parameter transmission line model is assumed, depicted in Fig. 3.1. It is assumed that neutral wires are removed from the model using Kron's reduction and transpositions accounted for. In this model, the phase voltages and currents at any point of the line are given as [63, 64]

$$\mathbf{u}(l) = \begin{bmatrix} \underline{U}_a(l) \\ \underline{U}_b(l) \\ \underline{U}_c(l) \end{bmatrix}, \quad \mathbf{i}(l) = \begin{bmatrix} \underline{I}_a(l) \\ \underline{I}_b(l) \\ \underline{I}_c(l) \end{bmatrix}, \quad (3.5)$$

where l is the distance toward the beginning of the line and $\underline{U}_i(l)$ and $\underline{I}_i(l)$ are the voltage and current phasors in phase i .

The voltages and currents can be related through Kirchhoff's laws as [63]

$$\frac{d\mathbf{u}(l)}{dl} = \mathbf{Z}\mathbf{i}(l), \quad (3.6)$$

$$\frac{d\mathbf{i}(l)}{dl} = \mathbf{Y}\mathbf{u}(l), \quad (3.7)$$

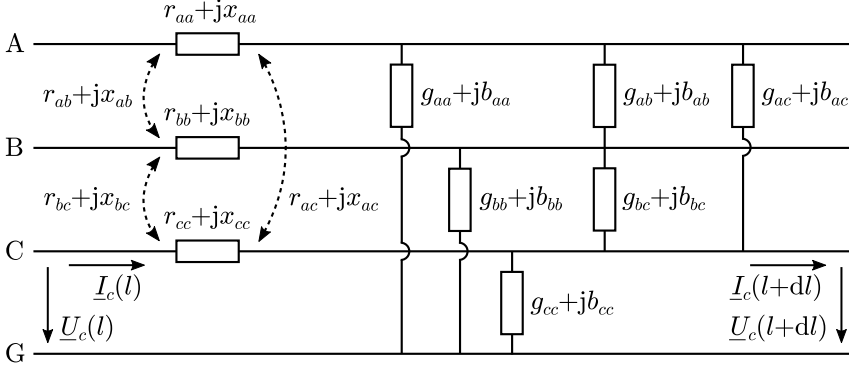


Figure 3.1 Multiconductor distributed parameter model of a three phase transmission line. Voltages and currents are given as functions of the position along the length of the line. The line is divided into infinitesimally short sections of length dl with per unit distance parameters $\tilde{z}_{aa} = r_{aa} + jx_{aa}$ [Ω/km], etc.

which can be further differentiated into

$$\frac{d^2 \mathbf{u}(l)}{dl^2} = \mathbf{ZY} \mathbf{u}(l), \quad (3.8)$$

$$\frac{d^2 \mathbf{i}(l)}{dl^2} = \mathbf{YZ} \mathbf{i}(l). \quad (3.9)$$

The matrices \mathbf{Z} and \mathbf{Y} contain the parameters of the line model, i.e.

$$\mathbf{Z} = \begin{bmatrix} \tilde{z}_{aa} & \tilde{z}_{ab} & \tilde{z}_{ac} \\ \tilde{z}_{ab} & \tilde{z}_{bb} & \tilde{z}_{bc} \\ \tilde{z}_{ac} & \tilde{z}_{bc} & \tilde{z}_{cc} \end{bmatrix}. \quad (3.10)$$

When looking at phase quantities, it can be seen that there are no closed form solutions to the equations

$$\frac{d\underline{U}_a(l)}{dl} = \mathbf{Z}_{aa} \underline{I}_a(l) + \mathbf{Z}_{ab} \underline{I}_b(l) + \mathbf{Z}_{ac} \underline{I}_c(l), \quad (3.11)$$

$$\frac{d^2 \underline{U}_a(l)}{dl^2} = \mathbf{\Gamma}_{aa}^2 \underline{U}_a(l) + \mathbf{\Gamma}_{ab}^2 \underline{U}_b(l) + \mathbf{\Gamma}_{ac}^2 \underline{U}_c(l), \quad \text{etc.} \quad (3.12)$$

where $\mathbf{\Gamma}^2 = \mathbf{ZY}$. However, there is a general solution with respect to the matrices in (3.8) and (3.9).

The matrix $\mathbf{\Gamma} = (\mathbf{ZY})^{1/2}$ is also termed the propagation matrix and the matrix equivalent of the characteristic impedance is defined as $\mathbf{Z}_C = \mathbf{\Gamma}^{-1} \mathbf{Z}$. Equations (3.8) and (3.9) can be solved to express [65]

$$\mathbf{u}(l) = \cosh(\mathbf{\Gamma}l) \mathbf{u}(0) + \sinh(\mathbf{\Gamma}l) \mathbf{Z}_C \mathbf{i}(0), \quad (3.13)$$

$$\mathbf{i}(l) = \mathbf{Z}_C^{-1} \sinh(\mathbf{\Gamma}l) \mathbf{u}(0) + \mathbf{Z}_C^{-1} \cosh(\mathbf{\Gamma}l) \mathbf{Z}_C \mathbf{i}(0), \quad (3.14)$$

where $\cosh \mathbf{M} = [\exp(\mathbf{M}) + \exp(-\mathbf{M})]/2$ and $\sinh \mathbf{M} = [\exp(\mathbf{M}) - \exp(-\mathbf{M})]/2$.

The voltage of one phase at a distance l can then be expressed as

$$\begin{aligned}\underline{U}_a(l) &= (\cosh \mathbf{\Gamma}l)_{aa}\underline{U}_a(0) + [\sinh(\mathbf{\Gamma}l)\mathbf{Z}_C]_{aa}\underline{I}_a(0) \\ &+ (\cosh \mathbf{\Gamma}l)_{ab}\underline{U}_b(0) + [\sinh(\mathbf{\Gamma}l)\mathbf{Z}_C]_{ab}\underline{I}_b(0) \\ &+ (\cosh \mathbf{\Gamma}l)_{ac}\underline{U}_c(0) + [\sinh(\mathbf{\Gamma}l)\mathbf{Z}_C]_{ac}\underline{I}_c(0),\end{aligned}\quad (3.15)$$

which displays the coupling of phase quantities even more clearly. From (3.15) it can be seen that on a multiconductor line the voltages and currents of one phase are not accurately modeled by the two conductor line equations. If such a model is nevertheless used, the physical meaning of its parameters change.

If the whole length L of the line is considered, the sending end voltages and currents are expressed from the receiving end as follows

$$\begin{bmatrix} \mathbf{u}_1 \\ \mathbf{i}_1 \end{bmatrix} = \begin{bmatrix} \cosh(\mathbf{\Gamma}L) & \sinh(\mathbf{\Gamma}L)\mathbf{Z}_C \\ \mathbf{Z}_C^{-1}\sinh(\mathbf{\Gamma}L) & \mathbf{Z}_C^{-1}\cosh(\mathbf{\Gamma}L)\mathbf{Z}_C \end{bmatrix} \begin{bmatrix} \mathbf{u}_2 \\ \mathbf{i}_2 \end{bmatrix}, \quad (3.16)$$

where $\mathbf{u}_1 = \mathbf{u}(L)$, $\mathbf{u}_2 = \mathbf{u}(0)$, etc. Clearly $[\mathbf{u}_2, \mathbf{i}_2]^\top = \mathbf{J}^{-1}[\mathbf{u}_1, \mathbf{i}_1]^\top$, where \mathbf{J} is the given matrix forming the system of equations.

In this notation, we can express the total power injected into the line at the sending end as

$$\underline{S}(L) = \mathbf{i}^\dagger(L)\mathbf{u}(L) = \mathbf{i}_1^\dagger\mathbf{u}_1 = \underline{U}_a(L)\underline{I}_a^*(L) + \underline{U}_b(L)\underline{I}_b^*(L) + \underline{U}_c(L)\underline{I}_c^*(L), \quad (3.17)$$

where \dagger denotes the conjugate transpose. The power flowing out of the line at the other end can be computed similarly.

Based on this, the losses across the length of the line become

$$\underline{\Delta S}_L = \mathbf{i}_1^\dagger\mathbf{u}_1 - \mathbf{i}_2^\dagger\mathbf{u}_2 = \mathbf{i}^\dagger(L)\mathbf{u}(L) - \mathbf{i}^\dagger(0)\mathbf{u}(0), \quad (3.18)$$

where the voltage and current phasors in three phases are the quantities measured by PMUs.

The hyperbolic functions are holomorphic, thus $(\cosh \mathbf{M})^\dagger = \cosh(\mathbf{M}^\dagger)$. For a line of length L , we can express the losses as

$$\begin{aligned}\underline{\Delta S}_L &= \mathbf{i}_1^\dagger\mathbf{u}_1 \\ &+ \mathbf{u}_1^\dagger \sinh(\dagger L)^\dagger (\mathbf{Z}^{-1})^\dagger \cosh(L)\mathbf{u}_1 + \mathbf{i}_1^\dagger \mathbf{Z}^\dagger (\mathbf{\Gamma}^{-1})^\dagger \cosh(\dagger L)^\dagger (\mathbf{Z}^{-1})^\dagger \sinh(\mathbf{\Gamma}L)\mathbf{\Gamma}^{-1}\mathbf{Z}\mathbf{i}_1 \\ &- \mathbf{i}_1^\dagger \mathbf{Z}^\dagger (\mathbf{\Gamma}^{-1})^\dagger \cosh(\dagger L)^\dagger (\mathbf{Z}^{-1})^\dagger \cosh(L)\mathbf{u}_1 - \mathbf{u}_1^\dagger \sinh(\dagger L)^\dagger (\mathbf{Z}^{-1})^\dagger \sinh(\mathbf{\Gamma}L)\mathbf{\Gamma}^{-1}\mathbf{Z}\mathbf{i}_1\end{aligned}\quad (3.19)$$

The hyperbolic functions can be expanded in series as follows

$$\cosh(\mathbf{M}) = \mathbf{I} + \frac{\mathbf{M}^2}{2!} + \frac{\mathbf{M}^4}{4!} + \dots, \quad (3.20)$$

$$\sinh(\mathbf{M}) = \mathbf{M} + \frac{\mathbf{M}^3}{3!} + \frac{\mathbf{M}^5}{5!} + \dots, \quad (3.21)$$

where \mathbf{I} is the identity matrix.

For a sufficiently short line section of length Δl , it can be assumed that $(\mathbf{\Gamma}\Delta l)^2$ and $(\mathbf{\Gamma}\Delta l)^3$ become negligible compared to \mathbf{I} and $\mathbf{\Gamma}\Delta l$. By equating the hyperbolic functions to the first terms in the series expansions, the losses across the short section are simplified

so that

$$\underline{\Delta S}_{\Delta l} = \mathbf{u}^\dagger(\Delta l) \mathbf{Y}^\dagger \mathbf{u}(\Delta l) \Delta l + \mathbf{i}^\dagger(\Delta l) \mathbf{Z} \mathbf{i}(\Delta l) \Delta l + O[(\Delta l)^2] \quad (3.22)$$

Thus, at a location l the losses across an infinitesimally short section of the line are

$$d\underline{\Delta S}(l) = \mathbf{u}^\dagger(l) \mathbf{Y}^\dagger \mathbf{u}(l) dl + \mathbf{i}^\dagger(l) \mathbf{Z} \mathbf{i}(l) dl, \quad (3.23)$$

which can be integrated over the length of the line to obtain total losses

$$\underline{\Delta S}_L = \int_0^L \mathbf{u}^\dagger(l) \mathbf{Y}^\dagger \mathbf{u}(l) dl + \int_0^L \mathbf{i}^\dagger(l) \mathbf{Z} \mathbf{i}(l) dl. \quad (3.24)$$

The obtained result displays clear analogy with the two conductor transmission line, especially considering that $\mathbf{Y}^\dagger = \mathbf{G} - j\mathbf{B}$ (since \mathbf{Y} is symmetric) and $|a|^2 = \underline{a}^* \underline{a}$. Similarly to the two conductor case, we can also separate the expression for losses into a sum of four separate terms, i.e.

$$\underline{\Delta S}_L = \Delta P_J + \Delta P_C + j(\Delta Q_I - \Delta Q_C). \quad (3.25)$$

These four terms can be expressed as

$$\Delta P_J = \int_0^L \mathbf{i}^\dagger(l) \mathbf{R} \mathbf{i}(l) dl, \text{ etc.} \quad (3.26)$$

In more detail, the term expressed in scalar values becomes

$$\begin{aligned} \mathbf{i}^\dagger(l) \mathbf{R} \mathbf{i}(l) &= \underline{I}_a(l) \underline{I}_b^*(l) \mathbf{R}_{ab} + \underline{I}_a(l) \underline{I}_c^*(l) \mathbf{R}_{ac} + \underline{I}_b(l) \underline{I}_a^*(l) \mathbf{R}_{ab} + \underline{I}_b(l) \underline{I}_c^*(l) \mathbf{R}_{bc} \\ &+ \underline{I}_c(l) \underline{I}_a^*(l) \mathbf{R}_{ac} + \underline{I}_c(l) \underline{I}_b^*(l) \mathbf{R}_{bc} + |\underline{I}_a(l)|^2 \mathbf{R}_{aa} + |\underline{I}_b(l)|^2 \mathbf{R}_{bb} + |\underline{I}_c(l)|^2 \mathbf{R}_{cc}, \end{aligned} \quad (3.27)$$

which gives the sum of losses in resistances from all three phases. Similar expressions hold for the rest of the terms

Due to the mutual coupling between phases, it is difficult to analyse the components of losses further in the phase domain. It is complicated to interpret the physical meaning of the terms in the sum, mostly the mutual parameters, because of the Kron's reduction and other operations carried out in the calculation of line parameter matrices. For this reason, the analysis is continued in the symmetrical component domain.

3.2.3 Losses on Multiconductor Lines in Symmetrical Component Domain

On a single circuit three phase transmission line, the zero, positive, and negative sequence voltages and currents

$$\mathbf{u}_S(l) = [\underline{U}_0(l), \underline{U}_+(l), \underline{U}_-(l)]^T, \quad (3.28)$$

$$\mathbf{i}_S(l) = [\underline{I}_0(l), \underline{I}_+(l), \underline{I}_-(l)]^T, \quad (3.29)$$

are obtained by linear transformations $\mathbf{u}_S(l) = \mathbf{T}_S^{-1} \mathbf{u}(l)$ and $\mathbf{i}_S(l) = \mathbf{T}_S^{-1} \mathbf{i}(l)$, where

$$\mathbf{T}_S = \begin{bmatrix} 1 & 1 & 1 \\ 1 & e^{j4\pi/3} & e^{j2\pi/3} \\ 1 & e^{j2\pi/3} & e^{j4\pi/3} \end{bmatrix}. \quad (3.30)$$

It can also be noted that $\mathbf{T}_S^{-1} = \mathbf{T}_S^\dagger/3$.

The terms in the expression of transmission losses $\underline{\Delta S}_L$ in the phase domain can be rewritten as [66]

$$\begin{aligned} \mathbf{i}^\dagger(l)\mathbf{Z}\mathbf{i}(l) &= \mathbf{i}^\dagger(l)\mathbf{T}_S\mathbf{T}_S^{-1}\mathbf{Z}\mathbf{T}_S\mathbf{T}_S^{-1}\mathbf{i}(l) = [\mathbf{T}_S^\dagger\mathbf{i}(l)]^\dagger[\mathbf{T}_S^{-1}\mathbf{Z}\mathbf{T}_S][\mathbf{T}_S^{-1}\mathbf{i}(l)] \\ &= [3\mathbf{T}_S^{-1}\mathbf{i}(l)]^\dagger[\mathbf{T}_S^{-1}\mathbf{Z}\mathbf{T}_S][\mathbf{T}_S^{-1}\mathbf{i}(l)] = 3\mathbf{i}_S^\dagger(l)\mathbf{Z}_S\mathbf{i}_S(l) \end{aligned} \quad (3.31)$$

and

$$\begin{aligned} \mathbf{u}^\dagger(l)\mathbf{Y}^\dagger\mathbf{u}(l) &= [3\mathbf{T}_S^{-1}\mathbf{u}(l)]^\dagger[1/3\mathbf{T}_S^\dagger\mathbf{Y}^\dagger\mathbf{T}_S][\mathbf{T}_S^{-1}\mathbf{u}(l)] \\ &= [3\mathbf{T}_S^{-1}\mathbf{u}(l)]^\dagger[1/3\mathbf{T}_S^\dagger\mathbf{Y}^\dagger\mathbf{T}_S]^\dagger[\mathbf{T}_S^{-1}\mathbf{u}(l)] \\ &= 3[\mathbf{T}_S^{-1}\mathbf{u}(l)]^\dagger[\mathbf{T}_S^{-1}\mathbf{Y}^\dagger\mathbf{T}_S]^\dagger[\mathbf{T}_S^{-1}\mathbf{u}(l)] = 3\mathbf{u}_S^\dagger(l)\mathbf{Y}_S^\dagger\mathbf{u}_S(l). \end{aligned} \quad (3.32)$$

This yields another equivalent expression for transmission losses, now in the symmetrical component domain

$$\underline{\Delta S}_L = 3 \int_0^L \left[\mathbf{i}_S^\dagger(l)\mathbf{Z}_S\mathbf{i}_S(l) + \mathbf{u}_S^\dagger(l)\mathbf{Y}_S^\dagger\mathbf{u}_S(l) \right] dl. \quad (3.33)$$

The matrices $\mathbf{Z}_S = \mathbf{T}_S^{-1}\mathbf{Z}\mathbf{T}_S$ and $\mathbf{Y}_S = \mathbf{T}_S^{-1}\mathbf{Y}\mathbf{T}_S$ contain the sequence impedances and admittances of the transmission line and are directly calculable from the reduced impedance and admittance matrices \mathbf{Z} and \mathbf{Y} [67]. The positive and negative sequence impedances become

$$\underline{z}_+ = \underline{z}_- = (\mathbf{Z}_S)_{22} = (\mathbf{Z}_S)_{33} = (\mathbf{Z}_{aa} + \mathbf{Z}_{bb} + \mathbf{Z}_{cc} - \mathbf{Z}_{ab} - \mathbf{Z}_{bc} - \mathbf{Z}_{ac})/3, \quad (3.34)$$

and the zero sequence impedance is

$$\underline{z}_0 = (\mathbf{Z}_S)_{11} = (\mathbf{Z}_{aa} + \mathbf{Z}_{bb} + \mathbf{Z}_{cc} + 2\mathbf{Z}_{ab} + 2\mathbf{Z}_{bc} + 2\mathbf{Z}_{ac})/3, \quad (3.35)$$

where 11, etc. are the row-column indexes of the matrix elements. Other sequence parameters can be found as corresponding elements of \mathbf{Z}_S or \mathbf{Y}_S .

In most transmission lines the off-diagonal elements in these matrices are significantly smaller than the diagonal elements, e.g.

$$(\mathbf{Z}_S)_{12} = [\mathbf{Z}_{aa} - (\mathbf{Z}_{bb} + \mathbf{Z}_{cc})/2 + (\mathbf{Z}_{ab} + \mathbf{Z}_{ac})/2 - \mathbf{Z}_{bc}]/3 \quad (3.36)$$

In fact, in ideally transposed lines, the off-diagonal elements are exactly zero so that the sequence impedance and admittance matrices are diagonal.

This also implies that the sequence transformation matrix \mathbf{T}_S is a correct variant of both of the modal transformation matrices for ideally transposed lines [63]. In this case, the multiconductor line in the symmetrical component domain can be viewed as three independent two conductor lines and the correct sequence impedances and admittances can be computed from the corresponding voltages and currents as in (1.20) and (1.21) [32].

Another situation when (3.33) is significantly simplified occurs when the load on the line is symmetric. In this case the negative and zero sequence voltages and currents are negligible and the total transmission losses across the line become

$$\underline{\Delta S}'_L = 3 \int_0^L \left(|I_+(l)|^2 \underline{z}_+ + |U_+(l)|^2 \underline{y}_+^* \right) dl. \quad (3.37)$$

When the line and the load are both slightly asymmetric, the off-diagonal elements of \mathbf{Z}_S and \mathbf{Y}_S are small and the products containing them (e.g. $\underline{I}_+(l)\underline{I}_0^*(l)(\mathbf{Z}_S)_{12}$, etc.) in (3.33) contribute negligibly to the total losses. We assume that, generally, in a transmission system, both asymmetries are small enough to warrant the use of the following approximation.

We define simplified diagonal sequence impedance and admittance matrices as

$$\langle \mathbf{z}_S \rangle = \langle \mathbf{r}_S \rangle + j\langle \mathbf{x}_S \rangle = \begin{bmatrix} z_0 & & \\ & z_+ & \\ & & z_- \end{bmatrix} \quad (3.38)$$

and $\langle \mathbf{y}_S \rangle = \langle \mathbf{g}_S \rangle + j\langle \mathbf{b}_S \rangle$, where the sequence impedances and admittances are computed from sequence voltages and currents (which in turn are calculated from measured phase quantities) as in (1.20) and (1.21). Total transmission losses can then be approximated as

$$\underline{\Delta S}_L \cong 3 \int_0^L \left[\mathbf{i}_S^\dagger(l) \langle \mathbf{z}_S \rangle \mathbf{i}_S(l) + \mathbf{u}_S^\dagger(l) \langle \mathbf{y}_S \rangle \mathbf{u}_S(l) \right] dl. \quad (3.39)$$

This allows us to compute the total transmission losses as four separate components as in (3.25) without including elements of the phase domain reduced impedance and admittance matrices \mathbf{Z} and \mathbf{Y} . The approximated loss components become

$$\Delta P_J \cong 3r_+ \int_0^L |\underline{I}_+(l)|^2 dl + 3r_- \int_0^L |\underline{I}_-(l)|^2 dl + 3r_0 \int_0^L |\underline{I}_0(l)|^2 dl, \quad (3.40)$$

$$\Delta P_C \cong 3g_+ \int_0^L |\underline{U}_+(l)|^2 dl + 3g_- \int_0^L |\underline{U}_-(l)|^2 dl + 3g_0 \int_0^L |\underline{U}_0(l)|^2 dl, \text{ etc.}, \quad (3.41)$$

where the sequence voltages and currents are computed as in (1.13) and (1.14) and integrated numerically. In the presented method, the parameters r_+ , g_+ , etc. are computed from measured phasors $\underline{U}_+(L)$, $\underline{U}_+(0)$, etc. according to (1.20) and (1.21). No prior knowledge about the parameters of the line is needed.

The equations above also include negative and zero sequence quantities in addition to the positive sequence. Even though it may seem unnatural to use negative and zero sequence quantities in steady state operation, the set of symmetrical components is an equivalent representation of phase quantities under any conditions. If the transmission line is transposed so that it can be considered balanced, these terms can be omitted and losses computed from positive sequence quantities only. If it is known that the line is not balanced, these terms can be included if possible. However, in most cases the asymmetry is small enough that the contribution from these terms is negligible.

The terms in ΔP_J represent active losses dissipated in resistances due to flow of current. Based on the transmission line model, it can be assumed that they correspond to Joule losses in the conductors. The terms in ΔP_C are also active losses and it can be assumed that these are mostly corona losses but could also include other possible losses (e.g. leakage). For the estimation of corona losses, similar assumptions have been used in previous studies [49, 51]. Equivalent expressions for ΔQ_I corresponding to inductive losses and ΔQ_C corresponding to capacitive generation are obtained with the reactances and susceptances.

The sequence resistances are commonly used quantities and the physical meaning of ΔP_J is simple to interpret. The same applies to reactive and capacitive sequence

reactances and the values of ΔQ_I and ΔQ_C . The value of ΔP_C is the difference between total active losses and Joule losses according to the transmission line model, i.e. $\Delta P_C = \Delta P_T - \Delta P_J$. Consequently, the value of ΔP_C can be seen as all active losses that are not Joule losses and the conductances are what represent these losses in the line model.

3.3 Uncertainty Propagation in Transmission Loss Monitoring

The commonly used principle of measuring transmission losses across the line can be expressed as

$$\underline{\Delta S} = \underline{S}_1 - \underline{S}_2 = \underline{V}_{a1} \underline{I}_{a1}^* + \underline{V}_{b1} \underline{I}_{b1}^* + \underline{V}_{c1} \underline{I}_{c1}^* - \underline{V}_{a2} \underline{I}_{a2}^* - \underline{V}_{b2} \underline{I}_{b2}^* - \underline{V}_{c2} \underline{I}_{c2}^*, \quad (3.42)$$

where * denotes the complex conjugate, the numbers in subscripts stand for the two ends of the line and letters stand for phases. The estimate of transmission losses is expressed as

$$\underline{\Delta s} = \underline{\Delta s}_a + \underline{\Delta s}_b + \underline{\Delta s}_c = v_{a1} i_{a1}^* + v_{b1} i_{b1}^* + v_{c1} i_{c1}^* - v_{a2} i_{a2}^* - v_{b2} i_{b2}^* - v_{c2} i_{c2}^* \quad (3.43)$$

where

$$\begin{aligned} \underline{\Delta s}_a &= v_{a1} i_{a1}^* - v_{a2} i_{a2}^* \\ &= v_{a1\text{re}}(i_{a1}^*)_{\text{re}} - v_{a1\text{im}}(i_{a1}^*)_{\text{im}} + jv_{a1\text{re}}(i_{a1}^*)_{\text{im}} + jv_{a1\text{im}}(i_{a1}^*)_{\text{re}} \\ &\quad - v_{a2\text{re}}(i_{a2}^*)_{\text{re}} + v_{a2\text{im}}(i_{a2}^*)_{\text{im}} - jv_{a2\text{re}}(i_{a2}^*)_{\text{im}} - jv_{a2\text{im}}(i_{a2}^*)_{\text{re}} \\ &= v_{a1\text{re}} i_{a1\text{re}} + v_{a1\text{im}} i_{a1\text{im}} - jv_{a1\text{re}} i_{a1\text{im}} + jv_{a1\text{im}} i_{a1\text{re}} \\ &\quad - v_{a2\text{re}} i_{a2\text{re}} - v_{a2\text{im}} i_{a2\text{im}} + jv_{a2\text{re}} i_{a2\text{im}} - jv_{a2\text{im}} i_{a2\text{re}}, \quad \text{etc.} \end{aligned} \quad (3.44)$$

Here the components of voltage and current phasors are the quantities measured by PMUs.

In order to ensure that the functions analysed in uncertainty propagation are holomorphic (and differentiable) the complex conjugate of the current phasor is assumed to be the measured quantity instead of the current phasor that is actually measured. This means that losses are seen as a function of measured voltage and current, where the complex conjugate representation of current is assumed, i.e. $\underline{\Delta s}_a = f(v_{a1}, i_{a1}^*, v_{a2}, i_{a2}^*)$, etc. These functions are differentiable with respect to $v_{a1}, i_{a1}^*, v_{a2}, i_{a2}^*$, etc. and satisfy the Cauchy-Riemann equations. Considering the nature of complex conjugation, we can assume that the uncertainties in the conjugate are equal to the uncertainties of the complex quantity itself. Thus, the uncertainties are equated as follows

$$u_B(i_m^*) = u_B(i_m), \quad (3.45)$$

$$u_B(i_\phi^*) = u_B(i_\phi). \quad (3.46)$$

The uncertainties of measuring voltage and current phasors were given in (2.23).

The same principles of calculating uncertainties as discussed in Sec. 2.3 are applied. For the propagation of uncertainties, the Jacobians are found as

$$\mathbf{J}_{\underline{\Delta s}}(v_{a1}) = \begin{bmatrix} \frac{\partial \underline{\Delta s}_{\text{re}}}{\partial v_{a1\text{re}}} & \frac{\partial \underline{\Delta s}_{\text{re}}}{\partial v_{a1\text{im}}} \\ \frac{\partial \underline{\Delta s}_{\text{im}}}{\partial v_{a1\text{re}}} & \frac{\partial \underline{\Delta s}_{\text{im}}}{\partial v_{a1\text{im}}} \end{bmatrix} = \begin{bmatrix} i_{a1\text{re}} & i_{a1\text{im}} \\ -i_{a1\text{im}} & i_{a1\text{re}} \end{bmatrix}, \quad (3.47)$$

$$\mathbf{J}_{\underline{\Delta s}}(i_{a1}^*) = \begin{bmatrix} \frac{\partial \underline{\Delta s}_{\text{re}}}{\partial (i_{a1}^*)_{\text{re}}} & \frac{\partial \underline{\Delta s}_{\text{re}}}{\partial (i_{a1}^*)_{\text{im}}} \\ \frac{\partial \underline{\Delta s}_{\text{im}}}{\partial (i_{a1}^*)_{\text{re}}} & \frac{\partial \underline{\Delta s}_{\text{im}}}{\partial (i_{a1}^*)_{\text{im}}} \end{bmatrix} = \begin{bmatrix} v_{a1\text{re}} & -v_{a1\text{im}} \\ v_{a1\text{im}} & v_{a1\text{re}} \end{bmatrix}, \quad (3.48)$$

$$\mathbf{J}_{\underline{\Delta}s}(v_{a2}) = \begin{bmatrix} -i_{a2\text{re}} & -i_{a2\text{im}} \\ i_{a2\text{im}} & -i_{a2\text{re}} \end{bmatrix}, \quad (3.49)$$

$$\mathbf{J}_{\underline{\Delta}s}(i_{a2}^*) = \begin{bmatrix} -v_{a2\text{re}} & v_{a2\text{im}} \\ -v_{a2\text{im}} & -v_{a2\text{re}} \end{bmatrix}, \text{ etc.} \quad (3.50)$$

The uncertainties $u(\Delta s_{\text{re}})$ and $u(\Delta s_{\text{im}})$ can then be extracted from the covariance matrix, computed as

$$\mathbf{C}(\underline{\Delta}s) = \mathbf{C}(\underline{\Delta}s_a) + \mathbf{C}(\underline{\Delta}s_b) + \mathbf{C}(\underline{\Delta}s_c), \quad (3.51)$$

where

$$\begin{aligned} \mathbf{C}(\underline{\Delta}s_a) &= \mathbf{J}_{\underline{\Delta}s}(v_{a1})\mathbf{U}(v_{a1})\mathbf{R}(v_{a1}) [\mathbf{J}_{\underline{\Delta}s}(v_{a1})\mathbf{U}(v_{a1})]^\top \\ &+ \mathbf{J}_{\underline{\Delta}s}(i_{a1}^*)\mathbf{U}(i_{a1}^*)\mathbf{R}(i_{a1}^*) [\mathbf{J}_{\underline{\Delta}s}(i_{a1}^*)\mathbf{U}(i_{a1}^*)]^\top \\ &+ \mathbf{J}_{\underline{\Delta}s}(v_{a2})\mathbf{U}(v_{a2})\mathbf{R}(v_{a2}) [\mathbf{J}_{\underline{\Delta}s}(v_{a2})\mathbf{U}(v_{a2})]^\top \\ &+ \mathbf{J}_{\underline{\Delta}s}(i_{a2}^*)\mathbf{U}(i_{a2}^*)\mathbf{R}(i_{a2}^*) [\mathbf{J}_{\underline{\Delta}s}(i_{a2}^*)\mathbf{U}(i_{a2}^*)]^\top, \text{ etc.} \end{aligned} \quad (3.52)$$

Analysis of uncertainties in transmission loss components calculated as in (3.40) or (3.41) is somewhat more difficult. The squared absolute value (magnitude) of a phasor $|i|^2 = ii^*$ is not differentiable with respect to i or i^* . However, it is possible to approximate the uncertainties if the numerical integration is simplified to only use two points—the ends of the line measured directly. This results in loss components of the form

$$\begin{aligned} \Delta P_J &= 3r_+L \frac{|I_+(0)|^2 + |I_+(L)|^2}{2} + 3r_-L \frac{|I_-(0)|^2 + |I_-(L)|^2}{2} \\ &+ 3r_0L \frac{|I_0(0)|^2 + |I_0(L)|^2}{2}, \text{ etc.} \end{aligned} \quad (3.53)$$

This does not require the actual losses to be calculated with this approximation, this measurement model is only assumed for uncertainty analysis.

Let us denote the first term of (3.53) above as ΔP_{J+} and the currents so that $|I_+(0)| = I_{2+}$ and $|I_+(L)| = I_{1+}$ giving

$$\Delta P_{J+} = 3r_+L \frac{I_{1+}^2 + I_{2+}^2}{2}. \quad (3.54)$$

The uncertainty of this quantity can be evaluated as

$$u(\Delta P_{J+}) = \sqrt{\left(\frac{\partial \Delta P_{J+}}{\partial r_+} u(r_+)\right)^2 + \left(\frac{\partial \Delta P_{J+}}{\partial I_{1+}} u(I_{1+})\right)^2 + \left(\frac{\partial \Delta P_{J+}}{\partial I_{2+}} u(I_{2+})\right)^2} \quad (3.55)$$

and similarly for the other terms of the sum in (3.53). The uncertainties $u(r_+)$, $u(I_{1+})$, and $u(I_{2+})$ can be calculated based on the equations given in Sec. 2.3. Uncertainties of other loss components can be approximated similarly by using the appropriate parameters and currents or voltages.

3.4 Validation of Estimated Corona Losses

Some results of monitoring of corona losses were presented in Publication II and Publication IV. However, it became clear that these monitoring periods were too short to observe various levels of losses in different conditions. For a more thorough analysis, transmission losses on two transmission lines were monitored for a period of 128 days from 8 January to 15 May 2018. In addition to PMU measurements, weather data was gathered from seven weather observation stations during the same period.

Both of the transmission lines are a part of the Estonian 330 kV transmission system. One of the lines is 170 km long, spanning in the North to South direction in the Eastern part of Estonia. The other line is 210 km long, spanning in the West to East direction in Northern Estonia. Weather stations closest to the transmission lines were identified. There are four weather stations close to each of the lines, one common to both, not more than 30 km from the line corridor. The weather data was also used to approximate line conductor temperature based on the IEEE and Cigre guidelines [33, 34].

It is very difficult to validate the results of estimated corona losses without another method of measurement for comparison. Dedicated corona loss measurements on these transmission lines would be very difficult and expensive to organize. However, two different ways of assessing the results are presented. Firstly, the uncertainties of measured corona losses have been analyzed. Secondly, the relationship between the occurrence of corona losses and significant weather conditions have been analyzed.

One of the more recent dedicated corona loss measurements carried out in Sweden presented an analysis of measured corona losses and observed weather conditions [51]. These results have been used for comparison with the results obtained from PMU measurements. Similarly to this study, estimated corona losses have been plotted against conductor temperature, relative air humidity, average wind velocity, and average phase voltage. Other parameters were either not possible to observe or deemed less useful in this comparison.

Transmission losses on one of the lines over a 36 hour period have been plotted in Fig. 3.2. The figure presents measurements with a 10 s step averaged with a moving window of 30 samples. Uncertainty intervals have been calculated based on information available about the instrumentation chain (see Chap. 2 and Appendix A). What is important to note is that the uncertainty of measuring corona losses is significantly smaller than the uncertainty of measuring Joule losses.

There is a small but noticeable negative bias in the measured values of corona losses seen in Fig. 3.2, which should be considered when interpreting the results. The bias is consistent over time and explained by the uncertainty analysis. Similar small negative values have also been reported in earlier long term monitoring results [51]. In order to illustrate this effect, the values have not been adjusted in this example. For hourly corona loss values presented in the following figures, the negative bias has been removed. For each transmission line, a constant offset has been determined for the entire monitoring period.

In Fig. 3.3, hourly corona losses in one week of winter have been plotted for both of the transmission lines. In order to illustrate the weather conditions, ambient air temperature from two weather stations is also plotted in Fig. 3.4. In this week, nightly temperatures dropped to -20°C quite often, also coinciding with significant levels of corona losses. However, the weather dependence of corona losses is more nuanced than just the influence of air temperature [51, 58].

Figs. 3.5 and 3.6 show corona losses plotted against conductor temperature, air humidity, average wind velocity, and average phase voltage on the two transmission lines.

Even though the data is sparser, it can be seen that the dependence of corona losses on the various parameters is very similar to what was presented in [51]. This indicates that the results of monitoring of corona losses with PMUs are comparable to the results of dedicated measurements.

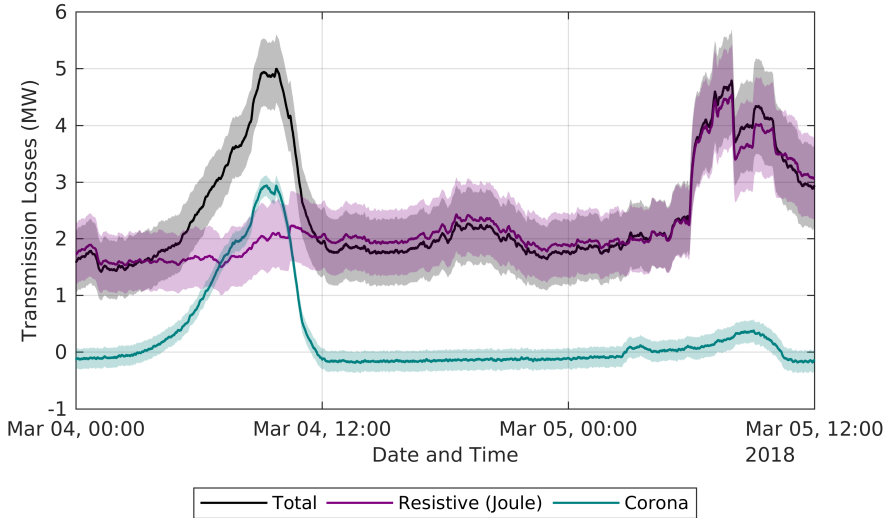


Figure 3.2 Transmission losses calculated from PMU measurements of one transmission line over a period of 36 hours. Total active losses and estimated components corresponding to resistive and corona losses are plotted with their uncertainty intervals.

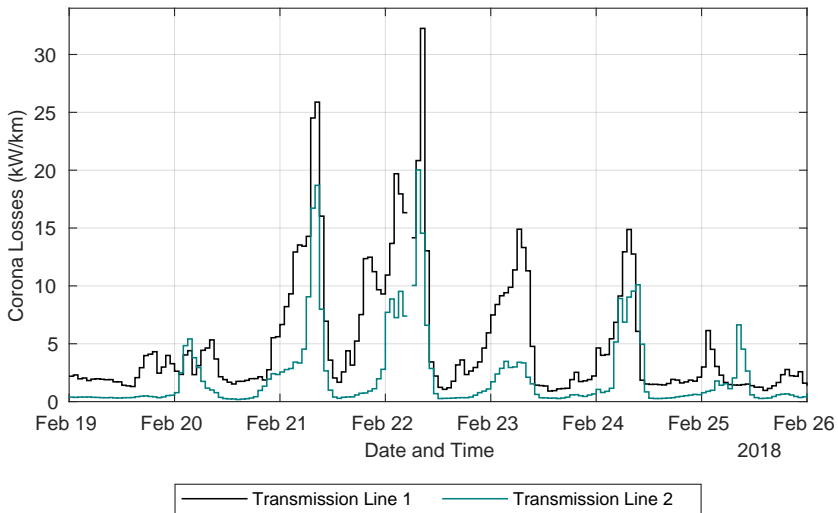


Figure 3.3 Hourly corona losses estimated from PMU measurements of two transmission lines over the span of one week. For a better comparison, hourly average loss power per unit length is given.

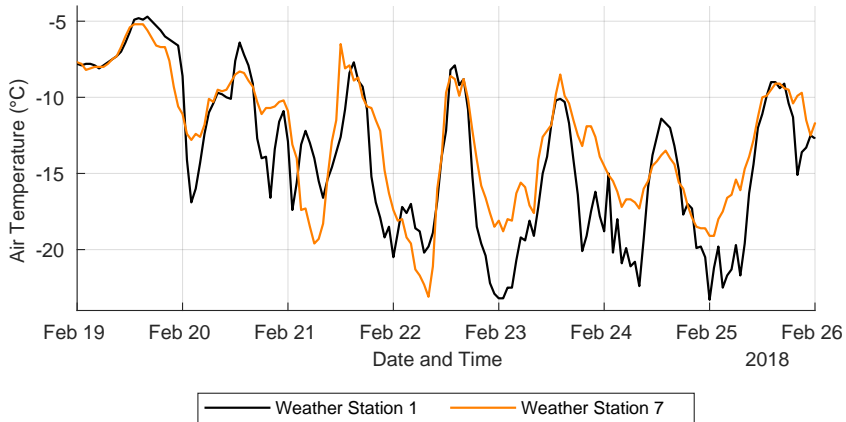


Figure 3.4 Ambient air temperature measurements from two weather stations during the week observed in Fig. 3.3.

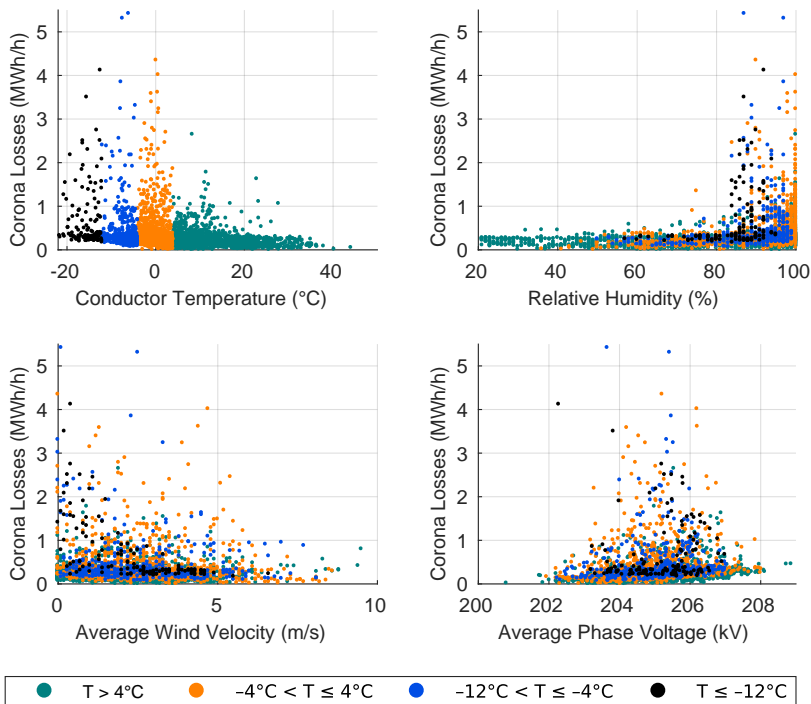


Figure 3.5 The dependence of corona losses on various measurable quantities on transmission line 1. Hourly corona losses are plotted against hourly weather measurements from one weather station and average phase voltage measured by PMUs.

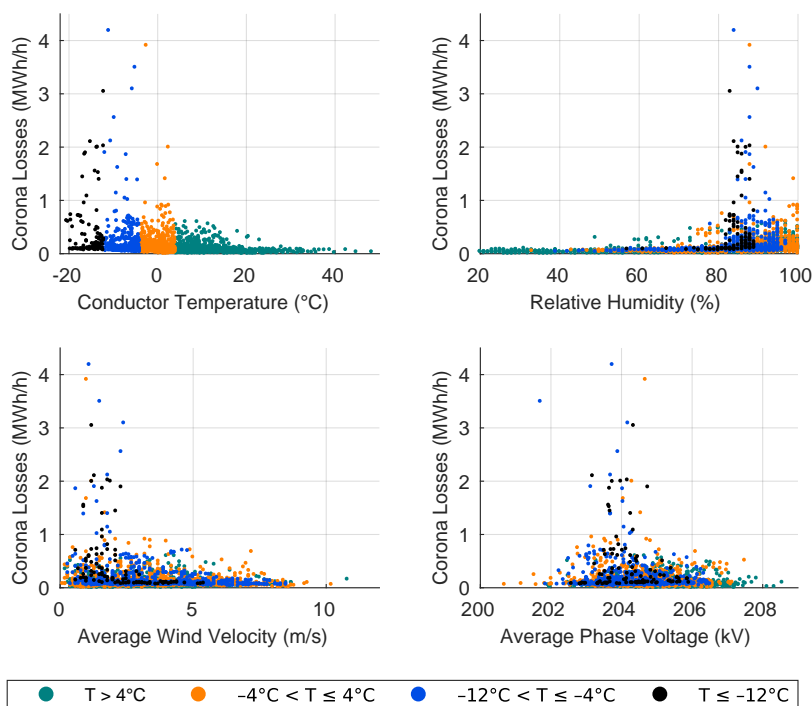


Figure 3.6 The dependence of corona losses on various measurable quantities on transmission line 2. Hourly corona losses are plotted against hourly weather measurements from one weather station and average phase voltage measured by PMUs.

3.5 Conclusions

This chapter demonstrated the applicability of PMU measurements for the monitoring of components of transmission losses. Based on the transmission line model, equations were derived that allow separate components of transmission losses to be calculated. These components can be assumed to correspond to different types of transmission losses, i.e. resistive (Joule) and corona losses. The main value of the application is seen in the ability to detect and monitor corona losses using the WAMS infrastructure. The results enable further research into forecasting of corona losses based on weather forecasts.

The method was tested on measurement data from two operational transmission lines over a four month period, focusing on validating the results of measured corona losses. The observation period included days with harsh winter conditions when corona losses are likely to occur. In addition to measured corona losses, weather observation data was gathered for the same period. Based on the dependence of corona losses on various measurable quantities, the obtained results were compared to an earlier study that used dedicated measurement equipment. The comparison of measured corona losses and corresponding weather conditions indicate that the method provides plausible results. The assessment is further corroborated by the analysis of uncertainty propagation that indicated sufficiently high accuracy in the measurements.

4 Monitoring of Power System Inertia

In an AC power system the balance between generated and consumed power at any given moment is tightly linked with frequency. If load drops below the level of generation, generators synchronized to system frequency speed up and frequency starts to increase. Conversely, when generation falls below the level of consumption, synchronously connected generators are slowed down and frequency starts to decrease. In order to restore the balance of generation and load and maintain the set system frequency, the power system is equipped with frequency control systems.

As a part of the effort to decelerate climate change, there has been a significant increase in electric energy generation with wind turbines and photovoltaic (PV) panels. These generating units have certain technical differences from conventional units when it comes to sustaining the frequency of an AC power system. PV panels generate direct voltage, which is converted to AC with a power electronic (PE) converter. Wind turbines rotate at variable speeds and a large share of the commercially installed wind turbines also use PE converters to supply a fixed frequency AC voltage to the grid. This means that PV panels and a large share of wind turbines lack the kind of inertial response that is provided by rotating machines connected to the grid.

The transition to larger shares of generation from PE-connected renewable energy sources (RES) is bringing about many challenges. The Horizon 2020 project “Massive INTEGRATION of power Electronic devices” (MIGRATE) is finding solutions to a variety of these challenges, including stability issues, changes in protection and control, and decrease in power quality. A changing inertial response is one of the investigated problems; the challenges associated with it have already been observed around the world [68–76].

Larger penetration of renewable sources is decreasing inertia on one hand, but also changing its distribution in the system and leading to formation of low inertia areas on the other hand. This leads to the problems of determining and monitoring values of inertia, considering the time varying nature of inertia, and operating a system with low inertia areas. For a TSO, the main requirement for monitoring the inertia of the system (or inertia of an area) is to estimate the time available to deploy a response, and to define the sensitivity between a frequency change and an appropriate corrective power response. During the MIGRATE project, decreasing inertia was ranked as the most important issue in a survey taken by 11 TSOs [77]. This indicates a need for improved inertia monitoring capabilities.

This chapter presents a new method of monitoring inertia of a power system and inertia of areas of the system. The method is completely measurement based and uses measurement data from normal operating conditions, not specific disturbances. The main hypothesis of this chapter is that it is possible to estimate inertia by observing ambient dynamics between active power and frequency during normal operation of the system. The proposed method and the feasibility of this kind of monitoring is demonstrated on real measurement data. The work was presented in Publication III.

4.1 Basics of Inertia and Frequency Dynamics

In order to discuss estimating inertia or area inertia, it is helpful to analyze a theoretical model of the dynamics it affects. The dynamics between power and frequency instantly after the occurrence of a power mismatch can be modelled by the swing equation. In a power system with several generators, the equation for the i th generator is

$$\frac{df_i}{dt} = \frac{P_{iM} - P_{iE}}{2H_i S_{in}} f_n, \quad (4.1)$$

where P_{iM} is the output mechanical power of the machine, while P_{iE} is its electrical load power, f_i is the electrical frequency, H_i the inertia constant, S_{in} rated apparent power, and f_n the rated steady state frequency of the system. The model excludes damping effects and mechanical power is assumed to be constant. This is the basic equation that shows the effect of inertia—the larger the inertia, the lower the rate of change of frequency (RoCoF).

It is possible to apply an equivalent equation to a power system or an area of the system as an approximation. In this case, it is assumed that the area (or system) behaves like a single generator by aggregating the frequencies of the buses of the area (or system). The aggregated frequency is also referred to as the center of inertia (COI) frequency, evaluated as a weighted average of frequencies [78]

$$f_{j,\text{COI}} = \frac{\sum_i^N H_i S_{in} f_i}{\sum_i^N H_i S_{in}}, \quad (4.2)$$

where f_i are the frequencies of all of the N nodes comprising the area weighted by the inertia of each node (nodes assumed to include no inertia are effectively excluded).

For the aggregated frequency of an area j , the following swing equation can be written

$$\frac{df_j}{dt} = \frac{P_{jM} - P_{jE}}{M_j} = \Delta P_j / M_j, \quad (4.3)$$

expressed in terms of M_j . In other publications, the quantity M_j has been defined in terms of angular frequency [78, 79], but in this work it is expressed in terms of frequency, i.e. its value expressed for a single machine would be $M_i = 2H_i S_{in} / f_n$.

The common assumption is that M_j should be an aggregated value based on inertia constants of all of the machines in the area (aggregated similarly to the COI frequency). However, practice has shown that the actual proportionality term between the change in power and RoCoF is often larger than that [80]. In this work, the definition of an effective inertia is assumed instead. Effective inertia is the actual proportionality term between a step in power (ΔP_j) and RoCoF (df_j/dt), equivalent to M_j , given by the state of the system. By definition in the swing equation, it is effectively an angular momentum and its units are $\text{J} \cdot \text{s}$ or $\text{W} \cdot \text{s}^2$ [78].

The swing equation only applies during a short period of time after a power mismatch has occurred. Shortly after that, primary frequency control (also termed frequency containment control or FCC) is actuated, which limits the frequency deviation, stops it at the nadir or peak value, and returns the frequency to a new stable value. Following that, secondary frequency control (also termed frequency restoration control or FRC) returns the frequency to its set value. Secondary control is automated in some systems and operator controlled in others. These steps are illustrated in Fig. 4.1 depicting the course of a frequency disturbance in a two area system.

Primary frequency control is carried out at the turbine-generator unit level. The dynamics of frequency control can be described by a set of differential equations, which in turn can be modelled as a control system. For a simpler analysis, we will look at this as a linear control system, with the schematic given in Fig. 4.2. The main components of a unit—the governor, the turbine, and the generator—are represented by corresponding transfer functions $H_G(s)$, $H_T(s)$, $H_M(s)$ and R is the droop of the governor [21]. The inputs ΔP_R and ΔP_L specify changes in the power set-point reference and load, respectively, while the output is the frequency deviation $\Delta f = f - f_n$.

With a set of simplifications, an area of a power system (or an entire system) can be

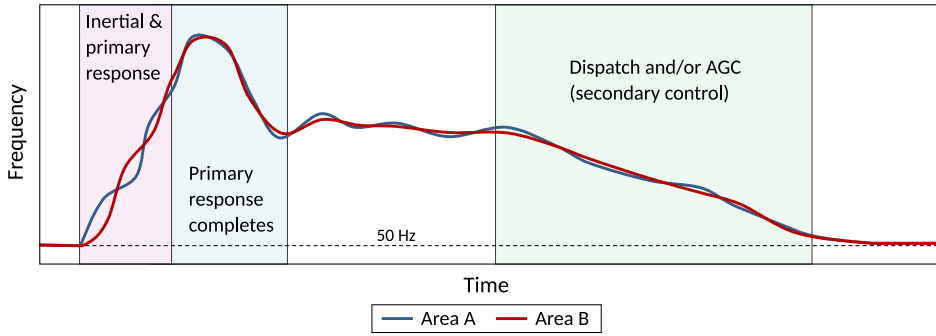


Figure 4.1 Example of a frequency excursion in a two area power system following the trip of a large load in area A. The inertial response and the beginning of primary frequency control can be seen in the first few seconds. Primary response completes in tens of seconds and is followed by dispatch changes in a minute or a few after the disturbance. All given time spans are indicative and depend on the system.

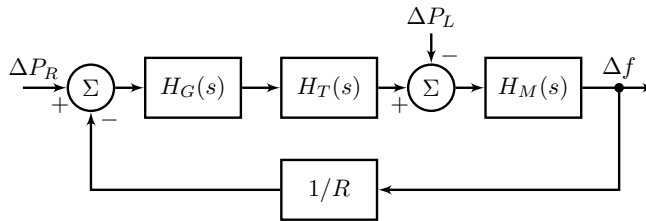


Figure 4.2 Model of a generating unit with the turbine-generator, governor, and droop control dynamics included.

modeled similarly. In this case, the inertia of all rotating machines (and the frequency dependence of load) is lumped into a single area (or system) block and different governor-turbine systems are summed as parallel branches and lumped together by evaluating an equivalent droop. Based on that, a model for a multi-area interconnected system can be obtained by including tie-line elements that model the power exchanges between the areas [21]. The tie-lines are modeled as basic integrator blocks with a gain determined by line parameters. For a two area system, such a model is shown in Fig. 4.3, where ΔP_{Ri} are the changes in power set-point values and ΔP_{Li} changes in load of each area.

The simplified model can be used to exemplify some aspects of the dynamics between active power and frequency. For example, the effects of different levels of area inertia can be seen by simulating the model. In Fig. 4.4, the frequency response of the two area system following the simulated trip of a generator is shown. The inertia of one area is kept constant, while inertia in the area where the disturbance occurs is varied. The figure only shows the first swing in the frequency response as this is where the effect of area inertia can be seen most clearly. For comparison, the system COI frequency is also plotted.

The initial slope in area frequency deviation following a step change in power is proportional to the effective area inertia as it is defined in this work. More precisely, the slope is equal to the derivative of frequency, i.e. RoCoF, which is proportional to effective inertia and the change in power. Later in the chapter, these principles are used in validating the results of inertia estimation.

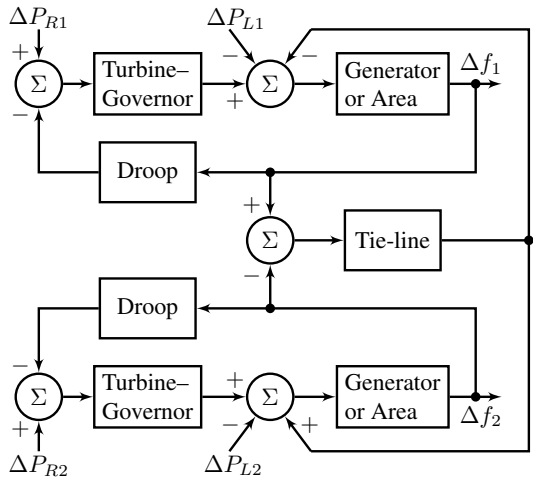


Figure 4.3 Dynamic model of the frequency control of a two-area power system.

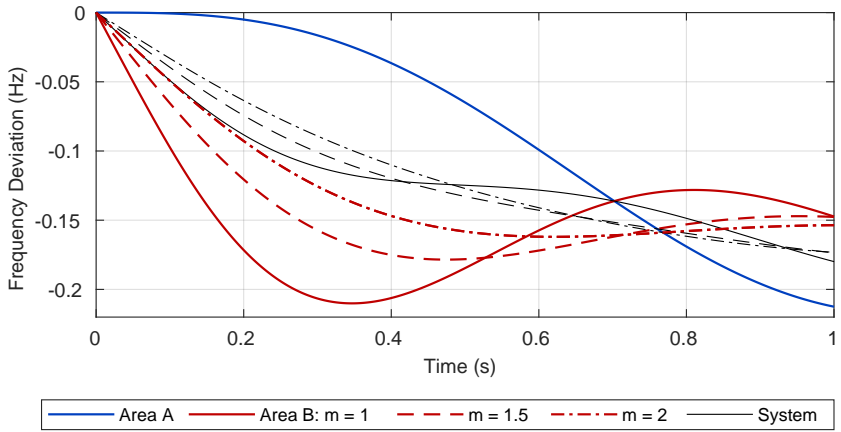


Figure 4.4 Simulated frequency disturbance in a two area power system. The inertia of area B is varied over three cases proportionally to the inertia of area A. The value $m = M_B/M_A$ is the ratio of inertia in area B to inertia in area A and it takes the values 1, 1.5, and 2.

4.2 Available Methods of Estimating Inertia

There are certain indicators of inertia available that are presently being used by TSOs [68, 81, 82]. These indicators are based on the sum of known inertia constants. Through its SCADA/EMS system, a TSO has the information about which generators are operating and synchronized to the grid at a given moment. Any synchronized generator contributes to the inertial response of the system proportionally to its rotating mass. Based on which generators are on-line at a given moment, it is possible to sum their inertia constants and obtain a measure of total inertia available from rotating machines. This figure can be further corrected by some factor that considers the difference between this sum and the effective inertia of the system [80, 83, 84].

More direct estimation of inertia has been carried out based on frequency disturbances. If there is a significant load disturbance of known size in the system (e.g. trip of a load or a generator), it is possible to fit an effective inertia value to the swing equation or fit the frequency excursion itself. During the first few hundred milliseconds to a few seconds, depending on the size of the system, there is a nearly linear change in frequency following such a disturbance. In this interval, the rate of change of frequency (RoCoF) is proportional to the size of the disturbance and the effective inertia of the system. However, this approach can only be used when a significant disturbance occurs.

In one of the earliest examples, polynomial models were fitted to recorded frequency disturbances [85]. Known size of disturbance was used to estimate inertia from the lowest order component of the polynomial model. In a later approach, a simpler solution was applied where only the linear term was estimated [86]. More recently, it was proposed to use measured values of RoCoF supplied by PMUs to estimate inertia [87]. The results of such estimation from the power system of Great Britain have been demonstrated [88]. Further improvements were proposed and another demonstration offered with measurement data from the GB system in [89].

In more recent years, research has also focused on on-line estimation of inertia from continuous or ambient measurements. However, the proposed methods have concentrated on estimating either inertia constants of individual machines or sums of inertia constants of a set of machines, not the effective inertial response of the system. Machine learning methods have been applied to train models for the relationship between measured frequency deviations and known sum of inertia constants values [90, 91]. After training, these models can predict the sum of inertia constants values from measured frequencies. In another approach, a method of updating or estimating the inertia constants of certain machines in the system based on continuous frequency measurements has been proposed [92].

Another approach to on-line inertia estimation is the use of a perturbation. A controllable load is modulated in order to generate a known perturbation pattern in the system. The response of the system to this known signal is analyzed and inertia is estimated. The use of the micro perturbation method and system identification for the estimation of an equivalent inertia constant of a system was proposed in [93]. A perturbation based on-line inertia estimation method is being offered as a commercial product but detailed principles of its implementation are proprietary [94]. However, such methods are intrusive and in general TSOs have avoided deploying monitoring tools that rely on intrusive methods.

4.3 Estimation of Area Inertia from Ambient Measurements

4.3.1 Main Principles

During normal operation of the power system, there are small changes in demand and supply occurring all the time. A real power system is never in an ideal steady state, because with millions of electric devices, changes in load are happening nearly continuously. In this work, these small load variations during normal operation are referred to as ambient conditions. In these conditions, during normal operation, it is quite difficult to distinguish the inertial response of the system from frequency control, voltage control, electro-mechanical dynamics, and stabilizing actions. However, as this work demonstrates, it is possible and feasible in practice to estimate inertia from ambient measurement data.

The main hypothesis behind the proposed approach is that by observing ambient load changes and corresponding frequency changes over a sufficiently long time period, it is possible to infer the effective inertia value from the pattern of dynamics between them. It is assumed that it is possible to identify a dynamic model that behaves similarly to the

observed dynamics between active power and frequency. If a sufficiently good model is found, it is possible to estimate the inertial response of the actual observed system based on the identified model.

We propose that once a power system has been divided into appropriately defined areas, an approximate control system modeling the dynamics between frequency and active power can be identified. This is based on the assumption that the observed ambient dynamics can be fitted to a linear control system. The dynamic model discussed in the previous section (depicted in Fig. 4.3) has two different types of inputs—load changes and generator set-point changes. If we assume that the system is observed only during such time periods when generator set-points are not changed or change very little, the corresponding inputs can be removed and the system is further simplified, as shown in Fig. 4.5. The assumption means that data from time periods when generator dispatch is changed, e.g. automatic generation control (AGC), should be excluded.

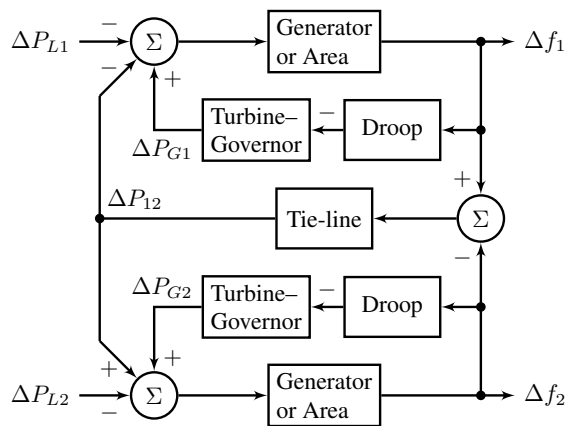


Figure 4.5 Simplified model of dynamics between active power and frequency. This model does not consider generator set-point changes.

Once it is assumed that measurements are taken only when generator set-points are not changed, the model can be assumed to have load changes as inputs and frequency deviations as outputs. If sufficient measurement data is available, it is possible to fit a model to the observed dynamics between the inputs and the corresponding outputs. In this simplified analysis of the dynamics of inertial response and frequency control, the multi-area system becomes a multi-input multi-output system with load changes as inputs and frequency changes as outputs. Among other parameters, this model would include the inertia of each area.

The areas assumed in the model have aggregated frequency, load, generation, and controls. The areas should be formed so that all of these components of the model can be aggregated appropriately. The areas have to be consistent in terms of network topology—all nodes forming a monitored area have to be directly connected to at least one other node of the area and areas have to be separable by clear boundaries. In order to aggregate frequencies, areas should be formed out of nodes which have frequencies close to each other. The distance between frequencies is understood the same way as in generator coherency analysis or inter-area oscillations, where clusters of nodes with close frequencies are formed. An example of aggregating the frequencies of a two area system is given in Fig. 4.6.

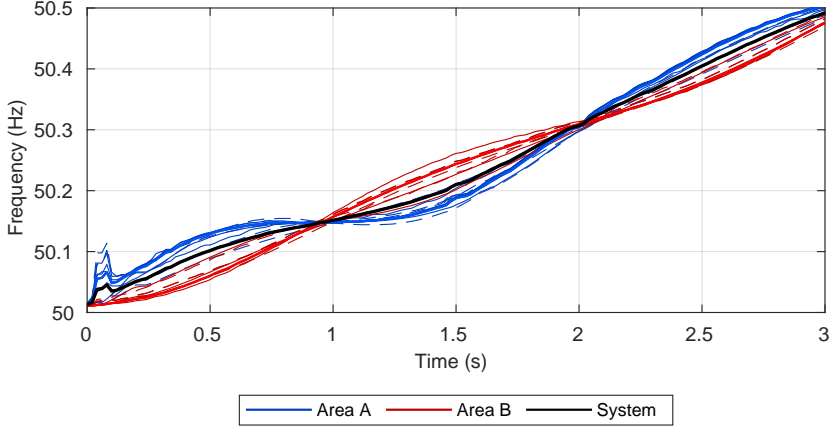


Figure 4.6 Frequencies of single nodes aggregated into area frequencies, denoted by thick colored lines. Thin solid lines represent frequencies of nodes with generation and dashed lines nodes without generation. Thick black line gives the whole system COI frequency.

4.3.2 Inputs and Outputs

The area frequency aggregation is based on a simplification of the center of inertia frequency (defined in (4.2)). The frequency of area j is evaluated as a weighted average of measured frequencies

$$f_j = \frac{\sum_i^{N_j} w_i f_i}{\sum_i^{N_j} w_i}, \quad (4.4)$$

where f_i are the frequencies of the N_j nodes that are measured in area j . The weights w_i are picked based on analyzing the system and making assumptions about which nodes contribute more to the inertia of the area. In the simplest case, all nodes which are assumed to contribute some inertia are weighted equally and all other measured nodes weighted by zero.

Since the nominal value of frequency that the control system is attempting to achieve is known, it is possible to use the deviations from nominal frequency as the outputs. After evaluating the aggregated value, the frequency deviation in area j can be expressed as

$$\Delta f_j = f_j - f_n, \quad (4.5)$$

which is the j th output of the model.

The inputs of the system, i.e. the changes in load, are significantly more difficult to measure with PMUs as load is so widely dispersed. On a transmission system level, the measurement of a larger number of load feeders may become feasible in a not too distant future, but is not something that can be expected at present. This means that more common PMU measurements have to be used to approximate the changes in load. For a practical implementation of the method studied in this paper, a sufficient number of PMUs are required on transmission lines and generators participating in primary frequency control.

Fortunately, if power flows between the defined areas and a majority of generators that participate in primary frequency control can be monitored, it is possible to approx-

imate load changes. The main assumption is that when small changes over time are considered, the changes in load and generation are sufficiently close to each other. The approximate change in load in area j would thus be

$$\Delta P_{Lj} \cong \sum_i \Delta P_{Gji} + \sum_k \Delta P_{Tjk} \quad (4.6)$$

where ΔP_{Gji} is the change in output power of the i th generator (or a group of generators) participating in primary frequency control in area j and ΔP_{Tjk} is the change in power transmitted from the k th to the j th area. All changes are evaluated with respect to the first value in the time series, i.e. $\Delta P = 0$ at $t = 0$.

Monitoring all generators participating in primary frequency control can still be unachievable at present. Also, it may be that not all lines connecting the areas are monitored with PMUs. In these cases, additional approximations have to be made. In a case where one of several parallel lines is monitored, the power flow on that line can be scaled to estimate flow in the corridor. When there is a generator behind a radial part of the network and the power flow into that part is measured, the radial part may be seen as a generator as an approximation. Examples of such cases are given in the following section where the method is applied in practice.

In order to identify the dynamics between load changes and resulting frequency deviations it is necessary to monitor the system for a sufficiently long period. Following a disturbance, the inertial response in frequency can be seen in the first few seconds, while the primary control (governor) response takes place in a time frame of tens of seconds. It can be assumed that a period of at least 1–2 minutes should be observed in order to capture enough variations in the system, but the period should not have to exceed 10 minutes. In practice, measurement periods of 2–6 minutes have been applied.

There are two main considerations to take into account while selecting the measurement periods. Firstly, these periods should exclude any time when automatic generation control (AGC) is acting or any other generator set-point changes are being made. A simple way to handle this is to consider the time these actions are executed and assume a buffer time for the associated effects to take place (e.g. 60 to 90 s). Secondly, it would be advisable to start and end the measurement periods at instances when area rate of change of frequency (i.e. df/dt or RoCoF) crosses zero. This is done in order to improve the efficiency of the system identification algorithm. This is relatively simple to implement even with noisy RoCoF measurements from PMUs.

4.3.3 System Identification

The next part of the estimation process is applying system identification on the obtained input–output data. The main difficulty in the continuous monitoring of inertia is that ambient load variations are generally small and do not excite the dynamic system significantly. This means that a suitable system identification procedure is needed that is not sensitive to the low level of excitation. Some aspects of this problem have been studied in Publication V, comparing various system identification methods applied in a similar way on the example of analyzing inter-area modes.

The study presented in Publication V also offers insights to some other aspects of the system identification process. Most of the relevant dynamics of the system can be captured by a lower order model and the particular order itself may be varied in a range of orders. The order has to be large enough to capture the main dynamics but should still be small enough not to become too complicated or computationally expensive. In fact, it is possible to identify models in a range of orders from the same dataset and obtain a

number of similar but independent estimates.

The System Identification Toolbox in Matlab offers a selection of ready to use system identification tools and has been used in the presented method [95]. In the comparison of available identification algorithms presented in Publication V, it was determined that the implementation of ARMAX is the best suited and most robust tool for the given type of problem. The procedure presented in this paper uses this system identification method, but the general concept of area inertia estimation is not dependent on this particular implementation.

ARMAX in Matlab is a system identification technique based on the autoregressive-moving-average model with exogenous inputs. It results in a polynomial model, which is a generalized variant of a transfer function, expressing a relationship between an input, an output, and a noise term [95]. For a multi-input-multi-output (MIMO) ARMAX model with n_u inputs and n_y outputs, the input-output relationships for the l th output of the model can be expressed as

$$\sum_{j=1}^{n_y} A_{lj}(q)y_j(t) = \sum_{i=1}^{n_u} B_{li}(q)u_i(t - n_{ki}) + C_l(q)e_l(t), \quad (4.7)$$

where A_{lj} , B_{li} , and, C_l are polynomials of orders n_A , n_B , and n_C expressed in q^{-1} , and n_{ki} are the input-output delays in terms of number of samples. Polynomial models are discrete time (i.e. z -domain) linear systems.

Due to the nature of the system identification problem that was set up, the models have an equal number of inputs and outputs corresponding to the number of areas the system is divided into. As noted earlier, we apply system identification that attempts to fit a number of models in a range of orders $n = n_{\min}, \dots, n_{\max}$ for each dataset. Within each iterated order, the various variables defining model order are equal, i.e. $n = n_A = n_B = n_C$. All input-output relationships are symmetric in the sense that in each identification attempt elements of the order matrices are equal. Input-output delays n_{ki} are assumed to be zero.

To summarize, estimated area load variations and corresponding frequency deviations in each of the areas are set as input and output time series. For each of these datasets, ARMAX models are identified using a range of orders. In each iteration of model order, all polynomial orders are set equal to the same value. After that, a number of models is obtained. All successfully identified systems are checked for stability based on the z -domain stability criterion (all poles should be within a unit circle around zero) and unstable models are discarded.

4.3.4 Inertia Estimation

Once we have identified approximate models describing the dynamics between load and frequency variations, it is still necessary to determine the effective inertia of each area. The ARMAX models include the effective inertia but not as an explicit value. For this reason, it is necessary to further analyze the identified models; one possible procedure is presented below.

First of all, the discrete time ARMAX models are converted into continuous time using the `d2c` function in Matlab. This is not successful in every case and the resulting models are checked once again for stability, this time with the s -domain criterion (real part of poles should be less than zero). The remaining models are ready to be reduced to a lower order.

Following that, the continuous time models are reduced to a lower order using a set of functions available in Matlab. The models are first transformed into a balanced state-

space realization. Next, insignificant states are identified and removed to form a reduced order system. The system is then transformed from the state-space representation into a continuous time transfer function. This is done using the `ssdata`, `balreal`, `modred`, and `ss2tf` functions in the System Identification Toolbox [96].

The expected structure of the transfer functions is of the generic form

$$H(s) = \frac{b_{n-1}s^{n-1} + b_{n-2}s^{n-2} + \dots + b_0}{a_n s^n + a_{n-1}s^{n-1} + \dots + a_0}. \quad (4.8)$$

The `ss2tf` tends to give marginal but non-zero values for the term b_n , resulting in the same dynamics but a different formal structure. In order to simplify the estimation of the effective inertia values, these b_n terms are set to zero in the presented implementation.

To understand how the effective inertia can be determined, we can look at a simplified example. If we have a single unit with no governor or frequency control, we can model the swing equation as a first order transfer function

$$H(s) = \frac{1}{Ms + D} = \frac{1/M}{s + D/M}, \quad (4.9)$$

where M is the effective inertia and D is frequency dependence of load [21]. The unit impulse response of this system is given by

$$h(t) = \frac{1}{M} \exp\left(-\frac{D}{M}t\right). \quad (4.10)$$

Clearly, instantly after the perturbation, at $t = 0$, the impulse response is equal to the inverse of the effective inertia. More precisely, the initial response of the system to a load disturbance is what we consider to be the effective inertia. Because we use load changes as inputs, the proportionality term is negative, i.e. $h(0) = -1/M$.

The identified transfer functions are more detailed than the single machine model without controls. However, the inertial response is still the fastest acting and we can assume that it determines the first instance of the impulse response. This means that the inertia of each area can be determined by the value of its unit impulse response at $t = 0$. For a transfer function with the structure given in (4.8), the estimates—i.e the first value of the impulse response—can be evaluated from the ratio of b_{n-1} to a_n .

In the MIMO model it is also possible to determine the impulse response of the system, which provides an additional estimate of total system inertia (in addition to the sum of area inertia values). This is based on the principle that system COI frequency is an average of area frequencies weighted by the inertia of each area. Once area inertia values have been determined, it is possible to calculate system inertia from the unit impulse response of the whole system.

Based on responses of all N areas to a unit impulse in area k , the system inertia can be expressed as

$$M_{Sk} = -\frac{\sum_{i=1}^N 1/h_{ii}(0)}{\sum_{i=1}^N h_{ki}(0)/h_{ii}(0)}, \quad (4.11)$$

where $h_{ki}(0)$ is the response of the i th output of the MIMO system at time $t = 0$ to a unit impulse in the k th input. The $1/h_{ii}(0)$ values correspond to the effective inertia of each area and weight the output frequency deviation of each area so that the sum corresponds to the system COI frequency. It has been observed that in practice these estimates tend to have a lower variance than the sum of area inertia values.

One of the important aspects of the presented method is that several estimates are obtained from one period of monitoring data. The multiple ARMAX models identified with various model orders provide a number of estimates for area inertia, which can then be averaged. However, there are commonly a few poorly identified models that introduce outliers far from a realistic inertia value, which have to be detected and removed.

We propose to use the median absolute deviation (MAD), a robust median based statistic, defined as [97–99]

$$s_{\text{MAD}}(X) = c \operatorname{med}(|X - \operatorname{med}(X)|), \quad (4.12)$$

where $\operatorname{med}(X)$ denotes the median of a sample $X = \{x_i | i = 1, \dots, n\}$, x_i are the values in that sample, and c is a term introduced to achieve consistency with the standard deviation of a certain distribution [98]. Any value x_i for which

$$\frac{|x_i - \operatorname{med}(X)|}{s_{\text{MAD}}(X)} > k \quad (4.13)$$

is considered an outlier and discarded. The cut-off factor k is chosen in conjunction with c and the assumed distribution. If a normal distribution is assumed, c takes the value of 1.4826 and k can be set to 2 for a 95% interval and 3 for a 99% interval [98].

To recap, the ARMAX models identified from the input–output time series are first converted into continuous time polynomial models. Following that, their order is reduced to form low order transfer function models. From these transfer functions, the effective inertia of each area is evaluated corresponding to each ARMAX model with a different initial model order n . The outliers in the obtained sample of estimated inertia values are removed based on the MAD statistic and the area inertia estimated as the arithmetic mean of the remaining values.

The main procedure is presented in Algorithm 1 in a simplified way. The presented pseudo code skips the selection of measurement periods, allocation of measurements signals to the input–output time series, and detection of outliers in the results, but it presents the essential parts of the algorithm. Matlab and System Identification Toolbox functions are used [95]. A time period, range of model orders, area configuration, and ARMAX system identification parameters are assumed. After outliers are removed, the remaining M_{jn} values are the estimates of effective area inertia.

The described implementation is dependent on the System Identification Toolbox, which provided several pre-built tools for a prototype solution. However, the general concept is not necessarily dependent on any specific tool and the tools that were used are all based on published knowledge. In fact, it is quite likely that the concept of estimating area inertia could be implemented in a simpler and more efficient manner in future iterations. Once again, the main aim of the work is to demonstrate that ambient load and frequency variations are significant enough to use for the estimation of power system inertia, not to provide a finalized tool for the task.

4.3.5 Further Extensions of the Method

As an ending note to the description of this inertia estimation method, it should be said that the presented implementation assumes that an entire synchronous system is being analyzed. The principles—and even the same implementation with small modifications—can be applied to estimating the inertia of an area or a few adjacent areas in a larger system. Returning to Fig. 4.3, we can see that inter-area flows can be used to create a boundary and exclude parts of the system. However, this approach has not been fully developed yet.

Algorithm 1 Inertia estimation for one monitoring period

```
1: input  $t_{\text{begin}}, t_{\text{end}}, n_{\text{min}}, n_{\text{max}}, n_{\text{red}}, j_{\text{areas}}$ 
2: for all areas  $j = 1$  to  $j_{\text{areas}}$  do
3:    $Y_j \leftarrow f_j([t_{\text{begin}}, t_{\text{end}}]) - f_n$  ▷ Output
4:    $U_j \leftarrow \Delta P_{L_j}([t_{\text{begin}}, t_{\text{end}}]) - \Delta P_{L_j}(t_{\text{begin}})$  ▷ Input
5: end for
6: for model orders  $n = n_{\text{min}}$  to  $n_{\text{max}}$  do
7:    $D_n \leftarrow \text{armax}(U, Y, n)$  ▷ Discrete time
8: end for
9: for all stable  $D_n$  do
10:   $C_n \leftarrow \text{d2c}(D_n)$  ▷ Continuous time
11: end for
12: for all stable  $C_n$  do
13:   $R_n \leftarrow \text{ct2ss}(C_n, n_{\text{red}})$  ▷ Reduced order
14:  for all areas  $j$  do
15:     $a_{n_{\text{red}}}^{(j,n)}, b_{n_{\text{red}}-1}^{(j,n)} \leftarrow \text{ss2tf}(R_n, j)$ 
16:     $M_{jn} \leftarrow -a_{n_{\text{red}}}^{(j,n)} / b_{n_{\text{red}}-1}^{(j,n)}$  ▷ Inertia estimates
17:  end for
18: end for
19: function  $\text{ct2ss}(A, n)$ 
20:  return  $\text{modred}(\text{balreal}(\text{ssdata}(A)), n)$ 
21: end function
```

In addition to that, the method can be extended to analyze other aspects of frequency dynamics. For example, it is possible to predict the frequency response to any given disturbance, either a load or generation trip of given size. Consequently, it is also possible to predict the extreme frequency following this disturbance, i.e. the frequency nadir or peak. A preliminary study of this approach has been presented in Publication VI.

4.4 Validation of Inertia Estimation

4.4.1 Test System

The method has been tested on the Icelandic power system. The Icelandic system is a relatively small island system with a typical load around 1–2 GW and total installed generating capacity of 3 GW. In present terms, the system has a large number of PMU measurement points relative to its size, with more than 30 PMUs and around 200 measured voltage and current signals. A simplified schematic of the system is given in Fig. 4.7. The schematic includes all significant buses, generators, and lines and four large industrial loads, denoted by ILA, ILB, ILC, and ILZ. Total MVA ratings of power plants are given next to the symbols.

Generators colored black in Fig. 4.7 are monitored directly by PMUs, i.e. their power flows are measured. However, generators in blue are not monitored yet and their output power flows are approximated based on power flows on certain lines. For example, changes in generated power at Vatnsfell (VAF), Lagarfoss (LAG), and Laxá (LAX) can be approximated in a fairly simple manner by observing power changes on lines VF1, LF1, and LA1, respectively. Also, Svartsengi (SVA) and Reykjanes (REY) can be grouped together and approximated by summing up changes on lines SN1 and FI2, denoted by the smaller dashed area. These are all rather reasonable approximations as the loads in these locations are either relatively constant or small.

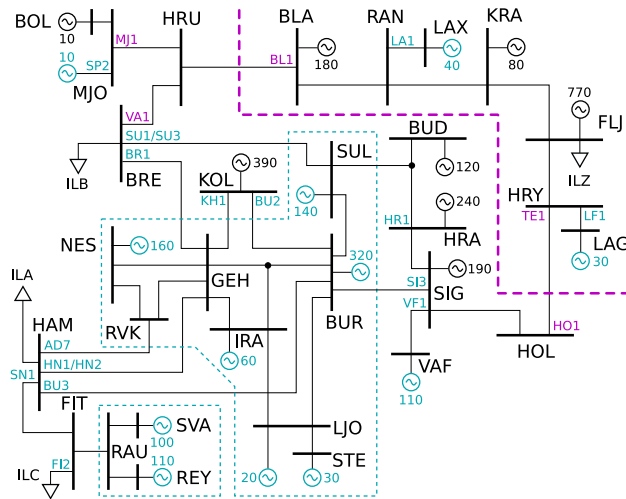


Figure 4.7 Simplified schematic of the Icelandic power system. Larger black labels denote substations, smaller colored labels denote transmission lines. Total rated MVA of all generators at each plant given next to symbol.

Changes in generation at Sultartangi (SUL), Búrfell (BUR), Nesjavellir (NES), Írafoss (IRA), Steingrím (STE), and Ljósafoss (LJO) are more difficult to approximate. Currently, all of these generators are grouped together and changes in generation approximated based on power flows measured on lines SI3, SU3, BR1, BU3, HN1, AD7, KH1, and approximated power flows on lines BU2 and HR1. Power flow on line BU2 is approximated based on generation at Kolviðarhóll (KOL) and power on line KH1. Power flow on HR1 towards Sultartangi (SUL) is approximated as the sum of power from Hrauneyjafoss (HRA) and Búðarháls (BUD). This grouping is represented by the larger dashed area.

The system has two main load centers, one in the west and one in the east. In terms of centers of inertia (COI), the system can be split quite naturally from the two long lines that connect these two areas. The purple dashed line in Fig. 4.7 shows this split. Line labels written in purple denote the power flow measurements used to calculate area boundary power flows. Load variations are approximated based on (4.6), including the approximations used to find changes in power generated by the units that are not monitored. Frequencies at Kolviðarhóll (KOL), Sígalda (SIG), Hrauneyjafoss (HRA), and Búðarháls (BUD) were used for the western part and weighted by 1.5, 1.0, 1.0, and 0.5, and Fljótisdalur (FLJ), Krafla (KRA), and Blanda (BLA) were assigned to the eastern part with weights of 3.0, 1.0, and 0.5, respectively. These weights apply to area COI frequencies, not a whole system COI frequency. Frequency deviations were calculated for the aggregated areas using (4.4) and (4.5).

4.4.2 Validation of Method

The method was validated on a combination of measurements from both ambient conditions and frequency disturbances. The effective area inertia values were estimated from ambient measurements using the presented method. These measurements were gathered from time periods preceding frequency disturbances, meaning that the inertia values were estimated right before the events. The disturbances were then used to analyze the performance of the method. A total of 16 events were selected for the study, 14 of these were load trips (industrial loads at either ILA, ILB or ILC) and two were generator trips.

Only so-called “clean” events were selected, i.e. disturbances where a single unit tripped at a moment when the system could be considered to be in steady-state and no other disturbance followed immediately. All disturbances took place in the western part of the system.

The accuracy of estimated inertia values was quantified by a comparison of the RoCoF of the recorded event and the corresponding RoCoF predicted from the inertia value for the given disturbance. From the disturbances, RoCoF was estimated as the slope of a linear fit to measured frequency during the period of 0.2 to 0.4 s after the trip. The jump in frequency is a measurement effect of the disturbance causing a step change in voltage phase angle, which cleared in 160 ms in most cases but an additional 2 cycle margin was assumed. The change in load, i.e. ΔP , was determined from the measured power at the tripped unit as the largest deviation during the first 0.3 s after the trip. Some events are presented in detail with plots of recorded frequency excursions, also explaining the selection of these time frames.

System identification was applied so that ARMAX models of orders 9 to 28 were identified, i.e. 20 models with different model orders. In each case with six consecutive measurement periods, the first identification was made with five iterations and each following made with three iterations using the results of the previous measurement as a starting point. The least squares non-linear fitting method was used inside the ARMAX routine and the input-output delay was set to zero. Identified models were reduced to 4th order transfer functions. MAD based outlier detection assumed a normal distribution and a 95% confidence interval.

4.4.3 Detailed Analysis of Intermediate Results

In order to explain the application of the method better, data is presented from each step of it on the example of one case (event number 2 and the preceding measurements). First of all, a little over 40 minutes of monitoring data is presented in Fig. 4.8. From this longer period, six smaller sets of measurement data were selected by a preprocessing algorithm. In the algorithm, a minimum length (4 min in this case) was specified and measurement

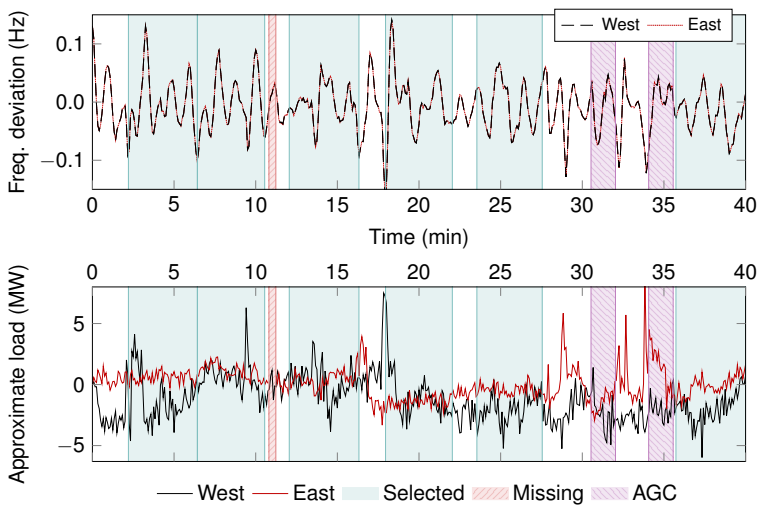


Figure 4.8 Example of monitoring data used for the estimation of effective area and system inertia. Frequency deviations and load, approximated as in (4.6), plotted for the western and eastern areas. Six selected measurements, periods with missing data, and AGC operation marked by shaded areas.

periods were selected so that they started and ended at $df/dt = 0$, while avoiding moments when data was missing or AGC was operating. All of this is from ambient conditions, preceding a load trip that took place 42 minutes after the start of monitoring.

On each of these six measurements, the system identification procedures were applied. Up to 20 approximate models were identified from each measurement, out of which usually 10–15 remained after checking for stability, converting to continuous time, and reducing model order. As an example, the step responses of the 12 stable reduced order models identified from the first measurement period (as shown in Fig. 4.8) were evaluated. The step responses are presented in Fig. 4.9, where a step change in load was assumed in the western area and frequency deviations were calculated for both areas. The actual measured frequency excursion caused by the disturbance is plotted alongside model outputs. Since the models were identified before the disturbance took place, the model outputs are seen as predictions of the event.

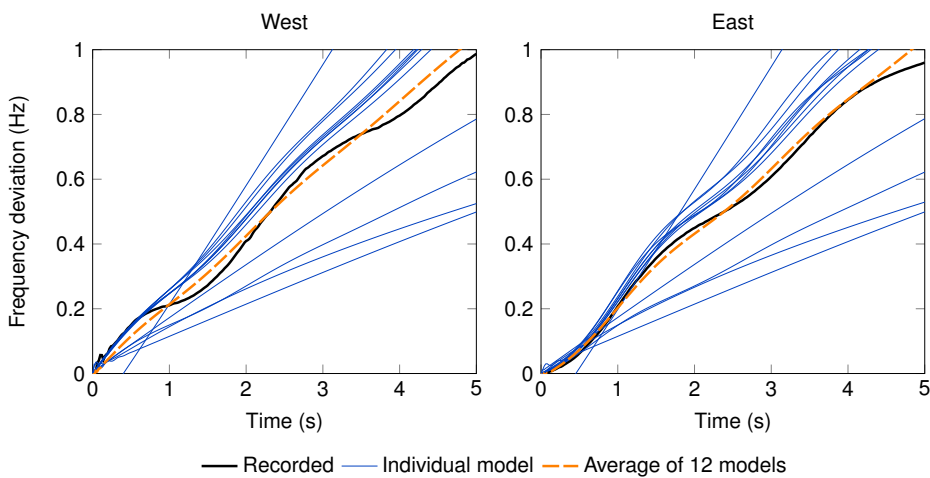


Figure 4.9 Step responses of individual models obtained from system identification applied on a single measurement period. Actual recorded frequency and average step response from 12 models plotted for comparison.

Following that, for each measurement, the step responses of these 10...15 models were averaged. The averaged outputs of the models identified from all six measurement periods (spanning 40 minutes before the event as shown in Fig. 4.8) are plotted in Fig. 4.10. Again, the load loss that caused the frequency disturbance in the end of the monitoring period was modeled as a step response. The examples in Fig. 4.9 and Fig. 4.10 have been presented in order to illustrate the principles of the proposed method. The comparison of recorded frequency disturbances and the outputs of the identified models provides a way of validating the algorithm. The presented results show that the response of the system has been identified with good accuracy and most importantly the inertial response has been captured accurately.

The main results of the method are presented in Fig. 4.11, where estimates of inertia from each measurement period are plotted. The figure shows individual estimates extracted from individual models and presents which values were accepted and which rejected as outliers. It also gives the average inertia value estimated from each measurement and shows the bound based on the MAD method that was used to detect outliers.

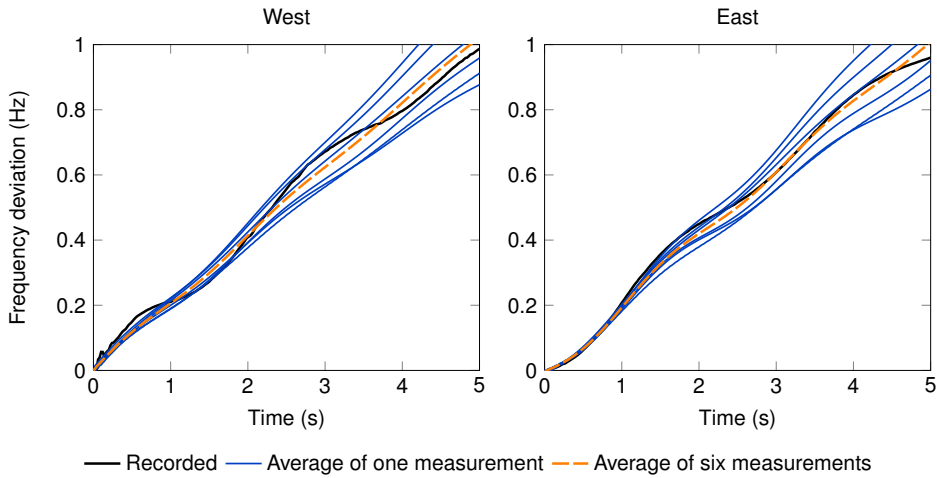


Figure 4.10 Averaged step responses of models obtained from system identification applied on the six measurement periods. Each line corresponds to the average step response of all models found from one measurement period. Actual recorded frequency and a further average of the six measurements combined plotted for comparison.

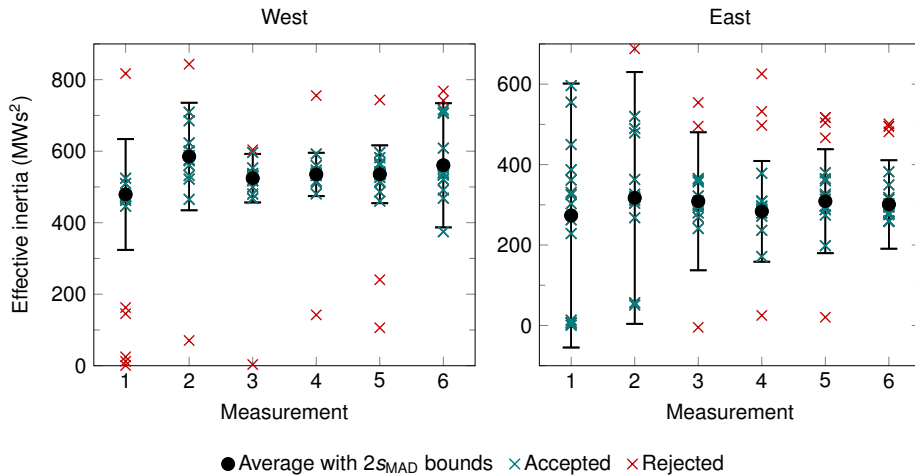


Figure 4.11 Individual inertia estimates from the six measurements. Average inertia for each measurement is plotted, alongside all accepted values and outliers that were rejected based on the MAD criterion.

4.4.4 Assessment of Inertia Estimation Results

In this study, the results of the six measurements before the disturbance were further combined, decreasing variance in the estimates of inertia. The value of effective inertia estimated from the ambient monitoring data was then used to predict the RoCoF of the following frequency disturbance in each of the 16 cases. However, the cases were also analyzed in detail in order to validate the results more thoroughly. For this, the recorded frequency excursions were visually compared to predictions from the identified models and a RoCoF slope based on the estimated inertia. Recorded power of each tripped unit was used to determine the amount of load or power lost in the event. Fig. 4.12 presents

this kind of validation of the event analyzed in the examples of the previous subsection and Fig. 4.13 presents similar data for another validation event.

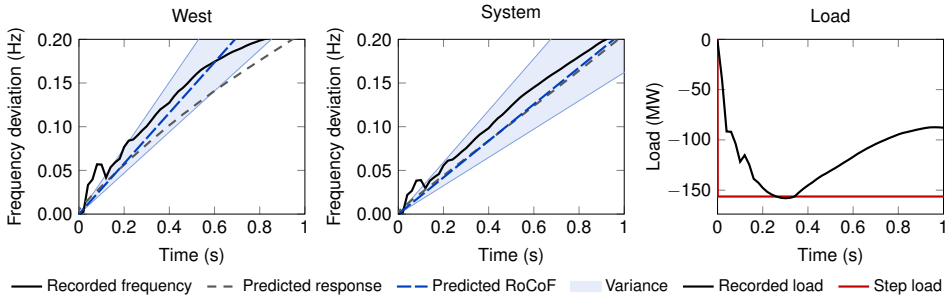


Figure 4.12 Details of validation with event number 2. Measured COI frequency in the western area and entire system plotted in left and center graphs, alongside the responses predicted by the identified models and RoCoF slopes predicted from estimated inertia. Variance in predicted RoCoF based on two standard deviations of all inertia values given as shaded area. Rightmost graph shows the measured power at the tripped unit and the equivalent step signal used as the input of identified models. The magnitude of the step was also used as the ΔP when predicting RoCoF.

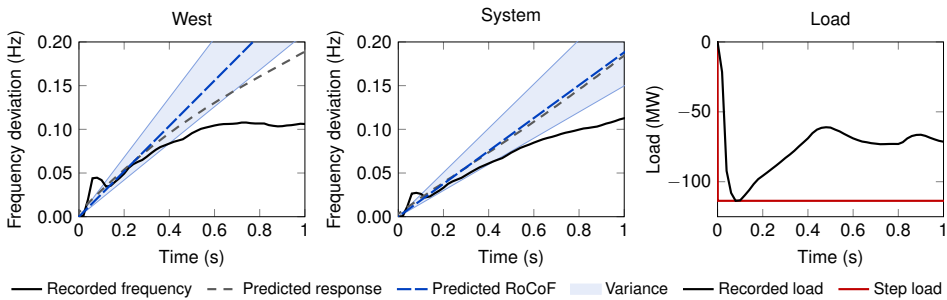


Figure 4.13 Details of validation with event number 16, everything plotted identically to Fig. 4.12.

Measurements from all 16 cases were processed with the proposed method and effective inertia of the western part and the entire system were estimated. However, there were no reference values of inertia with known accuracy available to compare them to. In order to analyze the overall performance of the method, RoCoF values were compared instead. For each event, a RoCoF value and the amount of load (or generation) lost were estimated from the PMU measurements. The inertia values estimated from ambient measurements before the events were used to predict RoCoF values of corresponding disturbances.

A comparison of these results over all 16 cases are presented in Fig. 4.14 and Fig. 4.15 for the western area and the whole system, respectively. (No suitable validation events occurred in the eastern part of the system.) Differences between RoCoF values estimated from recorded frequencies and predicted from inertia values are presented in Fig. 4.16. The average difference was 20% for the western area and 12% for the whole system. However, these should not be seen strictly as errors, since the RoCoF and ΔP values of the events were also approximated. An example of this is seen in Fig. 4.13, where the predicted RoCoF slope aligns very well with the recorded disturbance, but the period of 0.2–0.4 s is not appropriate for calculating the approximate RoCoF.

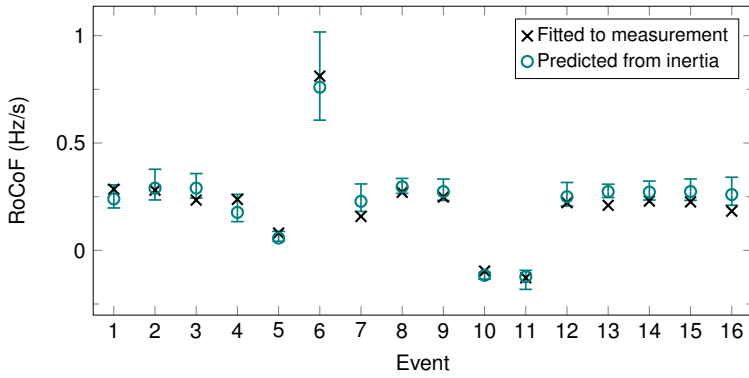


Figure 4.14 Comparison of approximate RoCoF after each disturbances and corresponding RoCoF predicted from estimated inertia values for the western part of the system. Variance bounds based on two standard deviations of all inertia samples of each case.

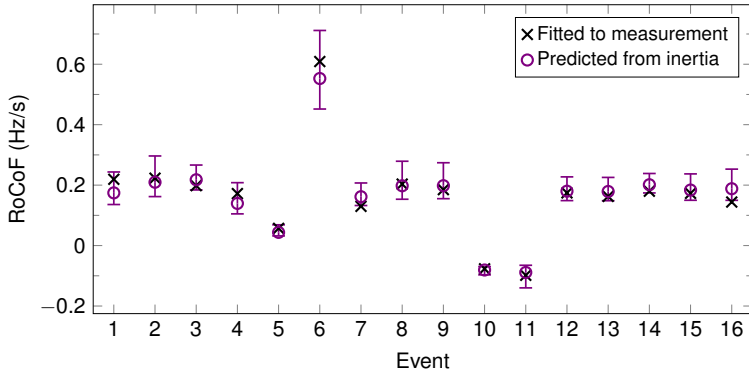


Figure 4.15 Comparison of approximate RoCoF after each disturbances and corresponding RoCoF predicted from estimated inertia values for the entire system. Variance bounds based on two standard deviations of all inertia samples of each case.

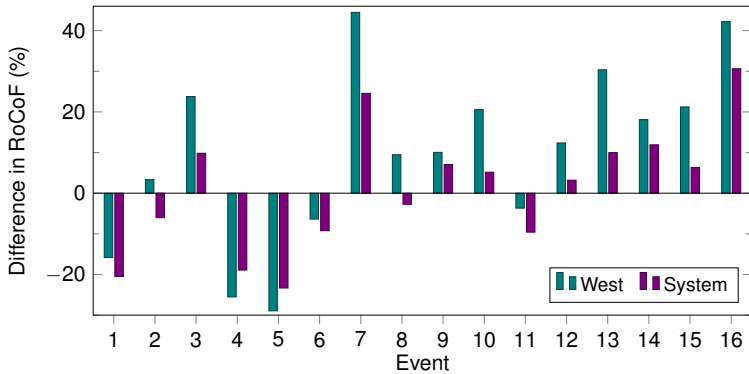


Figure 4.16 Differences between approximate RoCoF and the corresponding value predicted from estimated inertia. Per cent difference of prediction from approximate RoCoF is given.

In computation time, processing one measurement period took around 20–50% of its length using a single core on a regular office laptop (Core i5-4200U@1.6 GHz, 12GB RAM). If the total length of all measurement periods in all 16 cases was 380 min then the total time the code took to process all of it was 140 min. On average it took 22 s to analyze one minute of monitoring data or 37% of its length.

4.5 Conclusions

This chapter demonstrated the possibility of monitoring the effective inertia of a power system and its areas based on measurements from normal operating conditions. The developed method can be executed continuously so that close to real-time estimates of inertia can be obtained. The method is based on detecting the patterns of dynamics between active power and frequency in ambient measurement data. The presented implementation is based on system identification, but the method could possibly be realized with different algorithms.

The most important result of the work is demonstrating that effective inertia can be monitored in a close to continuous manner, not only when frequency disturbances occur. This would enable the TSO to determine an adequate response to a frequency disturbance and the time available to deploy it. Inertia estimation was tested and validated on measurement data from a real power system. The method provided good and consistent results—considering the variance bounds, RoCoF was not underestimated in any of the validation events.

Summary

This thesis presented the development of new applications for wide area monitoring of power systems. The work contributed to two topic areas where the use of PMU measurements has been investigated and applied—monitoring of transmission lines and estimating inertia. Necessary background information was given in an introductory chapter and the contributions were organized into three chapters following that.

The first chapter introduced synchronized phasor measurements and provided a brief overview of the history behind the technology. Phasor measurement units, their primary functions, and their main accuracy requirements were described. Wide area monitoring systems and some of their most commonly deployed applications were introduced. As the final part of the chapter, monitoring of transmission line parameters based on PMU measurements was introduced as another common WAMS application. This application in its basic implementation was demonstrated on real measurement data, leading to the next chapter.

The second chapter presented an analysis of the accuracy of monitoring transmission line parameters based on PMU measurements in real world conditions. Errors in measured voltage and current phasors and the propagation of uncertainty into estimated line parameters were analyzed. The principles of uncertainty analysis in two-dimensional quantities were applied as it is appropriate for complex valued measurements. The analysis was carried out on the same measurement results that were introduced in the first chapter and the problems seen there were explained in detail.

The third chapter introduced the monitoring of separate components of transmission losses enabled by PMU measurements. Based on a detailed model of the transmission line, expressions were derived for the components of transmission losses. Active losses were separated into resistive (Joule) losses dissipated in the series resistances and other losses, mostly assumed to be corona losses. Expressions were also derived for consumed and generated reactive power as separate components, but the work concentrated on the estimation of corona losses. Monitoring of corona losses was demonstrated and analyzed on measurement data from two transmission lines.

The fourth chapter developed a continuous measurement based method for monitoring the effective inertia of the system and its areas. The chapter presented the main principles of frequency control in power systems and explained the effects of inertia and area inertia. A method was proposed that enables the estimation of inertia from ambient measurement data, i.e. measurements from normal operation of the power system. Estimation of system and area inertia from ambient measurements was demonstrated and validated on real world measurement data.

Contributions

The work presented in Chap. 2 and Publication I offered a detailed analysis of the accuracy of transmission line parameter monitoring based on PMU measurements. Even though it is clear that measured phasors may have different errors in magnitude and angle (or real and imaginary components), the principles of analyzing uncertainties in complex quantities had not been applied in PMU measurements. This work showed that these principles are applicable, well suited, and offer valuable information about the accuracy of measurements. It was also demonstrated what accuracy of line parameter monitoring can be achieved in a real installation, considering the accuracy of measurement devices, and how the accuracy varies in changing conditions. It was concluded that uncalibrated metering class transformers are generally not accurate enough to enable the monitoring

of transmission line resistance with the commonly used implementation of line parameter monitoring.

In Chap. 3 and Publication II a new method of monitoring corona losses on transmission lines was proposed and demonstrated. While traditionally the measurement of corona losses has required dedicated measurement setups and techniques, the proposed monitoring based on PMUs would not have such requirements. PMUs already installed on transmission lines can be utilized for more detailed transmission loss monitoring. The uncertainty analysis carried out based on Chap. 2 indicated that the uncertainty in measured corona losses was sufficiently low to obtain usable information. The results of monitoring corona losses over a period of four months of various weather conditions showed good agreement with results of previous studies on corona losses.

Finally, Chap. 4 and Publication III demonstrate the feasibility of estimating the inertia of a power system and its areas from ambient PMU measurements. While previous methods of estimating inertia from PMU measurements have relied on significant disturbances in the system, the proposed method could be run nearly continuously. Disturbances do not occur regularly, meaning that disturbance based methods cannot provide an estimate at any given time. A continuous inertia monitoring method based on ambient measurements would provide a current estimate for the operator when it is needed. This is critical information that enables to prepare and deploy an appropriate response in case of a significant event.

Practical Implementation

The monitoring methods demonstrated in the thesis have been tested on real measurement data from operating power systems; however, they are not production grade tools. In order to deploy these as monitoring tools used in practice, they would require further development. Practical tools would have to be more robust, e.g. handle bad and missing data, etc. The thesis has documented all of the details necessary for the implementation of the methods.

The monitoring of transmission loss components is relatively simple to implement in existing wide area monitoring software. The loss components are calculated with explicit expressions and the computations can be made in real-time. The method could also be implemented in contemporary SCADA/EMS software if it handles synchronized phasor measurements. In the analysis of losses, the sampling frequency can be quite low, but the time synchronization of measurements is critical. Certain aspects of the method would also require refinement, e.g. fixing the negative values of measured corona losses when corona losses are negligible.

The implementation used to demonstrate the feasibility of estimating effective inertia from ambient measurements is experimental. A practical tool would have to automate the continuous selection of measurement data, considering possible limitations, e.g. dispatch changes, etc. The estimation is computationally intensive and execution times could be improved with further development and optimization. A practical tool would also have to assess the quality of the results if the system identification routine does not perform sufficiently well on a given set of measurement data. The configuration of areas in the tool should consider the effects of line switching if this can have a significant impact in a particular system.

Further Work

The demonstrated method for monitoring corona losses requires PMUs at both ends of the transmission line. If the PMUs are available and the combined accuracy of the measurement devices is sufficient, it is possible to monitor corona losses continuously. If several lines spread around the system (or an area) can be monitored, a more general overview of corona losses in the system (or the area) can be obtained. Furthermore, if weather monitoring data is available from locations close to the monitored transmission lines, it is possible to collect the combined information about corona losses and weather conditions. Larger amounts of such historical data could be used to develop tools for forecasting corona losses based on forecast weather conditions. Further research will investigate applying machine learning methods to constructing corona loss forecasting tools.

There are several aspects of the inertia estimation methods where further work could be done. A thorough theoretical analysis of the system identification problem could offer better insights into selection of the appropriate system identification method and model orders. Based on that, the implementation could be optimized and improved. A commercially viable application would have to address data gaps and other data quality issues, automate the acquisition of set-point change time-stamps, and optimize the algorithm for faster running times. The concept is designed to be general and has been proven to work in one real power system. Further trials in other power systems with different characteristics would be of value, particularly where there is more power electronic penetration and variable inertia. Correlations between potential influences on effective inertia, causes of variations in inertia, and potential forecasting of effective inertia could be studied if more data is collected and analyzed.

References

- [1] IEE, "Discussion on 'A method of measuring and displaying generator rotor angle', 'Generator rotor angle measurement by stroboscopic means' and 'Power-system phase-angle measurements' before the joint meeting of the Measurement and Control Section and the Supply Section, 29th April, 1958," *Proceedings of the IEE - Part A: Power Engineering*, vol. 105, no. 24, pp. 617–619, December 1958.
- [2] J. N. Prewett, "A method of measuring and displaying generator rotor angle," *Proceedings of the IEE - Part A: Power Engineering*, vol. 105, no. 24, pp. 605–608, December 1958.
- [3] E. B. Powell and M. E. Harper, "Generator rotor angle measurement by stroboscopic means," *Proceedings of the IEE - Part A: Power Engineering*, vol. 105, no. 24, pp. 609–612, December 1958.
- [4] F. Moran, "Power-system phase-angle measurements," *Proceedings of the IEE - Part A: Power Engineering*, vol. 105, no. 24, pp. 613–617, December 1958.
- [5] R. C. Raupach and G. E. Stemler, "A fast response instrument for measurement of power system phase angles," *IEEE Transactions on Power Apparatus and Systems*, vol. PAS-87, no. 1, pp. 187–189, Jan 1968.
- [6] P. N. Nield, "Remote measurement of phase angle," *Electrical Engineers, Proceedings of the Institution of*, vol. 119, no. 5, pp. 548–556, May 1972.
- [7] G. Missout and P. Girard, "Measurement of bus voltage angle between Montreal and Sept-Iles," *IEEE Transactions on Power Apparatus and Systems*, vol. PAS-99, no. 2, pp. 536–539, March 1980.
- [8] P. Bonanomi, "Phase angle measurements with synchronized clocks-principle and applications," *IEEE Transactions on Power Apparatus and Systems*, vol. PAS-100, no. 12, pp. 5036–5043, Dec 1981.
- [9] A. G. Phadke, J. S. Thorp, and M. G. Adamiak, "A new measurement technique for tracking voltage phasors, local system frequency, and rate of change of frequency," *IEEE Transactions on Power Apparatus and Systems*, vol. PAS-102, no. 5, pp. 1025–1038, May 1983.
- [10] J. S. Thorp, A. G. Phadke, and K. J. Karimi, "Real time voltage-phasor measurement for static state estimation," *IEEE Transactions on Power Apparatus and Systems*, vol. PAS-104, no. 11, pp. 3098–3106, Nov 1985.
- [11] "IEEE standard for synchrophasor measurements for power systems," *IEEE Std C37.118.1-2011 (Revision of IEEE Std C37.118-2005)*, pp. 1–61, Dec 2011.
- [12] A. Phadke and J. Thorp, *Synchronized Phasor Measurements and Their Applications*. Springer, 2008.
- [13] M. Löper, U. Salumäe, and J. Kilter, "Assessment of higher harmonics influence to PMU measurement accuracy," in *2017 IEEE PES Innovative Smart Grid Technologies Conference Europe (ISGT-Europe)*, Sept 2017, pp. 1–6.

- [14] I. Kamwa, J. Beland, G. Trudel, R. Grondin, C. Lafond, and D. McNabb, "Wide-area monitoring and control at Hydro-Quebec: past, present and future," in *2006 IEEE Power Engineering Society General Meeting*, 2006.
- [15] T. Rauhala, K. Saarinen, M. Latvala, M. Laasonen, and M. Uusitalo, "Applications of phasor measurement units and wide-area measurement system in Finland," in *2011 IEEE Trondheim PowerTech*, June 2011, pp. 1–8.
- [16] M. Larsson, L. F. Santos, A. Suranyi, W. Sattinger, and R. Notter, "Monitoring of oscillations in the continental European transmission grid," in *IECON 2013 - 39th Annual Conference of the IEEE Industrial Electronics Society*, Nov 2013, pp. 4774–4778.
- [17] J. Chen, P. Shrestha, S. H. Huang, N. D. R. Sarma, J. Adams, D. Obadina, and J. Ballance, "Use of synchronized phasor measurements for dynamic stability monitoring and model validation in ERCOT," in *2012 IEEE Power and Energy Society General Meeting*, July 2012, pp. 1–7.
- [18] S. Clark, D. Wilson, N. Al-Ashwal, F. Macleod, P. Mohapatra, J. Yu, P. Wall, P. Dattaray, V. Terzija, P. Ashton, and M. Osborne, "Addressing emerging network management needs with enhanced WAMS in the GB VISOR project," in *2016 Power Systems Computation Conference (PSCC)*, June 2016, pp. 1–7.
- [19] E. Scholtz, R. F. Nuqui, D. Julian, and A. R. Grightmire, "Real-time power-line sag monitoring using time-synchronized power system measurements," Patent US7 620 517B2, Nov, 2009.
- [20] M. Weibel, W. Sattinger, P. Rothermann, U. Steinegger, M. Zima, and G. Biedenbach, "Overhead line temperature monitoring pilot project," in *2006 Cigre Session*, Paris, France, 2006.
- [21] P. Kundur, *Power System Stability and Control*. McGraw-Hill, 1993.
- [22] P. Kundur, J. Paserba, V. Ajjarapu, G. Andersson, A. Bose, C. Canizares, N. Hatziargyriou, D. Hill, A. Stankovic, C. Taylor, T. V. Cutsem, and V. Vittal, "Definition and classification of power system stability IEEE/CIGRE joint task force on stability terms and definitions," *IEEE Transactions on Power Systems*, vol. 19, no. 3, pp. 1387–1401, Aug 2004.
- [23] D. E. Hedman, "Propagation on overhead transmission lines I—theory of modal analysis," *Power Apparatus and Systems, IEEE Transactions on*, vol. 84, no. 3, pp. 200–205, March 1965.
- [24] J. B. Faria and J. B. Mendez, "Modal analysis of untransposed bilateral three-phase lines—a perturbation approach," *Power Delivery, IEEE Transactions on*, vol. 12, no. 1, pp. 497–504, Jan 1997.
- [25] J.-A. Jiang, Y.-H. Liu, C.-W. Liu, J.-Z. Yang, and T.-M. Too, "An adaptive fault locator system for transmission lines," in *1999 IEEE Power Engineering Society Summer Meeting. Conference Proceedings (Cat. No. 99CH36364)*, vol. 2, 1999, pp. 930–936 vol.2.
- [26] J.-A. Jiang, J.-Z. Yang, Y.-H. Lin, C.-W. Liu, and J.-C. Ma, "An adaptive PMU based fault detection/location technique for transmission lines. I. theory and algorithms," *IEEE Transactions on Power Delivery*, vol. 15, no. 2, pp. 486–493, Apr 2000.

- [27] J.-A. Jiang, Y.-H. Lin, J.-Z. Yang, T.-M. Too, and C.-W. Liu, "An adaptive PMU based fault detection/location technique for transmission lines. II. PMU implementation and performance evaluation," *IEEE Transactions on Power Delivery*, vol. 15, no. 4, pp. 1136–1146, Oct 2000.
- [28] C. Indulkar and K. Ramalingam, "Estimation of transmission line parameters from measurements," *International Journal of Electrical Power & Energy Systems*, vol. 30, no. 5, pp. 337–342, 2008.
- [29] Y. Du and Y. Liao, "On-line estimation of transmission line parameters, temperature and sag using PMU measurements," *Electric Power Systems Research*, vol. 93, pp. 39–45, 2012.
- [30] T. Bi, J. Chen, J. Wu, and Q. Yang, "Synchronized phasor based on-line parameter identification of overhead transmission line," in *Third International Conference on Electric Utility Deregulation and Restructuring and Power Technologies, 2008. DRPT 2008.*, April 2008, pp. 1657–1662.
- [31] D. Shi, D. Tylavsky, N. Logic, and K. Koellner, "Identification of short transmission-line parameters from synchrophasor measurements," in *40th North American Power Symposium. NAPS '08*, Sept 2008, pp. 1–8.
- [32] S. Kurokawa, G. A. Asti, E. C. M. Costa, and J. Pissolato, "Simplified procedure to estimate the resistance parameters of transmission lines," *Electrical Engineering*, vol. 95, no. 3, pp. 221–227, 2013.
- [33] "IEEE standard for calculating the current-temperature relationship of bare overhead conductors," *IEEE Std 738-2012 (Revision of IEEE Std 738-2006 - Incorporates IEEE Std 738-2012 Cor 1-2013)*, pp. 1–72, Dec 2013.
- [34] "Thermal behaviour of overhead conductors," CIGRE working group 22.12 report, August 2002.
- [35] *Model 1133A Power Sentinel Operation Manual*, Arbiter Systems, Inc., Paso Robles, CA, USA, 2014.
- [36] "Instrument transformers — part 1: Current transformers," Standard IEC 60044-1:2002, 2002.
- [37] "Instrument transformers — part 2: Inductive voltage transformers," Standard IEC 60044-2:2002, 2002.
- [38] P. H. Dana and B. M. Penrod, "The role of GPS in precise time and frequency dissemination," *GPS World*, 1990.
- [39] L. Wang, J. Fernandez, J. Burgett, R. W. Conners, and Y. Liu, "An evaluation of network time protocol for clock synchronization in wide area measurements," in *2008 IEEE Power and Energy Society General Meeting - Conversion and Delivery of Electrical Energy in the 21st Century*, July 2008, pp. 1–5.
- [40] R. S. Singh, H. Hooshyar, and L. Vanfretti, "Assessment of time synchronization requirements for phasor measurement units," in *Proceedings of PowerTech 2015*, Eindhoven, Netherlands, June 2015.

- [41] D. M. E. Ingram, P. Schaub, D. A. Campbell, and R. R. Taylor, "Evaluation of precision time synchronisation methods for substation applications," in *2012 IEEE International Symposium on Precision Clock Synchronization for Measurement, Control and Communication Proceedings*, Sept 2012, pp. 1–6.
- [42] JCGM, "Evaluation of measurement data — guide to the expression of uncertainty in measurement," Guide JCGM 100:2008, 2008.
- [43] JCGM, "Evaluation of measurement data — supplement 2 to the "Guide to the expression of uncertainty in measurement" — extension to any number of output quantities," Guide JCGM 102:2011, 2011.
- [44] B. D. Hall, "On the propagation of uncertainty in complex-valued quantities," *Metrologia*, vol. 41, no. 3, pp. 173–177, 2004.
- [45] B. D. Hall, "Some considerations related to the evaluation of measurement uncertainty for complex-valued quantities in radio frequency measurements," *Metrologia*, vol. 44, no. 6, pp. L62–L67, 2007.
- [46] B. D. Hall, "Notes on complex measurement uncertainty – part 2," Industrial Research Limited, Tech. Rep. IRL 2557, 2012.
- [47] Elering, "Annual report," 2017.
- [48] R. Wilkins, "Corona loss tests on the 202-mile 60-cycle 220-Kv. Pit-Vaca transmission line of the Pacific Gas and Electric company," *Transactions of the American Institute of Electrical Engineers*, vol. XLIII, pp. 1148–1171, Jan 1924.
- [49] F. M. Cahen and J. M. Carteron, "The French 380-Kv system - measurement of corona losses on transmission lines under normal operating conditions," *Transactions of the American Institute of Electrical Engineers. Part III: Power Apparatus and Systems*, vol. 76, no. 3, pp. 1525–1531, April 1957.
- [50] V. L. Chartier, D. F. Shankie, and N. Kolcio, "The Apple Grove 750-kV project: Statistical analysis of radio influence and corona-loss performance of conductors at 775 kV," *IEEE Transactions on Power Apparatus and Systems*, vol. PAS-89, no. 5, pp. 867–881, May 1970.
- [51] F. J. Sollerkvist, A. Maxwell, K. Rouden, and T. M. Ohnstad, "Evaluation, verification and operational supervision of corona losses in Sweden," *Power Delivery, IEEE Transactions on*, vol. 22, no. 2, pp. 1210–1217, April 2007.
- [52] F. W. Peek, "The law of corona and dielectric strength of air—II," *Proceedings of the American Institute of Electrical Engineers*, vol. 31, no. 6, pp. 1085–1126, June 1912.
- [53] C. F. Harding, "Corona losses between wires at high voltages," *Proceedings of the American Institute of Electrical Engineers*, vol. 31, no. 7, pp. 1271–1285, July 1912.
- [54] F. W. Peek, "Comparison of calculated and measured corona loss curves," *Transactions of the American Institute of Electrical Engineers*, vol. 34, no. 1, pp. 269–278, Jan 1915.
- [55] I. Baran, M. Costea, and T. Leonida, "On the possibility of using weather forecast to predict corona losses," in *2013 8th International Symposium on Advanced Topics in Electrical Engineering (ATEE)*, May 2013, pp. 1–6.

- [56] J. J. Clade, C. H. Gary, and C. A. Lefevre, "Calculation of corona losses beyond the critical gradient in alternating voltage," *IEEE Transactions on Power Apparatus and Systems*, vol. PAS-88, no. 5, pp. 695–703, May 1969.
- [57] O. Nigol and J. G. Cassan, "Corona loss research at Ontario Hydro Coldwater project," *Transactions of the American Institute of Electrical Engineers. Part III: Power Apparatus and Systems*, vol. 80, no. 3, pp. 304–312, April 1961.
- [58] V. V. Burgodorf, N. P. Emelyanov, L. V. Timasheva, N. N. Tikhodeev, L. S. Perelman, L. V. Egorova, N. S. Kislova, and R. A. Sohakyan, "Guidelines for accounting for corona losses and corona interference when selecting conductors for 330-750 kV AC and 800-1500 kV DC overhead electric power transmission lines (in Russian)," GOST RD 34.20.172 (ГОСТ РД 34.20.172), 1974.
- [59] K. Lahti, M. Lahtinen, and K. Nousiainen, "Transmission line corona losses under hoar frost conditions," *IEEE Transactions on Power Delivery*, vol. 12, no. 2, pp. 928–933, Apr 1997.
- [60] Y. Solovyev, I. Gutman, O. Byrkjedal, and B. H. Thorsteinsson, "Practical methodology for calculation of corona losses induced by hoarfrost using operational measurements," *CIGRE Science & Engineering*, vol. 10, February 2018.
- [61] S. I. Sulakov, "Forecasting hourly corona losses applying statistical approach," in *2016 19th International Symposium on Electrical Apparatus and Technologies (SIELA)*, May 2016, pp. 1–4.
- [62] K. Tuttelberg and J. Kilter, "Real-time estimation of transmission losses from PMU measurements," in *Proceedings of PowerTech 2015*, Eindhoven, Netherlands, June 2015.
- [63] L. M. Wedepohl, "Application of matrix methods to the solution of travelling-wave phenomena in polyphase systems," *Proceedings of the IEE*, vol. 110, no. 12, pp. 2200–2212, 1963.
- [64] J. B. Anderson, Ed., *Analysis of Faulted Power Systems*. IEEE-Wiley, 1973.
- [65] J.-C. Li and Y.-P. Wu, "A distributed circuit model for three-phase transposed and untransposed transmission lines," *Electric Power Systems Research*, vol. 19, no. 3, pp. 187 – 194, 1990.
- [66] C. L. Fortescue, "Method of symmetrical co-ordinates applied to the solution of polyphase networks," *Proceedings of the AIEE*, vol. 37, no. 6, pp. 629–716, 1918.
- [67] R. Galloway, W. Shorrocks, and L. Wedepohl, "Calculation of electrical parameters for short and long polyphase transmission lines," *Proceedings of the IEE*, vol. 111, no. 12, pp. 2051–2059, December 1964.
- [68] E. Ørum, M. Kuivaniemi, M. Laasonen, A. Bruseth, E. Jansson, A. Danell, K. Elkington, and N. Modig, "Future system inertia," ENTSO-E Nordic Analysis Group, Tech. Rep., 2015.
- [69] I. Dudurych, M. Burke, L. Fisher, M. Eager, and K. Kelly, "Operational security challenges and tools for a synchronous power system with high penetration of non-conventional sources," *CIGRE Science & Engineering*, vol. 7, February 2017.

- [70] V. Gevorgian, Y. Zhang, and E. Ela, "Investigating the impacts of wind generation participation in interconnection frequency response," *IEEE Transactions on Sustainable Energy*, vol. 6, no. 3, pp. 1004–1012, July 2015.
- [71] S. Sharma, S. H. Huang, and N. Sarma, "System inertial frequency response estimation and impact of renewable resources in ERCOT interconnection," in *2011 IEEE Power and Energy Society General Meeting*, July 2011, pp. 1–6.
- [72] J. Conto, "Grid challenges on high penetration levels of wind power," in *2012 IEEE Power and Energy Society General Meeting*, July 2012, pp. 1–3.
- [73] N. W. Miller, M. Shao, S. Venkataraman, C. Loutan, and M. Rothleder, "Frequency response of California and WECC under high wind and solar conditions," in *2012 IEEE Power and Energy Society General Meeting*, July 2012, pp. 1–8.
- [74] H. Gu, R. Yan, and T. K. Saha, "Minimum synchronous inertia requirement of renewable power systems," *IEEE Transactions on Power Systems*, vol. 33, no. 2, pp. 1533–1543, March 2018.
- [75] R. Yan, T. K. Saha, N. Modi, N.-A. Masood, and M. Mosadeghy, "The combined effects of high penetration of wind and PV on power system frequency response," *Applied Energy*, vol. 145, pp. 320 – 330, 2015.
- [76] H. Pulgar-Painemal, Y. Wang, and H. Silva-Saravia, "On inertia distribution, inter-area oscillations and location of electronically-interfaced resources," *IEEE Transactions on Power Systems*, vol. 33, no. 1, pp. 995–1003, Jan 2018.
- [77] MIGRATE Work Package 1 – responsible partner: TenneT, "Migrate deliverable 1.1: Report on systemic issues," 2016, MIGRATE consortium.
- [78] P. M. Anderson and A. A. Fouad, *Power System Control and Stability, 2nd Edition*, M. E. El-Hawary, Ed. Wiley, 2002.
- [79] A. Ulbig, T. S. Borsche, and G. Andersson, "Impact of low rotational inertia on power system stability and operation," *IFAC Proceedings Volumes*, vol. 47, no. 3, pp. 7290 – 7297, 2014.
- [80] Y. Bian, H. Wyman-Pain, F. Li, R. Bhakar, S. Mishra, and N. P. Padhy, "Demand side contributions for system inertia in the gb power system," *IEEE Transactions on Power Systems*, vol. 33, no. 4, pp. 3521–3530, July 2018.
- [81] M. Kuivaniemi, "Estimation of generator inertia in the Nordic power system," Master's thesis, Tampere University of Technology, 2014.
- [82] M. Kuivaniemi, M. Laasonen, K. Elkington, A. Danell, N. Modig, A. Bruseth, E. Jansson, and E. Ørum, "Estimation of system inertia in the Nordic power system using measured frequency disturbances," in *Cigre symposium Across Borders – HVDC Systems and Market Integration*, Lund, Sweden, 2015.
- [83] P. M. Ashton, "Exploiting phasor measurement units for enhanced transmission network operation and control," Ph.D. dissertation, Brunel University, 2014. [Online]. Available: <http://bura.brunel.ac.uk/handle/2438/9063>

- [84] P. M. Ashton, C. S. Saunders, G. A. Taylor, A. M. Carter, and M. E. Bradley, "Inertia estimation of the GB power system using synchrophasor measurements," *IEEE Transactions on Power Systems*, vol. 30, no. 2, pp. 701–709, March 2015.
- [85] T. Inoue, H. Taniguchi, Y. Ikeguchi, and K. Yoshida, "Estimation of power system inertia constant and capacity of spinning-reserve support generators using measured frequency transients," *IEEE Transactions on Power Systems*, vol. 12, no. 1, pp. 136–143, Feb 1997.
- [86] D. P. Chassin, Z. Huang, M. K. Donnelly, C. Hassler, E. Ramirez, and C. Ray, "Estimation of WECC system inertia using observed frequency transients," *IEEE Transactions on Power Systems*, vol. 20, no. 2, pp. 1190–1192, May 2005.
- [87] P. Wall, F. González-Longatt, and V. Terzija, "Demonstration of an inertia constant estimation method through simulation," in *45th International Universities Power Engineering Conference UPEC2010*, Aug 2010, pp. 1–6.
- [88] P. M. Ashton, G. A. Taylor, A. M. Carter, M. E. Bradley, and W. Hung, "Application of phasor measurement units to estimate power system inertial frequency response," in *2013 IEEE Power Energy Society General Meeting*, July 2013, pp. 1–5.
- [89] P. Wall and V. Terzija, "Simultaneous estimation of the time of disturbance and inertia in power systems," *IEEE Transactions on Power Delivery*, vol. 29, no. 4, pp. 2018–2031, Aug 2014.
- [90] X. Cao, B. Stephen, I. F. Abdulhadi, C. D. Booth, and G. M. Burt, "Switching markov gaussian models for dynamic power system inertia estimation," *IEEE Transactions on Power Systems*, vol. 31, no. 5, pp. 3394–3403, Sept 2016.
- [91] A. Schmitt and B. Lee, "Steady-state inertia estimation using a neural network approach with modal information," in *2017 IEEE Power Energy Society General Meeting*, July 2017, pp. 1–5.
- [92] S. Guo, S. Norris, and J. Bialek, "Adaptive parameter estimation of power system dynamic model using modal information," *IEEE Transactions on Power Systems*, vol. 29, no. 6, pp. 2854–2861, Nov 2014.
- [93] J. Zhang and H. Xu, "Online identification of power system equivalent inertia constant," *IEEE Transactions on Industrial Electronics*, vol. 64, no. 10, pp. 8098–8107, Oct 2017.
- [94] H. Huomo and J. Alakontiola, "Grid frequency response," Patent Pending US20 160 248 254A1, Aug, 2016.
- [95] *MATLAB and System Identification Toolbox R2016b: User's Guide*, The MathWorks, Inc., Natick, Massachusetts, 2016.
- [96] L. Andersson, U. Jönsson, K. H. Johansson, and J. Bengtsson, "A manual for system identification," 2006.
- [97] F. R. Hampel, "The influence curve and its role in robust estimation," *Journal of the American Statistical Association*, vol. 69, no. 346, pp. 383–393, 1974.

- [98] P. J. Rousseeuw and C. Croux, "Alternatives to the median absolute deviation," *Journal of the American Statistical Association*, vol. 88, no. 424, pp. 1273–1283, 1993.
- [99] C. Leys, C. Ley, O. Klein, P. Bernard, and L. Licata, "Detecting outliers: Do not use standard deviation around the mean, use absolute deviation around the median," *Journal of Experimental Social Psychology*, vol. 49, no. 4, pp. 764 – 766, 2013.
- [100] J. H. Harlow, L. L. Grigsby, and J. D. McDonald, *Electric Power Transformer Engineering*. CRC Press, 2012.

Acknowledgments

I would like to thank my supervisor, Jako Kilter and the head of department, Ivo Palu for granting me the opportunities I have had during the PhD studies. I was fortunate to work on interesting and meaningful research and development projects.

I truly appreciate the patience of my partner, Monika during my extended stays abroad. Thank you for supporting me throughout this long endeavor.

The PhD studies have given me the opportunity to meet many great people. Connection to the Strong²rid project acquainted me with Luigi Vanfretti and Kjetil Uhlen and their students. I would like to greet Kjetil, Sigurd, Thuc, Luigi, Almas, Guðrún, and others who I met in Trondheim and Stockholm. Special thanks to Kjetil for accommodating my stay at NTNU.

The MIGRATE project led me to work with people from all over Europe. Most of all I would like to thank Landsnet for offering me a chance to work with them at their office in Reykjavík. My greetings to Ragnar, Birkir, Sam, Guðjón, and Douglas.

Weather data from the Estonian Environmental Agency has been used in this work.

Abstract

At present the monitoring and control of power systems is largely based on SCADA/EMS technologies. These tools provide significant amounts of useful information, yet still leave many processes and phenomena unobservable. In the last decade, wide area monitoring systems powered by phasor measurement units (PMU) have been deployed by many transmission system operators (TSO), becoming a prevalent technology that enables more detailed monitoring of the system. This has introduced a new generation of monitoring tools to the operation of power systems. The thesis presents new developments in wide area monitoring of power systems using synchronized phasor measurements.

Monitoring of transmission line parameters is a well-known application of PMU measurements. The thesis analyzes uncertainty propagation in this application in order to determine its accuracy and explain how it is affected by systematic measurement errors. The analysis considers the entire measurement chain, including instrument transformers, and the effects of errors from various sources. The principles of uncertainty analysis in two-dimensional quantities are applied as the measured phasors are complex valued quantities. It is shown how the uncertainties of measuring current and voltage phasors are propagated into the estimated quantities and what their resulting uncertainty is. The results describe the expected accuracy of the monitoring application in the given real world installation and help to explain the apparent errors in some of the measured results.

The energy needed to cover transmission losses is one of the largest expenses for a TSO. The thesis presents a new method developed to analyze transmission losses in more detail, with the emphasis on monitoring of corona losses. Based on a detailed transmission line model, equations are derived that allow separate components of transmission losses to be calculated from simultaneous measurements of voltage and current phasors. This allows corona losses to be monitored separately from total losses. Uncertainty analysis of measured corona losses indicates that the expected accuracy of the measurement chain is sufficient to obtain usable estimates. Four months of real world monitoring data of corona losses and weather conditions is used to validate the results based on the weather dependence of corona losses and comparisons to results of previous studies.

The increasing use of renewable energy sources is changing the inertial responses of power systems. The thesis demonstrates a method of estimating power system inertia from ambient measurements, i.e. normal operating conditions. While existing measurement based inertia estimation methods have relied solely on disturbances, the developed method can be applied nearly continuously. What is more, the method considers the system in terms of areas, allowing inertia of each area to be estimated separately. The method is based on observing the dynamics between changes in active power and corresponding deviations in frequency. System identification tools are applied to fit approximate models to these dynamic patterns. The identified models include the inertial response of the system among other dynamics. Inertia estimation from ambient measurements has been validated on measurement data from a real power system.

The presented work has several practical implications. The analysis of uncertainty propagation in transmission line monitoring characterizes confidence in the estimates of various monitored quantities. It gives a better understanding of what accuracy can be expected and what to change in order to improve accuracy. Continuous long-term monitoring of corona losses can be used to improve transmission loss forecasts which in turn would allow the cost of loss energy to be minimized. In systems with decreasing and variable inertia, it is becoming necessary to know the effective inertial response of the system in order to maintain its stable operation. TSOs can use the information to schedule appropriate responses to disturbances and improve frequency control measures.

Keywords

Area inertia, Corona losses, Effective inertia, Error propagation, Frequency control, Frequency dynamics, Inertial response, Instrument transformers, Loss content estimation, Measurement uncertainty, Phasor measurement units, Real-time monitoring, System identification, Transmission line monitoring, Transmission losses, Wide area monitoring

Lühikokkuvõte

Praegusel ajal põhineb enamike elektrisüsteemide jälgimine ja juhtimine SCADA/EMS süsteemidel. Need vahendid pakuvad suurel hulgal kasulikku infot, kuid on siiski mitmeid protsesse ja nähtusi, mida need jälgida ei võimalda. Viimase aastakümne jooksul on mitmed põhivõrguettevõtted hankinud faasimõõteseadmetel põhinevad laiseiresüsteemid, mis võimaldavad elektrisüsteemide üksikasjalikumalt jälgimist. Selle tehnoloogia kasutuselevõtule on järgnenud uus põlvkond elektrisüsteemide jälgimise rakendusi. Käesolev töö käsitleb uute faasimõõtmistel põhinevate laiseirerakenduste arendust.

Ülekandeliinide parameetrite jälgimine on üks levinud näide laiseirerakendustest. Käesolev töö analüüsib mõõtemääramatusi antud meetodil leitud liiniparameetrites eesmärgiga teha kindlaks mõõterakenduse täpsus ja selgitada süstemaatiliste mõõtevigade mõju. Analüüsis arvestatakse vigade allikaid kogu mõõteahelas, sh mõõtetrafode vead. Kuna mõõdetud faasorid on kompleksarvulised suurused, on lähtutud kahemõõtmeliste suuruste mõõtemääramatuste analüüsi põhimõtetest. Töös on näidatud, kuidas voolu- ja pingefaasorite mõõtemääramatused kanduvad otsitud suurustesse ning milliseks kujuneb nende mõõtemääramatus. Tulemused kirjeldavad rakenduse eeldatavat täpsust vaadeldud tingimustes ning aitavad selgitada ilmseid vigu osades saadud mõõtetulemustest.

Ülekandekadude katmiseks vajaliku energia ostmise on üks suuremaid kulutusi põhivõrguettevõtte eelarves. Doktoritöö esitleb ülekandekadude täpsemaks analüüsiks välja töötatud meetodit, põhirõhuga koroonakadude jälgimisel. Üksikasjaliku ülekandeliini mudeli alusel on tuletatud võrrandid, mille abil saab arvutada eraldi ülekandekadude komponendid samaaegselt mõõdetud pinge- ja voolufaasoritest. See võimaldab mõõta koroonakadusid eraldiseisvalt kogukadudest. Mõõtemääramatuste analüüsi põhjal võib eeldada, et mõõteahela täpsus on kasutatavate tulemuste saamiseks piisav. Tulemusi on valideeritud nelja kuu kohta kogutud koroonakadude mõõteandmete ja ilmavaatlusandmete põhjal, analüüsides mõõdetud koroonakadude sõltuvust ilmaoludest ja võrreldes tulemusi varasemate uuringute tulemustega.

Taastuvate energiaallikate suurenev kasutuselevõtt muudab elektrisüsteemide inertsi. Käesolev töö esitleb meetodit, mis võimaldab elektrisüsteemi inertsi määrata püsitalitluse mõõtmistest. Kui varasemad mõõtmistepõhised inertsi määramise meetodid on toimimiseks eeldanud sagedushäiringute esinemist, siis esitletavat meetodit võib rakendada pidevalt. Lisaks sellele käsitleb meetod elektrisüsteemi piirkondadena, mille inertsi on võimalik eraldiseisvalt määrata. Meetod põhineb aktiivvõimsuste ja sagedusemuutuste vaheliste dünaamiliste protsesside jälgimisel. Kasutatakse süsteemide identifitseerimise vahendeid, et lähendada mudelid mõõdetud dünaamilistele muutustele. Lähendatud mudelid sisaldavad muude elektrisüsteemi dünaamikaomaduste kõrval ka selle inertsi. Inertsi määramise meetodit on valideeritud ühe päris elektrisüsteemi püsitalitluse mõõteandmete põhjal.

Esitletud töö tulemustel on mitmeid praktilisi väljundeid. Mõõtemääramatuste analüüs ilmestab ülekandeliini parameetrite jälgimise usaldatavust. See annab parema ülevaate rakenduse oodatavast täpsusest ja võimalustest selle täpsust suurendada. Koroonakadude pidev pikaajaline jälgimine aitab täpsustada ülekandekadude prognoosi, mis võimaldab omakorda minimeerida kadude maksumust. Väheneva ja varieeruva inertsiiga elektrisüsteemides muutub inertsi jälgimine vajalikuks, et tagada nende stabiilne töö. Süsteemioperaator saab selle abil planeerida häiringute tasakaalustamist ja täiendada sageduse reguleerimise meetmeid.

Märksõnad

elektrisüsteemi inertts, faasimõõturid, koroonakaod, laiseire, mõjuv inertts, mõõtemääramatused, mõõtetrafod, piirkondlik inertts, reaajas jälgimine, sagedusdünaamika, sageduse reguleerimine, süsteemide identifitseerimine, ülekandekadude komponendid, ülekandeliinide jälgimine

Appendix A — Instrument Transformer Errors

This appendix presents information about instrument transformer errors. Errors reported in factory test reports are given in Tables 1–4. In the tables, U/U_n and I/I_n stand for ratios of measured and rated values. Magnitude errors are given in per cent and angle errors in minutes. The estimated burdens of the instrument transformers are as follows. At substation A, current transformer burden 1.5 VA and voltage transformer burden 2.0 VA; at substation B, current transformer burden 1.7 VA and voltage transformer burden 1.4 VA. Only the current transformer burden at substation A fits between the tested burden values. It is not reasonable to assume that the errors can be extrapolated for a burden value outside of the range between the two tested burdens [100]. The other three burden values are replaced by the lowest burden values that measurement errors were reported for.

Table 1 Current transformer errors at substation A.

Burden 1 VA, power factor not specified						
I/I_n	Phase A		Phase B		Phase C	
	δI (%)	$\delta\varphi_I$ (')	δI (%)	$\delta\varphi_I$ (')	δI (%)	$\delta\varphi_I$ (')
1.2	0.03	0.0	0.02	0.0	0.07	0.0
1.0	0.028	0.18	0.02	0.18	0.066	0.36
0.2	0.021	0.9	0.02	0.9	0.053	1.8
0.05	0.02	1.0	0.02	1.0	0.05	2.0
0.01	0.02	2.0	0.03	2.0	0.05	3.0
Burden 5 VA, power factor not specified						
1.2	0.01	-1.0	-0.01	0.0	0.04	0.0
1.0	0.01	-1.0	0	-1.0	0.04	0.0
0.2	-0.02	0.0	-0.02	0.0	0.02	0.0
0.05	-0.04	1.0	-0.03	1.0	0.0	2.0
0.01	-0.04	3.0	-0.04	2.0	-0.01	3.0

Table 2 Current transformer errors at substation B.

Burden 5 VA, power factor 1						
I/I_n	Phase A		Phase B		Phase C	
	δI (%)	$\delta\varphi_I$ (')	δI (%)	$\delta\varphi_I$ (')	δI (%)	$\delta\varphi_I$ (')
1.2	-0.01	0.2	-0.01	0.1	-0.02	0.1
1.0	-0.01	0.5	-0.01	0.2	-0.02	0.2
0.2	-0.01	0.6	-0.01	0.7	-0.02	0.7
0.05	-0.01	1.0	-0.01	1.3	-0.01	1.3
0.01	0.01	2.6	0.0	2.9	0.0	2.9
Burden 20 VA, power factor 0.8						
1.2	-0.05	-0.7	-0.03	-0.9	-0.03	-1.0
1.0	-0.05	-0.3	-0.03	-0.8	-0.03	-0.8
0.2	-0.06	0.1	-0.045	0.2	-0.05	0.2
0.05	-0.06	0.9	-0.05	1.2	-0.06	1.2
0.01	-0.06	2.8	-0.05	2.9	-0.06	2.3

Table 3 Voltage transformer errors at substation A.

Burden 25 VA, power factor not specified						
U/U_n	Phase A		Phase B		Phase C	
	δU (%)	$\delta\varphi_U$ (')	δU (%)	$\delta\varphi_U$ (')	δU (%)	$\delta\varphi_U$ (')
1.5	0.04	5.0	0.06	5.0	0.06	4.0
1.2	0.12	2.0	0.12	3.0	0.12	2.0
1.0					0.14	1.0
0.8	0.16	1.0	0.15	1.0	0.15	1.0
0.05					0.15	7.0
0.02	0.2	6.0	0.2	8.0	0.21	10.0
Burden 100 VA, power factor not specified						
1.2	-0.14	4.0	-0.12	5.0	-0.13	4.0
1.0					-0.11	3.0
0.8	-0.1	2.0	-0.08	4.0	-0.11	3.0

Table 4 Voltage transformer errors at substation B.

Burden 25 VA, power factor 0.8						
U/U_n	Phase A		Phase B		Phase C	
	δU (%)	$\delta\varphi_U$ (')	δU (%)	$\delta\varphi_U$ (')	δU (%)	$\delta\varphi_U$ (')
1.5	0.37	2.5	0.39	2.4	0.38	3.1
1.2	0.37	2.8	0.39	2.4	0.38	3.1
1.0	0.37	2.8	0.39	2.4	0.38	3.1
0.8	0.37	2.9	0.39	2.9	0.38	3.1
0.05	0.41	8.7	0.41	8.7	0.41	8.7
Burden 100 VA, power factor 0.8						
1.5	-0.27	9.2	-0.27	9.2	-0.27	9.2
1.2	-0.29	9.4	-0.25	9.3	-0.26	10.4
1.0	-0.29	9.8	-0.25	9.3	-0.26	10.4
0.8	-0.29	10.2	-0.25	10	-0.26	10.4
0.05	-0.18	18	-0.18	18	-0.18	18

Appendix B — Included Publications

Publication I

K. Tuttelberg and J. Kilter, "Uncertainty propagation in PMU-based transmission line monitoring," in *IET Generation, Transmission & Distribution*, vol. 12, no. 3, pp. 745–755.

Reproduced by permission of the Institution of Engineering & Technology

Uncertainty Propagation in PMU-based Transmission Line Monitoring

Kaur Tuttelberg^{1,*}, Jako Kilter¹

¹ Department of Electrical Power Engineering and Mechatronics, Tallinn University of Technology, Tallinn, Estonia
* E-mail: kaur.tuttelberg@ttu.ee

ISSN 1751-8644
doi: 10.1049/iet-gtd.2017.0244
www.ietdl.org

Abstract: This paper analyses the uncertainties of synchronised phasor measurement based transmission line monitoring applications. Uncertainty propagation is analysed in order to assess confidence in the accuracy of such monitoring applications and explain how systematic measurement errors affect the monitored quantities. Estimation of transmission losses and transmission line parameters are analysed as examples. The uncertainty analysis considers the entire measurement chain, i.e. it includes the measurement errors of instrument transformers and phasor measurement units (PMU) and the propagation of resulting uncertainties into quantities of interest. The paper adopts the principles of evaluating the uncertainties and their propagation in complex (i.e. two-dimensional) quantities, as this would be the most appropriate approach for phasors that can have different uncertainties in magnitude and angle. The paper demonstrates how uncertainties of measured voltages and currents are propagated into the estimated quantities and what accuracy can be expected from such monitoring applications in a common transmission system setting. The study also helps to understand better what causes most of the uncertainty (and inaccuracy) in particular quantities of interest. The analysis is carried out on real PMU measurements of an operating transmission line.

1 Introduction

Since the introduction of phasor measurement units and wide area measurement systems, a wide range of applications have been suggested and developed to better monitor power systems. Among the applications, the monitoring of transmission lines and their parameters are well known examples. However, the accuracy of the different wide area monitoring applications has not always been analysed in practice. This paper presents results of real world PMU measurement based transmission line monitoring applications accompanied by uncertainty analyses considering the measurement accuracy of both PMUs and other elements of the measurement chain. The analysis gives a better understanding of how different quantities are affected by measurement errors.

The uncertainties and their propagation in certain PMU measurement based estimations have been analysed before [1, 2]. Published analyses of such uncertainties have relied on recommended practices for measurements of one-dimensional quantities [3]; however, the uncertainties in PMU measurements are generally not equal in different dimensions (i.e. magnitude and angle). For two-dimensional quantities (e.g. phasors) a different approach is recommended when it is not assumed that the errors in the two dimensions (in this case real and imaginary components of a complex quantity) are equal [4–6]. This paper proposes to analyse uncertainty propagation in PMU measurements by considering the principles that apply to complex quantities [5, 7].

In a transmission system, PMUs can only measure voltages and currents through some transducers, which in most cases are instrument transformers. Most of the time discussions on wide area monitoring applications assume that instrument transformers are calibrated so that their measurement errors can be ideally compensated for. In recent years, the effects of instrument transformer measurement errors on PMU measurements have gained more attention [8, 9]. The measurement errors of instrument transformers are dependent on the measurands themselves and properties of connected measurement devices. In real installations, the available information may be limited to results of factory tests of instrument transformers and calculated values of burden and its power factor. Without on-site calibrations, instrument transformers contribute significant uncertainties that have to be accounted for.

Monitoring the operation and parameters of a transmission line is a well known application of wide area measurements [10, 11]. Such applications are based on simultaneous voltage and current phasor values obtained from synchronised PMU measurements from both ends of the transmission line. This paper looks at estimates of transmission losses and line parameters as examples and analyses the uncertainties of obtained results. As the paper demonstrates, some of the monitored quantities are very sensitive to the accuracy of the measurement chain, resulting in large relative uncertainties and occasional unrealistic values. The paper presents experimental data obtained from real PMU measurements of a 330 kV transmission line.

The objectives of the paper are threefold: firstly, to demonstrate the results of monitoring an actual high voltage transmission line based on PMU measurements and to analyse the apparent inconsistencies in some of the results; secondly, to explain how different quantities are affected by systematic measurement errors and where the inconsistencies come from; thirdly, to demonstrate how the uncertainty analysis of complex quantities applies to phasor measurements and their applications. The examined real world applications of line parameter and transmission loss estimation based on PMU measurements display occasional problems with accuracy, which are characterised by corresponding large uncertainties. The analysis gives insights into what causes these inaccuracies and what they depend on. The presented uncertainty analysis in complex quantities suits the studied applications well, since the monitored quantities are also complex valued or either the real or imaginary parts of complex values.

The paper is structured as follows. Section 2 summarises the main background of the presented work: the common estimation of transmission losses and line parameters from measured phasors is described in subsection 2.1 and the main aspects of uncertainty propagation in complex quantities are presented in subsection 2.2. In section 3, expressions are given to compute the uncertainties propagated into the quantities of interest. Experimental results are presented in section 4, a discussion carried out in section 5, and conclusions given in section 6.

2 Theoretical background

2.1 Monitoring of Transmission Lines

The monitoring of transmission lines with PMUs is based on simultaneous measurements of voltage and current phasors at both ends of the line. The quantities discussed in this paper, i.e. transmission losses and line parameters, can be calculated from these measurements. The accuracy of the calculated estimates depends solely on the accuracy of measured voltages and currents and their synchronisation (not considering simplifications in the mathematical models themselves).

The calculation of total transmission losses is trivial: the power at each end is computed from measured voltage and current phasors and their difference is found. The estimation of line parameters is slightly more involved. For a transposed line, it is commonly assumed that the effects of inter-phase coupling and geometrical asymmetry are removed by the transposition [10, 11].

In this case, single conductor distributed parameter line equations can be applied, so that the voltages and currents in any phase (or symmetrical component) are related by

$$\underline{V}_1 = \cosh(\gamma l)\underline{V}_2 + z_c \sinh(\gamma l)\underline{I}_2, \quad (1)$$

$$\underline{I}_1 = \frac{1}{z_c} \sinh(\gamma l)\underline{V}_2 + \cosh(\gamma l)\underline{I}_2, \quad (2)$$

where \underline{V}_1 and \underline{I}_1 are the voltage and current phasors at the beginning and \underline{V}_2 and \underline{I}_2 at the end of the line.

The equations can be solved explicitly for quantities γ and z_c as [12]

$$\gamma = \frac{1}{L} \operatorname{arcosh} \left[\frac{V_1 I_1 + V_2 I_2}{V_2 I_1 + V_1 I_2} \right], \quad (3)$$

$$z_c = \frac{V_2 \sinh(\gamma L)}{I_1 - I_2 \cosh(\gamma L)}, \quad (4)$$

where L is the total length of the line. The per unit distance line parameters—the impedance and admittance—are expressed as $z = \gamma z_c = r + jx$ and $y = \gamma/z_c = g + jb$.

Such estimations are often carried out by more advanced algorithms (e.g. least squares etc.) that reduce statistical (i.e. random) errors [10, 11]; in these cases, the equations are usually solved implicitly. The estimates are found as parameters fitted to a model, by minimising an error (not to be confused with measurement errors), etc. However, for the analytic expression of uncertainties, the explicit expressions for single data points are better suited. In order to reduce random errors, the explicitly evaluated values from repeated measurements can be averaged and the mean value taken as the result.

2.2 Uncertainties in Complex Quantities

PMUs measure voltage and current phasors as complex—or two-dimensional—quantities, with inherent uncertainties in both the magnitude and phase angle. Generally there is no reason to assume that the uncertainties in magnitude and angle are equal. An illustration of this is given in Fig. 1, where two measured voltage phasors are plotted. One of the phasors is accompanied by an ellipse, formed by the uncertainties of measuring its magnitude and angle.

The treatment of uncertainties in complex quantities requires some special considerations. In order to determine the uncertainty ellipse, like in the example of Fig. 1, a number of computations are made. The fundamentals are summarised below and elaborated on later for the specific quantities of interest in the scope of this paper.

A complex quantity \underline{x} may be estimated by some measured value \underline{x} written as

$$\underline{x} = x_{\text{re}} + jx_{\text{im}},$$

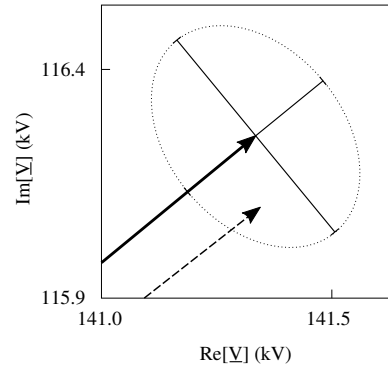


Fig. 1: Voltage phasors at separate ends of a transmission line measured by PMUs. One phasor is accompanied by its uncertainty ellipse.

where the real and imaginary parts are denoted by corresponding subscripts. The covariance matrix of this estimate \underline{x} is then given as

$$\mathbf{C}(\underline{x}) = \begin{bmatrix} [u(x_{\text{re}})]^2 & u(x_{\text{re}})r u(x_{\text{im}}) \\ u(x_{\text{im}})r u(x_{\text{re}}) & [u(x_{\text{im}})]^2 \end{bmatrix}, \quad (5)$$

where $u(x)$ denotes the uncertainty of x and $r = r(x_{\text{re}}, x_{\text{im}}) = r(x_{\text{im}}, x_{\text{re}}) = u(x_{\text{re}}, x_{\text{im}})/[u(x_{\text{re}})u(x_{\text{im}})]$ is the correlation between the real and imaginary components of \underline{x} [5].

The uncertainties of a quantity x , which is measured in terms of magnitude x_m and angle x_ϕ

$$x = x_m e^{jx_\phi}$$

are transformed from polar coordinates into the (Cartesian) complex plane. Firstly, a radial-tangential covariance matrix is formed

$$\mathbf{C}_{\text{rt}}(\underline{x}) = \begin{bmatrix} [u(x_m)]^2 & u(x_m)r_t u(x_\phi) \\ u(x_\phi)r_t u(x_m) & [u(x_\phi)]^2 \end{bmatrix}, \quad (6)$$

where $r_t \cong r(x_m, x_\phi)$ is the correlation between the magnitude and angle measurements and $u(x_t)$ is a tangential uncertainty component, found as [13]

$$u(x_t) = x_m \tan [u(x_\phi)]. \quad (7)$$

The matrix is then rotated by the measured angle x_ϕ

$$\mathbf{T} = \begin{bmatrix} \cos x_\phi & -\sin x_\phi \\ \sin x_\phi & \cos x_\phi \end{bmatrix}. \quad (8)$$

The covariance matrix for the quantity in the complex plane is obtained as [13]

$$\mathbf{C}(\underline{x}) = \mathbf{T}\mathbf{C}_{\text{rt}}(\underline{x})\mathbf{T}^\top. \quad (9)$$

If a stationary quantity \underline{x} is estimated as the mean of n repeated measurements \underline{x}_i , type A evaluation of uncertainty is carried out as follows

$$u_A(x_{\text{re}}, x_{\text{im}}) = \frac{1}{n(n-1)} \sum_{i=1}^n (x_{\text{re}} - x_{i\text{re}})(x_{\text{im}} - x_{i\text{im}}), \quad (10)$$

$[u_A(x_{\text{re}})]^2 = u_A(x_{\text{re}}, x_{\text{re}})$, and $[u_A(x_{\text{im}})]^2 = u_A(x_{\text{im}}, x_{\text{im}})$. If systematic errors are present in the measurement, type B uncertainties $u_B(x_{\text{re}})$, $u_B(x_{\text{im}})$, etc. are also evaluated [7]. If both types of

uncertainties are included, the resulting covariances are added so that

$$\mathbf{C}(\underline{x}) = \mathbf{C}_A(\underline{x}) + \mathbf{C}_B(\underline{x}). \quad (11)$$

The procedure of estimating a quantity \underline{Y} from the measurements of n quantities $\underline{X}_1, \underline{X}_2, \dots, \underline{X}_n$ can be expressed as [7]

$$\underline{Y} = f(\underline{X}_1, \underline{X}_2, \dots, \underline{X}_n). \quad (12)$$

An estimated value of \underline{Y} is then given as

$$\underline{y} = f(\underline{x}_1, \underline{x}_2, \dots, \underline{x}_n). \quad (13)$$

As the quantity of interest is estimated from a number of measured quantities, the propagation of uncertainties has to be analysed. The propagated uncertainties can be found from the covariance matrix of \underline{y} , computed as [5]

$$\mathbf{C}(\underline{y}) = \sum_{k=1}^n \sum_{l=1}^n \mathbf{W}(\underline{x}_k) \mathbf{R}(\underline{x}_k, \underline{x}_l) \mathbf{W}(\underline{x}_l)^T, \quad (14)$$

where

$$\begin{aligned} \mathbf{W}(\underline{x}_k) &= \mathbf{J}_y(\underline{x}_k) \mathbf{U}(\underline{x}_k) \\ &= \begin{bmatrix} \frac{\partial y_{re}}{\partial x_{kre}} & \frac{\partial y_{re}}{\partial x_{kim}} \\ \frac{\partial y_{im}}{\partial x_{kre}} & \frac{\partial y_{im}}{\partial x_{kim}} \end{bmatrix} \begin{bmatrix} u(x_{kre}) & 0 \\ 0 & u(x_{kim}) \end{bmatrix} \end{aligned} \quad (15)$$

and

$$\mathbf{R}(\underline{x}_k, \underline{x}_l) = \begin{bmatrix} r(x_{kre}, x_{lre}) & r(x_{kre}, x_{lim}) \\ r(x_{kim}, x_{lre}) & r(x_{kim}, x_{lim}) \end{bmatrix}, \quad (16)$$

which holds the correlations between the components of \underline{x}_k and \underline{x}_l .

The evaluation of Jacobians can be carried out based on the following notion [5]

$$\frac{\partial \underline{y}}{\partial \underline{x}} = \underline{z} \Rightarrow \mathbf{J}_y(\underline{x}) = \begin{bmatrix} z_{re} & -z_{im} \\ z_{im} & z_{re} \end{bmatrix}, \quad (17)$$

which simplifies the process in some cases.

For a certain confidence level p , the coverage factors $k_{2,p}$ are evaluated and the uncertainties given as follows

$$U_p(Y_{re}) = k_{2,p} u(y_{re}) = k_{2,p} \sqrt{\mathbf{C}_{11}(\underline{y})}, \quad (18)$$

$$U_p(Y_{im}) = k_{2,p} u(y_{im}) = k_{2,p} \sqrt{\mathbf{C}_{22}(\underline{y})}. \quad (19)$$

The coverage factors for 2-dimensional quantities have been treated in the above-referred sources [7].

The uncertainty of a measurement originates from different sources of error, which can be either random or systematic. Random errors are different in each repeated measurement and their effects can be reduced by increasing the number of independent repeated measurements. Resulting combined uncertainties can be evaluated by propagating the type A estimates of uncertainties, as in (10), etc. However, it should be noted that repeated measurements can only decrease the uncertainty when estimating a stationary quantity, not a quantity that changes in time.

Sometimes a measurement deviates from the correct value by a systematic error, which cannot be removed by repeated measurements. In general, such systematic effects should be identified and compensated for; however, this requires knowledge of appropriate correction factors, which is not always available [3, 9]. If systematic effects are not corrected for, type A evaluation would underestimate the resulting uncertainties. In this work, type B evaluation of uncertainties is applied in order to account for systematic effects that cannot be removed.

3 Uncertainties of estimates

3.1 Transmission Losses on a Line

The measured amount of transmission losses across the line can be described as

$$\begin{aligned} \underline{\Delta S} &= \underline{S}_1 - \underline{S}_2 = \underline{V}_{a1} \underline{I}_{a1}^* + \underline{V}_{b1} \underline{I}_{b1}^* + \underline{V}_{c1} \underline{I}_{c1}^* \\ &\quad - \underline{V}_{a2} \underline{I}_{a2}^* - \underline{V}_{b2} \underline{I}_{b2}^* - \underline{V}_{c2} \underline{I}_{c2}^*, \end{aligned} \quad (20)$$

where * denotes the complex conjugate, the numbers in subscripts stand for the two ends of the line and letters stand for phases. The estimate of transmission losses is expressed as

$$\begin{aligned} \underline{\Delta S} &= \underline{\Delta s}_a + \underline{\Delta s}_b + \underline{\Delta s}_c = \underline{v}_{a1} \underline{i}_{a1}^* + \underline{v}_{b1} \underline{i}_{b1}^* + \underline{v}_{c1} \underline{i}_{c1}^* \\ &\quad - \underline{v}_{a2} \underline{i}_{a2}^* - \underline{v}_{b2} \underline{i}_{b2}^* - \underline{v}_{c2} \underline{i}_{c2}^* \end{aligned} \quad (21)$$

where

$$\begin{aligned} \underline{\Delta s}_a &= \underline{v}_{a1} \underline{i}_{a1}^* - \underline{v}_{a2} \underline{i}_{a2}^* \\ &= \underline{v}_{a1re} (\underline{i}_{a1}^*)_{re} - \underline{v}_{a1im} (\underline{i}_{a1}^*)_{im} + j \underline{v}_{a1re} (\underline{i}_{a1}^*)_{im} + j \underline{v}_{a1im} (\underline{i}_{a1}^*)_{re} \\ &\quad - \underline{v}_{a2re} (\underline{i}_{a2}^*)_{re} + \underline{v}_{a2im} (\underline{i}_{a2}^*)_{im} - j \underline{v}_{a2re} (\underline{i}_{a2}^*)_{im} - j \underline{v}_{a2im} (\underline{i}_{a2}^*)_{re} \\ &= \underline{v}_{a1re} \underline{i}_{a1re} + \underline{v}_{a1im} \underline{i}_{a1im} - j \underline{v}_{a1re} \underline{i}_{a1im} + j \underline{v}_{a1im} \underline{i}_{a1re} \\ &\quad - \underline{v}_{a2re} \underline{i}_{a2re} - \underline{v}_{a2im} \underline{i}_{a2im} + j \underline{v}_{a2re} \underline{i}_{a2im} - j \underline{v}_{a2im} \underline{i}_{a2re}, \quad \text{etc.} \end{aligned} \quad (22)$$

Here the components of voltage and current phasors are the quantities measured by PMUs.

In order to ensure that the functions analysed in uncertainty propagation are holomorphic (and differentiable) the complex conjugate of current is assumed to be the measured quantity. This means that losses are seen as a function of measured voltage and current, where the complex conjugate representation of current is assumed, i.e. $\underline{\Delta s}_a = f(\underline{v}_{a1}, \underline{i}_{a1}^*, \underline{v}_{a2}, \underline{i}_{a2}^*)$, etc. These functions are differentiable with respect to $\underline{v}_{a1}, \underline{i}_{a1}^*, \underline{v}_{a2}, \underline{i}_{a2}^*$, etc. and satisfy the Cauchy–Riemann equations.

Uncertainties of type A are simply calculated following (10) to form covariance matrices $\mathbf{C}_A(\underline{v}_{a1})$, $\mathbf{C}_A(\underline{i}_{a1}^*)$, etc. In order to account for systematic effects, uncertainties of type B have to be evaluated with some assumed levels of systematic errors. Since the true systematic errors are not known, this can only be an estimate based on information about measurement devices that is available. Systematic errors should be assumed to be large enough to account for real errors yet still small enough to obtain meaningful uncertainty intervals.

With an uncalibrated instrument transformer, the systematic error for a certain value of the measured quantity can be as high as the maximum error permitted in the respective accuracy class. However, if more information is available, e.g. factory test reports, more refined assumptions of systematic errors can be made. In the standard, the maximum measurement errors of PMUs are only limited by the total vector error (TVE), which does not distinguish between different errors in different dimensions [14]. However, in most cases manufacturers report separate magnitude and angle errors, which can be used in the analysis. If only a limit on TVE is given, a judgement has to be made how large the share of magnitude and phase errors could be in this TVE limit.

Type B uncertainties in the measurements of voltage and current magnitudes are obtained by taking the product of the measured value and the combined relative errors of instrument transformers and PMUs; for angle measurements the absolute errors are combined

so that [3]

$$u_B(v_m) = v_m \sqrt{[\varepsilon_{rVT}]^2 + [\varepsilon_{vPMU}]^2} / k_p, \quad (23a)$$

$$u_B(v_\phi) = \sqrt{[\varepsilon_{pVT}]^2 + [\varepsilon_{pPMU}]^2} / k_p, \quad (23b)$$

$$u_B(i_m^*) = u_B(i_m) = i_m \sqrt{[\varepsilon_{rCT}(i_m)]^2 + [\varepsilon_{cPMU}]^2} / k_p, \quad (23c)$$

$$u_B(i_\phi^*) = u_B(i_\phi) = \sqrt{[\varepsilon_{pCT}(i_m)]^2 + [\varepsilon_{pPMU}]^2} / k_p, \quad (23d)$$

where ε_{rVT} and ε_{rCT} are the ratio errors and ε_{pVT} and ε_{pCT} the phase errors introduced in the voltage and current transformers according to their accuracy classes [15, 16]; ε_{vPMU} , ε_{cPMU} and ε_{pPMU} denote the voltage, current and phase measurement errors in the PMU.

How these errors are reported, depends on the manufacturer, but here they are assumed to be the uncertainties of the measured quantities at a confidence level p so that k_p is the corresponding 1-D coverage factor [3, 7]. The evaluated uncertainties are then transformed into the complex plane by Eqs. (7)–(9), assuming the measurement of magnitude and angle are independent of each other ($r_t = 0$).

There is no physical correlation between the magnitude and angle of a current phasor. However, the ratio and phase errors in the current transformer accuracy class vary with primary current and are, as such, dependent on the magnitude of measured current.

The voltage and current measurements are also assumed to be independent, i.e. all the correlations between voltage and current components are zero

$$r(v_{re}, i_{re}) = 0, \quad \text{etc.}$$

Thus, there are only two non-zero correlation matrices per every pair of phase voltage and current v_{a1} , i_{a1}^* , etc.

$$\mathbf{R}(v) = \begin{bmatrix} 1 & r(v_{re}, v_{im}) \\ r(v_{im}, v_{re}) & 1 \end{bmatrix} \quad (24)$$

and an equivalent for any current estimate i or i^* . The uncertainty matrices are formed as

$$\mathbf{U}(v) = \begin{bmatrix} u(v_{re}) & 0 \\ 0 & u(v_{im}) \end{bmatrix} \quad (25)$$

and again, an equivalent for a current i or i^* .

The elements of these four matrices are readily calculable from the elements of $\mathbf{C}(v)$, etc.

$$u(v_{re}) = \sqrt{\mathbf{C}_{11}(v)}, \quad (26)$$

$$u(v_{im}) = \sqrt{\mathbf{C}_{22}(v)}, \quad (27)$$

$$r(v_{re}, v_{im}) = \frac{\mathbf{C}_{12}(v)}{u(v_{re})u(v_{im})}, \quad (28)$$

where the indices specify an element of the matrix by the row and column numbers [13]. The covariance matrices include both type A and B uncertainties, i.e. $\mathbf{C}(v) = \mathbf{C}_A(v) + \mathbf{C}_B(v)$, if both are evaluated. The same applies to every voltage and current phasor v_{a1} , i_{a1}^* , etc.

For the propagation of uncertainties, the Jacobians are found as

$$\mathbf{J}_{\underline{\Delta s}}(v_{a1}) = \begin{bmatrix} \frac{\partial \Delta s_{re}}{\partial v_{a1re}} & \frac{\partial \Delta s_{re}}{\partial v_{a1im}} \\ \frac{\partial \Delta s_{im}}{\partial v_{a1re}} & \frac{\partial \Delta s_{im}}{\partial v_{a1im}} \end{bmatrix} = \begin{bmatrix} i_{a1re} & i_{a1im} \\ -i_{a1im} & i_{a1re} \end{bmatrix}, \quad (29)$$

$$\mathbf{J}_{\underline{\Delta s}}(i_{a1}^*) = \begin{bmatrix} \frac{\partial \Delta s_{re}}{\partial (i_{a1}^*)_{re}} & \frac{\partial \Delta s_{re}}{\partial (i_{a1}^*)_{im}} \\ \frac{\partial \Delta s_{im}}{\partial (i_{a1}^*)_{re}} & \frac{\partial \Delta s_{im}}{\partial (i_{a1}^*)_{im}} \end{bmatrix} = \begin{bmatrix} v_{a1re} & -v_{a1im} \\ v_{a1im} & v_{a1re} \end{bmatrix}, \quad (30)$$

$$\mathbf{J}_{\underline{\Delta s}}(v_{a2}) = \begin{bmatrix} -i_{a2re} & -i_{a2im} \\ i_{a2im} & -i_{a2re} \end{bmatrix}, \quad (31)$$

$$\mathbf{J}_{\underline{\Delta s}}(i_{a2}^*) = \begin{bmatrix} -v_{a2re} & v_{a2im} \\ -v_{a2im} & -v_{a2re} \end{bmatrix}, \text{ etc.} \quad (32)$$

The uncertainties $u(\Delta s_{re})$ and $u(\Delta s_{im})$ can then be extracted from the covariance matrix, computed as

$$\mathbf{C}(\underline{\Delta s}) = \mathbf{C}(\underline{\Delta s}_a) + \mathbf{C}(\underline{\Delta s}_b) + \mathbf{C}(\underline{\Delta s}_c), \quad (33)$$

where

$$\begin{aligned} \mathbf{C}(\underline{\Delta s}_a) &= \mathbf{J}_{\underline{\Delta s}}(v_{a1})\mathbf{U}(v_{a1})\mathbf{R}(v_{a1})[\mathbf{J}_{\underline{\Delta s}}(v_{a1})\mathbf{U}(v_{a1})]^\top \\ &+ \mathbf{J}_{\underline{\Delta s}}(i_{a1}^*)\mathbf{U}(i_{a1}^*)\mathbf{R}(i_{a1}^*)[\mathbf{J}_{\underline{\Delta s}}(i_{a1}^*)\mathbf{U}(i_{a1}^*)]^\top \\ &+ \mathbf{J}_{\underline{\Delta s}}(v_{a2})\mathbf{U}(v_{a2})\mathbf{R}(v_{a2})[\mathbf{J}_{\underline{\Delta s}}(v_{a2})\mathbf{U}(v_{a2})]^\top \\ &+ \mathbf{J}_{\underline{\Delta s}}(i_{a2}^*)\mathbf{U}(i_{a2}^*)\mathbf{R}(i_{a2}^*)[\mathbf{J}_{\underline{\Delta s}}(i_{a2}^*)\mathbf{U}(i_{a2}^*)]^\top, \end{aligned} \quad (34)$$

etc.

Similarly to the above, the uncertainty of estimating the power at one end of the line can be computed. Instead of the difference in (21) the power at one end is evaluated, the Jacobians in (29)–(30) are applied, etc.

3.2 Parameters of a Transmission Line

As described in Sec. 2.1, the impedance and admittance of a transposed transmission line can be estimated as

$$\underline{z} = \underline{\gamma}z_c, \quad (35)$$

$$\underline{y} = \frac{\underline{\gamma}}{z_c}, \quad (36)$$

where

$$\underline{\gamma} = \frac{\text{arcosh}(p)}{L}, \quad (37)$$

$$z_c = \frac{v_2 \sqrt{(p+1)(p-1)}}{i_1 - i_2 p}, \quad (38)$$

$$p \equiv \frac{q}{t} \equiv \frac{v_1 i_1 + v_2 i_2}{v_2 i_1 + v_1 i_2}.$$

The quantities p , q , and t have been introduced to shorten the notation. Here it is assumed that $q = f(v_1, i_1, v_2, i_2)$ and $t = f(v_1, i_1, v_2, i_2)$ are functions of complex representations of measured voltages and currents. These and other terms expressed using q and t are differentiable with respect to v_1 , i_1 , v_2 , and i_2 and satisfy the Cauchy–Riemann equations.

Once again, the uncertainties of current and voltage measurements can be handled by Eqs. (10) and (23)–(28). This leaves the

Jacobians to be found. The differentiation can be handled as follows

$$\forall \underline{x} \in \{v_1, v_2, i_1, i_2\} : \quad \frac{\partial z}{\partial \underline{x}} = z_c \frac{\partial \gamma}{\partial \underline{x}} + \gamma \frac{\partial z_c}{\partial \underline{x}}, \quad (39)$$

$$\frac{\partial y}{\partial \underline{x}} = \frac{1}{z_c} \frac{\partial \gamma}{\partial \underline{x}} - \frac{\gamma}{z_c^2} \frac{\partial z_c}{\partial \underline{x}}, \quad (40)$$

$$\frac{\partial \gamma}{\partial \underline{x}} = \frac{\partial p / \partial \underline{x}}{L \sqrt{(p+1)(p-1)}}, \quad (41)$$

$$\frac{\partial z_c}{\partial \underline{x}} = \frac{v_2 p (\partial p / \partial \underline{x}) + (\partial v_2 / \partial \underline{x}) (p+1)(p-1)}{\sqrt{(p+1)(p-1)} (i_1 - i_2 p)} - \frac{v_2 \sqrt{(p+1)(p-1)}}{(i_1 - i_2 p)^2} \left(\frac{\partial i_1}{\partial \underline{x}} - p \frac{\partial i_2}{\partial \underline{x}} - i_2 \frac{\partial p}{\partial \underline{x}} \right), \quad (42)$$

$$\frac{\partial p}{\partial \underline{x}} = \frac{1}{i_2^2} \left(t \frac{\partial q}{\partial \underline{x}} - q \frac{\partial t}{\partial \underline{x}} \right), \quad (43)$$

where the derivatives by the measured quantities are

$$\frac{\partial q}{\partial v_1} = i_1, \quad \frac{\partial t}{\partial v_1} = i_2, \quad (44a,b)$$

$$\frac{\partial q}{\partial v_2} = i_2, \quad \frac{\partial t}{\partial v_2} = i_1, \quad (44c,d)$$

$$\frac{\partial q}{\partial i_1} = v_1, \quad \frac{\partial t}{\partial i_1} = v_2, \quad (44e,f)$$

$$\frac{\partial q}{\partial i_2} = v_2, \quad \frac{\partial t}{\partial i_2} = v_1. \quad (44g,h)$$

The Jacobians are found by the procedure introduced in Eq. (17)

$$\forall \underline{x} \in \{v_1, v_2, i_1, i_2\} : \quad \mathbf{J}_z(\underline{x}) = \begin{bmatrix} \left(\frac{\partial z}{\partial \underline{x}} \right)_{re} & - \left(\frac{\partial z}{\partial \underline{x}} \right)_{im} \\ \left(\frac{\partial z}{\partial \underline{x}} \right)_{im} & \left(\frac{\partial z}{\partial \underline{x}} \right)_{re} \end{bmatrix}, \quad (45)$$

$$\mathbf{J}_y(\underline{x}) = \begin{bmatrix} \left(\frac{\partial y}{\partial \underline{x}} \right)_{re} & - \left(\frac{\partial y}{\partial \underline{x}} \right)_{im} \\ \left(\frac{\partial y}{\partial \underline{x}} \right)_{im} & \left(\frac{\partial y}{\partial \underline{x}} \right)_{re} \end{bmatrix}. \quad (46)$$

This leads to the covariance matrices

$$\mathbf{C}(z) = \sum_{\underline{x} \in \{v_1, v_2, i_1, i_2\}} \mathbf{J}_z(\underline{x}) \mathbf{U}(\underline{x}) \mathbf{R}(\underline{x}) [\mathbf{J}_z(\underline{x}) \mathbf{U}(\underline{x})]^T, \quad (47)$$

$$\mathbf{C}(y) = \sum_{\underline{x} \in \{v_1, v_2, i_1, i_2\}} \mathbf{J}_y(\underline{x}) \mathbf{U}(\underline{x}) \mathbf{R}(\underline{x}) [\mathbf{J}_y(\underline{x}) \mathbf{U}(\underline{x})]^T, \quad (48)$$

which hold information about the uncertainties $u(z_{re})$, $u(z_{im})$, $u(y_{re})$, and $u(y_{im})$ of the impedance and admittance estimates.

If ideal transposition is assumed, positive sequence impedance becomes the mean of three phase quantities, i.e.

$$\bar{z}_+ = (z_a + z_b + z_c) / 3 \quad (49)$$

the covariances become

$$\mathbf{C}(\bar{z}_+) = \mathbf{C}(z_a) + \mathbf{C}(z_b) + \mathbf{C}(z_c), \quad (50)$$

where

$$\mathbf{C}(z_a) = \sum_{\underline{x} \in \{v_{a1}, v_{a2}, i_{a1}, i_{a2}\}} (\mathbf{J}_z(\underline{x}) / 3) \mathbf{U}(\underline{x}) \mathbf{R}(\underline{x}) [(\mathbf{J}_z(\underline{x}) / 3) \mathbf{U}(\underline{x})]^T, \quad (51)$$

etc.

4 Experimental results

A 330 kV overhead transmission line, approximately 200 km long, in the Estonian power system was observed in the example measurements and calculations. The line is equipped with PMUs at both substations and its impedance has recently been measured with an off-line method and is available for reference. The PMUs are connected to voltage transformers of class 0.2 and current transformers of class 0.2S in one substation and instrument transformers of respective classes 0.5 and 0.5S at the other end. The CTs are rated at 1 kA and 2 kA, respectively. The PMUs installed in the system are identical and have an 0.01° angle measurement error, 0.03% current and 0.02% voltage magnitude relative measurement error, reported by the manufacturer.

None of the instrument transformers at either end of the line have been calibrated since they were commissioned. There is some information about their measurement accuracy from factory test reports, which give errors for a few operating points with two different burden values. The burdens of one set of current transformers are expected to be close to one of the tested values, in other cases, burdens are far smaller than the lowest tested value. While it is reasonable to interpolate between the given operating points (ratio of measured and rated voltage or current), it is difficult to assume that errors for real burden values can be found by extrapolating [17]. Thus, despite having this information, it is difficult to determine actual measurement errors and remove these systematic errors without introducing new ones. However, this information is useful in the uncertainty analysis as it gives a better understanding how measurement errors change with changes in current and voltage.

In the presented results, two uncertainty ranges are given for each measured quantity. In both cases, PMU errors reported by the manufacturer are used. In one case, instrument transformer errors are assumed to be as large as permitted in their accuracy class by the standards (referred to as accuracy class errors) [15, 16]. The correct values of monitored quantities should fall in these intervals as long as transformers comply to standards. In the other case, instrument transformer errors are based on manufacturer reported error data and the estimated values of burden. Based on these data, approximate instrument transformer errors are evaluated for all measurements (approximated reported errors). Because these errors are close to actual errors, either the higher or lower uncertainty bound of each quantity should be close to the correct value. Reported errors of all instrument transformers and estimated values of burden are presented in Appendix 9. In this work, time synchronization errors are assumed to be included in the angle errors. An 0.95 confidence level is assumed so that $k_p = 1.96$ and $k_{2,p} = 2.45$ [7].

In the monitoring of transmission lines based on PMU measurements, there are certain quantities that could be considered stationary, e.g. the reactance of a line, while others change in time. The various quantities change in time at different rates and if consecutive measurements are averaged, this rate of change has to be considered. Another aspect explained earlier is that the uncertainties resulting from systematic effects are not affected by averaging of repeated measurements. In the following figures, only the uncertainty intervals considering systematic errors are plotted. In this form, it can be seen from the data how the magnitudes of systematic errors compare to the extent of changes in time and random fluctuations. As the plots display, the extent of any random fluctuations is very well observable, while the average values in different periods are also visually apparent.

Measurements have been taken and analysed from a 14 hour period so that various changes in load and other possible factors would be present. Since the measurement period is long, not all acquired data points can be plotted legibly. Thus, the estimated values of monitored quantities without any averaging (based on single simultaneous measurements) are presented in 20 second steps instead. During the measurement period, the average ambient temperature varied in the range of $0-5^\circ\text{C}$ and average wind velocity was between 1–6 m/s. Measured load and hourly weather data were used to adjust the reference resistance to thermal conditions according to the IEEE and CIGRE guidelines [18, 19].

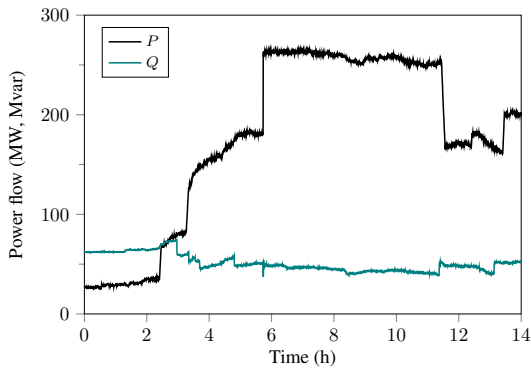


Fig. 2: Power transmitted over the line during the measurement period. Receiving end power plotted as real and imaginary components of total apparent power measured by the PMU.

Power flow measured at one end of the line is plotted in Fig. 2; presented results show the values of active and reactive power summed over the measured phases. Uncertainties were also evaluated; however they were two orders of magnitude smaller than the measured quantities and cannot be distinguished in the graph. Based on accuracy class errors, relative uncertainties were in the 0.5%–1.5% range, based on approximated reported errors, the relative uncertainty was around 0.4% throughout the period. The changes in active transmitted power are closely aligned with changes in current on the line, while reactive power follows changes in voltage. It should be noted that both random measurement errors and random fluctuations of load and other quantities are present in the data.

4.1 Estimation of Transmission Losses

Total active transmission losses on the line and the corresponding measurement uncertainty are presented in Fig. 3. Losses were calculated as the difference in sent and received power according to (21) and uncertainties with (23)–(33). It can be seen that the uncertainty of measurement was in the same order of magnitude as the measured values themselves and considerably larger than the extent of any random fluctuations. Relative uncertainties based on accuracy class errors ranged between 40–80%, while relative uncertainties based on approximated reported errors were around 30–40%. At higher levels

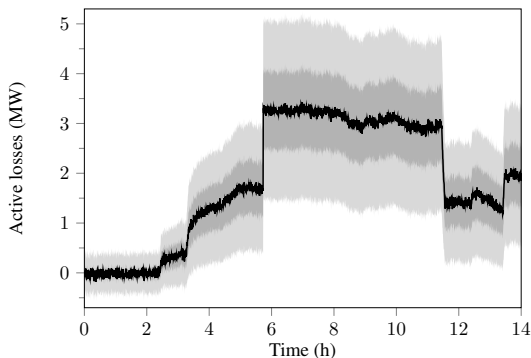


Fig. 3: Measured active power losses and the two uncertainty regions, depicted as black line and two filled grey areas, respectively. Lighter grey corresponds to uncertainties based on accuracy class errors and darker grey to uncertainties based on approximated reported errors. Total active losses are given as the difference of sent and received power measured by the PMUs.

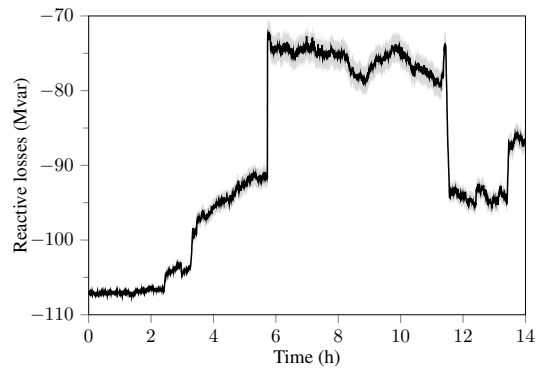


Fig. 4: Measured reactive power losses and their uncertainty, depicted as black line and filled grey area, respectively. Uncertainties based on accuracy class errors are shown, the uncertainty region based on approximated reported errors was too narrow to be distinguishable. Total reactive losses are given as the difference of sent and received power measured by the PMUs.

of measured active losses (or current), the evaluated uncertainties increased in absolute terms. However, in relative terms, they tended to be slightly lower. It is important to note that active losses are computed as the difference of two close values, i.e. active power at either end of the line.

Total reactive transmission losses on the line and the corresponding measurement uncertainties are presented in Fig. 4. Losses were calculated as the difference in sent and received power. Uncertainties based on accuracy class errors were significantly higher than uncertainties based on approximated reported errors; the latter are indiscernible in plotted data. The accuracy class error based uncertainty was an order of magnitude smaller than the measured values and in the same order of magnitude as random fluctuations in time. At higher loading of the line, the evaluated uncertainties increased in absolute terms. However, like with active losses, relative uncertainties did not necessarily increase with higher load.

4.2 Estimation of Line Parameters

Estimated values of line resistance and reactance and their uncertainties are given in Fig. 5 and Fig. 6. The impedance components were computed as the mean of the resistance and reactance of each of the phases as in (49), assuming an ideally balanced line, and uncertainties according to (23) and (47). For comparison the reference values from an off-line measurement are given. The value of reference resistance has been adjusted according to weather measurement data. The reference measurement of line impedance has a typical error of 0.5% in reactance and 10% in resistance. The reference value is an average of separate measurements made on phase conductors, carried out with special equipment.

The measured value of resistance presents large systematic measurement errors. The estimate deviates greatly from the reference value and displays larger changes in time than expected. However, the measurement also has large uncertainties and the resulting uncertainty intervals contain the reference value. The lower bound of uncertainties based on approximated reported errors approaches the reference value of resistance. The measured value of reactance is close to the reference and its uncertainty is relatively smaller than the uncertainty of resistance. The uncertainties of both quantities decrease when the load on the line increases. At higher loading of the line, there is a significant difference between uncertainties of reactance based on accuracy class errors and based on approximated reported errors. At higher loading of the line, uncertainties based on approximated reported errors become small enough that the uncertainty interval no longer includes the reference measurement.

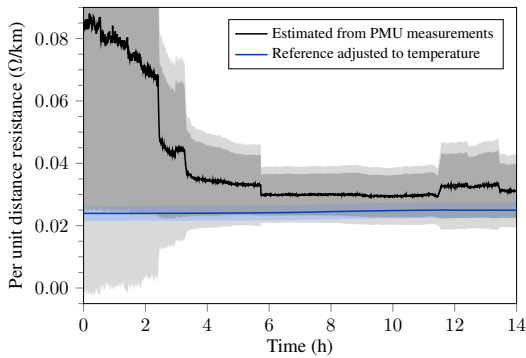


Fig. 5: Positive sequence resistance estimated from PMU measurement data and the two uncertainty regions, depicted as black line and two filled grey areas, respectively. Lighter grey corresponds to uncertainties based on accuracy class errors and darker grey to uncertainties based on approximated reported errors. Measured reference resistance adjusted according to line load and weather data given for comparison, blue line and error interval.

The lower bound of uncertainties of reactance based on approximated reported errors shows a reasonably stable value throughout the measurement period, but still includes some sudden variations.

Estimated values of shunt conductance and susceptance and their uncertainties are given in Fig. 7 and Fig. 8. Similarly to impedance, the admittances are computed as mean values of phase quantities. However, for these measurements there are no reference values available for comparison. The negative values of shunt conductance also indicate measurement errors, since the correct values could not be negative. The higher bound of uncertainties of conductance based on approximated reported errors shows a rather stable value throughout the measurement period and approaches zero. In shunt admittance measurements there is a significant difference between uncertainties based on accuracy class errors and uncertainties based on approximated reported errors. While the former greatly increase with higher load on the line, the latter show minimal dependence on loading of the line.

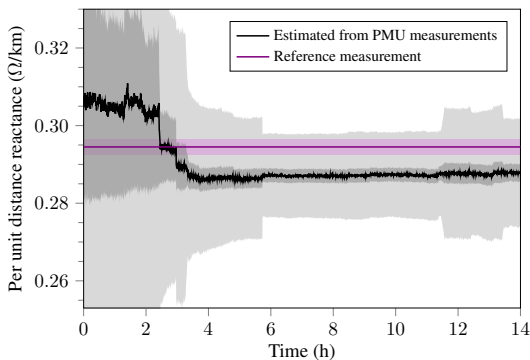


Fig. 6: Positive sequence reactance estimated from PMU measurement data and the two uncertainty regions, depicted as black line and two filled grey areas, respectively. Lighter grey corresponds to uncertainties based on accuracy class errors and darker grey to uncertainties based on approximated reported errors. Measured reference reactance given for comparison as a purple line and error interval.

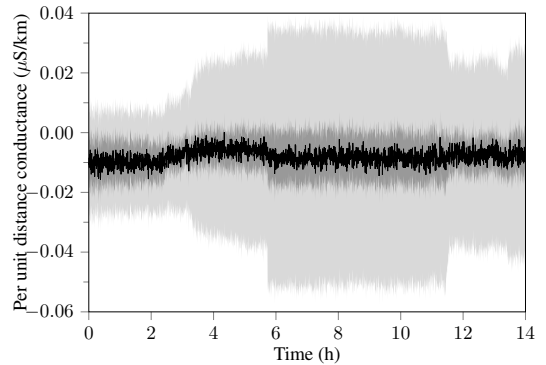


Fig. 7: Positive sequence shunt conductance estimated from PMU measurement data and the two uncertainty regions, depicted as black line and two filled grey areas, respectively. Lighter grey corresponds to uncertainties based on accuracy class errors and darker grey to uncertainties based on approximated reported errors.

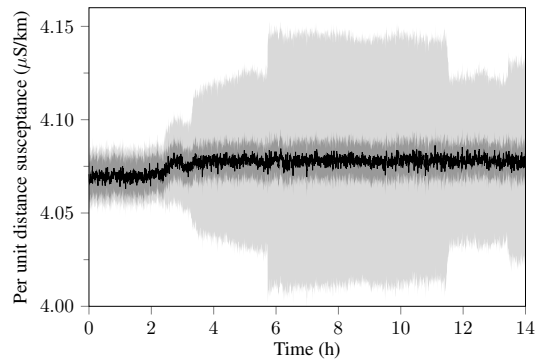


Fig. 8: Positive sequence shunt susceptance estimated from PMU measurement data and the two uncertainty regions, depicted as black line and two filled grey areas, respectively. Lighter grey corresponds to uncertainties based on accuracy class errors and darker grey to uncertainties based on approximated reported errors.

5 Discussion

The experimental results presented active and reactive transmission losses, line parameters and the uncertainties of monitoring these quantities based on PMU measurements. Two different uncertainty ranges were evaluated for each quantity, one assuming instrument transformer errors based on their accuracy classes, the other assuming approximations of measurement errors reported by manufacturers of instrument transformers. It can be observed how both the changes in certain estimated quantities and their uncertainties change with variations in active and reactive power, corresponding to variations in current and voltage (Fig 2). Some of these are clearly expected, e.g. changes in losses, while others are not, e.g. sudden variations in line parameters.

As expected, there were no problems with measuring power at one end of a transmission line. Assuming the devices do not exceed specified measurement error limits, both active and reactive power can be determined with relatively high confidence. Relative uncertainties were in the range of 0.4%–1.5%, which is close to the measurement errors allowed for instrument transformers. When looking at transmission losses as the difference of sent and received power, confidence in estimates decreases significantly. This is especially true with active power losses, which themselves range from close to 0

up to 3.3 MW, with uncertainties up to 1.8 MW. This is a common problem in estimating any quantity that is found as the difference of two close values, which in this case is active power at each end. There were differences between the two different uncertainty ranges; however, both changed similarly with changes in loading of the line.

The parameters of a transmission line are generally expected to change little in time. The resistance of conductors does change with temperature, increasing approximately 3–5% with a 10 °C increase in temperature, while inductance and capacitance are expected to change less. A larger current would contribute to the gradual heating of a conductor with a time constant of a few minutes. Shunt conductance differs from other parameters, as it is instead a way to represent active losses that are not dissipated as heat in the resistance. However, neither resistance, reactance, nor susceptance are expected to change in steps, as instant changes corresponding to varying current or voltage. The positive sequence line model is a simplification that can affect the results to some extent, but it is a very well established model and its behaviour in normal operating conditions is expected to be very predictable.

The major share of changes in time seen in the presented results of estimated line parameters could not be physically correct and are assumed to be caused by measurement inaccuracy instead. The calculated uncertainties considering the possible extent of measurement errors support this assumption. The uncertainties based on approximated reported errors assume errors that are close to true values and their lower bounds showed more reasonable values for both resistance and reactance throughout the measurement period. However, even there some sudden variations were still present, corresponding to changes in voltage and current. The estimated reactance was around 3% lower than the reference. The narrower uncertainty interval may underestimate some systematic errors; at the same time, the reference value of line impedance was obtained with a different measurement technique, which could also explain a small difference.

In the estimate of resistance, it can be seen that the values were closer to the expected true value only at higher loading of the line, i.e. with larger measured current. The estimate of reactance differed from the reference value most of the time, but was more stable at higher loading of the line. Both uncertainty regions for both resistance and reactance became narrower as the loading of the line increased, indicating a dependence on current. As seen in Appendix 9, current magnitude errors vary little with varying current, while current angle errors increase significantly with lower measured current. Thus, estimates of reactance are especially influenced by current angle errors. Estimates of resistance also improved at higher loading of the line, because current transformers are more accurate when they are measuring a current closer to the rated value. However, there were still significant errors present. This is mostly because the impedance of the line essentially determines the voltage drop across it and voltage drop is once again a difference of two close values. Also, reported voltage magnitude errors are also the ones closest to accuracy class limits.

Correct shunt parameters are not known and it is difficult to determine whether they were more accurate at higher or lower loading of the line. Here it is especially important to compare the two different uncertainty intervals. While uncertainties based on accuracy class errors would indicate that confidence in the measurements decreases with higher loading of the line, uncertainties based on approximated reported errors do not show this. In fact, throughout the measurement period uncertainties based on approximated reported errors remained nearly constant. In case of conductances, the higher bound of uncertainties based on approximated reported errors was also close to zero. These uncertainty estimates may underestimate some of the systematic errors, but they demonstrate that accuracy class errors clearly overestimate the uncertainty of shunt parameters at higher loading of the line.

The study revealed apparent measurement errors in both the estimated resistance and reactance of the line. At the same time, the possibility of such inaccuracies were indicated by the presented analysis of uncertainty propagation. It can also be seen that if more accurate estimates of these quantities were needed, either calibration or replacement of the instrument transformers would be required (generally, over-dimensioning of current transformers and burdens

outside the prescribed range should be avoided if more accurate PMU measurements are desired). In general, such uncertainty analyses provide useful information about the confidence that can be had in the obtained results and help to understand the causes of estimation errors. Similar analyses would be encouraged when monitoring tools based on PMU measurements are being developed and deployed.

The standard for PMUs only limits the accuracy of phasors to 1% total vector error (TVE) [14]. This has two different but important implications in the context of transmission line monitoring and uncertainty analysis. If a PMU did indeed have errors as large as 1% in the measured phasors, the accuracy of the discussed applications would be significantly poorer and the errors could be several times larger than seen in the examples. Moreover, since TVE does not distinguish between magnitude and phase errors, it is also difficult to analyse uncertainties in phasors and complex quantities derived from phasors based on this information. If the accuracy of a PMU was given as a TVE limit, it would have to be separated into magnitude error and phase error components that would result in this TVE, but the share of either component would be unknown. Assuming errors corresponding to 1% TVE in the uncertainty analysis would result in uncertainty intervals several times wider than seen in the examples.

6 Conclusions

The presented work served three main objectives: firstly, to demonstrate the accuracy—or lack thereof—of transmission line monitoring applications based on PMU measurements enabled by common metering instrument transformers. Secondly, to explain the sources of these inaccuracies and their dependence on different instrument transformer errors. Thirdly, to demonstrate the applicability and usefulness of analysing uncertainty propagation in terms of complex quantities in phasor measurement applications. It was seen that clear measurement errors are present in the results. The uncertainty analysis helped to understand how the errors of measuring voltages and currents are propagated into the estimates. It was also shown that the principles of analysing uncertainty propagation in complex quantities apply well and provide useful information about the confidence in obtained results.

The analysis gave a thorough overview of how these monitoring applications are affected by measurement errors, what accuracy can be expected, and under which conditions certain estimates become more accurate. In estimates of power and transmission losses, uncertainties are similar under various operating conditions. Power flow and reactive power balance can be monitored quite accurately, while active losses have large but rather constant relative uncertainties. The impedance of a line can be monitored better when the loading of the line is larger, but acceptable resistance estimates require significantly higher measurement accuracy in any case. Shunt admittance parameters are difficult to verify, but their uncertainties based on approximated reported errors were not very large and behaved similarly under varying operating conditions.

7 Acknowledgement

This work has been mainly sponsored by the Estonian TSO, Elering, with additional support from the STRONgrid research project and Tallinn University of Technology research grant B22. Weather data from the Estonian Environmental Agency has been used in this work.

8 References

- 1 S. Chakrabarti and E. Kyriakides, "PMU measurement uncertainty considerations in WLS state estimation," *Power Systems, IEEE Transactions on*, vol. 24, no. 2, pp. 1062–1071, May 2009.
- 2 S. Chakrabarti, E. Kyriakides, and M. Albu, "Uncertainty in power system state variables obtained through synchronized measurements," *Instrumentation and Measurement, IEEE Transactions on*, vol. 58, no. 8, pp. 2452–2458, Aug 2009.
- 3 JCGM, "Evaluation of measurement data — guide to the expression of uncertainty in measurement," Guide JCGM 100:2008, 2008.

4 N. M. Ridler and M. J. Salter, "An approach to the treatment of uncertainty in complex S-parameter measurements," *Metrologia*, vol. 39, no. 3, pp. 295–302, 2002.

5 B. D. Hall, "On the propagation of uncertainty in complex-valued quantities," *Metrologia*, vol. 41, no. 3, pp. 173–177, 2004.

6 JCGM, "Evaluation of measurement data — supplement 2 to the "Guide to the expression of uncertainty in measurement" — extension to any number of output quantities," Guide JCGM 102:2011, 2011.

7 B. D. Hall, "Notes on complex measurement uncertainty – part 2," Industrial Research Limited, Tech. Rep. IRL 2557, 2012.

8 R. S. Singh, H. Hooshyar, and L. Vanfretti, "Assessment of time synchronization requirements for phasor measurement units," in *Proceedings of PowerTech 2015*, Eindhoven, Netherlands, June 2015.

9 A. Monti, C. Muscas, and F. Ponci, Eds., *Phasor Measurement Units and Wide Area Monitoring Systems*. Academic Press, 2016.

10 C. Indulkar and K. Ramalingam, "Estimation of transmission line parameters from measurements," *International Journal of Electrical Power & Energy Systems*, vol. 30, no. 5, pp. 337–342, 2008.

11 Y. Du and Y. Liao, "On-line estimation of transmission line parameters, temperature and sag using PMU measurements," *Electric Power Systems Research*, vol. 93, pp. 39–45, 2012.

12 S. Kurokawa, G. A. Asti, E. C. M. Costa, and J. Pissolato, "Simplified procedure to estimate the resistance parameters of transmission lines," *Electrical Engineering*, vol. 95, no. 3, pp. 221–227, 2013.

13 B. D. Hall, "Some considerations related to the evaluation of measurement uncertainty for complex-valued quantities in radio frequency measurements," *Metrologia*, vol. 44, no. 6, pp. L62–L67, 2007.

14 "IEEE standard for synchrophasor measurements for power systems," *IEEE Std C37.118.1-2011 (Revision of IEEE Std C37.118-2005)*, pp. 1–61, Dec 2011.

15 "Instrument transformers — part 1: Current transformers," Standard IEC 60044-1:2002, 2002.

16 "Instrument transformers — part 2: Inductive voltage transformers," Standard IEC 60044-2:2002, 2002.

17 J. H. Harlow, L. L. Grigsby, and J. D. McDonald, *Electric Power Transformer Engineering*. CRC Press, 2012.

18 "IEEE standard for calculating the current-temperature relationship of bare overhead conductors," *IEEE Std 738-2012 (Revision of IEEE Std 738-2006 - Incorporates IEEE Std 738-2012 Cor 1-2013)*, pp. 1–72, Dec 2013.

19 "Thermal behaviour of overhead conductors," CIGRE working group 22.12 report, August 2002.

9 Instrument Transformer Errors

Exact burden values are not known for the measurement setup, but are estimated to be as follows. At line end 1, current transformer burden of 1.5 VA and voltage transformer burden of 2.0 VA were assumed; at line end 2, current transformer burden of 1.7 VA and voltage transformer burden of 1.4 VA were assumed. Only one of these values lies between the two burden values which measurement errors were reported for. It cannot be assumed that it is correct to extrapolate the errors for a burden value outside of the range between the two tested burdens. For this reason, the other three burden values were replaced by the lowest burden values that measurement errors were reported for. Measurement errors assumed in the uncertainty analysis were found by interpolating between the reported measurement errors as seen in Tables 1–4. In the tables, U/U_n and I/I_n stand for ratios of measured and rated values. Magnitude errors are given in per cent and angle errors in minutes. In Table 1, some values are reported only for one transformer.

Table 1 Voltage transformer errors at line end 1, according to manufacturer.

Burden 25 VA, power factor not specified						
U/U_n	Phase A		Phase B		Phase C	
	δU (%)	$\delta\varphi_U$ (')	δU (%)	$\delta\varphi_U$ (')	δU (%)	$\delta\varphi_U$ (')
1.5	0.04	5.0	0.06	5.0	0.06	4.0
1.2	0.12	2.0	0.12	3.0	0.12	2.0
1.0					0.14	1.0
0.8	0.16	1.0	0.15	1.0	0.15	1.0
0.05					0.15	7.0
0.02	0.2	6.0	0.2	8.0	0.21	10.0

Burden 100 VA, power factor not specified						
U/U_n	Phase A		Phase B		Phase C	
	δU (%)	$\delta\varphi_U$ (')	δU (%)	$\delta\varphi_U$ (')	δU (%)	$\delta\varphi_U$ (')
1.2	-0.14	4.0	-0.12	5.0	-0.13	4.0
1.0					-0.11	3.0
0.8	-0.1	2.0	-0.08	4.0	-0.11	3.0

Table 2 Voltage transformer errors at line end 2, according to manufacturer.

Burden 25 VA, power factor 0.8						
U/U_n	Phase A		Phase B		Phase C	
	δU (%)	$\delta\varphi_U$ (')	δU (%)	$\delta\varphi_U$ (')	δU (%)	$\delta\varphi_U$ (')
1.5	0.37	2.5	0.39	2.4	0.38	3.1
1.2	0.37	2.8	0.39	2.4	0.38	3.1
1.0	0.37	2.8	0.39	2.4	0.38	3.1
0.8	0.37	2.9	0.39	2.9	0.38	3.1
0.05	0.41	8.7	0.41	8.7	0.41	8.7

Burden 100 VA, power factor 0.8						
U/U_n	Phase A		Phase B		Phase C	
	δU (%)	$\delta\varphi_U$ (')	δU (%)	$\delta\varphi_U$ (')	δU (%)	$\delta\varphi_U$ (')
1.5	-0.27	9.2	-0.27	9.2	-0.27	9.2
1.2	-0.29	9.4	-0.25	9.3	-0.26	10.4
1.0	-0.29	9.8	-0.25	9.3	-0.26	10.4
0.8	-0.29	10.2	-0.25	10	-0.26	10.4
0.05	-0.18	18	-0.18	18	-0.18	18

Table 3 Current transformer errors at line end 1, according to manufacturer.

Burden 1 VA, power factor not specified						
I/I_n	Phase A		Phase B		Phase C	
	δI (%)	$\delta\varphi_I$ (')	δI (%)	$\delta\varphi_I$ (')	δI (%)	$\delta\varphi_I$ (')
1.2	0.03	0.0	0.02	0.0	0.07	0.0
1.0	0.028	0.18	0.02	0.18	0.066	0.36
0.2	0.021	0.9	0.02	0.9	0.053	1.8
0.05	0.02	1.0	0.02	1.0	0.05	2.0
0.01	0.02	2.0	0.03	2.0	0.05	3.0

Burden 5 VA, power factor not specified						
I/I_n	Phase A		Phase B		Phase C	
	δI (%)	$\delta\varphi_I$ (')	δI (%)	$\delta\varphi_I$ (')	δI (%)	$\delta\varphi_I$ (')
1.2	0.01	-1.0	-0.01	0.0	0.04	0.0
1.0	0.01	-1.0	0	-1.0	0.04	0.0
0.2	-0.02	0.0	-0.02	0.0	0.02	0.0
0.05	-0.04	1.0	-0.03	1.0	0.0	2.0
0.01	-0.04	3.0	-0.04	2.0	-0.01	3.0

Table 4 Current transformer errors at line end 2, according to manufacturer.

Burden 5 VA, power factor 1						
I/I_n	Phase A		Phase B		Phase C	
	δI (%)	$\delta\varphi_I$ (')	δI (%)	$\delta\varphi_I$ (')	δI (%)	$\delta\varphi_I$ (')
1.2	-0.01	0.2	-0.01	0.1	-0.02	0.1
1.0	-0.01	0.5	-0.01	0.2	-0.02	0.2
0.2	-0.01	0.6	-0.01	0.7	-0.02	0.7
0.05	-0.01	1.0	-0.01	1.3	-0.01	1.3
0.01	0.01	2.6	0.0	2.9	0.0	2.9

Burden 20 VA, power factor 0.8						
I/I_n	Phase A		Phase B		Phase C	
	δI (%)	$\delta\varphi_I$ (')	δI (%)	$\delta\varphi_I$ (')	δI (%)	$\delta\varphi_I$ (')
1.2	-0.05	-0.7	-0.03	-0.9	-0.03	-1.0
1.0	-0.05	-0.3	-0.03	-0.8	-0.03	-0.8
0.2	-0.06	0.1	-0.045	0.2	-0.05	0.2
0.05	-0.06	0.9	-0.05	1.2	-0.06	1.2
0.01	-0.06	2.8	-0.05	2.9	-0.06	2.3

Publication II

K. Tuttelberg and J. Kilter, "Estimation of transmission loss components from phasor measurements," in *International Journal of Electrical Power & Energy Systems*, vol. 98, pp. 62-71.

Estimation of Transmission Loss Components from Phasor Measurements

Kaur Tuttelberg^{a,*}, Jako Kilter^a

^a*Department of Electrical Power Engineering and Mechatronics,
Tallinn University of Technology, Tallinn, Estonia*

Abstract

This paper presents a method to estimate separate components of transmission losses from synchronised phasor measurements in terms of losses in the corresponding elements of the transmission line model. This means separate estimates of Joule losses in series resistive elements and active losses dissipated in the shunt conductive elements, e.g. corona and leakage, and both the consumed and generated reactive power in inductive and capacitive elements of the model are found. The main aim and benefit of the method is a new way to detect corona losses on transmission lines. To facilitate this, the needed mathematical expressions are derived for the estimation of transmission losses from simultaneous, i.e. time-synchronised, phasor measurements based on a distributed parameter multiconductor transmission line model. The efficacy of the derived expressions is analysed in PSCAD simulations and on real data from phasor measurement units (PMU).

Keywords: Transmission line measurements, Transmission losses, Loss content estimation, Phasor measurement units, Real-time monitoring

1. Introduction

For many transmission system operators (TSO) operating in deregulated markets, it is their task to forecast the energy consumed as transmission losses and procure it on the electricity market. Purchases of energy to cover system imbalances amount to millions of euros annually even in a small transmission system like the one in Estonia [1]. Around 30% of total imbalance consists of internal system imbalances, out of which a significant part comes from incorrectly estimated transmission losses. While Joule losses are generally forecast rather accurately, the majority of forecasting errors are caused by difficulties in estimating corona losses. In a cold climate, the share of corona losses can be significant and improvements in forecasting these losses could mean considerable savings.

A common way to forecast Joule losses is to run network simulations with forecast load and find the losses based on the network model. Such an approach is not possible with the other main cause of active losses, corona losses, which have to be forecast separately. Unlike load forecasting, this is a more uncommon task and hindered by lack of available data. Empirical corona loss models are difficult to tune and measurement data is needed for statistical methods. This paper presents a method to estimate transmission losses as separate components based on PMU measurements to provide a source for both instantaneous and historical data about corona losses, which could be applied in statistical methods and forecasting algorithms.

At the first glance, computing transmission losses from phasors measured at both ends of a line is trivial: the product of the voltage phasor and the conjugate of current phasor yields the power; and the sum of the differences in sent and received power in all of the phases results in overall transmission losses. This is indeed a correct way to determine the total active losses and reactive consumption (or generation) from phasors measured at both ends of a transmission line. However, as PMUs provide more data than conventional metering (SCADA/EMS), there is potential for differentiating between types of active losses and both the consumption and generation of reactive power on a transmission line.

In a circuit model of a transmission line, like the distributed parameter line model, the transmission losses on the line can be viewed as a sum of losses in the elements of the circuit. Instead of directly computing the difference in sent and received power, transmission losses can be calculated as a sum of components, corresponding to losses in different elements of the model as long as the physical meaning of the element is clear [2]. Measurement of time-synchronised phasors enables the parameters (e.g. resistance, etc.) of the line model to be estimated, which in turn enables the computation of loss components. As long as the parameters of the model are estimated only from measured voltage and current phasors, the overall losses are the same no matter which (physically correct) expression is used. The important difference is that the terms in the sum computed from line parameters can be attributed to different types of losses according to which elements of the model they occur in.

*Corresponding author

Email address: kaur.tuttelberg@ttu.ee (Kaur Tuttelberg)

In this paper, the expressions for the losses dissipated in the distributed elements of a multiconductor transmission line are first analysed in the phase domain, considering the effects of mutual coupling. However, the derived equations are based on explicit values of line parameters—both the self and mutual series and shunt elements—and, as such, depend on the estimation of these parameters. It is difficult to estimate all of the parameters describing a multiconductor transmission line at once only from phasors measured at the ends of the line [3–5]. Even if they were available, in phase domain it is also difficult to interpret the physical meaning of some of these parameters. For these reasons simplified expressions in the symmetrical component domain are also derived in this paper. This simplification is equivalent to assuming conditions when the effects of mutual coupling between the sequence quantities is sufficiently small, like in [6, 7], which can easily be applied in real PMU measurements.

The paper includes an experimental part, where the different expressions derived for transmission losses computed from measured voltage and current phasors are analysed based on both measured and simulated data. For the analyses, real PMU measurement data was obtained from 330 kV transmission lines in the Estonian power system. In addition to that, supporting analyses were carried out based on numerical simulations made in PSCAD.

The experimental results indicate that the method can indeed be used to distinguish between different types of transmission losses, i.e. Joule losses and other active losses, and analyse the consumption and generation of reactive power on the line. Like in line parameter estimation applications, results are strongly influenced by the accuracy of measured voltages and currents. Despite this, the results could be useful in applications where it is enough to detect changes in time, e.g. determining correlations between changes in corona losses and weather for transmission loss forecasting tools.

The paper consists of five sections. Section 2 summarises common methods of estimating corona losses and the theoretical background of transmission line models used in this paper. In section 3, expressions for transmission losses are derived. The simulated and measured data and their analyses are presented in section 4 and discussed in section 5. Conclusions are summarised in section 6.

2. Theoretical Background

2.1. Methods of Estimating Corona Losses

Going back to the earliest research on corona losses, empirical formulas have been deduced from experiments in order to estimate these losses [8–10]. These empirical formulas usually take one of the following two forms [11]. Expressed in terms of voltages as

$$\Delta P_{C,U} = f(U, U_C), \quad (1)$$

where U is voltage on the conductor, U_C is the critical or corona on-set voltage, and f is an empirical function [10, 12]. Expressed in terms of electric field strengths

$$\Delta P_{C,E} = f(E, E_C), \quad (2)$$

where E is the superficial electric field strength, E_C is the critical or corona on-set electric field strength, and f is an empirical function [13].

The empirical functions and the critical or on-set values are determined experimentally and depend on a wide variety of factors. These include, but are not limited to, design of the conductor or bundle, conductor surface properties, air pressure, temperature, humidity, precipitation, extent of frost on conductors, etc. [8–14]. Several such empirical formulas are available, however, it is difficult to apply these on operational transmission lines in the power system. Without experimental verification, it is very difficult to determine the unknown parameters of these empirical formulas. Experimental measurements of corona losses on operating transmission lines have been carried out, but these require specialised test equipment [15–17], and are not easily transferred from case to case.

Another way of estimating corona losses is to apply statistical methods [11, 18, 19]. The variable share of corona losses is mostly caused by changes in weather conditions, while the dependence on conductor properties and line configuration are more constant in time. By collecting large enough amounts of weather data and applying statistical methods, it is possible to develop models that can estimate and forecast corona losses [11, 19]. However, even in this case it is necessary to obtain at least some information about historical values of corona losses in order to determine these correlations with weather conditions. The method presented in this paper aims to provide a solution for obtaining this data.

2.2. Two Conductor Transmission Lines

While looking at a distributed parameter two conductor transmission line, it is assumed that the line consists of a series of infinitesimally short two-port sections. Every segment of the line can be viewed as a Γ -section with a series impedance and shunt admittance. The parameters of every section are given as $\underline{z}dl$ and $\underline{y}dl$, where $\underline{z} = r + jx$ is the per unit distance impedance, $\underline{y} = g + jb$ the per unit distance admittance, and dl denotes the infinitesimally small length of the section.

The voltages and currents at two ends of such a line (currents in one conductor and voltages between the conductors) are related by

$$\underline{U}(l) = \cosh(\underline{\gamma}l)\underline{U}(0) + \underline{z}_c \sinh(\underline{\gamma}l)\underline{I}(0), \quad (3)$$

$$\underline{I}(l) = \frac{1}{\underline{z}_c} \sinh(\underline{\gamma}l)\underline{U}(0) + \cosh(\underline{\gamma}l)\underline{I}(0), \quad (4)$$

where $\underline{U}(l)$ and $\underline{I}(l)$ are the voltage and current phasors at a distance l toward the beginning of the line ($\underline{U}(0)$ and $\underline{I}(0)$)

are the phasors at the end of the line). The per unit distance line parameters—the impedance and admittance—are included in the propagation constant $\gamma = (\underline{z}\underline{y})^{1/2}$ and characteristic impedance $\underline{z}_c = (\underline{z}/\underline{y})^{1/2}$.

The inverse problem of equations (3) and (4)—finding the line parameters—can also be solved if the simultaneous voltages and currents at both ends are known. Writing the sum and the difference of the two equations results in

$$\begin{aligned}\underline{U}(l) + \underline{z}_c \underline{I}(l) &= [\underline{U}(0) + \underline{z}_c \underline{I}(0)] e^{\gamma l}, \\ \underline{U}(l) - \underline{z}_c \underline{I}(l) &= [\underline{U}(0) - \underline{z}_c \underline{I}(0)] e^{-\gamma l},\end{aligned}$$

By expressing the characteristic impedance from one equation, the other can be written as

$$\begin{aligned}\underline{U}(l) - \underline{I}(l) \frac{\underline{U}(0)e^{\gamma l} - \underline{U}(l)}{\underline{I}(l) - \underline{I}(0)e^{\gamma l}} \\ = e^{-\gamma l} \left(\underline{U}(0) - \underline{I}(0) \frac{\underline{U}(0)e^{\gamma l} - \underline{U}(l)}{\underline{I}(l) - \underline{I}(0)e^{\gamma l}} \right).\end{aligned}$$

Multiplying by the common denominator of the fractions yields the explicit expressions [3]

$$\gamma = \frac{1}{L} \operatorname{arccosh} \left[\frac{\underline{U}(L)\underline{I}(L) + \underline{U}(0)\underline{I}(0)}{\underline{U}(0)\underline{I}(L) + \underline{U}(L)\underline{I}(0)} \right], \quad (5)$$

$$\underline{z}_c = \frac{\underline{U}(L) - \underline{U}(0) \cosh(\gamma L)}{\underline{I}(0) \sinh(\gamma L)}, \quad (6)$$

where L is the length of the line.

2.3. Multiconductor Transmission Lines

As a simplification, multiconductor transmission lines are sometimes modelled as combinations of two conductor lines. However, for a more accurate and complete analysis, realistic transmission lines are modelled by multiconductor line models, which also consider the mutual coupling between the phases of a transmission line and the coupling between lines in case of a multiple circuit transmission line. This is an accurate model relating the measured quantities, i.e. voltages and currents at the ends of the line.

The parameters of a transmission line are mainly defined by the properties of conductors, geometry of the line and the earth return path [20]. Resistance and sag of conductors are also affected by temperature. Various sources describe how the parameters can be computed from line design data [20–22].

In matrix notation, line parameters are expressed as an impedance matrix

$$\mathbf{Z} = \mathbf{R} + j\omega\mathbf{L} = \begin{bmatrix} \mathbf{Z}_{aa} & \mathbf{Z}_{ab} & \mathbf{Z}_{ac} \\ \mathbf{Z}_{ba} & \mathbf{Z}_{bb} & \mathbf{Z}_{bc} \\ \mathbf{Z}_{ca} & \mathbf{Z}_{cb} & \mathbf{Z}_{cc} \end{bmatrix} \quad (7)$$

and admittance matrix

$$\mathbf{Y} = \mathbf{G} + j\omega\mathbf{C}. \quad (8)$$

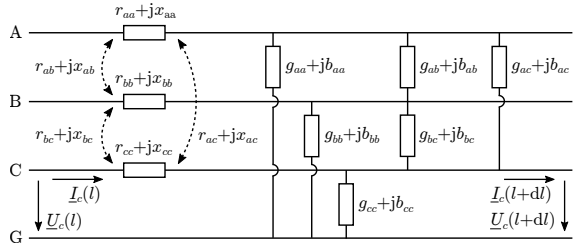


Figure 1: Schematic of the distributed parameter model of a three phase transmission line. Parameters correspond to elements of line parameter matrices after Kron's reduction, which introduces fictitious mutual resistance terms in addition to the usual mutual reactances. Voltages and currents shown in one phase.

Similar matrices are evaluated for multiple circuit lines. The parameter matrices are mostly defined by the geometry of the line, properties of conductors, and return path [20, 21]. If neutral conductors (lightning protection wires) are present, the matrices are reduced by Kron's reduction so that their dimension is given by the number of phases only [22]. In simulations, all conductances in \mathbf{Y} are generally assumed to be zero.

A schematic of the distributed parameter model for a multiconductor transmission line is given in Fig 1. For comparison, the two conductor line model appears when two of the phases and all mutual terms between phases are removed. Parameters correspond to elements of line parameter matrices, i.e. $\mathbf{Z}_{aa} = r_{aa} + jx_{aa}$ and $\mathbf{Y}_{aa} = g_{aa} + jb_{aa}$, etc.

On a single circuit three phase transmission line, the phase voltages and currents at any point of the line are given as [22, 23]

$$\mathbf{u}(l) = \begin{bmatrix} \underline{U}_a(l) \\ \underline{U}_b(l) \\ \underline{U}_c(l) \end{bmatrix}, \quad \mathbf{i}(l) = \begin{bmatrix} \underline{I}_a(l) \\ \underline{I}_b(l) \\ \underline{I}_c(l) \end{bmatrix}, \quad (9)$$

where l is the distance toward the beginning of the line and $\underline{U}_i(l)$ and $\underline{I}_i(l)$ are the voltage and current phasors in phase i .

According to Kirchhoff's laws, these quantities are related by the following differential equations [23]

$$\frac{d^2 \mathbf{u}(l)}{dl^2} = \mathbf{Z}\mathbf{Y}\mathbf{u}(l), \quad (10)$$

$$\frac{d^2 \mathbf{i}(l)}{dl^2} = \mathbf{Y}\mathbf{Z}\mathbf{i}(l). \quad (11)$$

The matrix $\mathbf{\Gamma} = (\mathbf{Z}\mathbf{Y})^{1/2}$ is termed the propagation matrix and the matrix equivalent of the characteristic impedance is defined as $\mathbf{Z}_C = \mathbf{\Gamma}^{-1}\mathbf{Z}$. Equations (10) and (11) are solved to express [24]

$$\mathbf{u}(l) = \cosh(\mathbf{\Gamma}l)\mathbf{u}(0) + \sinh(\mathbf{\Gamma}l)\mathbf{Z}_C\mathbf{i}(0), \quad (12)$$

$$\mathbf{i}(l) = \mathbf{Z}_C^{-1} \sinh(\mathbf{\Gamma}l)\mathbf{u}(0) + \mathbf{Z}_C^{-1} \cosh(\mathbf{\Gamma}l)\mathbf{Z}_C\mathbf{i}(0), \quad (13)$$

where $\cosh \mathbf{M} = [\exp(\mathbf{M}) + \exp(-\mathbf{M})]/2$ and $\sinh \mathbf{M} = [\exp(\mathbf{M}) - \exp(-\mathbf{M})]/2$.

The system above contains six independent complex equations. The line parameter matrices, either \mathbf{Z} and \mathbf{Y} or $\mathbf{\Gamma}$ and \mathbf{Z}_C , contain 12 complex variables. As the inverse problem, the line parameters are difficult to find from simultaneously measured voltage and current phasors only. A theoretical solution exists in the modal domain, however, the required modal transformation matrices are unknown themselves [3].

3. Transmission Losses

3.1. Losses on Two Conductor Transmission Lines

Transmission losses across a two conductor line of length L can be computed as $\underline{U}(L)\underline{I}^*(L) - \underline{U}(0)\underline{I}^*(0)$, where $*$ denotes the complex conjugate. On the other hand, at a location l , the losses in the distributed elements are $|\underline{I}(l)|^2 z dl$ and $|\underline{U}(l)|^2 y dl$. If we integrate the losses in the infinitesimally short sections over the length of the line, the active transmission losses and reactive power balance become

$$\Delta P = r \int_0^L |\underline{I}(l)|^2 dl + g \int_0^L |\underline{U}(l)|^2 dl, \quad (14)$$

$$\Delta Q = x \int_0^L |\underline{I}(l)|^2 dl - b \int_0^L |\underline{U}(l)|^2 dl, \quad (15)$$

where the reactive power of the capacitance is considered to be negative.

By first evaluating line parameters from simultaneous phasor measurements, the equations for $\underline{I}(l)$ and $\underline{U}(l)$ can be solved and integrated numerically. Thus, we can also express and compute the total losses as $\underline{U}(L)\underline{I}^*(L) - \underline{U}(0)\underline{I}^*(0) = \Delta P + j\Delta Q$ [2].

It is common to simplify the transmission line and model it as a two conductor line; however, this simplification should first be analysed with respect to the quantity of interest. On a multiconductor transmission line, the phase voltages and currents are mutually coupled, affecting the power losses in different phases. Before transmission losses can be modelled on a two-conductor line, they are analysed on the multiconductor transmission line model in the following subsections.

3.2. Losses on Multiconductor Lines in Phase Domain

In the matrix-vector notation of the multiconductor transmission line, we can express the total power injected into the line at the sending end as

$$\begin{aligned} \underline{S}(L) &= \mathbf{i}^\dagger(L)\mathbf{u}(L) = \mathbf{i}_1^\dagger \mathbf{u}_1 \\ &= \underline{U}_a(L)\underline{I}_a^*(L) + \underline{U}_b(L)\underline{I}_b^*(L) + \underline{U}_c(L)\underline{I}_c^*(L), \end{aligned} \quad (16)$$

where † denotes the conjugate transpose. The power flowing out of the line at the other end can be computed similarly.

Based on this, the losses across the length of the line become

$$\underline{\Delta S}_L = \mathbf{i}_1^\dagger \mathbf{u}_1 - \mathbf{i}_2^\dagger \mathbf{u}_2 = \mathbf{i}^\dagger(L)\mathbf{u}(L) - \mathbf{i}^\dagger(0)\mathbf{u}(0), \quad (17)$$

where the voltage and current phasors in three phases are the quantities measured by PMUs.

The hyperbolic functions are holomorphic, thus $(\cosh \mathbf{M})^\dagger = \cosh(\mathbf{M}^\dagger)$. For a line of length L , we can express the losses as

$$\begin{aligned} \underline{\Delta S}_L &= \mathbf{i}_1^\dagger \mathbf{u}_1 + \mathbf{u}_1^\dagger \sinh(\mathbf{\Gamma}^\dagger L)\mathbf{\Gamma}^\dagger(\mathbf{Z}^{-1})^\dagger \cosh(\mathbf{\Gamma}L)\mathbf{u}_1 \\ &+ \mathbf{i}_1^\dagger \mathbf{Z}^\dagger(\mathbf{\Gamma}^{-1})^\dagger \cosh(\mathbf{\Gamma}^\dagger L)\mathbf{\Gamma}^\dagger(\mathbf{Z}^{-1})^\dagger \sinh(\mathbf{\Gamma}L)\mathbf{\Gamma}^{-1}\mathbf{Z}\mathbf{i}_1 \\ &- \mathbf{i}_1^\dagger \mathbf{Z}^\dagger(\mathbf{\Gamma}^{-1})^\dagger \cosh(\mathbf{\Gamma}^\dagger L)\mathbf{\Gamma}^\dagger(\mathbf{Z}^{-1})^\dagger \cosh(\mathbf{\Gamma}L)\mathbf{u}_1 \\ &- \mathbf{u}_1^\dagger \sinh(\mathbf{\Gamma}^\dagger L)\mathbf{\Gamma}^\dagger(\mathbf{Z}^{-1})^\dagger \sinh(\mathbf{\Gamma}L)\mathbf{\Gamma}^{-1}\mathbf{Z}\mathbf{i}_1 \end{aligned} \quad (18)$$

The hyperbolic functions can be expanded in series as follows

$$\cosh(\mathbf{M}) = \mathbf{I} + \frac{\mathbf{M}^2}{2!} + \frac{\mathbf{M}^4}{4!} + \dots, \quad (19)$$

$$\sinh(\mathbf{M}) = \mathbf{M} + \frac{\mathbf{M}^3}{3!} + \frac{\mathbf{M}^5}{5!} + \dots, \quad (20)$$

where \mathbf{I} is the identity matrix.

For a sufficiently short line section of length Δl , it can be assumed that $(\mathbf{\Gamma}\Delta l)^2$ and $(\mathbf{\Gamma}\Delta l)^3$ become negligible compared to \mathbf{I} and $\mathbf{\Gamma}\Delta l$. By equating the hyperbolic functions to the first terms in the series expansions, the losses across the short section are simplified so that

$$\begin{aligned} \underline{\Delta S}_{\Delta l} &= \mathbf{u}^\dagger(\Delta l)\mathbf{Y}^\dagger \mathbf{u}(\Delta l)\Delta l + \mathbf{i}^\dagger(\Delta l)\mathbf{Z}\mathbf{i}(\Delta l)\Delta l \\ &+ O[(\Delta l)^2] \end{aligned} \quad (21)$$

Thus, at a location l the losses across an infinitesimally short section of the line are

$$d\underline{\Delta S}(l) = \mathbf{u}^\dagger(l)\mathbf{Y}^\dagger \mathbf{u}(l)dl + \mathbf{i}^\dagger(l)\mathbf{Z}\mathbf{i}(l)dl, \quad (22)$$

which can be integrated over the length of the line to obtain total losses

$$\underline{\Delta S}_L = \int_0^L \mathbf{u}^\dagger(l)\mathbf{Y}^\dagger \mathbf{u}(l)dl + \int_0^L \mathbf{i}^\dagger(l)\mathbf{Z}\mathbf{i}(l)dl. \quad (23)$$

The obtained result displays clear analogy with the two conductor transmission line, especially considering that $\mathbf{Y}^\dagger = \mathbf{G} - j\mathbf{B}$ (since \mathbf{Y} is symmetric) and $|a|^2 = a^*a$. Similarly to the two conductor case, we can also separate the expression for losses into a sum of four separate terms, i.e.

$$\underline{\Delta S}_L = \Delta P_J + \Delta P_C + j(\Delta Q_I - \Delta Q_C). \quad (24)$$

These four terms can be expressed as

$$\Delta P_J = \int_0^L \mathbf{i}^\dagger(l)\mathbf{R}\mathbf{i}(l)dl, \text{ etc.} \quad (25)$$

In more detail, the term expressed in scalar values becomes

$$\begin{aligned} \mathbf{i}^\dagger(l)\mathbf{R}\mathbf{i}(l) &= \underline{I}_a(l)\underline{I}_b^*(l)\mathbf{R}_{ab} + \underline{I}_a(l)\underline{I}_c^*(l)\mathbf{R}_{ac} \\ &\quad + \underline{I}_b(l)\underline{I}_a^*(l)\mathbf{R}_{ab} + \underline{I}_b(l)\underline{I}_c^*(l)\mathbf{R}_{bc} \\ &\quad + \underline{I}_c(l)\underline{I}_a^*(l)\mathbf{R}_{ac} + \underline{I}_c(l)\underline{I}_b^*(l)\mathbf{R}_{bc} \\ &\quad + |\underline{I}_a(l)|^2\mathbf{R}_{aa} + |\underline{I}_b(l)|^2\mathbf{R}_{bb} + |\underline{I}_c(l)|^2\mathbf{R}_{cc}, \end{aligned} \quad (26)$$

which gives the sum of losses in resistances from all three phases. Similar expressions hold for the rest of the terms

Due to the mutual coupling between phases, it is difficult to analyse the components of losses further in the phase domain. It is complicated to interpret the physical meaning of the terms in the sum, mostly the mutual parameters, because of the Kron's reduction and other operations carried out in the calculation of line parameter matrices. For this reason, the analysis is continued in the symmetrical component domain.

3.3. Losses on Multiconductor Lines in Symmetrical Component Domain

On a single circuit three phase transmission line, the zero, positive, and negative sequence voltages and currents

$$\mathbf{u}_S(l) = [\underline{U}_0(l), \underline{U}_+(l), \underline{U}_-(l)]^\top, \quad (27)$$

$$\mathbf{i}_S(l) = [\underline{I}_0(l), \underline{I}_+(l), \underline{I}_-(l)]^\top, \quad (28)$$

are obtained by linear transformations $\mathbf{u}_S(l) = \mathbf{T}_S^{-1}\mathbf{u}(l)$ and $\mathbf{i}_S(l) = \mathbf{T}_S^{-1}\mathbf{i}(l)$, where

$$\mathbf{T}_S = \begin{bmatrix} 1 & 1 & 1 \\ 1 & e^{j4\pi/3} & e^{j2\pi/3} \\ 1 & e^{j2\pi/3} & e^{j4\pi/3} \end{bmatrix}. \quad (29)$$

It can also be noted that $\mathbf{T}_S^{-1} = \mathbf{T}_S^\dagger/3$.

The terms in the expression of transmission losses $\underline{\Delta S}_L$ in the phase domain can be rewritten as [25]

$$\begin{aligned} \mathbf{i}^\dagger(l)\mathbf{Z}\mathbf{i}(l) &= \mathbf{i}^\dagger(l)\mathbf{T}_S\mathbf{T}_S^{-1}\mathbf{Z}\mathbf{T}_S\mathbf{T}_S^{-1}\mathbf{i}(l) \\ &= [\mathbf{T}_S^\dagger\mathbf{i}(l)]^\dagger[\mathbf{T}_S^{-1}\mathbf{Z}\mathbf{T}_S][\mathbf{T}_S^{-1}\mathbf{i}(l)] \\ &= [3\mathbf{T}_S^{-1}\mathbf{i}(l)]^\dagger[\mathbf{T}_S^{-1}\mathbf{Z}\mathbf{T}_S][\mathbf{T}_S^{-1}\mathbf{i}(l)] \\ &= 3\mathbf{i}_S^\dagger(l)\mathbf{Z}_S\mathbf{i}_S(l) \end{aligned} \quad (30)$$

and

$$\begin{aligned} \mathbf{u}^\dagger(l)\mathbf{Y}^\dagger\mathbf{u}(l) &= [3\mathbf{T}_S^{-1}\mathbf{u}(l)]^\dagger[1/3\mathbf{T}_S^\dagger\mathbf{Y}^\dagger\mathbf{T}_S][\mathbf{T}_S^{-1}\mathbf{u}(l)] \\ &= [3\mathbf{T}_S^{-1}\mathbf{u}(l)]^\dagger[1/3\mathbf{T}_S^\dagger\mathbf{Y}^\dagger\mathbf{T}_S]^\dagger[\mathbf{T}_S^{-1}\mathbf{u}(l)] \\ &= 3[\mathbf{T}_S^{-1}\mathbf{u}(l)]^\dagger[\mathbf{T}_S^{-1}\mathbf{Y}\mathbf{T}_S]^\dagger[\mathbf{T}_S^{-1}\mathbf{u}(l)] \\ &= 3\mathbf{u}_S^\dagger(l)\mathbf{Y}_S^\dagger\mathbf{u}_S(l). \end{aligned} \quad (31)$$

This yields another equivalent expression for transmission losses, now in the symmetrical component domain

$$\underline{\Delta S}_L = 3 \int_0^L \left[\mathbf{i}_S^\dagger(l)\mathbf{Z}_S\mathbf{i}_S(l) + \mathbf{u}_S^\dagger(l)\mathbf{Y}_S^\dagger\mathbf{u}_S(l) \right] dl. \quad (32)$$

The matrices $\mathbf{Z}_S = \mathbf{T}_S^{-1}\mathbf{Z}\mathbf{T}_S$ and $\mathbf{Y}_S = \mathbf{T}_S^{-1}\mathbf{Y}\mathbf{T}_S$ contain the sequence impedances and admittances of the transmission line and are directly calculable from the reduced impedance and admittance matrices \mathbf{Z} and \mathbf{Y} [20]. The positive and negative sequence impedances become

$$\begin{aligned} \underline{z}_+ = \underline{z}_- &= (\mathbf{Z}_S)_{22} = (\mathbf{Z}_S)_{33} \\ &= (\mathbf{Z}_{aa} + \mathbf{Z}_{bb} + \mathbf{Z}_{cc} - \mathbf{Z}_{ab} - \mathbf{Z}_{bc} - \mathbf{Z}_{ac})/3, \end{aligned} \quad (33)$$

and the zero sequence impedance is

$$\begin{aligned} \underline{z}_0 &= (\mathbf{Z}_S)_{11} \\ &= (\mathbf{Z}_{aa} + \mathbf{Z}_{bb} + \mathbf{Z}_{cc} + 2\mathbf{Z}_{ab} + 2\mathbf{Z}_{bc} + 2\mathbf{Z}_{ac})/3, \end{aligned} \quad (34)$$

where 11, etc. are the row-column indexes of the matrix elements. Other sequence parameters can be found as corresponding elements of \mathbf{Z}_S or \mathbf{Y}_S .

In most transmission lines the off-diagonal elements in these matrices are significantly smaller than the diagonal elements, e.g.

$$(\mathbf{Z}_S)_{12} = [\mathbf{Z}_{aa} - (\mathbf{Z}_{bb} + \mathbf{Z}_{cc})/2 + (\mathbf{Z}_{ab} + \mathbf{Z}_{ac})/2 - \mathbf{Z}_{bc}]/3 \quad (35)$$

In fact, in ideally transposed lines, the off-diagonal elements are exactly zero so that the sequence impedance and admittance matrices are diagonal.

This also implies that the sequence transformation matrix \mathbf{T}_S is a correct variant of both of the modal transformation matrices for ideally transposed lines [23]. In this case, the multiconductor line in the symmetrical component domain can be viewed as three independent two conductor lines and the correct sequence impedances and admittances can be computed from the corresponding voltages and currents as in (5) and (6) [3].

Another situation when (32) is significantly simplified occurs when the load on the line is symmetric. In this case the negative and zero sequence voltages and currents are negligible and the total transmission losses across the line become

$$\underline{\Delta S}'_L = 3 \int_0^L \left(|\underline{I}_+(l)|^2 \underline{z}_+ + |\underline{U}_+(l)|^2 \underline{y}_+^* \right) dl. \quad (36)$$

When the line and the load are both slightly asymmetric, the off-diagonal elements of \mathbf{Z}_S and \mathbf{Y}_S are small and the products containing them (e.g. $\underline{I}_+(l)\underline{I}_0^*(l)(\mathbf{Z}_S)_{12}$, etc.) in (32) contribute negligibly to the total losses. We assume that, generally, in a transmission system, both asymmetries are small enough to warrant the use of the following approximation.

We define simplified diagonal sequence impedance and admittance matrices as

$$\langle \mathbf{z}_S \rangle = \langle \mathbf{r}_S \rangle + j\langle \mathbf{x}_S \rangle = \begin{bmatrix} \underline{z}_0 & & \\ & \underline{z}_+ & \\ & & \underline{z}_- \end{bmatrix} \quad (37)$$

and $\langle \mathbf{y}_S \rangle = \langle \mathbf{g}_S \rangle + j\langle \mathbf{b}_S \rangle$, where the sequence impedances

and admittances are computed from sequence voltages and currents (which in turn are calculated from measured phase quantities) as in (5) and (6). Total transmission losses can then be approximated as

$$\underline{\Delta S}_L \cong 3 \int_0^L \left[\mathbf{i}_S^\dagger(l) \langle \mathbf{z}_S \rangle \mathbf{i}_S(l) + \mathbf{u}_S^\dagger(l) \langle \mathbf{y}_S \rangle^\dagger \mathbf{u}_S(l) \right] dl. \quad (38)$$

This allows us to compute the total transmission losses as four separate components as in (24) without including elements of the phase domain reduced impedance and admittance matrices \mathbf{Z} and \mathbf{Y} . The approximated loss components become

$$\begin{aligned} \Delta P_J \cong & 3r_+ \int_0^L |\underline{I}_+(l)|^2 dl + 3r_- \int_0^L |\underline{I}_-(l)|^2 dl \\ & + 3r_0 \int_0^L |\underline{I}_0(l)|^2 dl, \end{aligned} \quad (39)$$

$$\begin{aligned} \Delta P_C \cong & 3g_+ \int_0^L |\underline{U}_+(l)|^2 dl + 3g_- \int_0^L |\underline{U}_-(l)|^2 dl \\ & + 3g_0 \int_0^L |\underline{U}_0(l)|^2 dl, \text{ etc.}, \end{aligned} \quad (40)$$

where the sequence voltages and currents are computed as in (3) and (4) and integrated numerically. In the presented method, the parameters r_+ , g_+ , etc. are computed from measured phasors $\underline{U}_+(L)$, $\underline{U}_+(0)$, etc. according to (5) and (6). No prior knowledge about the parameters of the line is needed.

It is important to discuss the use of negative and zero sequence quantities in the above equations. If the monitored transmission line is transposed and can be considered balanced, these terms can be omitted and losses computed from positive sequence quantities only. If it is known that the line is not balanced well, these terms may be used. Even though it may seem unnatural to use negative and zero sequence quantities in steady state operation, the set of symmetrical components is an equivalent representation of phase quantities under any conditions. In most cases, the asymmetry is small enough and the contribution from negative and zero sequence terms is negligible.

The terms in ΔP_J representing active losses dissipated in resistances are current dependent. Based on the properties of the transmission line model, it can be assumed that they correspond to Joule losses in the conductors. The terms in ΔP_C are voltage dependent active losses and it can be assumed that these are mostly corona losses but could also include other possible losses (e.g. leakage). For the estimation of corona losses, similar assumptions have been used in previous studies [16, 18]. Equivalent expressions for ΔQ_I corresponding to inductive losses and ΔQ_C corresponding to capacitive generation are obtained with the reactances and susceptances.

The sequence resistances are commonly used quantities and the physical meaning of ΔP_J is simple to interpret. The same applies to reactive and capacitive sequence

reactances and the values of ΔQ_I and ΔQ_C . The value of ΔP_C will always be the difference between total active losses and Joule losses, i.e. $\Delta P_C = \Delta P_T - \Delta P_J$. In this light, the value of ΔP_C can be seen as all active losses that are not Joule losses and the conductances are what represent these losses in the line model.

4. Experimental Results

The estimation of transmission losses from measured phasors was analysed on PMU measurements of actual 330 kV transmission lines. However, it is difficult to reliably estimate the phase domain line parameter matrices present in (23), etc. (including both self and mutual parameters) from PMU measurements alone. Thus, the analysis was supplemented by PSCAD simulations, where this data is available and the different expressions of losses could be analysed on realistic transmission line models. The PSCAD simulations have not been intended to emulate the exact conditions of real measurements, but to verify the equivalence of different expressions for transmission losses and analyse the simplifications made in using the symmetrical component transformation. Corona effects are not modelled in EMTP calculations, hence the simulations assumed zero corona losses (i.e. shunt conductances were set to zero). This means that resistive active losses should ideally be equal to total active losses.

4.1. Monitored and Simulated Transmission Lines

Two real lines were observed in the presented measurements, while simulated data was obtained from a single model. The real lines have various sections with different geometry and are transposed in sections of uneven length; the length of the first observed line (denoted as L1) is 170 km and the length of the other line (L2) is 210 km. Both of the lines can be considered as single circuit lines. The simulated line was modelled based on the most characteristic pylon of the line L1, specified in Fig. 2a, with heights given at the pylon. The simulated line was also modelled with the length of 170 km, and a sag of 9 m on all conductors, the diameters were 2.8 cm in phase and 1.1 cm in neutral conductors, the resistances at 20 °C were 0.0746 Ω/km and 0.412 Ω/km, respectively. The phases were transposed from a configuration of ABC to CAB and CAB to BCA at 104 km and 116 km, respectively, like on the real line L1. Earth resistivity was assumed to be 1000 Ω·m.

A simplified circuit diagram of the line model simulated in PSCAD is shown in Fig. 2b, without depicting the transposition points. The circuit incorporated a universal transmission line model (phase domain frequency dependent model), a variable load, and an ideal voltage source. Between the source and the load, the voltages and currents on the line were simulated in all of the three phases and transformed into phasors. The initial case was simulated with a varying symmetric load with $\cos \varphi = 0.97$.

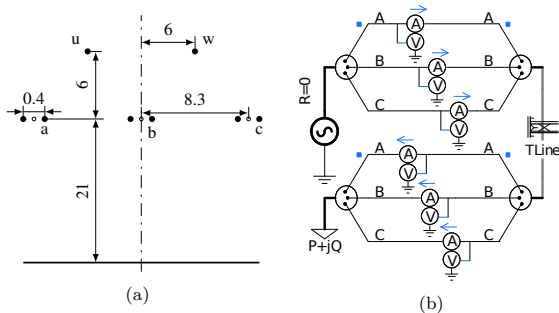


Figure 2: (a) Geometry of the simulated transmission line; all dimensions in meters with heights given at pylons. (b) Simplified PSCAD circuit diagram of simulation setup; transpositions not depicted.

Based on that, simulations with unbalanced load were also made, where the load in phase A, denoted \underline{S}_A , was a reference for the other two, so that $\underline{S}_B = (1 + k)\underline{S}_A$ and $\underline{S}_C = (1 - k)\underline{S}_A$. For the estimation of losses according to (23) the impedance and admittance matrices (not available with real measurements) of the line model generated in PSCAD were recorded [26, 27].

4.2. Estimation of Losses on Simulated Transmission Line

The results of estimating the losses as components (the estimate of Joule losses in ΔP_J and estimate of active shunt losses in ΔP_C) in the PSCAD simulation are plotted in Fig. 3. For varying balance of load in the phases the values of 0, 0.15, and 0.3 were used for k (so that $\underline{S}_B = (1 + k)\underline{S}_A$ and $\underline{S}_C = (1 - k)\underline{S}_A$). Total active losses were calculated separately from (17) and (23) as $\Delta P_T = \text{Re}[\underline{\Delta S}_L]$ (the latter with recorded line parameter matrices). However, with exact model parameters and precise numerical integration, the results were equal to a

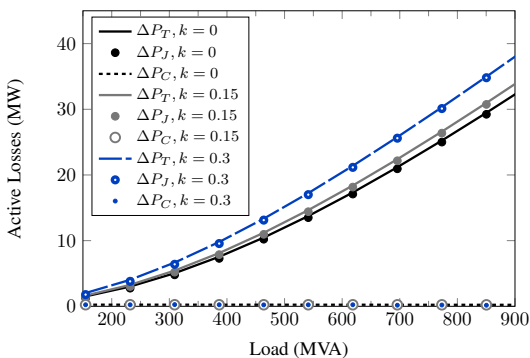


Figure 3: Results of PSCAD simulation, where total active transmission losses (ΔP_T) were computed as the direct difference in sent and received power and as components corresponding to losses dissipated in series resistances (ΔP_J) and shunt conductances (ΔP_C) under varying load conditions. Here k is an asymmetry factor so that $\underline{S}_B = (1 + k)\underline{S}_A$ and $\underline{S}_C = (1 - k)\underline{S}_A$.

high precision (differences below 0.1%) and the overlapping curves have not been plotted separately. The components of active losses ΔP_J and ΔP_C were computed from (39) and (40), with the parameters computed from sequence voltages and currents according to (5) and (6).

Results of the simulation show that the approximate estimates given in (39) and (40) behaved as expected, even with asymmetric load and despite the small asymmetry of the modelled transmission line. The value of ΔP_J was close to the direct estimate of losses as the difference in sent and received power. The value of ΔP_C was not exactly zero, showing some inaccuracy in the assumption that sequence quantities can be analysed with two conductor line models; however, the values were negligibly small (approximately 0.2 MW in this case, which is below 2% at medium simulated loads) and did not vary with changes in load.

4.3. Estimation of Losses on Real Transmission Lines

The measurement data from real transmission lines was used to study the feasibility of estimating the separate components of transmission losses. Measurement data was gathered with identical PMUs that have an 0.01° angle measurement error, 0.03% current and 0.02% voltage magnitude maximum relative measurement error, reported by the manufacturer. On line L1, voltage transformers of class 0.5 and current transformers of class 0.5S are installed at both ends, while ratings of current transformers are 1 kA and 2 kA. On line L2, PMUs are connected to voltage transformers of class 0.2 and current transformers of class 0.2S in one substation and instrument transformers of respective classes 0.5 and 0.5S at the other end. The CTs are rated at 1 kA and 2 kA, respectively. Measurement errors of instrument transformers on line L2 from factory test reports are given in Appendix A.

It is known that transmission line monitoring applications based on PMU measurements can be very sensitive to errors in measured voltages and currents, mainly due to instrument transformer errors [28, 29]. To analyse the possible effects of systematic measurement errors, uncertainties of estimated results are also presented. Specific details of the uncertainty analysis are not presented here, but the principles are well known [30–32]. A detailed discussion on such uncertainty analyses can be found in [33]. For the results from line L1, uncertainty ranges assume the maximum allowed measurement errors in the instrument transformers (according to standards [34, 35]) and PMUs (reported by manufacturer) combined. For line L2, some information about instrument transformer errors is also available from the manufacturers. Thus, uncertainties of results for line L2 were analysed based on this data and PMU errors reported by the manufacturer. These are not necessarily effective errors, but show the possible extents of the approximated systematic errors.

During the observed periods, the total active power transmitted over line L1 decreased from approximately 450 MW to around 340 MW, while on line L2 it rose from 25

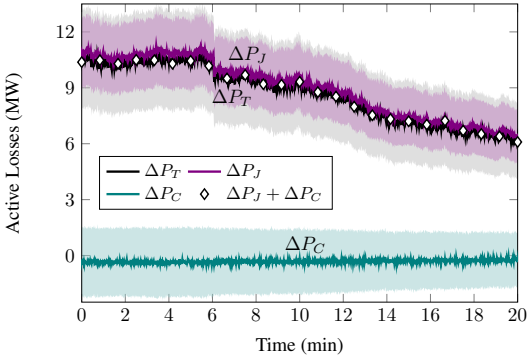


Figure 4: Results of PMU measurements on line L1, where total active transmission losses (ΔP_T) were computed as the direct difference in sent and received power and as components corresponding to losses dissipated in series resistances (ΔP_J) and shunt conductances (ΔP_C). Uncertainty intervals plotted as shaded areas.

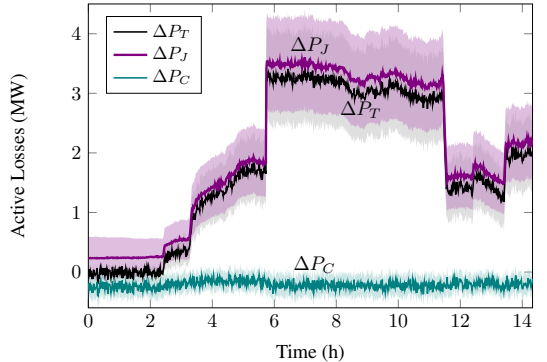


Figure 5: Results of PMU measurements on line L2, where total active transmission losses (ΔP_T) were computed as the direct difference in sent and received power and as components corresponding to losses dissipated in series resistances (ΔP_J) and shunt conductances (ΔP_C). Uncertainty intervals plotted as shaded areas.

MW to 200 MW. On the transmission line L1, the active losses were estimated as the real part of (17), i.e. $\Delta P_T = \text{Re}[\underline{\Delta S}_L]$, the values of ΔP_J and ΔP_C were estimated from (39) and (40), seen in Fig. 4. For comparison, the sum of ΔP_J and ΔP_C from (39) and (40) is also plotted in Fig. 4. Uncertainty intervals assuming maximum systematic errors from instrument transformers permitted by their accuracy classes are also plotted. These intervals show the minimum and maximum values the estimates could have if instrument transformers had the largest permitted errors and PMUs had errors as large as the limits given by the manufacturer (95% confidence).

On the transmission line L2, the total losses ΔP_T and the values of ΔP_J and ΔP_C were plotted, seen in Fig. 5. The estimates of reactive power consumed and generated in the line are presented in Fig. 6, where total losses are taken as the imaginary part of (17), i.e. $\Delta Q_T = \text{Im}[\underline{\Delta S}_L]$, and ΔQ_I and ΔQ_C are computed analogously to ΔP_J and ΔP_C with the corresponding estimates of x_0 , b_0 , x_+ , etc. Measurements were taken in fair weather conditions (10–20 °C ambient temperature, moderate wind, no precipitation). Uncertainty intervals for active losses and their components were calculated assuming approximated systematic errors based on instrument transformer error data given in Appendix A and maximum errors of PMUs specified by the manufacturer.

The data in Fig. 4 and Fig. 5 demonstrate similar behaviour on the two different transmission lines. In both cases, the estimate of ΔP_C was close to zero and invariant of changing transmitted power; however, the small values that were estimated were negative (discussed in more detail below). The estimate ΔP_J was close to total active losses, displaced by the value of ΔP_C . The two different equivalent estimates of total losses shown in Fig. 4 were indistinguishable from each other. Assuming more realistic instrument transformer errors approximated from manufacturer data resulted in smaller uncertainty intervals, es-

pecially for the estimates of corona losses.

In Fig. 6 the reactive power balance on line L2 is plotted, showing expected behaviour in the observed quantities. Inductive losses changed with load similarly to Joule losses, while capacitive generation changed little and followed voltage variations. Similar results were obtained from measurements on line L1, not plotted here. Uncertainties were too small to be distinguishable in the plot.

On line L2, another set of measurements was obtained in frosty weather when it was snowing. The same quantities, i.e. real part of total losses and ΔP_J and ΔP_C from (39) and (40), are plotted in Fig. 7. At the same level of total losses as in the previous data seen in Fig. 5, the share of ΔP_J and ΔP_C was noticeably different. During the time when active losses were at the same level in the first period, voltages differed less than 3% and currents up to 5%

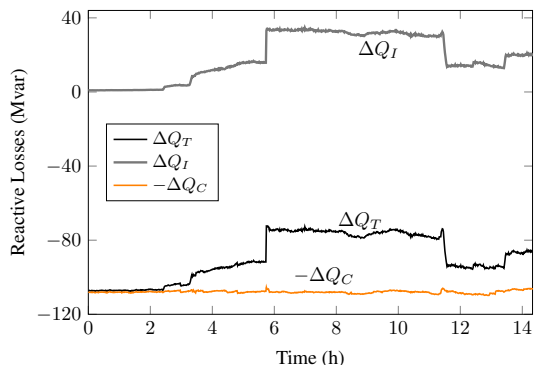


Figure 6: Results of PMU measurements on line L2, where total reactive transmission losses (ΔQ_T) were computed as the direct difference in sent and received power and as components corresponding to losses consumed in series reactances (ΔQ_I) and generated in shunt susceptances ($-\Delta Q_C$).

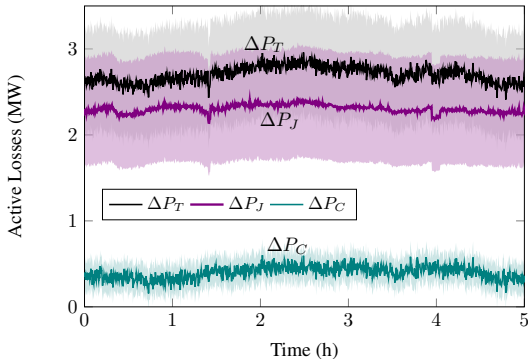


Figure 7: Results of PMU measurements on line L2, where total active transmission losses (ΔP_T) and its components (ΔP_J , ΔP_C) were calculated in frosty weather conditions. Uncertainty intervals plotted as shaded areas.

from the values in the second period. From the small negative values, the estimate of ΔP_C rose by about 0.5 MW (or 20% of total active losses) for the second measurement period. Uncertainties accounting for the possible effects of systematic errors from instrument transformers were similar to those in the first period. The estimated corona losses varied in time similarly to what has been shown in experiments with specialised measurement equipment [16].

The small consistent negative values in the loss component given by the shunt conductances in fair weather conditions are similar to the small erroneous estimates of active shunt losses that were seen in the simulations. However, the values were negative and slightly larger. It is assumed that in addition to the approximation errors, all estimates are also affected by errors in measurement accuracy. PMUs measure the data from the output channels of instrument transformers, which introduce small but present systematic errors that are propagated into the estimates [28, 33]. For this reason, the uncertainties of the estimates were also analysed and presented. The uncertainties consider the possible systematic errors introduced by the measurement devices and thus demonstrate the sensitivity to such errors.

5. Discussion

In the experimental results, values of components calculated from symmetrical components of voltages and currents were analysed and compared to direct differences in sent and received power. The inductive losses and capacitive generation were computed as separate components and behaved as expected. Active losses were separated into a component assumed to contain Joule losses in the series resistances while the second component was assumed to consist mostly of corona losses. Comparing measurements from fair weather and more corona prone weather gave the indication that corona losses can be estimated to a certain

degree, however the accuracy of this is hard to determine definitively. The experimental results were obtained only from single circuit transmission lines.

There are two factors that can affect the accuracy of obtained estimates: the simplification of using the symmetrical component transform and the accuracy of measured voltage and current phasors (which are the basis of all estimated quantities). On a single circuit line, it was shown both mathematically and by a simulation that the effect of the simplification is marginal. However, the accuracy of measured phasors can have a significant effect on the accuracy of estimated losses. An uncertainty analysis was carried out and the uncertainties of estimates are presented alongside the results. The uncertainty intervals show the possible effects of systematic errors from instrument transformers and PMUs.

In the estimated values of corona losses, the direction of the systematic errors should also be considered. When corona losses are expected to be small or close to zero and the estimated values are slightly below zero, there is a bias so that values of corona losses are underestimated. In the second measurement period, voltages, currents, and power were similar to the values of parts of the first period. During these similar periods, Joule losses were also similar, while there was a noticeable increase in corona losses. It is reasonable to assume that at this time, the systematic errors were also similar and it is more likely that corona losses were again underestimated rather than overestimated.

In general, if more accurate PMU measurements are desired, it would be recommendable not to overdimension measurement type current transformers but to select them according to real loading of transmission lines. At the same time, the burdens of instrument transformers should not be outside the tested ranges of burdens, i.e. the burden values the instrument transformers are designed for should also be considered. Any improvement in the accuracy of measuring voltages and currents would improve the estimates of components of losses.

Future work will mainly concentrate on the applicability of described measurements. The Estonian TSO, Elering has made preliminary tests of applying the data in transmission loss forecasting, with promising results. In the future, data from more transmission lines will be analysed for a better overview of the system. There is still a need to analyse the estimation of transmission losses from more accurate measurements of voltage and current phasors, which requires calibrated measurement equipment. Additionally, the estimated loss components would have to be compared to suitable reference measurements with better accuracy.

6. Conclusions

This paper proposes a novel approach to estimate separate components of losses on a transmission line as a sum of

losses dissipated in the respective elements of the transmission line model. In order to do this, the necessary expressions to calculate transmission losses from PMU measurements collected simultaneously from two ends of a multiconductor transmission line have been derived (for the general case of a single circuit three phase line).

With the results presented in this paper, it was shown that more information can be obtained about different types of transmission losses, e.g. changes in corona losses can be detected. Real-time monitoring of transmission losses and their components can be implemented at the cost of additional calculations on the measurement data. The method enables monitoring of instantaneous and recording of historical transmission loss data, with potential applications in transmission loss forecasting algorithms.

Acknowledgements

This work has been mainly sponsored by the Estonian TSO, Elering, with additional support from the STRONGrid research project and Tallinn University of Technology research grant B22.

- [1] Elering, Annual report (2016).
- [2] K. Tuttelberg, J. Kilter, Real-time estimation of transmission losses from PMU measurements, in: *Proceedings of PowerTech 2015*, Eindhoven, Netherlands, 2015. doi:10.1109/PTC.2015.7232313.
- [3] S. Kurokawa, G. A. Asti, E. C. M. Costa, J. Pissolato, Simplified procedure to estimate the resistance parameters of transmission lines, *Electrical Engineering* 95 (3) (2013) 221–227. doi:10.1007/s00202-012-0255-5.
- [4] S. Kurokawa, J. Pissolato, M. C. Tavares, C. M. Portela, A. J. Prado, A new procedure to derive transmission-line parameters: applications and restrictions, *Power Delivery, IEEE Transactions on* 21 (1) (2006) 492–498. doi:10.1109/TPWRD.2005.852296.
- [5] D. Shi, D. J. Tylavsky, K. M. Koellner, N. Logic, D. E. Wheeler, Transmission line parameter identification using PMU measurements, *European Transactions on Electrical Power* 21 (4) (2011) 1574–1588. doi:10.1002/etep.522.
- [6] C. Indulkar, K. Ramalingam, Estimation of transmission line parameters from measurements, *International Journal of Electrical Power & Energy Systems* 30 (5) (2008) 337–342. doi:10.1016/j.ijepes.2007.08.003.
- [7] S. S. Mousavi-Seyedi, F. Aminifar, S. Afsharnia, Parameter estimation of multiterminal transmission lines using joint PMU and SCADA data, *Power Delivery, IEEE Transactions on* 30 (3) (2015) 1077–1085. doi:10.1109/TPWRD.2014.2369500.
- [8] F. W. Peek, The law of corona and dielectric strength of air—II, *Proceedings of the American Institute of Electrical Engineers* 31 (6) (1912) 1085–1126. doi:10.1109/PAIEE.1912.6659840.
- [9] C. F. Harding, Corona losses between wires at high voltages, *Proceedings of the American Institute of Electrical Engineers* 31 (7) (1912) 1271–1285. doi:10.1109/PAIEE.1912.6660631.
- [10] F. W. Peek, Comparison of calculated and measured corona loss curves, *Transactions of the American Institute of Electrical Engineers* 34 (1) (1915) 269–278. doi:10.1109/T-AIEE.1915.4765217.
- [11] I. Baran, M. Costea, T. Leonida, On the possibility of using weather forecast to predict corona losses, in: *2013 8th International Symposium on Advanced Topics in Electrical Engineering (ATEE)*, 2013, pp. 1–6. doi:10.1109/ATEE.2013.6563437.
- [12] J. J. Clade, C. H. Gary, C. A. Lefevre, Calculation of corona losses beyond the critical gradient in alternating voltage, *IEEE Transactions on Power Apparatus and Systems PAS-88* (5) (1969) 695–703. doi:10.1109/TPAS.1969.292359.
- [13] O. Nigol, J. G. Cassan, Corona loss research at ontario hydro coldwater project, *Transactions of the American Institute of Electrical Engineers. Part III: Power Apparatus and Systems* 80 (3) (1961) 304–312. doi:10.1109/AIEEPAS.1961.4501032.
- [14] K. Lahti, M. Lahtinen, K. Nousiainen, Transmission line corona losses under hoar frost conditions, *IEEE Transactions on Power Delivery* 12 (2) (1997) 928–933. doi:10.1109/61.584415.
- [15] R. Wilkins, Corona loss tests on the 202-mile 60-cycle 220-Kv. pit-vaca transmission line of the pacific gas and electric company, *Transactions of the American Institute of Electrical Engineers XLIII* (1924) 1148–1171. doi:10.1109/T-AIEE.1924.5061066.
- [16] F. M. Cahen, J. M. Carteron, The french 380-Kv system - measurement of corona losses on transmission lines under normal operating conditions, *Transactions of the American Institute of Electrical Engineers. Part III: Power Apparatus and Systems* 76 (3) (1957) 1525–1531. doi:10.1109/AIEEPAS.1957.4499833.
- [17] V. L. Chartier, D. F. Shankie, N. Kolcio, The apple grove 750-kV project: Statistical analysis of radio influence and corona-loss performance of conductors at 775 kv, *IEEE Transactions on Power Apparatus and Systems PAS-89* (5) (1970) 867–881. doi:10.1109/TPAS.1970.292650.
- [18] F. J. Sollerkvist, A. Maxwell, K. Rouden, T. M. Ohnstad, Evaluation, verification and operational supervision of corona losses in Sweden, *Power Delivery, IEEE Transactions on* 22 (2) (2007) 1210–1217. doi:10.1109/TPWRD.2006.881598.
- [19] S. I. Sulakov, Forecasting hourly corona losses applying statistical approach, in: *2016 19th International Symposium on Electrical Apparatus and Technologies (SIELA)*, 2016, pp. 1–4. doi:10.1109/SIELA.2016.7543053.
- [20] R. Galloway, W. Shorrocks, L. Wedepohl, Calculation of electrical parameters for short and long polyphase transmission lines, *Proceedings of the IEE* 111 (12) (1964) 2051–2059. doi:10.1049/piee.1964.0331.
- [21] A. Déri, G. Tevan, Mathematical verification of Dubanton’s simplified calculation of overhead transmission line parameters and its physical interpretation, *Archiv für Elektrotechnik* 63 (4–5) (1981) 191–198. doi:10.1007/BF01574875.
- [22] J. B. Anderson (Ed.), *Analysis of Faulted Power Systems*, IEEE-Wiley, 1973.
- [23] L. M. Wedepohl, Application of matrix methods to the solution of travelling-wave phenomena in polyphase systems, *Proceedings of the IEE* 110 (12) (1963) 2200–2212. doi:10.1049/piee.1963.0314.
- [24] J.-C. Li, Y.-P. Wu, A distributed circuit model for three-phase transposed and untransposed transmission lines, *Electric Power Systems Research* 19 (3) (1990) 187 – 194. doi:10.1016/0378-7796(90)90031-W.
- [25] C. L. Fortescue, Method of symmetrical co-ordinates applied to the solution of polyphase networks, *Proceedings of the AIEE* 37 (6) (1918) 629–716. doi:10.1109/PAIEE.1918.6594104.
- [26] A. Morched, B. Gustavsen, M. Tartibi, A universal model for accurate calculation of electromagnetic transients on overhead lines and underground cables, *IEEE Transactions on Power Delivery* 14 (3) (1999) 1032–1038. doi:10.1109/61.772350.
- [27] B. Gustavsen, G. Irwin, R. Mangelrød, D. Brandt, K. Kent, Transmission line models for the simulation of interaction phenomena between parallel AC and DC overhead lines, in: *Proceedings of International Conference on Power System Transients, Budapest, Hungary*, 1999.
- [28] R. S. Singh, H. Hooshyar, L. Vanfretti, Assessment of time synchronization requirements for phasor measurement units, in: *Proceedings of PowerTech 2015*, Eindhoven, Netherlands, 2015. doi:10.1109/PTC.2015.7232728.
- [29] A. Monti, C. Muscas, F. Ponci (Eds.), *Phasor Measurement Units and Wide Area Monitoring Systems*, Academic Press, 2016.
- [30] JCGM, Evaluation of measurement data — supplement 2 to the “Guide to the expression of uncertainty in measurement” — extension to any number of output quantities, *Guide JCGM 102:2011* (2011).

- [31] B. D. Hall, On the propagation of uncertainty in complex-valued quantities, *Metrologia* 41 (3) (2004) 173–177. doi:10.1088/0026-1394/41/3/010.
- [32] B. D. Hall, Some considerations related to the evaluation of measurement uncertainty for complex-valued quantities in radio frequency measurements, *Metrologia* 44 (6) (2007) L62–L67.
- [33] K. Tuttleberg, J. Kilter, Uncertainty propagation in PMU-based transmission line monitoring, Submitted for review.
- [34] Instrument transformers — part 1: Current transformers, Standard IEC 60044-1:2002 (2002).
- [35] Instrument transformers — part 2: Inductive voltage transformers, Standard IEC 60044-2:2002 (2002).
- [36] J. H. Harlow, L. L. Grigsby, J. D. McDonald, *Electric Power Transformer Engineering*, CRC Press, 2012.

Appendix A. Instrument Transformer Errors

Instrument transformer measurement errors reported in factory test reports are given in Tables A.3–A.2. In the tables, U/U_n and I/I_n stand for ratios of measured and rated values. Magnitude errors are given in per cent and angle errors in minutes. Errors for each measurement point assumed in the uncertainty analysis were found by interpolating between the reported errors. The estimated burdens of the instrument transformers are as follows. At line end 1, current transformer burden 1.5 VA and voltage transformer burden 2.0 VA; at line end 2, current transformer burden 1.7 VA and voltage transformer burden 1.4 VA. Only the current transformer burden at end 1 fits between the tested burden values. It is not reasonable to assume that the errors can be extrapolated for a burden value outside of the range between the two tested burdens [36]. The other three burden values are replaced by the lowest burden values that measurement errors were reported for.

Table A.1: Current transformer errors on line L2 at end 1.

Burden 1 VA, power factor not specified						
I/I_n	Phase A		Phase B		Phase C	
	δI (%)	$\delta\varphi_I$ (')	δI (%)	$\delta\varphi_I$ (')	δI (%)	$\delta\varphi_I$ (')
1.2	0.03	0.0	0.02	0.0	0.07	0.0
1.0	0.028	0.18	0.02	0.18	0.066	0.36
0.2	0.021	0.9	0.02	0.9	0.053	1.8
0.05	0.02	1.0	0.02	1.0	0.05	2.0
0.01	0.02	2.0	0.03	2.0	0.05	3.0
Burden 5 VA, power factor not specified						
1.2	0.01	-1.0	-0.01	0.0	0.04	0.0
1.0	0.01	-1.0	0	-1.0	0.04	0.0
0.2	-0.02	0.0	-0.02	0.0	0.02	0.0
0.05	-0.04	1.0	-0.03	1.0	0.0	2.0
0.01	-0.04	3.0	-0.04	2.0	-0.01	3.0

Table A.2: Current transformer errors on line L2 at end 2.

Burden 5 VA, power factor 1						
I/I_n	Phase A		Phase B		Phase C	
	δI (%)	$\delta\varphi_I$ (')	δI (%)	$\delta\varphi_I$ (')	δI (%)	$\delta\varphi_I$ (')
1.2	-0.01	0.2	-0.01	0.1	-0.02	0.1
1.0	-0.01	0.5	-0.01	0.2	-0.02	0.2
0.2	-0.01	0.6	-0.01	0.7	-0.02	0.7
0.05	-0.01	1.0	-0.01	1.3	-0.01	1.3
0.01	0.01	2.6	0.0	2.9	0.0	2.9
Burden 20 VA, power factor 0.8						
1.2	-0.05	-0.7	-0.03	-0.9	-0.03	-1.0
1.0	-0.05	-0.3	-0.03	-0.8	-0.03	-0.8
0.2	-0.06	0.1	-0.045	0.2	-0.05	0.2
0.05	-0.06	0.9	-0.05	1.2	-0.06	1.2
0.01	-0.06	2.8	-0.05	2.9	-0.06	2.3

Table A.3: Voltage transformer errors on line L2 at end 1.

Burden 25 VA, power factor not specified						
U/U_n	Phase A		Phase B		Phase C	
	δU (%)	$\delta\varphi_U$ (')	δU (%)	$\delta\varphi_U$ (')	δU (%)	$\delta\varphi_U$ (')
1.5	0.04	5.0	0.06	5.0	0.06	4.0
1.2	0.12	2.0	0.12	3.0	0.12	2.0
1.0					0.14	1.0
0.8	0.16	1.0	0.15	1.0	0.15	1.0
0.05					0.15	7.0
0.02	0.2	6.0	0.2	8.0	0.21	10.0
Burden 100 VA, power factor not specified						
1.2	-0.14	4.0	-0.12	5.0	-0.13	4.0
1.0					-0.11	3.0
0.8	-0.1	2.0	-0.08	4.0	-0.11	3.0

Table A.4: Voltage transformer errors on line L2 at end 2.

Burden 25 VA, power factor 0.8						
U/U_n	Phase A		Phase B		Phase C	
	δU (%)	$\delta\varphi_U$ (')	δU (%)	$\delta\varphi_U$ (')	δU (%)	$\delta\varphi_U$ (')
1.5	0.37	2.5	0.39	2.4	0.38	3.1
1.2	0.37	2.8	0.39	2.4	0.38	3.1
1.0	0.37	2.8	0.39	2.4	0.38	3.1
0.8	0.37	2.9	0.39	2.9	0.38	3.1
0.05	0.41	8.7	0.41	8.7	0.41	8.7
Burden 100 VA, power factor 0.8						
1.5	-0.27	9.2	-0.27	9.2	-0.27	9.2
1.2	-0.29	9.4	-0.25	9.3	-0.26	10.4
1.0	-0.29	9.8	-0.25	9.3	-0.26	10.4
0.8	-0.29	10.2	-0.25	10	-0.26	10.4
0.05	-0.18	18	-0.18	18	-0.18	18

Publication III

K. Tuttelberg J. Kilter, D. Wilson, and K. Uhlen, "Estimation of power system inertia from ambient wide area measurements," in *IEEE Transactions on Power Systems*, accepted for publication.

© 2018 IEEE. Reprinted with permission

Estimation of Power System Inertia from Ambient Wide Area Measurements

Kaur Tuttelberg, *Student Member, IEEE*, Jako Kilter, *Senior Member, IEEE*,
Douglas Wilson, and Kjetil Uhlen, *Member, IEEE*

Abstract—This study presents a method of estimating the effective inertia of a power system from ambient frequency and active power signals measured by PMUs. Most importantly, we demonstrate that inertia can be estimated from ambient measurement data, not only from disturbances. This leads to the possibility of monitoring inertia in a close to continuous manner in the time scale of minutes or tens of minutes. The method allows the system to be divided into a number of areas and the effective inertia of each area to be estimated as a separate quantity. In principle, inertia is estimated by observing the dynamics between changes in active power and resulting frequency deviations during normal operation of the system. The method is based on applying system identification on these measurements and extracting inertia values from identified models. Efficacy of the method is demonstrated on results of real measurements from the Icelandic power system.

Index Terms—Frequency control, Frequency dynamics, Inertial response, Phasor measurement units, Wide area monitoring

I. INTRODUCTION

THE INCREASING share of power generating units connected to the system through power electronics is displacing synchronous generation. Larger penetration of renewable sources is both decreasing inertia [1], [2], [3] and changing its distribution in the system, leading to formation of low inertia areas [4], [5]. The associated challenges have been acknowledged and investigated in North America [1], [2], [6], [7], [8], Europe [4], [3], [9], Australia [10], [11], and elsewhere [5]. Some of the important arising questions are determining and monitoring values of inertia [2], [3], [9], considering the time varying nature of inertia [4], [12], and areas with low inertia [4], [5]. This study presents a method of estimating the inertia of different areas of the power system from ambient PMU measurements of active power and frequency. For a transmission system operator (TSO), the main requirement for monitoring the effective inertia of the system (or areas of it) is to estimate the time available to deploy a response, and to define the sensitivity between a frequency change and an appropriate corrective power response [2], [13].

K. Tuttelberg and J. Kilter are with the Department of Electrical Power Engineering and Mechatronics, Tallinn University of Technology, Tallinn, Estonia (e-mail of corresponding author: kaur.tuttelberg@tu.ee).

D. Wilson is with GE Grid Solutions, Edinburgh, United Kingdom.

K. Uhlen is with the Department of Electric Power Engineering, Norwegian University of Science and Technology, Trondheim, Norway.

This project has received funding from the European Union's Horizon 2020 research and innovation programme under grant agreement No 691800 (MIGRATE project).



With any attempt at estimating inertia in a power system it is important to discuss the definition of inertia, or in this case, *effective* inertia. Effective inertia defines the relationship between a change in the power balance of the system or area and the rate of change of frequency of that area, which differs from a more conventional interpretation of inertia related to physical spinning mass and inertia time constants. The majority of inertia in its conventional meaning is contributed by the physical spinning mass of synchronous generators, but there are other elements of the system that can contribute to the effective inertial response of the system [14] (and even more so in the future), e.g. voltage and frequency dependence of load and power electronic interfaces for generation, load, and storage. The method presented in this paper separates the system into areas and estimates the (effective) inertia of each area—area inertia—by observing the dynamics between active power and frequency changes.

The estimation of inertia from recorded disturbances has been researched and tested in recent years. Inertia values of single units [15], [16], system areas [17], [18], and entire systems [19], [20] have been derived from PMU measurements of frequency events. Inertia has also been approximated from other information, like statuses of generators or correlation with total demand [2], [3], [9]. However, no attempts of estimating inertia more continuously from ambient measurements have been demonstrated so far. Different related parameter and model identification methods have been presented, e.g. estimation of low-order dynamic equivalent models from PMU measurements has been proposed [21] and identification of governor models has been demonstrated on real PMU measurements [22], [23]. A previous paper from the authors presented a comparison of different system identification methods applied on similar measurement data as in this study [24].

The main complication in estimating inertia is that during normal operation, the inertial response of the system cannot readily be distinguished from frequency control, voltage control, electro-mechanical dynamics, and stabilizing actions. The proposed approach identifies a combined model of inertial response and primary control from measured ambient dynamics, circumventing this limitation. The inertia estimates are found by fitting a model to the observed dynamics and extracting parameters corresponding to inertia from the model. There is an inherent approximation in fitting the complex non-linear behavior of a power system to such a model; however, the simplification provides practically useful information for contracting and deploying frequency controls, including fast frequency response.

In this study, the proposed method is demonstrated on the example of the Icelandic power system and has been tested on real measurement data from this system. The Icelandic system is a relatively small isolated island with scattered generation and good coverage of PMU measurements. The method has been applied on ambient wide area measurements as intended. The models identified in the process of area inertia estimation have been validated on recorded frequency events. Even though testing the method on simulated data would give direct information about the accuracy of results in a controlled environment, testing it on real measurement data is significantly better for demonstrating its feasibility in real world conditions.

The theoretical background of the problem is covered in section II. The specifics of system identification and extraction of inertia values is described in section III. Test calculations on the measurements from the Icelandic power system are presented in section IV and discussed in section V. Conclusions are given in section VI.

II. THEORETICAL BACKGROUND

In order to discuss the proposed system identification, it is helpful to analyze a theoretical model of the dynamics we are interested in. In the following, a simplified model of the dynamics between active power and frequency is given. This is done in order to analyze what data is needed to identify a model for these kinds of dynamics. These models or these particular model structures will not be directly used in any estimations.

The dynamics between power and frequency during a short period of time following a power mismatch occurrence can be modelled by the swing equation. For a single generator i , the equation commonly used in power systems engineering is expressed as

$$\frac{df_i}{dt} = \frac{P_{iM} - P_{iE}}{2H_i S_{in}} f_n, \quad (1)$$

where P_{iM} is the output mechanical power of the machine, while P_{iE} is its electrical load power, f_i is the electrical frequency, H_i the inertia constant, S_{in} rated apparent power, and f_n the rated steady state frequency of the system. The model excludes damping effects and mechanical power is usually assumed to be constant.

As an approximation, an equivalent equation can be applied to an area of a system (or an entire system). For the aggregated frequency immediately after a load change in an area j we write another form of the swing equation

$$\frac{df_j}{dt} = \frac{P_{jM} - P_{jE}}{M_j} = \Delta P_j / M_j, \quad (2)$$

expressed in terms of M_j . In other publications, the quantity M_j has been defined in terms of angular frequency [25], [26], but in this paper, its value expressed for a single machine is $M_i = 2H_i S_{in} / f_n$, i.e. it is expressed in terms of frequency. In this paper, we assume this form of the swing equation and define the effective inertia of an area as a proportionality term between df_j/dt and ΔP_j , equivalent to M_j . It should be noted that if the effective inertia is deduced from observed

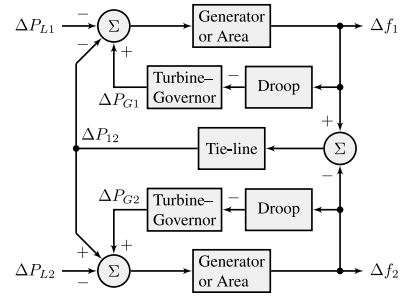


Fig. 1: Dynamic model of frequency control of a two-area power system with generator set-point changes disabled.

dynamics between power and frequency, then, contrary to its conventional definition, this proportionality term may also include other effects, not only the inertia of synchronous machines.

The inertia of a single synchronous machine is commonly represented by an inertia constant H , given in seconds. When several machines are lumped together, their inertia constants are weighted by the rated power of each machine. However, when observing the dynamics between active power and frequency, it is not practical to consider the rated power of every possible rotating machine and it is difficult to consider other possible effects contributing to the effective inertia. It is more convenient to use the single proportionality term M_j instead. By definition in the swing equation, it is effectively an angular momentum and its units are $J \cdot s$ or $W \cdot s^2$ [26].

Once the power mismatch event has occurred and frequency has started to deviate from its previous value, the frequency deviation is fed into a closed control loop, where governors counteract the power imbalance in the system. This control, mostly known as primary frequency control, but also frequency containment control, is carried out at the turbine-generator unit level. For a simpler analysis, we will look at this as a linear control system. The main components of a unit—the governor, the turbine, and the generator—are represented by corresponding transfer functions [27]. The inputs specify changes in the power set-point reference and load, while the output is the frequency deviation.

With a set of simplifications, an area of a power system (or an entire system) can be modeled similarly. In this case, the inertia of all rotating machines (and the frequency dependence of load) is lumped into a single area (or system) block and different governor-turbine systems are summed as parallel branches and lumped together by evaluating an equivalent droop. Based on that, a model for a multi-area interconnected system can be obtained by including tie-line elements that model the power exchanges between the areas [27]. The tie-lines are modeled as basic integrator blocks with a gain determined by line parameters.

This model can be simplified further when we analyze only primary frequency control, i.e. model the dynamics before any secondary control would be issued. In this case the power set-point values of generators remain unchanged and the corresponding inputs in the control system can be disregarded. A

schematic of the model following that is given in Fig. 1, where ΔP_{Li} are the changes in load of each area and $\Delta f_i = f_i - f_n$ the frequency deviations. In this simplified analysis of the dynamics of inertial response and frequency control, the multi-area system becomes a multi-input multi-output system with load changes as inputs and frequency changes as outputs.

The described model treats each area as a single node with aggregated load, generation, and control loops and a unified value of frequency. In such a model it is important to define areas that on a system level can be aggregated. The described treatment is also dependent on the possibility of analyzing the system in a period of time when the power set-points of all of the generators remain unchanged or change very little (i.e. $\forall i : \Delta P_{Ri} \approx 0$).

III. SYSTEM IDENTIFICATION

It is proposed that once a power system has been divided into a number of appropriately defined areas, an approximate control system modelling the dynamics between frequency and active power can be identified. This is based on the assumption that the dynamics can be approximated as a linear control system with a structure that is in principle similar (but not necessarily identical) to the model discussed in the previous section (as in Fig. 1). During periods of time when generator set-points are not changed, the model can be assumed to have load changes as inputs and frequency deviations as outputs. If sufficient measurement data is available, it is possible to fit a model to the observed dynamics between the inputs and the corresponding outputs. Among other parameters, this model would include the inertia of each area.

A. Inputs and Outputs

The proposed methodology can only be applied on areas that are aggregated meaningfully, with two main requirements. The areas have to be consistent in terms of network topology—all nodes forming an area have to be directly connected to at least one other node of the area and areas have to be separable by clear boundaries. More importantly, the areas should consist of nodes that have frequencies close to each other. This is simple to understand with the example of inter-area oscillations, where the frequencies of the nodes in one area oscillate against the frequencies of the nodes forming another area. Knowledge about such areas in the power system can be used as a basis and analysis of measured frequency signals can be used to refine the separation into areas.

When an area is aggregated in order to model it similarly to the control system in Fig. 1, its center of inertia frequency is commonly used [26]. The center of inertia frequency is evaluated as a weighted average of frequencies

$$f_{COI} = \frac{\sum_i^N H_i S_{in} f_i}{\sum_i^N H_i S_{in}}, \quad (3)$$

where f_i are the frequencies of all of the N nodes comprising the area weighted by the inertia of each node (nodes assumed to include no inertia are effectively excluded). Clearly, a degree of prior knowledge about inertia values of larger generators across the area is assumed when evaluating this quantity.

In this method, we use an aggregated area frequency that is a simplification of the center of inertia frequency. The frequency of area j is evaluated as a weighted average of measured frequencies

$$f_j = \frac{\sum_i^{N_j} w_i f_i}{\sum_i^{N_j} w_i}, \quad (4)$$

where f_i are the frequencies of the N_j nodes that are measured in area j . The weights w_i are picked based on analyzing the system and selecting frequency signals that reflect the general distribution of inertia in each area. The weights should consider which nodes contribute more to the inertia of the area but also consider its possible variability in time and the quality of frequency signals. In the simplest case, all nodes which are assumed to contribute some inertia are weighted equally and all other measured nodes weighted by zero.

In system identification, the input–output data can be pre-processed in different ways. It is common to subtract either the mean value or the first value of the time series, but sometimes the data is also detrended or processed in other ways [28]. Since we know the nominal value of frequency that the control system is attempting to achieve, it is possible to use the deviations from nominal frequency as the outputs. After evaluating the aggregated value, the frequency deviation in area j can be expressed as

$$\Delta f_j = f_j - f_n, \quad (5)$$

which is the j th output of the identified system.

Once the areas are formed and aggregated, it would be simple in principle to sum up all load changes in the areas to determine the inputs of the system. However, in order to do this directly, it would have to be possible to monitor the majority of load. Measuring load has not been the first priority when allocating PMU measurement resources and even if it becomes more common to monitor load feeders, it would take time until a sufficient share of them are covered. This means that more common PMU measurements have to be used to approximate the changes in load. When PMUs are installed in the system, they are most often set up to measure power flows on transmission lines, followed by monitoring of generators.

Fortunately, if power flows between the defined areas and a majority of generators that participate in primary frequency control can be monitored, it is possible to approximate load changes. The main assumption is that when small changes over time are considered, the changes in load and generation are sufficiently close to each other. The approximate change in load in area j would thus be

$$\Delta P_{Lj} \cong \sum_i \Delta P_{Gji} + \sum_k \Delta P_{Tjk} \quad (6)$$

where ΔP_{Gji} is the change in output power of the i th generator (or a group of generators) participating in primary frequency control in area j and ΔP_{Tjk} is the change in power transmitted from the k th to the j th area. All changes are evaluated with respect to the first value in the time series, i.e. $\Delta P = 0$ at $t = 0$.

In order to identify the dynamics between load changes and resulting frequency deviations it is necessary to monitor the

system for a sufficiently long period. Following a disturbance, the inertial response in frequency can be seen in the first few seconds, while the primary control (governor) response takes place in a time frame of tens of seconds. It can be assumed that a period of at least 1...2 minutes should be observed in order to capture enough variations in the system, but the period should not have to exceed 10 minutes. In practice, measurement periods of 2...6 minutes have been applied.

There are two main considerations to take into account while selecting the measurement periods. Firstly, these periods should exclude any time when automatic generation control (AGC) is acting or any other generator set-point changes are being made. A simple way to handle this is to consider the time these actions are executed and assume a buffer time for the associated effects to take place (e.g. 60 to 90 s). Secondly, it would be advisable to start and end the measurement periods at instances when area rate of change of frequency (i.e. df/dt or RoCoF) crosses zero. This is done in order to improve the efficiency of the system identification algorithm. This is relatively simple to implement even with noisy RoCoF measurements from PMUs.

B. System Identification

The next part of the estimation process is applying system identification on the obtained input–output data. Ambient load variations are generally small and they excite the dynamic system weakly. This means that a suitable system identification procedure is needed that is not sensitive to the low level of excitation. Some aspects of this problem have been studied in previous work, comparing various system identification methods applied in a similar way but with the example of analysing inter-area modes [24].

Regardless of which system identification method is used, a certain model order has to be specified. Even a small area of a power system contains many complicated control systems, making it very difficult to determine a correct order for such a model. However, most of the relevant dynamics of the system can be captured by a lower order model and the particular order itself may vary to some extent [24]. The order has to be large enough to capture the main dynamics but should still be small enough not to become too complicated or computationally expensive. In fact, it is possible to identify models of various orders from the same dataset and obtain a number of similar estimates [24].

The System Identification Toolbox in Matlab offers a selection of ready to use system identification tools and has been used in the presented method [28]. In a comparison of available identification algorithms, it was determined that the implementation of ARMAX is the best suited and most robust tool for the given type of problem [24]. The procedure presented in this paper uses this system identification method, but the general concept of area inertia estimation is not dependent on this particular implementation. Due to the complexity of identifying systems with many inputs and outputs, it would be recommendable to divide the system into two to four main areas of interest.

ARMAX in Matlab is a system identification technique based on the autoregressive–moving-average model with ex-

ogenous inputs. It results in a polynomial model, which is a generalized variant of a transfer function, expressing a relationship between an input, an output, and a noise term [28]. For a multi-input–multi-output (MIMO) ARMAX model with n_u inputs and n_y outputs, the input–output relationships for the l th output of the model can be expressed as

$$\sum_{j=1}^{n_y} A_{lj}(q)y_j(t) = \sum_{i=1}^{n_u} B_{li}(q)u_i(t - n_{ki}) + C_l(q)e_l(t), \quad (7)$$

where A_{lj} , B_{li} , and C_l are polynomials of orders n_A , n_B , and n_C expressed in q^{-1} , and n_{ki} are the input–output delays in terms of number of samples. Polynomial models are discrete time (i.e. z -domain) linear systems and in this application the time step is determined by the sampling rate of PMU measurements.

Due to the nature of the system identification problem that was set up, the models have an equal number of inputs and outputs corresponding to the number of areas the system is divided into. As noted earlier, we apply system identification that attempts to fit a number of models in a range of orders $n = n_{\min}, \dots, n_{\max}$ for each dataset. Within each iterated order, the various variables defining model order are equal, i.e. $n = n_A = n_B = n_C$. All input–output relationships are symmetric in the sense that in each identification attempt elements of the order matrices are equal. Input–output delays n_{ki} are determined with tools provided in Matlab once for a given system and assumed constant after that (a default value of zero is also sufficient in practice).

C. Inertia Estimation

Once we have identified approximate models describing the dynamics between load changes and frequency variations, it is still necessary to determine the effective inertia of each area. The ARMAX models include the effective inertia but not as an explicit value, thus, it is necessary to further analyze the identified models. A simple way to obtain results is to evaluate the step response of the ARMAX model and observe its initial slope. However, if sufficiently good models are identified, it is possible to extract inertia values from their parameters. One possible procedure for that is presented below.

First of all, the discrete time ARMAX models are converted into continuous time using the `d2c` function in Matlab. This is not successful in every case and the resulting models are checked once again for stability, this time with the s -domain criterion (real part of poles should be less than zero). The remaining polynomial models are ready to be reduced to lower order transfer functions.

The continuous time models are reduced to a lower order using a set of functions available in Matlab. The models are first transformed into a balanced state-space realization. Next, insignificant states are identified and removed to form a reduced order system. The system is then transformed from the state-space representation into a continuous time transfer function. This is done using the `ssdata`, `balreal`, `modred`, and `ss2tf` functions in the System Identification Toolbox [29].

The expected structure of the transfer functions is of the generic form

$$H(s) = \frac{b_{n-1}s^{n-1} + b_{n-2}s^{n-2} + \dots + b_0}{a_n s^n + a_{n-1}s^{n-1} + \dots + a_0}. \quad (8)$$

The `ss2tf` tends to give marginal but non-zero values for the term b_n , resulting in the same dynamics but a different formal structure. In order to simplify the estimation of the effective inertia values, these b_n terms are set to zero in the presented implementation.

To understand how the effective inertia can be determined, we can look at a simplified example. If we have a single unit with no governor or frequency control, we can model the swing equation as a first order transfer function

$$H(s) = \frac{1}{Ms + D} = \frac{1/M}{s + D/M}, \quad (9)$$

where M is the effective inertia and D is frequency dependence of load [27]. The unit impulse response of this system is given by

$$h(t) = \frac{1}{M} \exp\left(-\frac{D}{M}t\right). \quad (10)$$

Clearly, instantly after the perturbation, at $t = 0$, the impulse response is equal to the inverse of the effective inertia. More precisely, the initial response of the system to a load disturbance is what we consider to be the effective inertia. Because we use load changes as inputs, the proportionality term is negative, i.e. $h(0) = -1/M$.

The identified transfer functions are more detailed than the single machine model without controls. However, the inertial response is still the fastest acting and we can assume that it determines the first instance of the impulse response. This means that the inertia of each area can be determined by the value of its unit impulse response at $t = 0$. For a transfer function with the structure given in (8), the estimates—i.e. the first value of the impulse response—can be evaluated either with the impulse function, as the gain value of the zero-pole model from `tf2zpk` or most simply as the ratio of a_n to $-b_{n-1}$.

In the MIMO model it is also possible to determine the impulse response of the system, which provides an additional estimate of total system inertia (in addition to the sum of area inertia values). This is based on the principle that system COI frequency is an average of area frequencies weighted by the inertia of each area. Once area inertia values have been determined, it is possible to calculate system inertia from the unit impulse response of the whole system.

Based on responses of all N areas to a unit impulse in area k , the system inertia can be expressed as

$$M_{Sk} = -\frac{\sum_{i=1}^N 1/h_{ii}(0)}{\sum_{i=1}^N h_{ki}(0)/h_{ii}(0)}, \quad (11)$$

where $h_{ki}(0)$ is the response of the i th output of the MIMO system at time $t = 0$ to a unit impulse in the k th input. The $1/h_{ii}(0)$ values correspond to the effective inertia of each area and weight the output frequency deviation of each area so that the sum corresponds to the system COI frequency. It has been

observed that in practice these estimates tend to have a lower variance than the sum of area inertia values.

One of the important aspects of the presented method is that several estimates are obtained from one period of monitoring data. The multiple ARMAX models identified with various model orders provide a number of estimates for area inertia, which can then be averaged. However, there are commonly a few poorly identified models that introduce outliers far from a realistic inertia value, which have to be detected and removed.

We propose to use the median absolute deviation (MAD), a robust median based statistic, defined as [30], [31], [32]

$$s_{\text{MAD}}(X) = c \text{med}(|X - \text{med}(X)|), \quad (12)$$

where $\text{med}(X)$ denotes the median of a sample $X = \{x_i \mid i = 1, \dots, n\}$, x_i are the values in that sample, and c is a term introduced to achieve consistency with the standard deviation of a certain distribution [31]. Any value x_i for which

$$\frac{|x_i - \text{med}(X)|}{s_{\text{MAD}}(X)} > k \quad (13)$$

is considered an outlier and discarded. The cut-off factor k is chosen in conjunction with c and the assumed distribution. If a normal distribution is assumed, c takes the value of 1.4826 and k can be set to 2 for a 95% interval and 3 for a 99% interval [31].

IV. TEST CALCULATIONS

A. Test System

The method has been tested on the Icelandic power system. The Icelandic system is a relatively small island system with a typical load around 1...2 GW and total installed generating capacity of 3 GW. In present terms, the system has a large number of PMU measurement points relative to its size, with more than 30 PMUs and around 200 measured voltage and current signals. A simplified schematic of the system is given in Fig. 2. The schematic includes all significant buses, generators, and lines and four large industrial loads, denoted by ILA, ILB, ILC, and ILZ. Total MVA ratings of power plants are given next to the symbols. The transmission system operator did not have a method of estimating or monitoring inertia at the time of this study.

Generators colored black in Fig. 2 are monitored directly by PMUs, i.e. their power flows are measured. However, generators in blue are not monitored yet and their output power flows are approximated. The simpler approximations are that the power flows on lines LA1, LF1, VF1, and SP2 are used as power measurements of the generators at LAX, LAG, VAF, and MJO respectively. Power flows on lines SN1 and FI2 are used to approximate the changes in generation at SVA and REY, units in the smaller area bounded by the blue dashed line. Additionally, all of the generation in the larger area bounded by the blue dashed line is approximated by power flows into or out of that area. These approximations may affect the accuracy of the results, but are sufficient to enable the application of this method.

The system has two main load centers, one in the west and one in the east. In terms of centers of inertia (COI), the

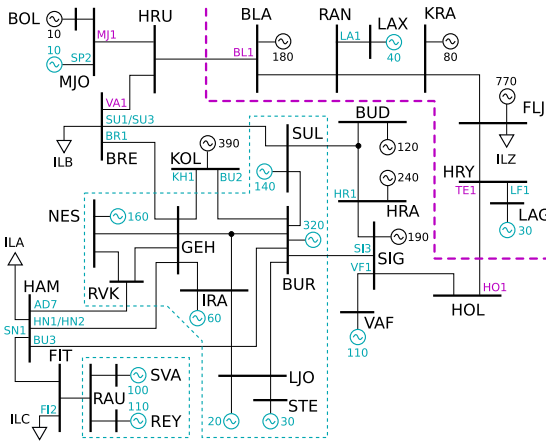


Fig. 2: Simplified schematic of the Icelandic power system. Larger black labels denote substations, smaller colored labels denote transmission lines. Total rated MVA of all generators at each plant given next to symbol.

system can be split quite naturally from the two long lines that connect these two areas, even though border nodes can deviate somewhat from their assigned area. The purple dashed line in Fig. 2 shows this split. Line labels written in purple denote the power flow measurements used to calculate area boundary power flows. Load variations are approximated based on (6), including the approximations used to find changes in power generated by the units that are not monitored.

Frequencies at KOL, SIG, HRA, and BUD were used for the western part and weighted by 1.5, 1.0, 1.0, and 0.5, and FLJ, KRA, and BLA were assigned to the eastern part with weights of 3.0, 1.0, and 0.5, respectively. The weight of BLA was set lower because it is a border node and its frequency differs more from frequencies of other nodes. These weights apply to area COI frequencies, not a whole system COI frequency. Frequency deviations were calculated for the aggregated areas using (4) and (5). It has been observed that in practice such an approach to evaluating area frequency and estimating effective area inertia is not very sensitive to the weights, meaning that crude assumptions are sufficient.

B. Validation of Method

The method was validated on a combination of measurements from both ambient conditions and frequency disturbances. The effective area inertia values were estimated from ambient measurements using the presented method. All measurements had a 50 Hz sampling rate. The measurements were gathered from time periods preceding frequency disturbances, meaning that the inertia values were estimated right before the events. The disturbances were then used to analyze the performance of the method. A total of 16 events were selected for the study, 14 of these were load trips (industrial loads at either ILA, ILB or ILC) and two were generator trips. Only so-called “clean” events were selected, i.e. disturbances where a single unit tripped at a moment when the system could be considered to be in steady-state and no other disturbance

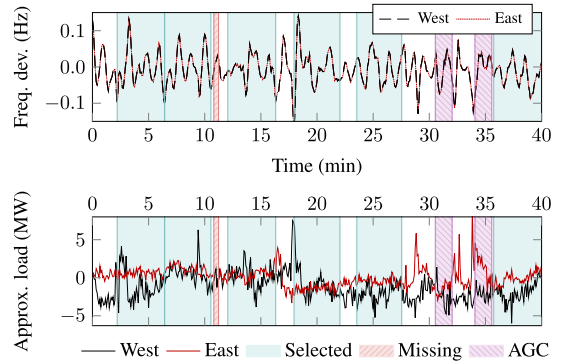


Fig. 3: Example of monitoring data used for the estimation of effective area and system inertia. Frequency deviations and load, approximated as in (6), plotted for the western and eastern areas. Six selected measurements, periods with missing data, and AGC operation marked by shaded areas.

followed immediately. All disturbances took place in the western part of the system.

The accuracy of estimated inertia values was quantified by a comparison of the RoCoF of the recorded event and the corresponding RoCoF predicted from the inertia value for the given disturbance. From the disturbances, RoCoF was estimated as the slope of a linear fit to measured frequency during the period of 0.2 to 0.4 s after the trip. The jump in frequency is a measurement effect of the disturbance causing a step change in voltage phase angle, which cleared in 160 ms in most cases but an additional 2 cycle margin was assumed. The change in load, i.e. ΔP , was determined from the measured power at the tripped unit as the largest deviation during the first 0.3 s after the trip.

System identification was applied so that ARMAX models of orders 9 to 28 were identified, i.e. 20 models with different model orders. In each case with six consecutive measurement periods, the first identification was made with five iterations and each following made with three iterations using the results of the previous measurement as a starting point. The least squares non-linear fitting method was used inside the ARMAX routine and the input–output delay was set to zero. Identified models were reduced to 4th order transfer functions. MAD based outlier detection assumed a normal distribution and a 95% confidence interval.

C. Inertia Estimation Results

In order to explain the application of the method better, a little over 40 minutes of monitoring data is presented in Fig. 3 as an example of input data. From this longer period, six smaller sets of measurement data were selected by a preprocessing algorithm. In the algorithm, a minimum length (4 min in this case) was specified and measurement periods were selected so that they started and ended at $df/dt = 0$, while avoiding moments when data was missing or AGC was operating. All of this is from ambient conditions, preceding a load trip that took place 42 minutes after the start of monitoring.

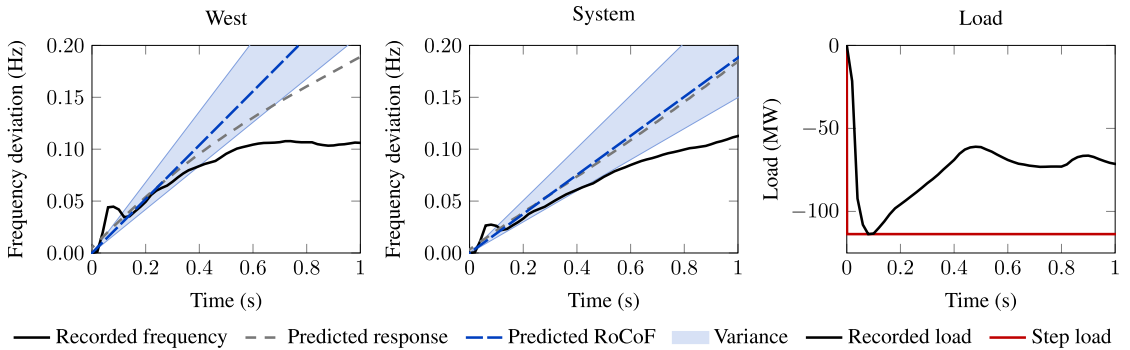


Fig. 4: Details of validation with event number 16. Measured COI frequency in the western area and entire system plotted in left and center graphs, alongside the responses predicted by the identified models and RoCoF slopes predicted from estimated inertia. Predictions were based on pre-event ambient data. Variance in predicted RoCoF based on two standard deviations of all inertia values given as shaded area. Rightmost graph shows the measured power at the tripped unit and the equivalent step signal used as the input of identified models. The magnitude of the step was also used as the ΔP when predicting RoCoF.

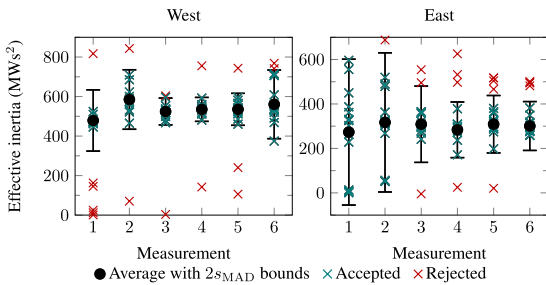


Fig. 5: Individual inertia estimates from the six measurements. Average inertia for each measurement is plotted, alongside all accepted values and outliers that were rejected based on the MAD criterion.

The main results of the method are presented in Fig. 5, where estimates of inertia from each measurement period are plotted. The figure shows individual estimates extracted from individual models and presents which values were accepted and which rejected as outliers. It also gives the average inertia value estimated from each measurement and shows the bound based on the MAD method that was used to detect outliers.

Following that, the results of the six measurements before the disturbance were further combined, decreasing variance in the estimates of inertia. The value of effective inertia estimated from the ambient monitoring data was then used to predict the RoCoF of the following frequency disturbance in each of the 16 cases. However, the cases were also analyzed in detail in order to validate the results more thoroughly. For this, the recorded frequency excursions were visually compared to predictions from the identified models and a RoCoF slope based on the estimated inertia. Recorded power of each tripped unit was used to determine the amount of load or power lost in the event. Fig. 4 presents this kind of validation of the case that showed the largest difference between predicted and comparison RoCoF values (area and system combined).

Measurements from all 16 cases were processed with the proposed method and effective inertia of the western part and

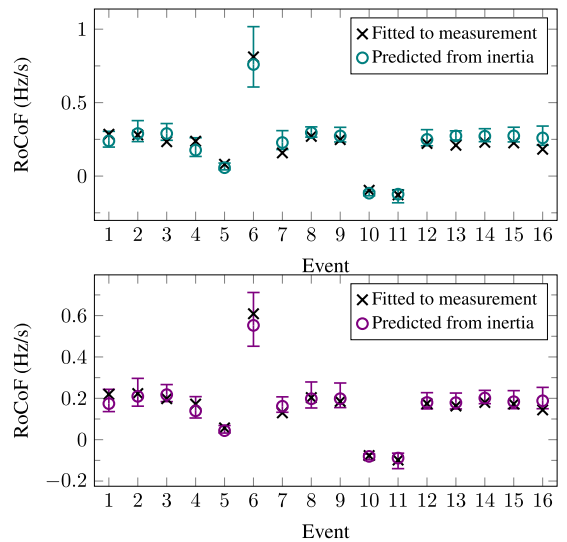


Fig. 6: Comparison of approximate RoCoF after each disturbances and corresponding RoCoF predicted from estimated inertia values for the western area (top) and the entire system (bottom). Variance bounds based on two standard deviations of all inertia samples of each case.

the entire system were estimated. However, there were no reference values of inertia with known accuracy available to compare them to. In order to analyze the overall performance of the method, RoCoF values were compared instead. For each event, a RoCoF value and the amount of load (or generation) lost were estimated from the PMU measurements. The inertia values estimated from ambient measurements before the events were used to predict RoCoF values of corresponding disturbances.

A comparison of these results over all 16 cases are presented in Fig. 6 for the western area and the whole system. (No suitable validation events occurred in the eastern part of the system.) Differences between RoCoF values estimated from

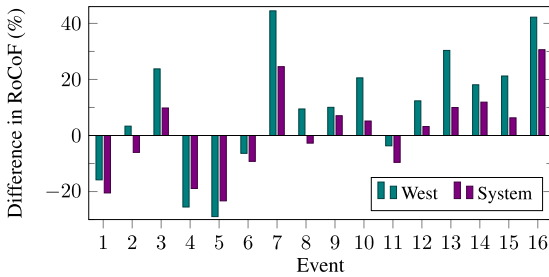


Fig. 7: Differences between approximate RoCoF and the corresponding value predicted from estimated inertia. Per cent difference of prediction from approximate RoCoF is given.

recorded frequencies and predicted from inertia values are presented in Fig. 7. The average difference was 20% for the western area and 12% for the whole system. However, these should not be seen strictly as errors, since the RoCoF and ΔP values of the events were also approximated. For example, in validation event 16 shown in Fig. 4, the first swing in the frequency of the western area started before 0.3 s, meaning the linear fit between 0.2 and 0.4 s was incorrect.

In computation time, processing one measurement period took around 20...50% of its length using a single core on a regular office laptop (Core i5-4200U@1.6 GHz, 12GB RAM). If the total length of all measurement periods in all 16 cases was 380 min then the total time the code took to process all of it was 140 min. On average it took 22 s to analyze one minute of monitoring data or 37% of its length.

V. DISCUSSION

The method is based on first identifying the combined inertial and primary control response of the system and then extracting the value of inertia. This means that in order to find a good estimate of inertia, it is necessary that the inertial response is captured well enough in the identified system. The inertial and primary control responses can only be clearly separated in case of a distinct frequency disturbance. For these reasons, the models identified from ambient measurements were validated by comparing their inertial responses to recorded frequency disturbances.

Results of system identification were validated this way in all 16 cases. However, it is very difficult to quantify the quality of a model in this comparison. A scalar difference between the recorded and predicted time series could not consider the different dynamics in the system and was not suitable in many cases. Neither auto-correlation nor prediction error analysis could reliably describe the quality of identified models. Therefore, this type of validation was made as a visual comparison, with one example given in Fig. 4.

It was seen in the estimates of inertia (Fig. 5, measurements 1 and 2 of eastern area) that some results are clearly incorrect. The method is based on averaging a large number of estimates and detecting and removing outliers is an important part of that. While the MAD based outlier detection was suitable in most cases, in the example presented in Fig. 5 measurements 1 and 2 for the eastern part of the system showed that it does

not always perform ideally. However, for the bounds based on MAD to be very wide, there has to be a similar number of values that are clearly underestimating and overestimating the real value, meaning the average result is not significantly distorted as errors are canceled out.

It is nevertheless important to quantify the accuracy of the method and in order to do that, a comparison of RoCoF values was carried out. It is possible to analyze a recorded frequency excursion and approximate a RoCoF value based on a linear fit during a certain period of the measurement. In this study, it was also possible to monitor the power of the tripped units and determine the change in load during the disturbance. Based on estimated inertia values, it was then possible to calculate another RoCoF value from the ratio of change in power to inertia. These two RoCoF values could be directly compared to each other as seen in Fig. 6 and Fig. 7.

Even though the reference RoCoF from each disturbance was also approximated and not correct in every case (e.g. event 16), this comparison over 16 different cases still offers insight into the expected accuracy of the method. The differences ranged from a few per cent up to around 40% in a few cases, with a 12% average in values for the entire system and 20% for the western area. A very important result is that considering variance bounds, not a single prediction underestimated the RoCoF value caused by the disturbance. Even though some estimated effective inertia values predicted a slightly lower RoCoF, the upper bound gave a sufficiently conservative value in each case.

The computational cost of the algorithm is considerable and the time taken to process one measurement period can be in the same order of magnitude as its length. In the presented results, it took 20...50% of the length of the measurement period. If an average monitoring period of 4 min was assumed, then an on-line application could give the average effective inertia of this period 5...6 min after the start of measurement. The bulk of the computational work could be run in parallel (every model order is independent) and significantly shorter running times could be achieved on a more powerful computer. On the other hand, increasing the number of input-output pairs would increase the computational burden.

VI. CONCLUSIONS

The paper presented a method of estimating the effective inertia of a system and its areas from ambient wide area measurements, i.e. during normal system operation. The developed method would enable a close to continuous and close to real-time monitoring of inertia. The method is based on identifying both the inertial response and primary frequency control in the dynamics between active power and frequency.

The most important result of the work is demonstrating that effective inertia can be monitored based on ambient measurements, not only frequency disturbances. Thus, a TSO can determine the time available to deploy frequency response before frequency thresholds are crossed and load is lost or other secondary disturbances occur. This means that the amount of fast-acting reserve can be identified and allocated per area of the power system, and the response time requirements specified. While there is sometimes a sizable spread in

estimates, it was possible to determine a conservative estimate to define the maximum expected RoCoF in every disturbance case.

VII. ACKNOWLEDGMENT

We would like to thank Landsnet, the Icelandic TSO for providing measurement data for the study, with special thanks to Ragnar Gudmansson and Birkir Heimisson. We would also like to acknowledge Colin Foote (SP Energy Networks) for helpful comments about the manuscript.

REFERENCES

- [1] V. Gevorgian, Y. Zhang, and E. Ela, "Investigating the impacts of wind generation participation in interconnection frequency response," *IEEE Transactions on Sustainable Energy*, vol. 6, no. 3, pp. 1004–1012, July 2015.
- [2] S. Sharma, S. H. Huang, and N. Sarma, "System inertial frequency response estimation and impact of renewable resources in ERCOT interconnection," in *2011 IEEE Power and Energy Society General Meeting*, July 2011, pp. 1–6.
- [3] E. Ørum, M. Kuivaniemi, M. Laasonen, A. Bruseth, E. Jansson, A. Danell, K. Elkington, and N. Modig, "Future system inertia," ENTSO-E Nordic Analysis Group, Tech. Rep., 2015.
- [4] "Frequency stability evaluation criteria for the synchronous zone of continental Europe," ENTSO-E RG-CE System Protection & Dynamics Sub Group, Tech. Rep., March 2016.
- [5] H. Pulgar-Painemal, Y. Wang, and H. Silva-Saravia, "On inertia distribution, inter-area oscillations and location of electronically-interfaced resources," *IEEE Transactions on Power Systems*, vol. 33, no. 1, pp. 995–1003, Jan 2018.
- [6] J. Conto, "Grid challenges on high penetration levels of wind power," in *2012 IEEE Power and Energy Society General Meeting*, July 2012, pp. 1–3.
- [7] N. W. Miller, M. Shao, S. Venkataraman, C. Loutan, and M. Rothleder, "Frequency response of California and WECC under high wind and solar conditions," in *2012 IEEE Power and Energy Society General Meeting*, July 2012, pp. 1–8.
- [8] N. W. Miller, M. Shao, R. D'aquila, S. Pajic, and K. Clark, "Frequency response of the US Eastern Interconnection under conditions of high wind and solar generation," in *2015 Seventh Annual IEEE Green Technologies Conference*, April 2015, pp. 21–28.
- [9] I. Dudurych, M. Burke, L. Fisher, M. Eager, and K. Kelly, "Operational security challenges and tools for a synchronous power system with high penetration of non-conventional sources," *CIGRE Science & Engineering*, vol. 7, February 2017.
- [10] H. Gu, R. Yan, and T. K. Saha, "Minimum synchronous inertia requirement of renewable power systems," *IEEE Transactions on Power Systems*, vol. PP, no. 99, pp. 1–1, 2017.
- [11] R. Yan, T. K. Saha, N. Modi, N.-A. Masood, and M. Mosadeghy, "The combined effects of high penetration of wind and PV on power system frequency response," *Applied Energy*, vol. 145, pp. 320 – 330, 2015.
- [12] V. Trovato, I. M. Sanz, B. Chaudhuri, and G. Strbac, "Advanced control of thermostatic loads for rapid frequency response in Great Britain," *IEEE Transactions on Power Systems*, vol. 32, no. 3, pp. 2106–2117, May 2017.
- [13] W. Li, P. Du, and N. Lu, "Design of a new primary frequency control market for hosting frequency response reserve offers from both generators and loads," *IEEE Transactions on Smart Grid*, vol. PP, no. 99, pp. 1–1, 2017.
- [14] Y. Bian, H. Wyman-Pain, F. Li, R. Bhakar, S. Mishra, and N. P. Padhy, "Demand side contributions for system inertia in the GB power system," *IEEE Transactions on Power Systems*, vol. PP, no. 99, pp. 1–1, 2017.
- [15] P. Wall and V. Terzija, "Simultaneous estimation of the time of disturbance and inertia in power systems," *IEEE Transactions on Power Delivery*, vol. 29, no. 4, pp. 2018–2031, Aug 2014.
- [16] P. Wall, P. Regulski, Z. Rusidovic, and V. Terzija, "Inertia estimation using PMUs in a laboratory," in *IEEE PES Innovative Smart Grid Technologies, Europe*, Oct 2014, pp. 1–6.
- [17] G. Chavan, M. Weiss, A. Chakraborty, S. Bhattacharya, A. Salazar, and F. H. Ashrafi, "Identification and predictive analysis of a multi-area WECC power system model using synchrophasors," *IEEE Transactions on Smart Grid*, vol. 8, no. 4, pp. 1977–1986, July 2017.
- [18] J. D. Lara-Jimenez, J. M. Ramirez, and F. Mancilla-David, "Allocation of pmus for power system-wide inertial frequency response estimation," *IET Generation, Transmission Distribution*, vol. 11, no. 11, pp. 2902–2911, 2017.
- [19] P. M. Ashton, C. S. Saunders, G. A. Taylor, A. M. Carter, and M. E. Bradley, "Inertia estimation of the GB power system using synchrophasor measurements," *IEEE Transactions on Power Systems*, vol. 30, no. 2, pp. 701–709, March 2015.
- [20] P. M. Ashton, G. A. Taylor, A. M. Carter, M. E. Bradley, and W. Hung, "Application of phasor measurement units to estimate power system inertial frequency response," in *2013 IEEE Power Energy Society General Meeting*, July 2013, pp. 1–5.
- [21] M. Shiroei, B. Mohammadi-Ivatloo, and M. Parniani, "Low-order dynamic equivalent estimation of power systems using data of phasor measurement units," *International Journal of Electrical Power & Energy Systems*, vol. 74, pp. 134 – 141, 2016.
- [22] D. T. Duong, K. Uhlen, and E. A. Jansson, "Estimation of hydro turbine-governor system's transfer function from PMU measurements," in *Power and Energy Society General Meeting, 2016 IEEE*, July 2016.
- [23] S. H. Jakobsen and K. Uhlen, "Vector fitting for estimation of turbine governing system parameters," in *2017 IEEE Manchester PowerTech*, June 2017, pp. 1–6.
- [24] K. Tuttleberg, J. Kilter, and K. Uhlen, "Comparison of system identification methods applied to analysis of inter-area modes," in *Proceedings of International Power Systems Transients Conference 2017*, Seoul, South Korea, June 2017.
- [25] A. Ulbig, T. S. Borsche, and G. Andersson, "Impact of low rotational inertia on power system stability and operation," *IFAC Proceedings Volumes*, vol. 47, no. 3, pp. 7290 – 7297, 2014, 19th IFAC World Congress.
- [26] P. M. Anderson and A. A. Fouad, *Power System Control and Stability, 2nd Edition*, M. E. El-Hawary, Ed. Wiley, 2002.
- [27] P. Kundur, *Power System Stability and Control*. McGraw-Hill, 1993.
- [28] *MATLAB and System Identification Toolbox R2016b: User's Guide*, The MathWorks, Inc., Natick, Massachusetts, 2016.
- [29] L. Andersson, U. Jönsson, K. H. Johansson, and J. Bengtsson, "A manual for system identification," 2006.
- [30] F. R. Hampel, "The influence curve and its role in robust estimation," *Journal of the American Statistical Association*, vol. 69, no. 346, pp. 383–393, 1974.
- [31] P. J. Rousseeuw and C. Croux, "Alternatives to the median absolute deviation," *Journal of the American Statistical Association*, vol. 88, no. 424, pp. 1273–1283, 1993.
- [32] C. Leys, C. Ley, O. Klein, P. Bernard, and L. Licata, "Detecting outliers: Do not use standard deviation around the mean, use absolute deviation around the median," *Journal of Experimental Social Psychology*, vol. 49, no. 4, pp. 764 – 766, 2013.

Publication IV

K. Tuttelberg and J. Kilter, "Real-time estimation of transmission losses from PMU measurements," *2015 IEEE Eindhoven PowerTech*, Eindhoven, The Netherlands, June 2015.

© 2015 IEEE. Reprinted with permission

Real-Time Estimation of Transmission Losses from PMU Measurements

Kaur Tuttelberg, *Student Member, IEEE*, and Jako Kilter, *Member, IEEE*
 Department of Electrical Power Engineering,
 Tallinn University of Technology,
 Tallinn, Estonia
 kaur.tuttelberg@ttu.ee

Abstract—This paper discusses the application of PMU measurements in real-time estimation of transmission line power losses. Instead of directly computing the difference between sent and received power, the losses are estimated as separate components, calculated from line equations. On one hand, this provides more information about the operation of the line—active losses are split into Joule and corona losses and the balance of reactive power is separated into inductive losses and capacitive generation. On the other hand, it reveals large measurement errors in active losses on lightly loaded transmission lines, closely related to similar errors in estimated line parameters. This is demonstrated on examples of actual PMU measurements of a transmission line at low loads.

Index Terms—Phasor measurement units, Power transmission, Real-time monitoring, Transmission losses

I. INTRODUCTION

IN ADDITION to direct estimation of voltage and current phasors, PMU measurements can be applied in various secondary measurements, such as the real-time monitoring of transmission line parameters or transmission losses. Even though the identification of line parameters from phasor measurements has been covered extensively [1], [2], [3], little attention has been paid to the estimation of transmission losses. However, this information could prove beneficial to TSOs, who are required to buy the energy that is consumed as transmission losses. In various cases, e.g. system performance analysis, loss content estimation, etc. the TSOs may also be interested in different components of losses (e.g. corona losses).

In a physical interpretation of the line model, transmission losses and line parameters are directly related to each other, implying the same for the estimation of the respective quantities. Having PMU measurements available from both ends of a transmission line enables the active and reactive losses to be calculated directly as differences in sending and receiving end active and reactive power. At the same time, this measurement data enables the line parameters to be estimated. Knowledge of correct line parameters is sufficient to calculate each component of transmission losses separately, i.e. Joule losses, corona losses, inductive losses and capacitive

generation, which also sum up to the total differences in sent and received power.

In nearly all cases the published solutions for the parameter identification problem are demonstrated on simulated results only. This work presents real-world results of loss monitoring on a transmission line equipped with PMUs at both ends of the line. The application of available estimation methods on obtained measurements has indicated that not all line parameters (and the related components of transmission losses) can be estimated with sufficient accuracy when the load on the lines is small. Various estimates from measurements are analyzed in order to determine the usability of such estimation methods in practical applications.

This paper is divided into four sections. Section II describes the underlying theory and section III presents the results calculated from measurements. Main conclusions are summarized in section IV.

II. THEORETICAL BACKGROUND

For a transposed line, it can be assumed that the effects of coupling between phases and geometrical asymmetry are removed by the transposition. In this case, single conductor distributed parameter line equations are applied to model the transmission line. This assumption is the basis of most applications that estimate line parameters from PMU measurements [1], [2], [3].

In such models the voltages and currents in any phase (or symmetrical component) are related by

$$\underline{U}_l = \cosh(\gamma l)\underline{U}_0 + \underline{z}_c \sinh(\gamma l)\underline{I}_0, \quad (1)$$

$$\underline{I}_l = \frac{1}{\underline{z}_c} \sinh(\gamma l)\underline{U}_0 + \cosh(\gamma l)\underline{I}_0, \quad (2)$$

where \underline{U}_l and \underline{I}_l are the voltage and current phasors at a distance l toward the beginning of the line (\underline{U}_0 and \underline{I}_0 are the phasors at the end of the line). The per unit distance line parameters—the impedance and admittance—are included so that $\underline{z} = \gamma \underline{z}_c = r + jx$ and $\underline{y} = \gamma / \underline{z}_c = g + jb$.

From PMU measurement data, the total transmission losses can be calculated directly as

$$\underline{T}_L = \underline{S}_L - \underline{S}_0 = \underline{U}_L \underline{I}_L^* - \underline{U}_0 \underline{I}_0^*, \quad (3)$$

This work has been mainly sponsored by the Estonian TSO, Elering, with additional support from the STRON₂ research project and Tallinn University of Technology research grant B22.

where \underline{U}_L and \underline{I}_L are the phasors at the beginning of the line and $*$ denotes the complex conjugate. However, the losses can also be separated into components, as is commonly done on simpler line models.

The hyperbolic functions are holomorphic, thus $\cosh(\underline{a})^* = \cosh(\underline{a}^*)$. For a short line segment of length Δl , the losses can be expressed as

$$\begin{aligned} \underline{T}_{\Delta l} &= \underline{U}_{\Delta l} \underline{I}_{\Delta l}^* - \underline{U}_0 \underline{I}_0^* = \underline{U}_{\Delta l} \underline{I}_{\Delta l}^* \\ &+ \frac{1}{z_c^*} \cosh(\underline{\gamma} \Delta l) \sinh(\underline{\gamma}^* \Delta l) \underline{U}_{\Delta l} \underline{U}_{\Delta l}^* \\ &+ z_c \cosh(\underline{\gamma}^* \Delta l) \sinh(\underline{\gamma} \Delta l) \underline{I}_{\Delta l} \underline{I}_{\Delta l}^* \\ &- \cosh(\underline{\gamma} \Delta l) \cosh(\underline{\gamma}^* \Delta l) \underline{U}_{\Delta l} \underline{I}_{\Delta l}^* \\ &- \frac{z_c}{z_c^*} \sinh(\underline{\gamma} \Delta l) \sinh(\underline{\gamma}^* \Delta l) \underline{U}_{\Delta l} \underline{I}_{\Delta l}^*. \end{aligned} \quad (4)$$

The hyperbolic functions can be expanded in series as follows

$$\cosh(\underline{\gamma} l) = 1 + \frac{(\underline{\gamma} l)^2}{2!} + \frac{(\underline{\gamma} l)^4}{4!} + \dots, \quad (5)$$

$$\sinh(\underline{\gamma} l) = \underline{\gamma} l + \frac{(\underline{\gamma} l)^3}{3!} + \frac{(\underline{\gamma} l)^5}{5!} + \dots \quad (6)$$

When the value of Δl is small, then $|\underline{\gamma} \Delta l| \ll 1$ and $|(\underline{\gamma} \Delta l)^3| \ll |\underline{\gamma} \Delta l|$ and the series expansions can be simplified to only consist of first order terms. In this case the transmission losses become

$$\underline{T}_{\Delta l} = \underline{y}^* \underline{U}_{\Delta l} \underline{U}_{\Delta l}^* \Delta l + z \underline{I}_{\Delta l} \underline{I}_{\Delta l}^* \Delta l + O[(\underline{\gamma} \Delta l)^2]. \quad (7)$$

When Δl is small (i.e. the line segment is short), the voltages and currents can be considered approximately equal on the interval $[0, \Delta l]$ so that for any $l \in [0, \Delta l]$

$$\underline{T}_{\Delta l} \cong z \underline{I}_l \underline{I}_l^* \Delta l + \underline{y}^* \underline{U}_l \underline{U}_l^* \Delta l \quad (8)$$

which leads to

$$d\underline{T}_l = z |\underline{I}_l|^2 dl + \underline{y}^* |\underline{U}_l|^2 dl. \quad (9)$$

For the length of the line, the losses can then be expressed as

$$\underline{T}_L = z \int_0^L |\underline{I}_l|^2 dl + \underline{y}^* \int_0^L |\underline{U}_l|^2 dl. \quad (10)$$

It is assumed that the transmission losses can be split into components as

$$\underline{T}_L = \Delta P_J + \Delta P_C + j(\Delta Q_I + \Delta Q_G), \quad (11)$$

so that expressions equivalent to Joule losses, corona losses, inductive losses, and capacitive generation are, respectively,

$$\Delta P_J = r \int_0^L |\underline{I}_l|^2 dl, \quad (12a)$$

$$\Delta P_C = g \int_0^L |\underline{U}_l|^2 dl, \quad (12b)$$

$$\Delta Q_I = x \int_0^L |\underline{I}_l|^2 dl, \quad (12c)$$

$$\Delta Q_G = -b \int_0^L |\underline{U}_l|^2 dl, \quad (12d)$$

where r , g , x , and b are the per unit distance resistance, conductance, reactance and susceptance, respectively, i.e. components of z and y .

The line parameters can be expressed from (1) and (2), which can be explicitly solved for $\underline{\gamma}$ and z_c as [4]

$$\underline{\gamma} = \frac{1}{L} \operatorname{arccosh} \left[\frac{\underline{U}_L \underline{I}_L + \underline{U}_0 \underline{I}_0}{\underline{U}_0 \underline{I}_L + \underline{U}_L \underline{I}_0} \right], \quad (13)$$

$$z_c = \frac{\underline{U}_0 \sinh(\underline{\gamma} L)}{\underline{I}_L - \underline{I}_0 \cosh(\underline{\gamma} L)}. \quad (14)$$

When line parameters are calculated from PMU measurements, expressions for transmission losses in (3) and (11) yield equal results. However, the expressions in (12) include impedance and admittance components explicitly and distinguish between the different components of losses. The integrals can be solved analytically but may also be solved by numerical integration of (1) and (2).

The expression for losses given by (11) and (12) has two implications. When measurements have good accuracy, it is possible to monitor various types of losses separately. In this case more information about the operational state of the line can be obtained. However, test calculations presented later will show that at low loads significant errors appear in certain line parameters and associated loss components.

Just like the methods in [1], [2], [3], most applications of line parameter identification feature some advanced estimation procedures that increase the precision of estimates by decreasing statistical errors. This paper only presents the theoretical basis of calculating the desired values from single data points without any bad data mitigation techniques, as it is not in the scope of the paper. Values calculated from measured data, presented below, also indicate that the errors are dominantly systematic.

III. EXPERIMENTAL RESULTS

A medium length (≈ 200 km) 330 kV overhead transmission line in the Estonian power system was observed in the example measurements and calculations. The line is equipped with PMUs at both ends and its impedance has recently been measured by conventional off-line methods and is available for reference. At the present time, this transmission line mostly carries relatively small loads.

Two sets of measurements have been acquired from two separate days; both sets span over a duration of five hours. The first measurement period was in the afternoon of October 2nd and the other one in the morning of November 21st. Average ambient temperature in the first period was approximately 15 °C and -3 °C during the second period. Average wind velocities were around 2 m/s and 3 m/s, respectively.

During both measurement periods, the line was lightly loaded, with phase currents approximately 10% and 17% of the current transformer rated value. Current transformers are of class 0.2S at one end and 0.5S at the other end. The transmitted

power in both periods, measured by the PMU, is presented in Fig. 1, given as receiving end active and reactive power.

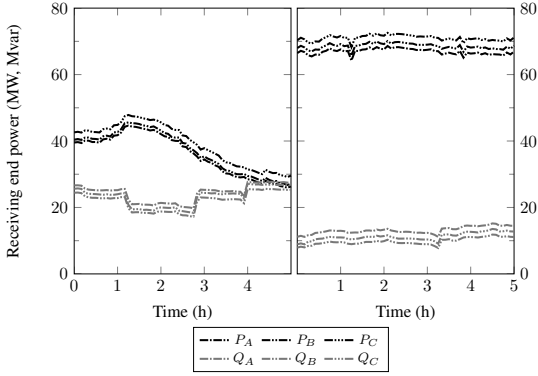


Fig. 1. Power transmitted over the line during two measurement periods. Receiving end power plotted as real and imaginary components of phase power measured by the PMU.

Fig. 2 presents total active losses, Joule losses, and corona losses in the transmission line, measured by PMUs. Losses computed from (3) and (11) are both plotted so that their equivalence can be verified. Active losses are separated into Joule and corona losses as in (12). Firstly, it can be seen that changes in active losses correspond to changes in transmitted power as is expected; the same is seen in Joule losses. Secondly, it can be seen that in the second period corona losses contribute a significant part to total active losses. However, in the first period, negative corona losses are estimated, which is a clear sign of measurement errors.

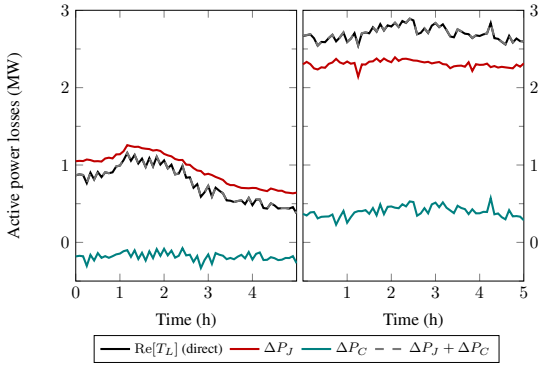


Fig. 2. Measured active power losses in the transmission line. Total active losses are given as the direct difference of values measured by the PMUs, as in (3), and as the sum of calculated Joule (ΔP_J) and corona losses (ΔP_C), as in (11). The separate active power loss components, as in (12), are also presented.

The effects of measurement errors are more prevalent in phase quantities. Fig. 3 presents active losses in each of the phases computed directly as differences in transmitted power

measured by the PMUs. In Fig. 4 active losses in phases are given as Joule and corona losses. In both figures the average total phase losses are given for comparison. Firstly, losses in phases are expected to be relatively as close to each other as the power transmitted over the line; however, this is not seen in estimated values. Secondly, in several cases estimated active losses are negative, which indicates that there are errors in the measurements.

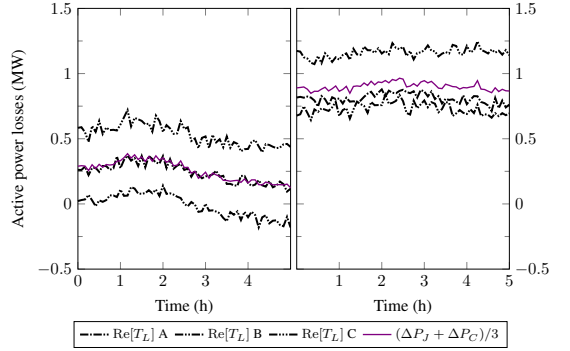


Fig. 3. Measured active losses by phases. Difference in sent and received active power, measured by PMUs, given for each phase separately. Average of the three phases given for scale.

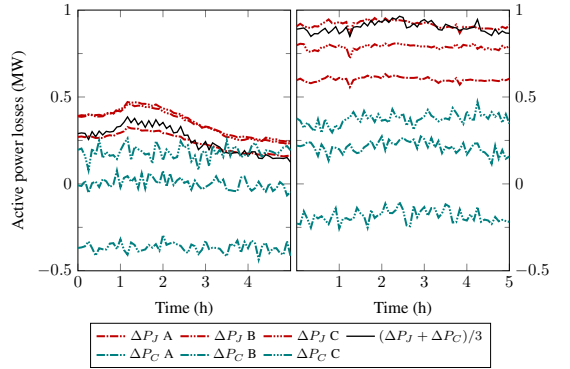


Fig. 4. Estimated Joule and corona losses by phases. Active losses separated into components, as in (12), computed from line parameters estimated from PMU measurement data. Average of the three phases given for scale.

The large difference in active losses and their components across phases can be analyzed by looking at estimated line parameters. Estimated values of series resistance and reactance are shown in Fig. 5 and Fig. 6 and shunt parameters in Fig. 7 and Fig. 8, where the quantities are computed from phase and positive sequence voltages and currents. Large differences in estimated resistances explain large differences in active losses. Similarly large discrepancies are present in estimated shunt conductances. Since the correct values are unknown, measured reference resistance has been converted to the value at ambient

temperature in order to provide some value for comparison. This is done according to $r_{\text{amb}} = r_{\text{ref}}[1 + \alpha(T_{\text{amb}} - T_{\text{ref}})]$, with α being the temperature coefficient for resistance.

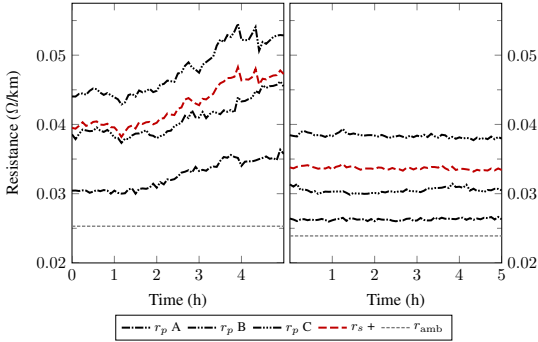


Fig. 5. Line series resistance (each phase separately and positive sequence) estimated from PMU measurement data by (13) and (14). Measured reference resistance converted to ambient temperature given for comparison.

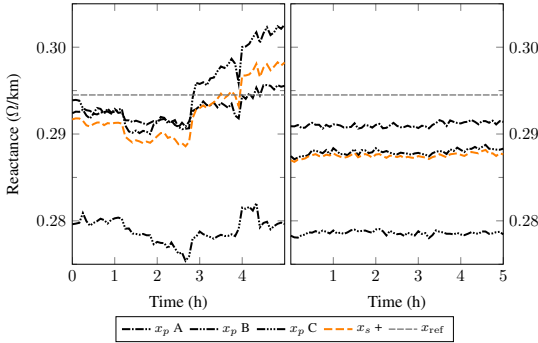


Fig. 6. Line series reactance (each phase separately and positive sequence) estimated from PMU measurement data by (13) and (14). Measured reference reactance given for comparison.

Some differences in phase reactances are also seen in Fig. 6, but in relative terms, these differences are an order of magnitude smaller than the ones present in resistance estimates. On the other hand, the estimates in the first measurement period seem to be affected by changes in power transmitted over the line. A similar tendency is seen in the resistance estimates (in Fig. 5), which worsen as the measured currents decrease. Shunt parameters (as shown in Fig. 7 and Fig. 8) remain rather constant, with the exception of positive sequence susceptance in the first measurement period.

Fig. 9 presents measured reactive losses as a direct difference in sent and received power measured by the PMUs. At the same time, estimated inductive losses and capacitive generation are plotted. Their average sum is given for comparison with direct estimates. As the errors in measured reactances are smaller than in resistances, the measured inductive losses

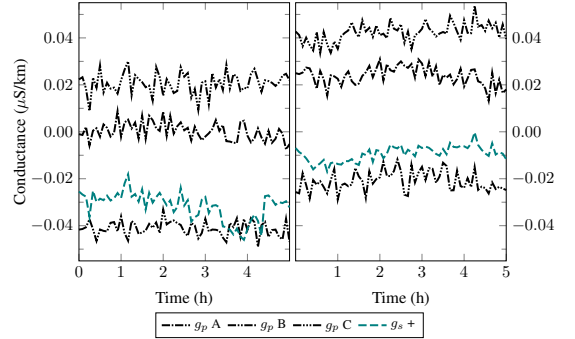


Fig. 7. Line shunt conductance (each phase separately and positive sequence) estimated from PMU measurement data by (13) and (14).

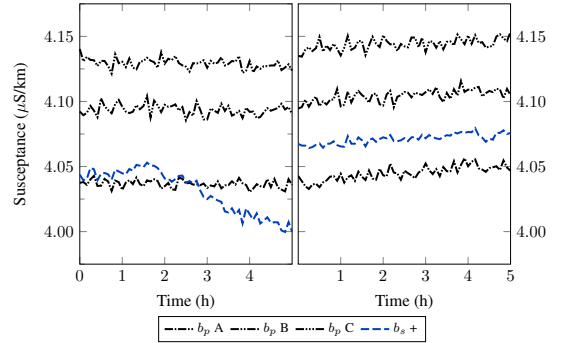


Fig. 8. Line shunt susceptance (each phase separately and positive sequence) estimated from PMU measurement data by (13) and (14).

differ significantly less in phases; the same applies when errors in conductances and susceptances and corresponding loss components are compared. No apparent problems can be seen in the estimation of reactive losses and its components.

IV. CONCLUSIONS

The paper presents the basic concept of estimating transmission losses from PMU measurements and complements it with expressions that allow Joule, corona, and inductive losses and capacitive generation to be computed as separate components on a distributed parameter line. The application of the method on real PMU measurement data shows that losses can be estimated as components but also indicates problems in the accuracy of some estimates. Analysis of the measurement data shows clearly that the direct calculation of active power losses in individual phases can produce unrealistic results. This is also closely related to large errors in the measurement of corresponding line parameters. On the other hand, it appears that reactive power, reactance, and susceptance can be measured reliably.

An important conclusion relevant to many PMU based line monitoring applications is that measurements of current

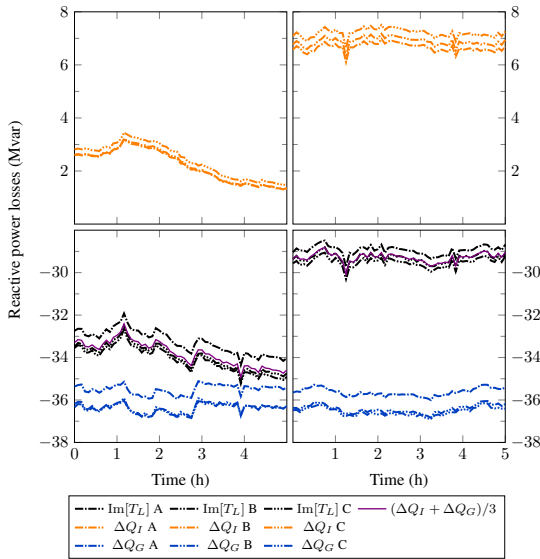


Fig. 9. Measured reactive losses; estimated inductive losses and capacitive generation. Phase reactive losses given as the direct difference of values measured by the PMUs, as in (3). Inductive losses (ΔQ_I) and capacitive generation (ΔQ_G) estimated from (12). Average of the three phases given for comparison.

phasors are significantly affected by errors in instrument transformers. Estimation of quantities that are simple to compute in principle, exhibits difficulties when the load on the line

is low. The effects are especially prevalent when estimating quantities which are related to the differences in active power at the two ends of the line. The errors seen in estimated losses may be acceptable in many cases, but the problem is also present in other estimates. For example, the measured values of phase resistances are too erroneous for the estimation of line temperature, if this was attempted.

The presented work indicates that further research is required in the application of PMU based line monitoring methods on real-world measurement data. In this paper, it is assumed that the errors are mostly caused by measurement errors in current transformers, however this question needs further study. It is also an open question how these measurement errors are propagated into estimated values. Additional research is required to establish when such measurements are reliable and when they are too much corrupted by measurement errors. More accurate methods should be sought for the estimation of line parameters from PMU measurements, which could also improve the estimation of transmission losses.

REFERENCES

- [1] C. Indulkar and K. Ramalingam, "Estimation of transmission line parameters from measurements," *International Journal of Electrical Power & Energy Systems*, vol. 30, no. 5, pp. 337–342, 2008.
- [2] Y. Du and Y. Liao, "On-line estimation of transmission line parameters, temperature and sag using PMU measurements," *Electric Power Systems Research*, vol. 93, pp. 39–45, 2012.
- [3] T. Bi, J. Chen, J. Wu, and Q. Yang, "Synchronized phasor based on-line parameter identification of overhead transmission line," in *Third International Conference on Electric Utility Deregulation and Restructuring and Power Technologies, 2008. DRPT 2008.*, April 2008, pp. 1657–1662.
- [4] S. Kurokawa, G. Asti, E. C. M. Costa, and J. Pissolato, "Simplified procedure to estimate the resistance parameters of transmission lines," *Electrical Engineering*, vol. 95, no. 3, pp. 221–227, 2013.

Publication V

K. Tuttelberg, J. Kilter, and K. Uhlen, "Comparison of system identification methods applied to analysis of inter-area modes," *International Conference on Power System Transients (IPST 2017)*, Seoul, South Korea, June 2017.

Comparison of system identification methods applied to analysis of inter-area modes

Kaur Tuttelberg, Jako Kilter, and Kjetil Uhlen

Abstract—This paper analyses and compares the applicability of various system identification techniques for modal analysis of a multi-area power system. The paper considers system identification applied on PMU measurements of frequency and active power to find a linear multi-input multi-output dynamic model of the primary frequency control of the power system. The multiple input–output pairs correspond to areas of the power system, enabling analysis of inter-area modes. The frequencies and damping ratios of inter-area modes obtained from the identified models are compared to the results of conventional modal analysis (i.e. small signal stability analysis of a linearised power system). Different system identification techniques are compared on simulated wide area PMU measurement data in order to determine the most suitable method for possible on-line analyses.

Keywords: Inter-area oscillations, Modal analysis, System identification, Wide area monitoring

I. INTRODUCTION

Information about critical modes and their damping ratios is a defining question in operating a large power system. In recent years, a number of novel real-time applications have been developed for the task, mostly based on wide area measurement systems; however, the different methods still come with their limitations and are being improved [1]. This paper analyses another approach based on wide area measurements: to apply system identification on a power system. In this case, a linear dynamic model is fitted to the observed changes in quantities and the model is then analysed to determine different properties of the dynamics of the system. In the context of this paper, analysis of inter-area modes based on such an identified model is studied.

System identification has been used before as an alternative way of performing modal analysis on simulated models. It has been suggested for use in cases when only certain modes are of interest, e.g. for PSS tuning [2], [3], but also suggested to overcome some limitations of conventional modal analysis tools [4], [5]. The concept has also been applied when the transfer functions themselves have been of particular interest [6], [7]. With the introduction of wide area measurements enabled by PMUs, the possibility of applying system identification on

measured data from the real system has already been studied to some extent as well [8], [9], [10]. Identification of governor models has been demonstrated on real PMU measurement data [11]. Also, methods of model order selection in similar solutions have been analysed [12].

Applying system identification entails a set of problems that have to be considered: mainly providing a suitable set of data, choosing the most appropriate identification method, and specifying the structure of the model. While the fitting algorithm may find a solution for any given dataset, the validity of the model has to be verified as well. In off-line simulations, all of these problems can be solved by hand if necessary, but on-line monitoring would require more automated and robust solutions. This paper compares different system identification techniques to find out which ones would be the most suitable and robust for on-line monitoring applications. The paper concentrates mostly on the choice of identification method and model order selection; less on data selection and model structure in terms of defining inputs and outputs.

This paper applies system identification in terms of a multi-input multi-output black box model, where each input–output pair corresponds to changes in load and frequency of an area of the power system. The paper only considers a very simple power system, where it is trivial to select a set of input and output data for the purpose of system identification. In a more complex system, the selection of inputs and outputs for a meaningful model is a problem by itself and is not treated in this paper. The obtained dynamic model can be seen as a simplified model of the dynamics of primary frequency control and the state of the model as a simplified estimate of the dynamic state of the power system. From the identified model, the frequency and damping ratio of the inter-area mode are extracted.

The implementation in this paper relies on pre-built tools included in the Matlab System Identification toolbox. Thus, the analysis is limited to the transfer function, state space model, and polynomial model estimation functions implemented in this toolbox. This covers a large variety of different possible models, however, many other methods are available for the identification of dynamic systems, e.g. time-domain vector fitting, neural network based learning systems, etc. The paper shows which ones of the classical system identification methods could be applicable in a more automated on-line monitoring application.

The study is based on the well known Kundur two area power system simulated in Digsilent Powerfactory. Based on simulated time series, models are fitted to the input–output data with different system identification methods implemented

This work has been supported by the Estonian TSO, Elering. K. Tuttelberg and J. Kilter are with the Department of Electrical Power Engineering, Tallinn University of Technology, Tallinn, Estonia (e-mail of corresponding author: kaur.tuttelberg@ttu.ee). K. Uhlen is with the Department of Electric Power Engineering, Norwegian University of Science and Technology, Trondheim, Norway.

Paper submitted to the International Conference on Power Systems Transients (IPST2017) in Seoul, South Korea June 26–29, 2017

in Matlab. Results of modal analysis reported by Powerfactory are compared to results obtained from the identified models. The results demonstrate that certain system identification methods are more consistent and robust than others, making them more suitable for automated analyses. The comparison of estimated modes indicates that inter-area modes can be detected with the model structure assumed in this paper.

The theoretical basis of the studied method is given in section II, with the specifics of applied system identification methods outlined in section III. Test calculations on the modelled power system are presented in section IV and discussed in section V. Conclusions are given in section VI.

II. THEORETICAL BACKGROUND

Primary frequency control is carried out at the turbine-generator unit level. The dynamics of frequency control can be described by a set of differential equations, which in turn can be modelled as a control system. The main components of a unit—the governor, the turbine, and the generator—are modelled by corresponding transfer functions. With a set of simplifications, an area of a power system (or an entire system) can be modelled similarly.

A simplified control system modeling the dynamics of a two area system is depicted in Fig. 1. Here the transfer functions $H_{GTi}(s) = H_{Gi}(s)H_{Ti}(s)$ for any area i model the governor-turbine systems summed as parallel branches and lumped together by evaluating an equivalent droop R_i . $H_{Si}(s)$ are the inertia of all rotating machines (and the frequency dependence of load) lumped into single area (or system) blocks. $H_{L12}(s)$ is the tie-line element, ΔP_{Ri} are the changes in power set-point values, ΔP_{Li} changes in load of each area, and Δf_i changes in frequencies [13].

This model can be simplified further when we analyse only primary frequency control, i.e. model the dynamics before any secondary control is issued. In this case the power set-point values of generators remain unchanged and the corresponding inputs in the control system can be disregarded. In this simplified analysis of the dynamics of secondary frequency control, the multi-area system becomes a multi-input multi-output system with load changes as inputs and frequency changes as outputs.

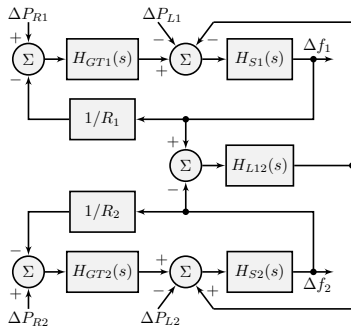


Fig. 1: Dynamic model of the frequency control of a two-area power system.

The described model treats each area as a single node with aggregated load, generation, and control loops and a unified value of frequency. In such a model it is important to define areas that on a system level can be aggregated. The described treatment is also dependent on the possibility of analysing the system in a period of time when the power set-points of all of the generators remain unchanged or change very little (i.e. $\forall i : \Delta P_{Ri} \approx 0$).

III. SYSTEM IDENTIFICATION

A. Input-Output Data

For a power system that has been divided into a number of appropriately defined areas, a simplified control system modelling the dynamics of its primary frequency control can be identified if sufficient measurement data is available. In other words, a model describing the relationships between changes in load in each of the areas and the corresponding frequency deviations can be fitted to a suitable set of measurement data. This paper analyses the application of various system identification techniques in estimating such fitted models from ambient measurements.

The outputs of the system, i.e. changes in frequency, are simple to measure with PMUs in principle. However, since the areas of the system are lumped into single nodes, some considerations have to be made in order to find the most representative value for the frequency of an area. The larger the areas are, the larger the differences in frequencies of single nodes can be. Information about the structure of the system should be used to combine a set of frequency measurements that best represent the frequency of the area.

The inputs of the system, i.e. the changes in load, are significantly more difficult to measure with PMUs as load is so widely dispersed. On a transmission system level, the measurement of load feeders may become feasible in a not too distant future, but is not something that can be expected at present. This means that more common PMU measurements have to be used to approximate the changes in load. For a practical implementation of the method studied in this paper, a sufficient number of PMUs are required on transmission lines and generators participating in primary frequency control.

This paper suggests two possible approximations. The first would be to estimate the changes in load from the changes in power produced by the generators that perform the significant part of primary frequency control and the power transmitted between areas. This means assuming that when small changes over time are considered, the changes in load and generation are sufficiently close to each other. The approximate change in load in area i would thus be

$$\Delta P_{Li} \cong \sum_j \Delta P_{Gji} + \sum_k \Delta P_{Tki} \quad (1)$$

where ΔP_{Gji} is the change in output power of the j th generator (or a group of generators) participating in primary frequency control in area i and ΔP_{Tki} is the change in power transmitted from the k th to the i th area.

The second option is to approximate the loads as power balances of substations. If a substation in the transmission

system has no generation capacity, the load in this node can be estimated as the sum of power on all of the lines coming into the substation, considering power flow directions. If power is also generated at the node, the generation is added to the power balance.

$$\Delta P_{Ln} \cong \sum_j \Delta P_{Gjn} + \sum_k \Delta P_{Fkn} \quad (2)$$

where ΔP_{Fkn} is the change in power flow from node k to node n and ΔP_{Gjn} is the change in generation in node n .

The proposed method assumes the availability of certain PMU measurements. Regardless of which approximation is used for changes in load, it is necessary to have PMU measurements from the generators that perform the significant part of primary frequency control. The first approximation for load changes requires that the power flows on tie-lines connecting the areas can be measured. For the second approximation of load changes, it is necessary that power flows on all transmission lines in the area can be determined. This does not necessarily require PMUs on all lines, but can also be computed from voltage magnitude and angle differences.

B. System Identification Methods and Model Order

The system identification methods tested in this paper are based on the built-in functions of the System Identification Toolbox in Matlab. The different methods include transfer function estimation by `tfest`, state space model estimation by `ssest` and `n4sid`, and polynomial model estimation by `polyest`, which in turn includes ARX (autoregressive with exogenous inputs), ARMAX (autoregressive–moving-average with exogenous inputs), Output-Error (OE), and Box–Jenkins (BJ) models.

The transfer function estimation method finds common transfer functions that have polynomials of orders np and nz as the denominator and numerator, respectively, while the state space model estimation finds common state space models of order nx . The different polynomial models can all be expressed as special cases of one general model. Given a MIMO polynomial model with nu inputs and ny outputs, the input–output relationships for the l th output of the general model can be expressed as

$$\sum_{j=1}^{ny} A_{lj}(q)y_j(t) = \sum_{i=1}^{nu} \frac{B_{li}(q)}{F_{li}(q)}u_i(t - nk_i) + \frac{C_l(q)}{D_l(q)}e_l(t), \quad (3)$$

where A_{lj} , B_{li} , C_l , D_l , and F_{li} are polynomials of orders na , nb , nc , nd , and nf expressed in q^{-1} . The ARX model is obtained when the C_l , D_l , and F_{li} polynomials are equal to one, OE when $A_{lj} = C_l = D_l = 1$, ARMAX when $D_l = F_{li} = 1$, and BJ when $A_{lj} = 1$ [14].

Due to the nature of the system identification problem that was set up, the models have an equal number of inputs and outputs corresponding to the number of areas the system is divided into. It is difficult to choose one fixed value of model order, despite the work that has been done on model order selection. This paper applies system identification that attempts to fit a number of models in a range of orders $n = n_{\min}, \dots, n_{\max}$ for each dataset and system identification

method. With each iterated order, the various variables defining model order are equal, i.e. $n = np = nx = na = nb = nc = nd = nf$. In transfer function estimation (`tfest`) the number of zeros is smaller than the number of poles by one, i.e. $nz = np - 1$. All input–output relationships are symmetric in the sense that in each identification attempt elements of the order matrices are equal. Input–output delay nk is determined with tools provided in Matlab.

While the `tfest` and `ssest` routines estimate continuous time models, `n4sid` and `polyest` provide discrete time models. In order to compare the results of modal analysis, all discrete time models are converted into continuous time models with the `d2c` function. All estimated models are first checked for stability and only stable ones are analysed further. For each data set a number of models of different orders are obtained and analysed.

IV. TEST CALCULATIONS

A. Test System and Simulations

The simulations were carried out on the well known Kundur two area power system [13], [15], implemented in Digsilent Powerfactory and depicted in Fig. 2. In these simulations, the system was replicated as closely as possible, except for exciter controls, which were replaced by pre-built models available in the software package, and governors, which were changed in order to have increased variety in the control system. Namely, the exciters were implemented as the SEXS models and the governor models HYG0V (generators G1 and G3) and TGOV1 (generators G2 and G4) were used. All parameters of the controllers were kept at default values, except for droop gains set at $R_1 = 0.05$, $R_2 = 0.03$, $R_3 = 0.04$, and $R_4 = 0.05$. A poorly damped inter-area mode was present in the system, however, it was stable under normal load variations; no PSS was implemented.

The datasets used in system identification were generated in time-domain dynamic simulations (RMS simulation in Powerfactory) of the test system with time varying loads. Each test case was run for a time period of 300 s, step changes in loads were introduced every second and the resulting dynamics of the system were simulated. Various datasets of real load data were adapted to form realistic time series of load changes. Simulated load data is presented in Fig. 3. All changes were made in the two load elements specified in the Kundur two area system (L_7 and L_9). Data was sampled with a time-step of 0.01 s from all simulations. For system identification, load changes approximated by (1) were recorded.

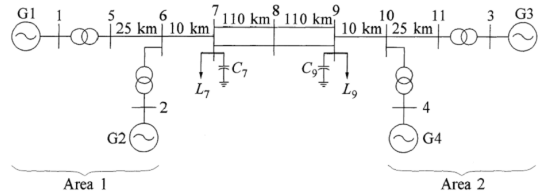


Fig. 2: Schematic of the two area power system used in simulations [13].

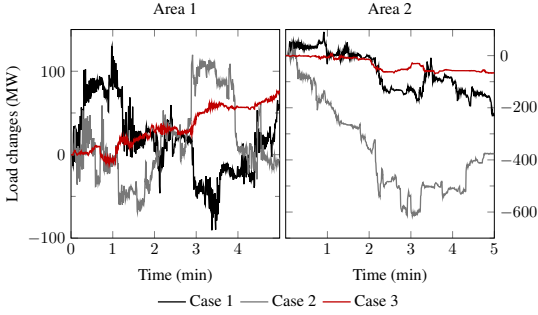


Fig. 3: Cumulative changes in simulated load with respect to initial load. Data from three different simulation cases are plotted.

In order to check the accuracy of the identified dynamic models, a separate set of validation data was simulated. For validation, frequency changes after a step change of load (an increase of 50 MW) in each of the areas were simulated and recorded separately. Based on the model used in all of the simulations, small-signal stability analysis was also carried out for the initial state of the system. The inter-area mode was characterised by the poles $-0.086 \pm j4.1$, which corresponds to a frequency of 0.65 Hz and a damping ratio of 0.021.

In the identified MIMO system, two input–output pairs were assumed, corresponding to the two areas. As explained earlier, inputs correspond to load changes and outputs to frequency changes in each of the areas. All identified models were black box without any additional information about the real system provided. Load was estimated as the difference between generation and power exchange between areas according to (1). Area frequencies were taken as the frequencies of buses 5 and 11, which were assumed to be the most central nodes of the two areas. Thus, in total seven measurements were assumed in the studied system: frequencies of buses 5 and 11 and power flows at bus 8 and all four generators.

B. Identification and Validation of Models

With the frequency changes and estimated load changes from the three simulation cases, models were identified with all of the methods mentioned in the previous section. All methods were applied to identify models of 20 different orders, ranging from 5 to 24. All iterative methods were set to use 5 iterations. A delay of $nk = 2$ or $0.02s$ was identified and used. All identified models were checked for stability, converted to continuous time if necessary, and step responses of stable models compared to validation data. A comparison based on a goodness-of-fit criterion was attempted with NRMSE (normalised root mean squared error), but the criterion failed to identify how well the models mimicked the dynamics of the system. Thus, the models obtained with different identification methods were validated in a visual comparison of step responses in this study.

Fig. 4 presents the comparisons of the simulated step changes and the step responses of the identified models obtained from simulation case 3 with `tfest` and `armax`

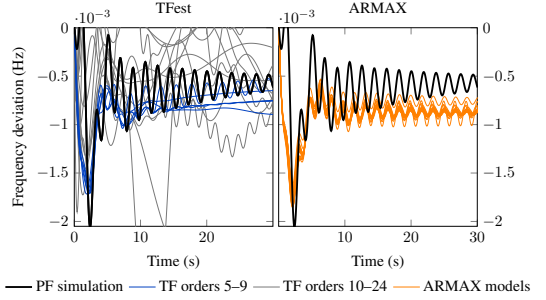


Fig. 4: Step responses of transfer function (TF) models identified with `tfest` and ARMAX polynomial models identified with `armax` from simulation case 3. Step responses of identified models are compared to a step change of load simulated separately in Powerfactory (PF). Frequency changes in area 2 after a step change of load in the same area (normalised to 1 MW) are plotted.

routines. In case of `tfest`, the step responses of the five lower order models are emphasised as these were the best fits. Even though the identified models captured the overall dynamics of frequency changes quite well, the inter-area oscillations were not very well identifiable. In case of `armax`, very consistent results were seen across all stable models.

The validation of models obtained with `ssest`, `n4sid`, `arx`, `oe`, and `bj` was carried out similarly. The state space models identified with `ssest` and `n4sid` were similar to each other and average in quality when compared to ARMAX models. Polynomial models identified with ARX were similar to ARMAX models, but there were significantly larger differences across models of different orders. Output-Error and Box–Jenkins methods performed very poorly in this application, with a small number of stable models and poor validation results. Some results from state space and ARX methods are also presented in the next subsection.

C. Comparison of System Identification Methods

Continuing with the examples of transfer function and ARMAX models, Fig. 5 presents the poles of all models

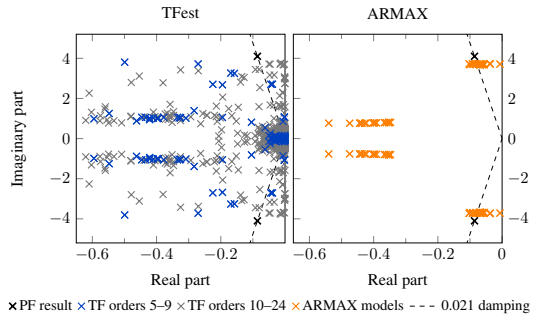


Fig. 5: Poles of transfer function (TF) models and ARMAX polynomial models identified from simulation case 3. Transfer function models of orders 5–9 are plotted in blue, while higher order models are in grey. Poles of estimated models are compared to poles of the inter-area mode identified in Powerfactory (PF). Not all calculated poles fit in the plotted region.

identified with the two methods from simulation case 3. In this study, the poles corresponding to the inter-area mode were identified by assuming an acceptance region for the values. Any pole in the region was assumed to correspond to the inter-area mode. In case of `tfest`, the five lower order models are once again emphasised. Few poles were found close to the expected point determined in modal analysis with Powerfactory. Contrary to that, results obtained with `armax` demonstrate very consistent and good performance. Identified models had poles close to the poles characterising the inter-area mode as found in conventional modal analysis.

The quality of models identified with other methods was similar to the quality seen in validation data. The state space model identification methods `ssest` and `n4sid` performed similarly to each other and provided results of average quality when compared to ARMAX models. Polynomial models identified with ARX had poles similar to the ones found from ARMAX models, but significant differences across model orders were present. Poles of models identified with Output-Error and Box-Jenkins methods were very different from expected correct results.

With all of the identified models, poles close to the correct poles of the inter-area mode were searched for. In most cases, the frequency of the identified mode was close to the expected correct value or at least in the same order of magnitude. In detecting the frequency of the inter-area mode, transfer function estimation with `tfest` performed worst (seen in Fig. 6), while models identified with `armax` gave the best results (seen in Fig. 7). Most of the frequency values obtained with the other methods were within $\pm 10\%$ of the correct value.

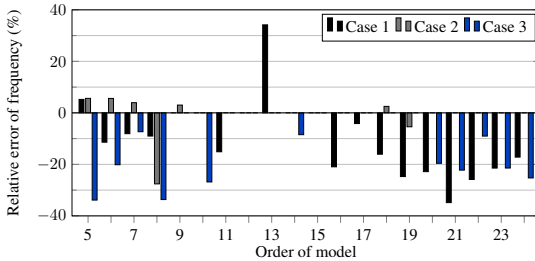


Fig. 6: Relative error of the inter-area mode frequency estimated from transfer function models identified from all three simulation cases.

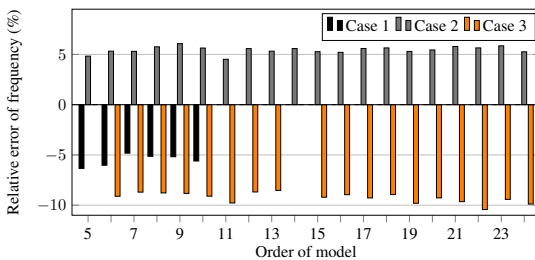


Fig. 7: Relative error of the inter-area mode frequency estimated from ARMAX polynomial models identified from all three simulation cases.

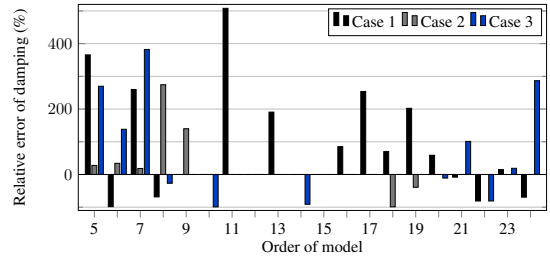


Fig. 8: Relative error of the inter-area mode damping ratio estimated from transfer function models identified from all three simulation cases.

From the identified models, the damping ratio of the inter-area mode was also estimated. In terms of estimating the damping ratio, the identified models performed significantly worse than in estimating the frequency of the mode. Like before, Output-Error and Box-Jenkins models did not provide good results. Both transfer function and state space model estimation provided largely varying results, seen in Fig. 8 and Fig. 9. While a few select models gave a good estimate, most models deviated greatly from expected values. Results of ARX models indicated an increase in accuracy with increasing model orders, seen in Fig. 10.

The accuracy of damping ratios estimated from ARMAX models can be seen in Fig. 11. Many of the ARMAX models provided estimates close to the correct value, while in general they tended to slightly underestimate the damping ratio. Overall the performance of ARMAX model identification was evidently better than that of the other methods. Averaging over

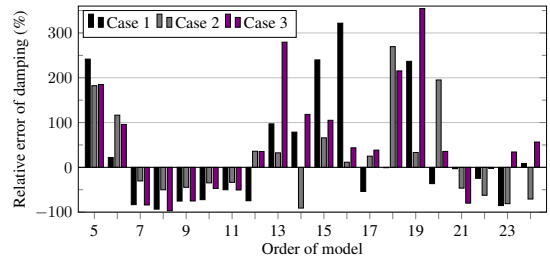


Fig. 9: Relative error of the inter-area mode damping ratio estimated from `n4sid` state space models identified from all three simulation cases.

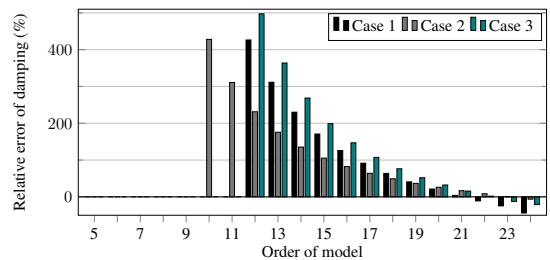


Fig. 10: Relative error of the inter-area mode damping ratio estimated from ARX polynomial models identified from all three simulation cases.

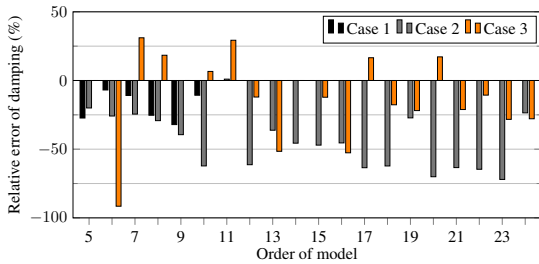


Fig. 11: Relative error of the inter-area mode damping ratio estimated from ARMAX polynomial models identified from all three simulation cases.

the results of all stable ARMAX models of various orders of each case gave damping ratios of 0.017, 0.012, and 0.018 in the three cases (or -19% , -43% , and -14% relative error).

V. DISCUSSION

Out of all the models found with different identification methods, different model orders, and based on different simulation cases, several gave accurate estimates of the frequency and damping ratio of the inter-area mode, while many also failed. However, it was evident that ARMAX polynomial models gave the best and most consistent approximations of the dynamics of the system across various model orders and simulation data. With any of the other studied methods, it would be hard to decide which models were good without validation. With ARMAX models, several similar and good models were obtained, providing redundancy and the ability to check the quality of models by comparing them to each other if good validation data would not be available.

The goal of the presented study was to determine the most suitable system identification method for the described approach to analysing inter-area modes. The paper also demonstrates that the monitoring of inter-area modes based on system identification is feasible, however, many questions remain open. The analysis was based on noiseless data sampled directly from the simulation, not real PMU measurements with limited accuracy. With noisy data, the problems of fitting to noise with higher model orders and additional filtering would also have to be considered. The solution applied in this paper assumed measurement periods where secondary frequency control was not issued or could be considered negligible. To make this assumption valid, additional data about generation set-point changes in the system are needed.

VI. CONCLUSIONS

The paper demonstrated the analysis of inter-area modes based on system identification. The aim of the study was to compare the different available system identification methods in order to find the most suitable one for the type of problem analysed in the paper. The study was based on the Kundur two area power system simulated in Digsilent Powerfactory. Three simulation cases were run, where load changed in time, attempting to mimic load variations in a realistic power system. Seven different system identification methods from the

System Identification Toolbox in Matlab were applied to fit models to the simulated data. Identified models were analysed to determine the frequency and damping ratio of the inter-area mode, which were also compared to the result found by conventional modal analysis.

The paper identified ARMAX polynomial models as the best suited system identification method for this problem. The paper also demonstrated the feasibility of monitoring inter-area modes based on system identification. With an increasing number of installed PMUs, system identification could be applied to estimate approximate dynamic models and dynamic states of the power system, enabling the analysis of critical modes and other parameters of the system. The approach could be applied in on-line monitoring of modes, PSS tuning, etc. Additional work is required to determine the practical applicability of such monitoring methods. Future work could also analyse alternative dynamic model identification methods and using the identified models to extract other parameters of the dynamics of the system.

REFERENCES

- [1] T. Jiang, L. Bai, G. Li, H. Jia, Q. Hu, and H. Yuan, "Estimating inter-area dominant oscillation mode in bulk power grid using multi-channel continuous wavelet transform," *Journal of Modern Power Systems and Clean Energy*, vol. 4, no. 3, pp. 394–405, 2016.
- [2] I. Kamwa and L. Gerin-Lajoie, "State-space system identification-toward MIMO models for modal analysis and optimization of bulk power systems," *IEEE Transactions on Power Systems*, vol. 15, no. 1, pp. 326–335, 2000.
- [3] I. Kamwa, "Using MIMO system identification for modal analysis and global stabilization of large power systems," in *Power Engineering Society Summer Meeting, 2000. IEEE*, vol. 2, 2000, pp. 817–822 vol. 2.
- [4] J. J. Sanchez-Gasca, K. Clark, N. W. Miller, H. Okamoto, A. Kurita, and J. H. Chow, "Identifying linear models from time domain simulations," *IEEE Computer Applications in Power*, vol. 10, no. 2, pp. 26–30, 1997.
- [5] H. Okamoto, A. Kurita, J. J. Sanchez-Gasca, K. Clark, N. W. Miller, and J. H. Chow, "Identification of equivalent linear power system models from electromagnetic transient time domain simulations using Prony's method," in *Decision and Control, 1996., Proceedings of the 35th IEEE Conference on*, vol. 4, 1996, pp. 3857–3863 vol.4.
- [6] J. R. Smith, F. Fatehi, C. S. Woods, J. F. Hauer, and D. J. Trudnowski, "Transfer function identification in power system applications," *IEEE Transactions on Power Systems*, vol. 8, no. 3, pp. 1282–1290, Aug 1993.
- [7] K. E. Bollinger and W. E. Norum, "Time series identification of interarea and local generator resonant modes," *IEEE Transactions on Power Systems*, vol. 10, no. 1, pp. 273–279, 1995.
- [8] J. W. Pierre, D. Trudnowski, M. Donnelly, N. Zhou, F. K. Tuffner, and L. Dosiek, "Overview of system identification for power systems from measured responses," *IFAC Proceedings Volumes*, vol. 45, no. 16, pp. 989 – 1000, 2012.
- [9] L. Dosiek and J. W. Pierre, "Estimating electromechanical modes and mode shapes using the multichannel ARMAX model," *IEEE Transactions on Power Systems*, vol. 28, no. 2, pp. 1950–1959, 2013.
- [10] N. Zhou, Z. Huang, L. Dosiek, D. Trudnowski, and J. W. Pierre, "Electromechanical mode shape estimation based on transfer function identification using PMU measurements," in *2009 IEEE Power Energy Society General Meeting, 2009*, pp. 1–7.
- [11] D. T. Duong, K. Uhlen, and E. A. Jansson, "Estimation of hydro turbine-governor system's transfer function from PMU measurements," in *Power and Energy Society General Meeting, 2016 IEEE*, July 2016.
- [12] V. S. Peric, T. Bogodorova, A. N. Mete, and L. Vanfretti, "Model order selection for probing-based power system mode estimation," in *Power and Energy Conference at Illinois (PECI), 2015 IEEE*, 2015, pp. 1–5.
- [13] P. Kundur, *Power System Stability and Control*. McGraw-Hill, 1993.
- [14] *MATLAB and System Identification Toolbox R2016b: User's Guide*, The MathWorks, Inc., Natick, Massachusetts, 2016.
- [15] M. Klein, G. J. Rogers, and P. Kundur, "A fundamental study of inter-area oscillations in power systems," *IEEE Transactions on Power Systems*, vol. 6, no. 3, pp. 914–921, Aug 1991.

Publication VI

K. Tuttelberg and J. Kilter, "Predicting frequency disturbances from wide area monitoring of ambient power system dynamics," *8th IEEE PES Innovative Smart Grid Technologies Conference Europe (ISGT Europe 2018)*, Sarajevo, Bosnia and Herzegovina, October 2018.

Predicting Frequency Disturbances From Wide Area Monitoring of Ambient Power System Dynamics

Kaur Tuttelberg, *Student Member, IEEE* and Jako Kilter, *Senior Member, IEEE*
Department of Electrical Power Engineering and Mechatronics,
Tallinn University of Technology,
Tallinn, Estonia
kaur.tuttelberg@ttu.ee

Abstract—This paper presents a method of predicting frequency deviations caused by a disturbance (e.g. trip of a load or a generator) based on continuous monitoring of the power system. The method is based on identifying an approximate model of the dynamics of the system from ambient PMU measurements using black box system identification. Once the model is found, possible events of significant load variations can be simulated in order to predict the ensuing frequency disturbances. The results characterize the inertial response of the system, the frequency nadir, time taken to reach the nadir, etc. The method has been demonstrated on PMU measurement data from a real power system as a part of the MIGRATE project.

Index Terms—Frequency stability, Frequency dynamics, Phasor measurement units, System identification, Wide area monitoring

I. INTRODUCTION

THE DEVELOPMENT towards larger shares of renewable sources in power generation is causing changes in the operation of power systems. While conventional generating units are synchronized to grid frequency, wind turbines and solar panels are unsynchronized and coupled to the grid through power electronics. The inertial response and frequency dynamics are changing, posing questions for the future about operating power systems with decreased levels of inertia, formation of low inertia areas in systems, and mitigating rapidly changing frequencies. These issues have been discussed in Europe [1], [2], [3], North America [4], [5], [6], [7], [8], Australia [9], [10], and elsewhere [11] and are currently being investigated in the Horizon 2020 MIGRATE project (Massive InteGRation of power Electronic devices).

This paper presents a method of monitoring the frequency dynamics of a power system and predicting its response to larger disturbances. The estimation is based on ambient data, i.e. normal operation, meaning it could be applied in a close to continuous manner. This enables the transmission system operator (TSO) to know the expected behavior of the system despite its changing composition. It becomes possible to determine the dynamics of the system following a specific disturbance, e.g. trip of a generating station, based on the present state not simulations. This further allows the TSO to

determine the time available to deploy a response and schedule an appropriate corrective power response.

This paper proposes to identify approximate dynamic models of the power system based on PMU measurements of active power flows and frequency. In previous research, different related parameter and model identification methods have been presented, e.g. estimation of low-order dynamic equivalent models from PMU measurements has been proposed [12] and identification of governor models has been demonstrated on real PMU measurements [13], [14]. A previous paper presented a comparison of different system identification methods applied on similar measurement data as in this study but with an application in analyzing inter-area modes [15].

The proposed method assumes that the system is divided into two or more areas that can be approximated as centers of inertia. Frequencies of the individual nodes comprising each area are aggregated into a single area frequency and the dynamics of this quantity are analyzed. At the same time, load variations in each of the areas are also aggregated and analyzed based on measured power flows. System identification is applied in terms of a multi-input multi-output black box model, where each input–output pair corresponds to changes in load and frequency of one of the areas.

The method has been tested and demonstrated on measurement data from the Icelandic power system. A number of frequency disturbances and periods preceding them have been recorded. Measurement periods preceding the events have been used to identify approximate models of the system. The identified models have then been used to predict the frequency excursions caused by the disturbances and the predictions have been compared to the actual recorded events.

The theoretical basis of the work is outlined in section II. Test calculations on measured data are presented and discussed in section III. Conclusions are given in section IV.

II. THEORETICAL BACKGROUND

A. Modeling principles

The applied system identification approach attempts to identify an approximated system that models the dynamics between active power and frequency in the system. In a theoretical analysis, these dynamics could be described by a set of differential equations, which in turn could be modelled as a linear control system. In this case, the inertial response and



main elements of primary control—the governors, turbines, and generators—would be modelled by corresponding transfer functions. With a set of simplifications, an area of a power system (or an entire system) could be modelled similarly [16]. This model is only discussed to provide a background and is not directly used in system identification.

In order to model areas of a system like this, they are commonly aggregated based on the center of inertia frequency [17]. The center of inertia frequency is evaluated as a weighted average of frequencies

$$f_{COI} = \frac{\sum_i^N H_i S_{ib} f_i}{\sum_i^N H_i S_{ib}}, \quad (1)$$

where f_i are the frequencies of all of the N nodes comprising the area weighted by the inertia H_i and rated power S_{ib} of each node.

For a two area power system, such a simplified control system is depicted in Fig. 1. In order to obtain this model, the governor–turbine systems are summed as parallel branches and lumped together by evaluating an equivalent droop. The inertia of all rotating machines (and the frequency dependence of load) is similarly lumped into single area (or system) blocks [16]. The inputs ΔP_{Ri} are the changes in power set-point values and ΔP_{Li} changes in load of each area; the outputs Δf_i are frequency deviations.

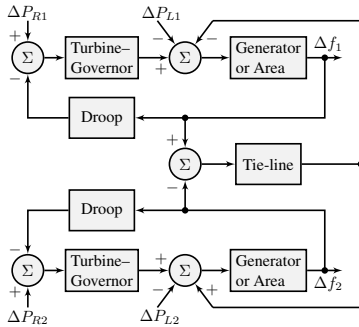


Fig. 1: Dynamic model of frequency control of a two-area power system.

If only primary frequency control is considered, the power set-point values of generators do not change and the corresponding inputs can be removed from the control system. In this simplified analysis of the dynamics of inertial response and primary frequency control, the multi-area system is modeled as a multi-input multi-output system with load changes as inputs and frequency deviations as outputs. The described model treats each area as a single node with aggregated load, generation, and control loops and a unified value of frequency. The described treatment assumes that the system is analyzed in a period of time when the power set-points of all of the generators remain unchanged or change very little.

B. Inputs and Outputs of the Model

The proposed methodology can only be applied on a system that is correctly aggregated into areas, with two main requirements. The areas have to be topologically consistent, i.e. all nodes forming an area have to be directly connected to at least one other node of the same area and areas have to have clear boundaries. The areas should be formed so that frequencies of buses inside an area do not commonly oscillate against each other.

In this method, an approximated center of inertia frequency is used as a basis for aggregating the area frequencies. Since not all nodes are monitored and inertia at any given time is not known, the calculation is simplified. The frequency of area j is evaluated as a weighted average

$$f_j = \frac{\sum_i^{N_j} w_i f_i}{\sum_i^{N_j} w_i}, \quad (2)$$

where f_i are the frequencies of the N_j nodes that are measured in area j . The weights w_i are based on assumptions about which nodes contribute more to the inertia of the area. After evaluating the aggregated value, the frequency deviation in area j can be expressed as

$$\Delta f_j = f_j - f_n, \quad (3)$$

which is the output j of the identified system.

Once the areas are formed and aggregated, it is necessary to determine load changes in the areas as the inputs of the system. However, load feeders are usually not monitored with PMUs yet, which means that more common PMU measurements have to be used to approximate the changes in load. If power flows between the defined areas and a majority of generators that participate in primary frequency control can be monitored, this can be done as follows. The approximate change in load in area j is expressed as

$$\Delta P_{Lj} \cong \sum_i \Delta P_{Gji} + \sum_k \Delta P_{Tjk} \quad (4)$$

where ΔP_{Gji} is the change in output power of the i th generator (or a group of generators) in area j and ΔP_{Tjk} is the change in power transmitted from the k th to the j th area. The main assumption is that when small changes over time are considered, the changes in load and generation are sufficiently close to each other.

At present, PMU measurement locations in systems are still limited and not all major generators and transmission lines are usually monitored. In these cases, additional approximation have to be made. In a case where one of several parallel lines is monitored, the power flow on that line can be scaled to estimate flow in the corridor. When there is a generator behind a radial part of the network and the power flow into that part is measured, the radial part may be seen as a generator as an approximation, etc.

C. System Identification

The next part of the estimation process is applying system identification on the obtained input–output data. Some aspects

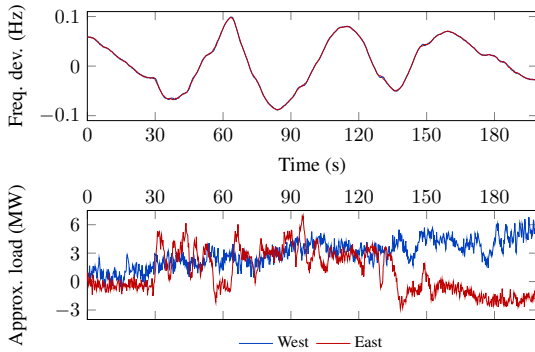


Fig. 3: Example of input–output data used in system identification. Frequency deviations (top graph) and approximated load changes (bottom graph) in one monitoring period have been plotted.

inputs and frequency deviations as outputs, the models could naturally be used to predict frequency changes following a certain power change. The responses were calculated either as a standard step response scaled to match the load or measured power output of the tripped load or unit. In the second case, the change of active power in the recorded event itself was used as the input of the model. Both types of calculations gave predicted frequency changes as outputs of the model, which could be compared to the recorded frequency disturbances.

C. Cases and Results

The first three events were generator trips at different power plants in the Western area. The tripped generators were operating at 45, 61, and 34 MW, respectively. The comparison of recorded disturbances and frequency changes predicted from identified models are presented in Fig. 4. For these three events, the disturbances were nearly ideal trips and were only simulated as step changes.

In all three cases, it was possible to identify models from ambient measurement data that captured some important dynamics of the system. In all three predicted events, the inertial response of the area was captured very well during the

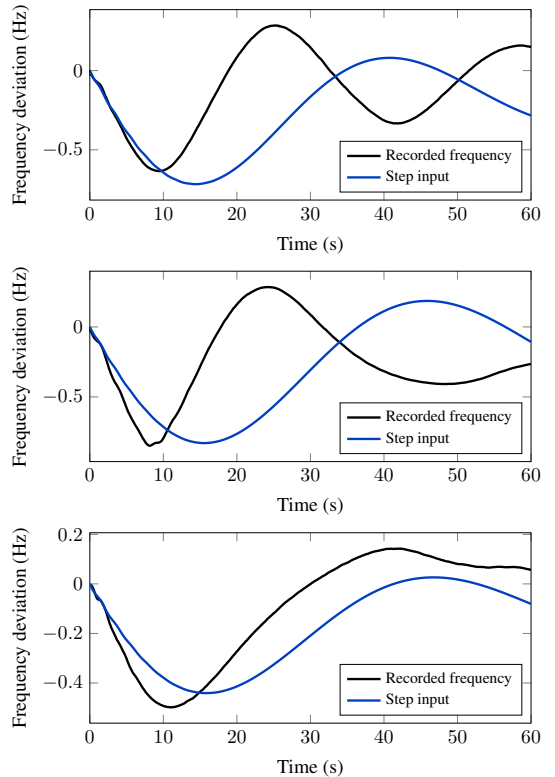


Fig. 4: Comparison of predicted and recorded frequency excursions following three separate trips of generators. Predicted frequency disturbances were found as step responses of identified models, where a step from zero to the amount of capacity lost was used as the input signal.

first 2...3 seconds. The extreme frequency deviations (corresponding to frequency nadir) were also predicted reasonably well, however, the moment in time when the minimum value was reached was delayed in all three events. The results are summarized in Table I. In the first two events, the prediction diverged from the recorded disturbance after going through the nadir, showing a lower frequency in the ensuing oscillation. In the third event, the prediction was lagging but was generally similar to the recorded frequency.

The following three events were trips of industrial loads of 123, 67, and 100 MW, respectively. However, only the first of those was a trip that was nearly identical to a step change in power. In the other two load trips, there was an initial peak in the load drop. The comparison of predicted and recorded frequency deviations following these three load trips are presented in Figs. 5–7, where the recorded and simulated load changes are plotted as well. In the latter two events, two different step changes were used as inputs to the identified models. In all three cases, real recorded load changes were also input into the identified models for an additional comparison.

TABLE I: Results of predicting the maximum or minimum frequency (extreme deviation). Errors calculated in terms of frequency deviation not absolute frequency. In time to extreme deviation (nadir or peak), error is given as the delay in prediction.

Event	Extreme frequency deviation			Time to extr. (s)	Delay (s)
	Real (Hz)	Predicted (Hz)	Error (%)		
Gen 1	-0.64	-0.71	10	9.3	5.0
Gen 2	-0.85	-0.82	3.5	8.1	7.4
Gen 3	-0.49	-0.44	10	10.7	5.0
Load 1	1.29	1.31	1.6	7.8	5.2
Load 2	0.79	0.84	6.3	9.7	5.6
Load 3	1.08	1.49	38	7.5	9.9

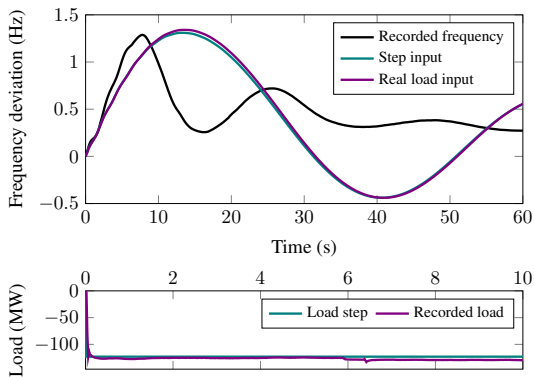


Fig. 5: Comparison of predicted and recorded frequency excursions following the trip of a load (top graph). Frequency disturbances were predicted using different input signals shown in the bottom graph.

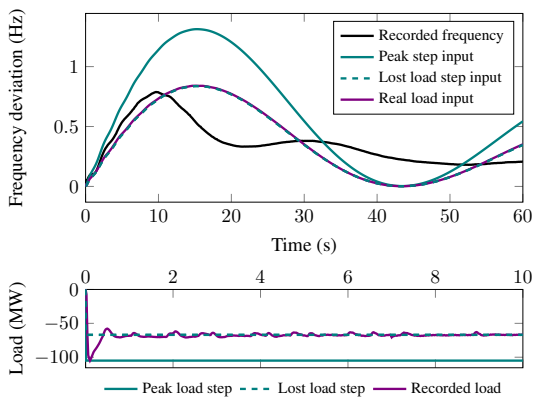


Fig. 6: Comparison of predicted and recorded frequency excursions following the trip of a load (top graph). Frequency disturbances were predicted using different input signals shown in the bottom graph.

The first load trip was similar to the generator trips observed above. The predicted inertial response was nearly identical to the recorded one and the frequency peak was predicted rather well, however, it had a delay. In the second event, a step input equal to the peak of the load change predicted the initial frequency deviation well, but gave a large overshoot. A step input equal to actual load lost gave a very similar result to using recorded power changes as the input. Both predicted the peak comparably to previous cases. In the third event, a step input equal to the peak of the load change predicted the initial frequency changes very well, however, it had a large overshoot due to overestimating the actual load lost, like in the previous event. However, in this case the step equal to load lost and recorded load changes as inputs also gave different results due to the disturbance differing greatly from a step change.

The errors of predicting extreme frequency deviations are again summarized in Table I. Values presented in the table

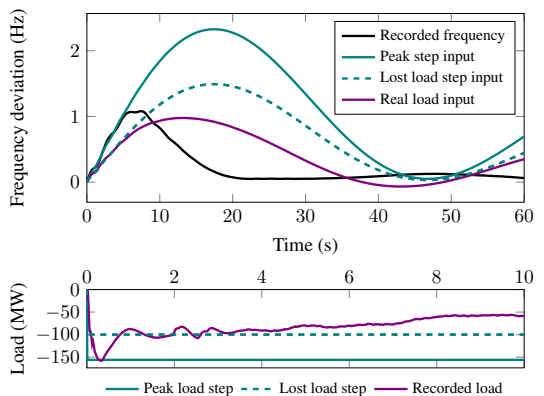


Fig. 7: Comparison of predicted and recorded frequency excursions following the trip of a load (top graph). Frequency disturbances were predicted using different input signals shown in the bottom graph.

are taken from predictions made with a step response equal to actual load lost in the event. In all cases except for the last load trip, the frequency peak was predicted relatively well. The last load trip differed from a step change and was more difficult to predict due to that. Using recorded load variations would have given a more accurate prediction, but this information is not known before an event has occurred.

In all six cases, the identified models performed the best during the first few seconds. Thus, the method managed to capture the inertial response and the period of primary frequency control. The inertial response was predicted well, while primary control was predicted somewhat less accurately. The predictions were relatively good until the extreme frequency deviation was reached. After that, most predictions diverged from recorded disturbances. However, the test system has automatic generation control (AGC), which usually initiates secondary frequency control 20...60 seconds after such disturbances. Since the system identification procedure intentionally excludes secondary control, the models are no longer valid once AGC action is initiated.

IV. CONCLUSIONS

The paper presented a method of predicting the course of frequency disturbances based on approximate dynamic models estimated from ambient PMU measurements. The method assumes that simplified models of the dynamics between active power and frequency can be obtained from monitoring the system during normal operation. These models can then be used to predict frequency deviations given a certain change in load, e.g. the trip of a large load or generator. The method was demonstrated on real measurement data from the Icelandic power system.

The test calculations demonstrated that the method is applicable on a real power system. PMU measurement data from six frequency disturbances and monitoring periods preceding these events were used to validate the method. Based on

monitoring the system during 20...30 minutes before an event, it was possible to predict some important characteristics of the frequency disturbances, e.g. the inertial response and the frequency nadir or peak. The work demonstrates that it is possible to identify important parameters of the dynamics of a power system from continuous monitoring of normal operation.

V. ACKNOWLEDGMENT

The authors would like to thank the Icelandic TSO Landsnet for the collaboration and for providing the measurement data.

REFERENCES

- [1] "Frequency stability evaluation criteria for the synchronous zone of continental Europe," ENTSO-E RG-CE System Protection & Dynamics Sub Group, Tech. Rep., March 2016.
- [2] E. rum, M. Kuivaniemi, M. Laasonen, A. Bruseth, E. Jansson, A. Danell, K. Elkington, and N. Modig, "Future system inertia," ENTSO-E Nordic Analysis Group, Tech. Rep., 2015.
- [3] I. Dudurych, M. Burke, L. Fisher, M. Eager, and K. Kelly, "Operational security challenges and tools for a synchronous power system with high penetration of non-conventional sources," *CIGRE Science & Engineering*, vol. 7, February 2017.
- [4] V. Gevorgian, Y. Zhang, and E. Ela, "Investigating the impacts of wind generation participation in interconnection frequency response," *IEEE Transactions on Sustainable Energy*, vol. 6, no. 3, pp. 1004–1012, July 2015.
- [5] S. Sharma, S. H. Huang, and N. Sarma, "System inertial frequency response estimation and impact of renewable resources in ERCOT interconnection," in *2011 IEEE Power and Energy Society General Meeting*, July 2011, pp. 1–6.
- [6] J. Conto, "Grid challenges on high penetration levels of wind power," in *2012 IEEE Power and Energy Society General Meeting*, July 2012, pp. 1–3.
- [7] N. W. Miller, M. Shao, S. Venkataraman, C. Loutan, and M. Rothleder, "Frequency response of California and WECC under high wind and solar conditions," in *2012 IEEE Power and Energy Society General Meeting*, July 2012, pp. 1–8.
- [8] N. W. Miller, M. Shao, R. D'quila, S. Pajic, and K. Clark, "Frequency response of the US Eastern Interconnection under conditions of high wind and solar generation," in *2015 Seventh Annual IEEE Green Technologies Conference*, April 2015, pp. 21–28.
- [9] H. Gu, R. Yan, and T. K. Saha, "Minimum synchronous inertia requirement of renewable power systems," *IEEE Transactions on Power Systems*, vol. PP, no. 99, pp. 1–1, 2017.
- [10] R. Yan, T. K. Saha, N. Modi, N.-A. Masood, and M. Mosadeghy, "The combined effects of high penetration of wind and PV on power system frequency response," *Applied Energy*, vol. 145, pp. 320 – 330, 2015.
- [11] H. Pulgar-Painemal, Y. Wang, and H. Silva-Saravia, "On inertia distribution, inter-area oscillations and location of electronically-interfaced resources," *IEEE Transactions on Power Systems*, vol. 33, no. 1, pp. 995–1003, Jan 2018.
- [12] M. Shiroei, B. Mohammadi-Ivatloo, and M. Parniani, "Low-order dynamic equivalent estimation of power systems using data of phasor measurement units," *International Journal of Electrical Power & Energy Systems*, vol. 74, pp. 134 – 141, 2016.
- [13] S. H. Jakobsen and K. Uhlen, "Vector fitting for estimation of turbine governing system parameters," in *2017 IEEE Manchester PowerTech*, June 2017, pp. 1–6.
- [14] D. T. Duong, K. Uhlen, and E. A. Jansson, "Estimation of hydro turbine-governor system's transfer function from PMU measurements," in *Power and Energy Society General Meeting, 2016 IEEE*, July 2016.
- [15] K. Tuttelberg, J. Kilter, and K. Uhlen, "Comparison of system identification methods applied to analysis of inter-area modes," in *Proceedings of International Power Systems Transients Conference 2017*, Seoul, South Korea, June 2017.
- [16] P. Kundur, *Power System Stability and Control*. McGraw-Hill, 1993.
- [17] P. M. Anderson and A. A. Fouad, *Power System Control and Stability, 2nd Edition*, M. E. El-Hawary, Ed. Wiley, 2002.
- [18] *MATLAB and System Identification Toolbox R2016b: User's Guide*, The MathWorks, Inc., Natick, Massachusetts, 2016.

Curriculum Vitae

Personal Information

Name	Kaur Tutteblerg
Date of birth	25 April 1990
E-mail	kaur.tuttelberg@ttu.ee

Institution and Occupation

Period	Description
Jan 2017–...	Tallinn University of Technology, School of Engineering, Department of Electrical Power Engineering and Mechatronics, Junior Researcher
July 2014–Dec 2016	Tallinn University of Technology, Faculty of Power Engineering, Department of Electrical Power Engineering, Chair of Power Systems, Junior Researcher
2011–2013	Goliath Wind Ltd, Electrical engineer

Education

Period	Description
2014–...	Tallinn University of Technology, Electrical Power Engineering, PhD
Jan 2016–June 2016	Norwegian University of Science and Technology (NTNU), Electrical Power Engineering
2013–2014	KTH Royal Institute of Technology, Nuclear Energy Engineering
2012–2014	Tallinn University of Technology, Electrical Power Engineering, MSc
2009–2012	Tallinn University of Technology, Electrical Power Engineering, BSc

Honors and Awards

Year	Description
2017	Smart specialisation scholarship
2015	Elering scholarship for power engineering
2014	Sigvard Eklund prize for the best nuclear engineering master's thesis in Sweden
2014	Estonian Academy of Sciences student research award
2014	Mati Jostov scholarship for PhD studies in power engineering
2014	2nd prize in the Estonian national student research awards in master's studies
2013	Kristjan Jaak scholarship for formal studies
2013	Rotalia Foundation scholarship

Supervised Dissertations

Mari Löper, Master's Diploma, 2016, (sup) Jako Kilter; Kaur Tuttelberg, Faasimõõteseadmete kasutamine koroonakadude määramiseks (Assessment of corona losses with phasor measurement units), Tallinn University of Technology Faculty of Power Engineering, Department of Electrical Power Engineering.

Tarmo Rähmonen, Master's Diploma, 2016, (sup) Jako Kilter; Kaur Tuttelberg, Ülekandevõrgu mõõtetrafode mõõtmisvigade kompenseerimine faasimõõtmistes (Compensation of transmission system instrument transformer measurement errors for phasor measurements), Tallinn University of Technology Faculty of Power Engineering, Department of Electrical Power Engineering.

Elulookirjeldus

Üldandmed

Nimi	Kaur Tutteblerg
Sünniaeg	25.04.1990
E-post	kaur.tuttelberg@ttu.ee

Töökohad ja ametid

Period	Description
01.2017–...	Tallinna Tehnikaülikool, Inseneriteaduskond, Elektroenergeetika ja mehhatroonika instituut, Nooremteadur
07.2014–12.2016	Tallinna Tehnikaülikool, Energeetikateaduskond, Elektroenergeetika instituut, Energiasüsteemide õppetool, Nooremteadur
2011–2013	Goliath Wind OÜ, elektriinsener

Haridustee

Period	Description
2014–...	Tallinna Tehnikaülikool, Elektroenergeetika, Filosoofiadoktor
01.2016–06.2016	Norwegian University of Science and Technology (NTNU), Elektroenergeetika
2013–2014	KTH Royal Institute of Technology, Tuumaenergeetika
2012–2014	Tallinna Tehnikaülikool, Elektroenergeetika, Tehnikateaduste magister
2009–2012	Tallinna Tehnikaülikool, Elektroenergeetika, Tehnikateaduste bakalaureus

Teaduspreemiad ja tunnustused

Aasta	Kirjeldus
2017	Nutika spetsialiseerumise stipendium
2015	Eleringi energeetikastipendium
2014	Sigvard Eklundi auhind parimale tuumatehnikaalasele magistritööle Rootsis
2014	Eesti Teaduste Akadeemia üliõpilastööde auhind
2014	Mati Jostovi nimeline energeetikaalase doktoriõppe stipendium
2014	Riikliku üliõpilaste teadustööde konkursi II preemia magistriastmes
2013	Kristjan Jaagu tasemeõppe stipendium
2013	Rotalia Foundation stipendium

Juhendatud väitekirjad

Mari Löper, magistrikraad, 2016, (juh) Jako Kilter; Kaur Tuttelberg, Faasimõõteseadmete kasutamine koroonakadude määramiseks, Tallinna Tehnikaülikool, Energeetika-teaduskond, Elektroenergeetika instituut.

Tarmo Rähmonen, magistrikraad, 2016, (juh) Jako Kilter; Kaur Tuttelberg, Ülekandevõrgu mõõtetrafode mõõtmisvigade kompenseerimine faasimõõtmistes, Tallinna Tehnika-ülikool, Energeetikateaduskond, Elektroenergeetika instituut.

